Holographic Microscopy : 3D Tracking of Gold Nanoparticles, Applications in Biology

Fadwa Joud El Merabi

DÉPARTEMENT DE PHYSIQUE DE
L'ÉCOLE NORMALE SUPÉRIEURE

LABORATOIRE KASTLER BROSSEL

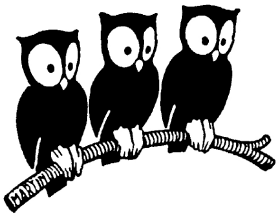

THÈSE DE DOCTORAT DE L'UNIVERSITÉ PARIS VI
spécialité : Physique Appliquée - Nanophotonique

présentée par
Fadwa JOUD EL MERABI

pour obtenir le grade de
Docteur de l'Université Pierre et Marie Curie Paris VI

Sujet de la thèse :

MICROSCOPIE HOLOGRAPHIQUE : SUIVI 3D DE NANOPARTICULES, APPLICATIONS EN BIOLOGIE

Soutenue à Paris le 10 octobre 2011 devant le jury composé de :

M.	Franck DUBOIS	Rapporteur
M.	Olivier HAEBERLÉ	Rapporteur
M.	Jean-François JOANNY	Président du jury
Mme.	Corinne FOURNIER	Examinatrice
M.	Jacques LANGLOIS	Examinateur
M.	Michel GROSS	Directeur de thèse
Mme.	Marie ABBOUD	Co-directrice de thèse
M.	Pierre DESBIOLLES	Membre invité

In the Name of God, the Merciful, the Compassionate

To my treasured wonderful mother Maha, to whom I owe each thought of hope, each smile of peace & serenity, each word of honesty & confidence, each stance of dignity, each thrill of success and every bit of my existence ...
To my beloved supporting father Assad
To the delight of my life, my lovely sister Salwa
To the soul of my very dear brother Ossman, my soul mate & my endless love
To my dearest uncle and aunt khalo Abdel Fattah & khalto Jumana
To my adorable uncle khalo Riad
To the soul of my very special grandmother tayta Souad

I dedicate this thesis ...

Remerciements

Et voilà, j'écris les remerciements de ma thèse de doctorat !! C'est un moment très émouvant que j'ai tant attendu. Il marque que cette longue aventure scientifique et humaine arrive à sa fin. Mon travail de thèse s'est déroulé d'Octobre 2008 à Septembre 2011 au Laboratoire Kastler Brossel au sein du Département de Physique de l'École Normale Supérieure de Paris. Je souhaite donc par ces quelques lignes exprimer mes sincères remerciements et témoigner de ma grande reconnaissance à tous ceux qui m'ont soutenue et qui ont contribué de près ou de loin à l'élaboration et la réussite de cette thèse.

Je désire remercier en premier lieu les membres du jury de ma thèse. Ma sincère reconnaissance s'adresse au Pr. Franck Dubois et au Pr. Olivier Haeberlé qui ont généreusement accepté de rapporter ma thèse. Je les remercie vivement pour le temps qu'ils ont consacré à la lecture de ce manuscrit. Je tiens aussi à exprimer ma profonde gratitude au Pr. Jean-François Joanny qui m'a fait l'honneur de présider le jury de ma thèse de doctorat. Je remercie aussi vivement Mme. Corinne Fournier, Pr. Jacques Langlois et Pr. Pierre Desbiolles d'avoir accepter de participer à ce jury de soutenance.

Mes remerciements les plus sincères s'adressent à Michel Gross, mon directeur de thèse. Merci Michel pour ton encadrement, pour ta disponibilité, pour ta confiance, pour ta souplesse, pour ton dynamisme, pour la liberté que tu m'as accordé et pour tout ce que j'ai appris à tes côtés. J'ai tellement apprécié ta gentillesse et tes qualités humaines remarquables. Grand merci aussi pour ton aide dans la procédure de location de mon appartement à Paris. Loin du cadre de la thèse, je n'oublierai surtout pas les discussions que nous avons eues concernant la politique au Moyen-Orient !!

Ma thèse a été réalisée en cotutelle avec l'Université Saint-Joseph de Beyrouth. Je souhaite exprimer ma profonde gratitude à Marie Abboud, ma co-directrice de thèse. Ce fut un réel plaisir de travailler avec toi Marie depuis le Master 1. Merci pour ton soutien continu, pour ta grande confiance, pour ton ouverture d'esprit, pour tes qualités humaines et pour tous les efforts que tu as fourni pour mener à bien cette collaboration.

J'aimerais remercier très vivement les membres de mon équipe "Optique des Nano-Objets" que j'ai côtoyés presque journalièrement tout le long de ces trois années de thèse. Je commence tout d'abord par le permanent de l'équipe

Jean Hare. Grand merci Jean pour ton aide continue depuis le tout début de ma thèse et aussi pour tous tes conseils administratifs précieux surtout pour les préparations de ma soutenance. Je suis reconnaissante également à mes collègues : Frédéric Verpillat, Yves Candela et Guoping Lin, auxquels je souhaite une très bonne continuation. Grand merci Frédéric pour tous les bons moments, pour les discussions qu'on a eues et surtout pour ton aide précieuse lors de mon déménagement. Je n'oublierai pas les moments drôles qu'on a vécus au labo et aussi à Marseille, Rouen et Munich ;-) et je me souviendrai toujours de cette visite de BMW world de Munich!! Grand merci aussi Yves. Je me souviens qu'on a démarré nos thèses exactement le même jour!! Merci pour tout ton aide, pour toutes les belles discussions qu'on a eues et merci surtout pour le grand interêt que tu montrais envers mes manips. Mais oui, il y aura un buffet Libanais au pot de ma thèse ;-) Grand merci aussi Guoping pour tous les bons moments qu'on a passés ensemble surtout à la cantine de l'ENS et au CEA à Saclay!!

Je n'oublierai pas les aides permanentes et le soutien que j'ai reçu de Pierre Desbiolles de l'équipe "Optique et Biologie" du laboratoire. Grand merci Pierre pour tout l'aide que tu m'as accordée, pour tes conseils précieux et pour la relecture et la correction de mes papiers.

Durant ma première année de thèse, j'ai été amenée à collaborer avec nos voisins de l'Institut Langevin (ESPCI). Cette collaboration a été enrichissante. Je tiens donc à remercier Gilles Tessier, Nilanthi Warnasooriya, Sara Y. Suck et Michael Atlan. Pour le côté "applications biologiques" de ma thèse, j'ai collaboré avec l'Institut Jacques Monod. Grand merci à Philippe Bun, qui m'a initiée, moi physicienne, à la culture cellulaire. J'ai apprécié le travail avec toi Philippe et crois moi pour la dernière fois : Il existe ;-) Merci aussi à Maïté Coppey-Moisan pour les discussions intéressantes qu'on a eues et pour m'avoir gentillement cédé une hotte à flux laminaire.

J'ai eu la grande chance de travailler au début de ma thèse avec Franck Laloë. Ce fut vraiment un plaisir et une expérience enrichissante d'avoir travaillé avec quelqu'un d'aussi compétent, respectueux et modeste. Merci Monsieur Laloë pour votre gentillesse, pour votre interêt envers le Liban et pour l'invitation chez vous à la campagne, j'en garde de très bons souvenirs.

Je désire remercier Paul Indelicato, le Directeur du Laboratoire Kastler Brossel, pour m'avoir acceuilli dans son laboratoire pendant les trois années de ma thèse. Je tiens aussi à remercier profondément tous les membres de l'équipe administrative du Laboratoire Kastler Brossel qui m'ont facilité

ma vie quotidienne au sein du laboratoire pendant ces trois ans. Merci à Thierry Tardieu pour la gestion administrative, Christophe Bernard pour la gestion des commandes et des missions, Dominique Giafferi pour la livraison des commandes et les achats externes. Je souhaite aussi remercier Mr. Didier Courtiade et David pour les travaux généraux et surtout pour m'avoir aidé, avec Dominique Giafferi, à transporter du matériel depuis Jussieu jusqu'à ma salle de manip au laboratoire. Merci aussi à Geneviève Tastevin de l'équipe "Helium 3 polarizé" du laboratoire qui est ma voisine de salle de manip. Merci également au Directeur de l'École Doctorale ED107 Mr. Roland Combescot, à la secrétaire de l'ED Mme. Marianne Peuch et à Mme. Patricia Zizzo du service des relations internationales de Paris 6.

Je tiens aussi à remercier des personnes de la Faculté des Sciences de l'Université Saint-Joseph de Beyrouth : le Doyen Toufic Rizk, Rita Matar la responsable des laboratoires de physique et Edgar Seif du service informatique.

Une pensée émue à mes très chères amies, Farah et Nour, que j'ai eu la chance de les avoir à mes côtés. Merci les filles pour tous les précieux inestimables moments qu'on a vécus ensemble, à Beit Mery, à Tripoli, à Beyrouth, à Baakline & Ba3daran... Merci Céline pour ton encouragement et pour tous les beaux moments qu'on a partagés à Beit Mery et puis à Paris. Myrna grand merci pour toutes tes pensées, tes sms, tes messages sur facebook et surtout pour le beau sourire que tu gardes toujours :-)

Je ne pourrai jamais oublier le soutien, l'encouragement quotidien et l'aide des personnes chères de ma nombreuse et merveilleuse famille. Je réserve une reconnaissance particulière à mes deux chers oncles Abdel Fattah et Riad et à ma chère tante Jumana. Grand merci pour votre aide continue, pour votre soutien inestimable, pour votre tendresse et grand amour qui m'ont rendue la vie vraiment plus agréable. Que Dieu vous protèges et vous procures santé, bonheur et longue vie. Je vous aime beaucoup.

Je ne peux, à ce moment de ma vie, que penser à ma très chère grande mère tayta Souad, qui pour elle "physique" est l'un des quelques mots qu'elle maîtrisait en Français. Je suis sure tayta que tu me voies maintenant de là où tu es et que tu es fière de ta petite fille, que tu as tant adorée, qui deviens maintenant Docteur!!

Un grand merci, du fond de mon coeur, à ma meilleure amie, ma très chère petite soeur Salwa, qui m'a accompagnée à Paris durant mes deux dernières années ici, qui m'a partagé mes heureux ainsi que difficiles moments

et qui me préparait des petits plats quand je rentrais tard du labo. Salwa tu es un précieux cadeau du ciel, que Dieu te protège et te procure santé, succès et tout le bonheur du monde. Je t'aime tant…

Une pensée d'amour à mon cher frère Ossman, qui nous a quitté très tôt… mais qui est-ce qui dit que ceux qui nous quittent par leur corps ne nous entendent et ne nous voient plus… ? Ossman tu vi toujours dans mon coeur, dans mon esprit et dans mes pensées… je te voies à côté de moi ce jour-là entrain de célébrer cet évènement marquant de ma vie. Et je te dis : je n'ai pas changé, je prends toujours le chemin qui me plaît, un seul chemin sur la terre, a réussi à me plaire celui qu'ensemble on suivait… tu me manques beaucoup…

Ces remerciements ne peuvent s'achever, sans une pensée pour mes chers parents. Tous les mots du monde ne sauraient exprimer l'immense amour que je vous porte, ni la profonde gratitude que je vous témoigne pour tous les efforts et les sacrifices que vous n'avez jamais cessé de consentir pour mon instruction et mon bien-être. Que Dieu tout puissant vous garde et vous procure santé, bonheur et longue vie . Merci papa pour ton soutien et encouragement continus, pour ta grande confiance et pour la tendre affection que tu m'as toujours témoigné. À ma précieuse mère qui a réussit beaucoup de fois à garder le moral à ma place et qui juste par sa présence donne un gôut spécial à ma vie, je dis : merci maman pour toutes tes prières, bénédictions, encouragements, dévouements et inestimables sacrifices. Je ne te remercierai jamais assez pour toute la tendresse, l'amour et le bonheur que tu m'as donné et pour tout ce que tu as fait pour moi, c'est à toi principalement que je dois ce que suis et ce que je serais. Que tu trouves dans ce travail le fruit de ta grande patience, de tes immenses sacrifices, de ton éternel dévouement et l'expression de mon profond amour. Ridaki !!

Enfin je dis : louange à Dieu qui m'a donné la force, la volonté, le courage, la patience et l'endurance jusqu'à l'accomplissement de cette thèse après un long et dur travail.

Fadwa Joud El Merabi
Paris, Septembre 2011

Holographic Microscopy : 3D Tracking of Gold Nanoparticles, Applications in Biology

Abstract:

In this thesis, we have developed a novel heterodyne digital holographic microscope combining the off-axis geometry and phase-shifting interferometry to detect and localize in three dimensions nanometric-sized colloidal gold particles used as biological markers in live cells environments. Genuine aliasing-free holograms are obtained using the phase-shifting technique that is performed using two accurately synchronized Acousto-Optic modulators, and since a heterodyne detection is performed, holograms are only shot-noise limited. We have also elaborated an ingenious numerical reconstruction method that offers striking advantages : reconstructed images do not suffer from longitudinal distortions, reconstruction parameters are obtained without an additional experimental calibration, aberrations compensation as well as lens curvature corrections are automatically obtained.

Using the developed optical apparatus and numerical processing procedure, we have been able to image and localize for the first time in the context of digital holographic microscopy, 40 nm gold particles attached to the integrin surface receptors of live 3T3 fibroblasts with a localization precision of 5 nm laterally and 100 nm in depth, when 32 images averaging is performed. Additionally, 3D mapping of the entire scattered field was achieved where the 3D exploration was performed within a relatively big volume $\sim (90 \times 90 \times 90)$ μm. Finally, we have been able to characterize the scattering regimes of the gold markers and cellular structures by analyzing the 3D shape of the corresponding scattering patterns that are easily accessible by digital holography.

Keywords:

Digital Holographic Microscopy, Gold Nanoparticles, 3T3 Fibroblasts, Integrin Receptors, Holographic Reconstruction, Heterodyne Detection, Optical Microscopy, Phase-Shifting Holography, Off-axis Holography, Acousto-optic Modulators

Microscopie Holographique : Suivi 3D de Nanoparticules d'Or, Applications en Biologie

Résumé:

Dans cette thèse, nous avons développé une nouvelle technique de microscopie holographique digitale hétérodyne pour détecter et localiser en trois dimensions des nanoparticules d'or utilisées comme marqueurs biologiques dans des cellules vivantes. On combine la géométrie hors-axe et l'interférométrie par décalage de phase, où deux modulateurs Acousto-Optique minutieusement synchronisés sont utilisés, afin d'obtenir des hologrammes sans alias. La détéction hétérodyne permet d'atteindre la limite de bruit théorique (shot-noise). Nous avons aussi élaboré une méthode de reconstruction numérique astucieuse : les images reconstruites ne souffrent pas de distortions longitudinales, les parmètres de reconstruction sont obtenus sans avoir besoin de les mesurer en effectuant une calibration expérimentale supplémentaire, la compensation des aberrations et les corrections de courbure de phase sont automatiquement obtenus.

Nous avons pu imager et localiser, pour la première fois dans le contexte de la microscopie holographique digitale, des billes d'or de 40 nm de diamètre, attachées aux récepteurs transmembrannaires intégrine de fibroblastes 3T3 vivantes avec une précision de localization de 5 nm latéralement et 100 nm en profondeur quand un moyennage sur 32 images est effectué. De plus, une exploration 3D, dans un volume relativement grand $\sim (90 \times 90 \times 90)$ μm, de la totalité du champ diffusé est obtenu. Finalement, nous avons pu caractériser les régimes de diffusion des marqueurs d'or et des structures cellulaires en analysant la forme 3D des motifs de diffusion correspondants qui sont facilement accessible par holographie digitale.

Mots-clés:

Microscopie Holographique Digitale, Nanoparticules d'Or, Fibroblastes 3T3, Récepteurs Intégrine, Reconstruction Holographique, Détection Hétérodyne, Microscopie Optique, Décalage de Phase, Holographie Hors-axe, Modulateurs Acousto-optiques

Table of Contents

Symbols & Notations **xvii**

Acronyms **xix**

1 Introduction **1**
1.1 Context . . . 1
1.2 Motivations and Scope of the thesis . . . 3
1.3 Manuscript Organization . . . 4

2 Optical Imagery of Complex Scattering Media **7**
2.1 Light-Matter Interaction : A Review . . . 8
2.1.1 The refractive index . . . 8
2.1.2 Scattering . . . 9
2.1.2.1 Rayleigh Scattering Regime . . . 9
2.1.2.2 Mie Scattering Regime . . . 10
2.1.2.3 The Phase Function . . . 10
2.1.2.4 The Anisotropy Factor . . . 11
2.1.3 Absorption . . . 12
2.1.4 Extinction . . . 13
2.2 Optical Imagery of Biological Media . . . 13
2.2.1 Optical Absorption of Biological Tissues . . . 14
2.2.2 Optical Scattering of Biological Tissues . . . 14
2.2.2.1 Coherent Scattering in Biological Tissues . . . 14
2.2.2.2 The Anisotropy Factor of Biological Tissues g_{bio} 15
2.3 Optical Imagery of Gold Nanoparticles as Biomarkers . . . 15
2.3.1 Synthesis of Gold Nanoparticles . . . 16
2.3.2 Optical Properties of Gold Nanoparticles . . . 16
2.3.2.1 Complex Refractive Index and Dielectric Constant of Gold . . . 17
2.3.2.2 Scattering of AuNps . . . 18
2.3.2.3 Absorption of AuNps . . . 20
2.3.3 Biological Properties of Gold Nanoparticles . . . 20
2.3.3.1 Cytotoxicity of AuNps . . . 20
2.3.3.2 Bioconjugation of AuNps . . . 20
2.4 Overview . . . 21

3 Holography : the principles **23**
3.1 Historical Introduction . . . 23
3.2 Physical basis of Holography . . . 25
3.2.1 Wave Theory of Light . . . 26
3.2.2 Interference Theory . . . 29
3.2.3 Coherence Requirements . . . 31
3.2.3.1 Temporal Coherence . . . 31
3.2.3.2 Spatial Coherence . . . 33
3.2.4 Diffraction Theory . . . 35
3.3 Theory of Classic Holographic Imaging . . . 36
3.3.0.1 Holographic Recording . . . 37
3.3.0.2 Optical Reconstruction . . . 39
3.3.0.3 Off-axis configuration in classic holography . . 41
3.3.0.4 Overview for classic holography . . . 43
3.4 Digital Holography . . . 44
3.4.1 Digital Recording of Holograms . . . 44
3.4.2 Numerical Reconstruction Approaches . . . 50
3.4.2.1 Reconstruction by the Fresnel Transformation 51
3.4.2.2 Reconstruction by the Angular spectrum method . . . 57

4 Heterodyne Digital Holography **65**
4.1 Phase-Shifting Digital Holography . . . 66
4.1.1 Phase-Shifting using a mirror mounted on a Piezoelectric Transducer . . . 67
4.1.2 Phase-Shifting using a pair of Acousto-Optic Modulators 68
4.1.2.1 Acousto-Optics Modulators . . . 68
4.1.2.2 Experimental Configuration for Heterodyne Phase-Shifting Holography . . . 69
4.1.2.3 Four phases Demodulation . . . 72
4.2 Holography at Ultimate Shot-Noise . . . 73
4.3 Application for the Imagery of Vibrating Objects . . . 74

5 Interferometric Heterodyne Digital Holographic Microscopy **81**
5.1 Optical Apparatus and General Reconstruction Scheme . . . 82
5.1.1 Optical Apparatus for the Holographic Microscope . . 82
5.1.2 Optical Arrangement for Reconstruction in Holographic Microscopy . . . 83
5.1.3 The principle of the Reconstruction In Heterodyne Holographic Microscopy . . . 85

5.2 First Step of The Reconstruction : Reconstruction of the Conjugate Image . . . 86
5.2.1 Determination of the lens, tilt and magnification parameters by a proper calibration of the setup . . . 86
5.2.1.1 The lens phase correction . . . 88
5.2.1.2 The off-axis Tilt phase correction . . . 91
5.2.1.3 The MO transfer magnification factor G . . . 92
5.2.1.4 Spatial Filtering . . . 93
5.2.2 Determination of the lens, tilt and magnification factor by reconstructing the image of the MO exit pupil . . . 93
5.2.2.1 Lens parameter . . . 94
5.2.2.2 The tilt parameter and Spatial filtering . . . 95
5.2.2.3 The magnification parameter G . . . 97
5.2.2.4 The Optical Etendue . . . 100
5.3 Second Step : 3D Reconstruction of the Object by propagation of the Angular Spectrum . . . 102
5.4 Abberations . . . 105
5.4.1 Propagation kernel for large Numerical Aperture MO . 106
5.4.2 Specimen maintained in a culture medium and imaged with an air MO . . . 107
5.4.3 Specimen uncovered with a coverslip and imaged with a cover glass corrected MO . . . 109
5.4.3.1 Abberations introduced by an improper glass coverslip correction . . . 109
5.4.3.2 Abberations correction : the principle . . . 110
5.4.3.3 Experimental results . . . 111
5.5 Overview of the Reconstruction procedure in Holographic Microscopy . . . 112

6 Digital Holographic Microscopy of Gold Nanoparticles in living cells 117
6.1 Biological Context . . . 117
6.2 Materials and Methods . . . 118
6.2.1 Biological Specimen Preparation . . . 118
6.2.1.1 Cell Line . . . 119
6.2.1.2 Cells preparation . . . 120
6.2.1.3 Preparation of Gold Conjugates . . . 121
6.2.1.4 Gold-Cells conjugation . . . 123
6.2.1.5 Specimen in the Observation Chamber . . . 125
6.2.2 Optical Methods . . . 125
6.2.2.1 Experimental Apparatus . . . 125

6.2.2.2 Sample Illumination . . . 129
6.2.2.3 Holograms Acquisition . . . 130
6.2.3 Reconstruction Procedure . . . 131
6.3 Experimental Results . . . 133
6.3.1 Gold Nanoparticles in live cells environments . . . 134
6.3.1.1 3T3 cells labeled with several gold particles . 134
6.3.1.2 3T3 cell labeled with a single gold particle . . 143
6.3.2 Unlabeled 3T3 Cell . . . 153
6.3.3 Free Gold Nanoparticles . . . 156
6.4 Overview . . . 165

7 Technical Developments 167
7.1 Preparation of Live Cells Specimens . . . 168
7.1.1 Cell Culture and the Observation Chamber . . . 168
7.1.2 Biological Specimen Preparation . . . 169
7.1.2.1 Preparation of Gold Conjugates . . . 169
7.1.2.2 Gold-Cells Conjugation . . . 170
7.1.3 Specimen in the Observation Chamber . . . 172
7.1.4 Eliminating Uncoupled Gold Conjugates . . . 172
7.2 Specimen Illumination Geometry . . . 173
7.2.1 Slant Illumination Geometry . . . 174
7.2.1.1 Materials and Methods . . . 174
7.2.1.2 Experimental Results . . . 179
7.2.2 TIR Illumination Geometry . . . 192
7.2.2.1 3T3 Cells conjugated to 80 nm AuNps . . . 193
7.2.2.2 3T3 Cells conjugated to 60 nm AuNps . . . 193
7.2.2.3 3T3 Cells conjugated to 40 nm AuNps . . . 195
7.3 Experiments using a Short Coherence Length Laser . . . 199
7.4 Overview . . . 201

8 Conclusion and Perspectives 203

A Biochemical Protocols 207
A.1 Biotinylation Protocol . . . 207
A.2 Gold Nanoparticles Coating Protocol . . . 214

B Published Papers 217
B.1 3D exploration of light scattering from live cells in the presence of gold nanomarkers using holographic microscopy . . . 217
B.2 Imaging gold nanoparticles in living cell environments using heterodyne digital holographic microscopy . . . 226
B.3 Shot Noise in Digital Holography . . . 237

B.4 Fringe-free holographic measurements of large-amplitude vibrations 251

List of Figures **255**

List of Tables **260**

Bibliography **263**

About The Author **275**

Symbols & Notations

σ_a	Absorption cross section
g	Anisotropy factor
τ_c	Coherence time
ℓ_c	Coherence length
$\tilde{n}$	Complex refractive index
ε	Complex dielectric constant
$\nabla\times$	Curl operator
d_{px}	Dimension of the camera's pixel
$\nabla\cdot$	Divergence operator
$\vec{E}$	Electric field
σ_e	Extinction cross section
f_{CCD}	Frame rate frequency of the camera
κ	Imaginary part of the refractive index
∇^2	Laplace operator
$\vec{B}$	Magnetic field
G	Microscope objective magnifying factor
d_{px}	Pixel's dimension of the conjugate image
c	Propagation speed of light in vacuum
μ_s'	Reduced scattering coefficient
σ_s	Scattering cross section
μ_s	Scattering coefficient
$p(\vec{s}, \vec{s}')$	Scattering phase function
$\Delta\nu$	Spectral bandwidth of light sources
λ	Wavelength
k	Wave number

Acronyms

AuNPs	Gold Nanoparticles
AOM	Acousto-Optic Modulator
BS	Beam Splitter
CCD	Charge Coupled Device
DC	Digital Counts
DH	Digital Holography
DHM	Digital Holographic Microscopy
DFT	Direct Fourier Transform
DMEM	Duelbecco's Modified Eagle's Medium
ECM	ExtraCellular Matrix
FFT	Fast Fourier Transform
FWHM	Full Width at Half Maximum
HBSS	Hank's Balanced Salt Solution
HWP	Half Wave Plate
IFT	Inverse Fourier Transform
MO	Microscope Objective
NA	Numerical Aperture
NIR	Near Infra Red
NPs	Nanoparticles
OD	Optical Density
PBS	Phosphate Buffered Saline
PEG	PolyEthylene Glycol
PBS	Polarizing Beam Splitter
PZT	Piezoelectric Transducer
rpm	Round Per Minute
SNR	Signal to Noise Ratio
TIR	Total Internal Reflection

Chapter 1

Introduction

Contents

1.1 Context 1
1.2 Motivations and Scope of the thesis 3
1.3 Manuscript Organization 4

1.1 Context

The importance of light in medicine dates back to ancient history where the healing power of light was attributed to mythological figures called "gods of light". Throughout human history, and with the advent of science and technology, the contribution of light in medicine has evolved. The invention of the microscope as well as the invention of the Laser were major milestones for the development of research in the field of biophotonics, a field that has emerged from research conducted at the interface of the physical and biological sciences.

Numerous optical imagery techniques have been developed in order to investigate biological tissues, at the cellular and subcellular levels, for medical diagnostic and therapeutic applications. Although these conventional imagery techniques produce high resolution images, they suffer from two main drawbacks :

- **Only intensity information is captured** : Since most recording materials are only intensity-sensitive, the phase information of the investigated specimen is lost during the imaging process. However, in biological imagery, the quantitative phase information is important since biological objects are characterized as transparent "phase objects" that exhibit weak intensity contrasts. Phase-contrast imagery techniques (e.g, Differential Interference Contrast DIC, Zernike etc...) should thus be employed in order to visualize biological objects.

- **Only two dimensional information can be obtained** : In order to achieve high lateral resolution, high Numerical Apertures (NA) should be considered. However, for high NA, the depth of focus ($\Delta z_{foc} = n\lambda/NA^2$ where λ is the wavelength and n the refractive index of the medium) is small. Hence, only two dimensional information of the investigated object can be obtained. In order to obtain full 3D information, images at several focal depths should be recorded. This requires a physical sectioning of the sample or a mechanical motion along the optical axis to scan the complete experimental volume. However, physical sectioning of a biological sample is invasive and the mechanical operation of scanning increases the acquisition time and increases consequently the exposure time which might damage the biological specimen. Furthermore, since scanning is needed in order to obtain 3D images, dynamics of the investigated specimen cannot be observed.

An alternative potential optical imagery method that allows to circumvent the drawbacks of conventional optical imagery techniques is Digital Holographic Microscopy (DHM). In DHM, two components of coherent light are superimposed : one fraction illuminates the specimen while the other part reaches the digital detector intact. The resulting interference pattern (hologram), contains amplitude as well as phase information in its intensity profile. The image of the illuminated specimen is then numerically reconstructed using Fourier optics-based algorithms. Full 3D information of the object is thus revealed from a single recorded hologram and without any sectioning or mechanical scanning since the focusing control is performed numerically during the reconstruction process (this is called the "numerical focusing" capability of DHM). Digital Holographic Microscopy is thus potentially adequate for the optical imagery of biological objects and can be used to monitor the dynamic changes of investigated specimens. Many worldwide research groups have used DHM for different biomedical applications : imaging various types of cells [Colomb *et al.* 2006b, Debailleul *et al.* 2008, Mann *et al.* 2006], studying cell cultures and their evolution during time [Dubois *et al.* 2008], investigating cellular dynamics [Kemper *et al.* 2006, Kemper & von Bally 2008, Jeong *et al.* 2007], monitoring laser microsurgery on cells [Yu *et al.* 2009], cell counting [Mölder *et al.* 2008], to cite some.

Many of the cellular constituents, like the nuclear receptors, some organelles, surface receptors, DNA molecules, enzymes etc... have typical dimensions in the nanometer scale. Hence, in order to investigate and characterize such objects, new tools capable of probing the nanometer world are needed. For this purpose, nanotechnology have provided a diverse set of nano-objects

that can be used for biological labelling. Particularly, gold nanoparticles present unique optical and biochemical properties that made them very appealing to probe biological systems. Gold nanoparticles are biocompatible and, given their chemical properties, they allow for custom functionalization and for preparation in wide size range. Furthermore, gold nanoparticles present excellent optical properties that result from the resonant excitation of collective oscillations of the particles' free electrons, also called surface plasmons, which cause large optical cross-sections at their respective resonance wavelengths [Kreibig & Vollmer 1995]. Gold nanoparticles are not only very bright but they also display an extreme photophysical stability. Since their signal is based on light scattering, gold nanoparticles do not blink or bleach and enable, unlike fluorescent dyes or quantum dots, continuous observation without limitations in total observation time.

Gold nanoparticles have been used for a broad range of biomedical applications. They have been used as biomarkers for live cell imaging using photothermal tracking [Lasne *et al.* 2006, Cognet *et al.* 2003, Boyer *et al.* 2003] and light scattering spectroscopy [Raschke *et al.* 2003] has been demonstrated. The detection of live oral cancer cells using gold nanoparticles has been obtained [El-Sayed *et al.* 2005]. Detection of DNA sequences using gold nanoparticles has been achieved [Storhoff *et al.* 2004] and they have also been used as vectors for tumor directed drug delivery [Paciotti *et al.* 2004] and many more biological applications [Sperling *et al.* 2008, Lee *et al.* 2009].

1.2 Motivations and Scope of the thesis

We have seen that digital holographic microscopy is a propitious tool for biomedical imagery. Additionally, the use of gold nanoparticles in this same application field is promising and offers exceptional assets. In this thesis, we have combined both tools and thus we have developed a scattering-based holographic microscope to detect and localize in three dimensions nanometric-sized colloidal gold particles used as biological markers in live cells environments.

The three-dimensional detection and localization of scattering gold nanoparticles, either spin coated on a glass substrate or in free motion within a water suspension, has been already achieved in our group in Laboratoire Kastler Brossel by Atlan et al. [Atlan *et al.* 2008]. In this thesis work, we go further and we target the 3D detection and localization of gold particles attached to cellular surface receptors of live cells.

1.3 Manuscript Organization

This thesis is organized into eight chapters and two sets of appendices. The main body of content in this manuscript is contained in Chapters 4 , 5 , 6 and 7 .

Chapter 2 "Optical Imagery of Complex Media" characterizes the light interaction with gold nanoparticles conjugated to biological cells. First, the basic concepts that describes a general light-matter interaction are reviewed. Then the optical properties of biological tissues are depicted. Finally, the optical detection and unique properties of gold nanoparticles as potential biological markers are presented.

The basic optical concepts and principles of holography are reviewed in Chapter 3 "Holography : the principles" . Both classic holography and digital holography are then presented. Approaches for numerical reconstruction of recorded holograms are finally discussed.

Chapter 4 "Heterodyne Digital Holography" is dedicated for the description of the adopted heterodyne detection-based holographic system that uses phase-shifting holography. Some possible direct applications are also presented.

The general description of the optical apparatus used for holographic microscopy experiments as well as the optical arrangement that is considered for the reconstruction process are described in Chapter 5 "Interferometric Heterodyne Digital Holographic Microscopy" . An exhaustive study of the reconstruction procedure that we used for the reconstruction of all our experimental data in this thesis is also provided while discussing about possible aberration corrections.

Chapter 6 "Digital Holographic Microscopy of Gold Nanoparticles in living cells" contains main experimental results obtained for gold nanoparticles conjugated to live cells. First, the biochemical procedure that we used in order to attach gold nanoparticles to live cells is outlined. Then a detailed description of the experimental apparatus is presented. Finally experimental results are depicted and discussed.

Some technical and experimental developments that tend to treat the limitations encountered in the previous chapter are presented in Chapter 7 "Technical Developments" .

Chapter 8 presents an overall conclusion with an outlook to possible future experimental developments.

The biochemical protocols that were used in this thesis are included in Appendix A whereas the published papers are attached in Appendix B .

Chapter 2

Optical Imagery of Complex Scattering Media

Contents

2.1 Light-Matter Interaction : A Review 8
2.1.1 The refractive index 8
2.1.2 Scattering 9
2.1.3 Absorption 12
2.1.4 Extinction 13
2.2 Optical Imagery of Biological Media 13
2.2.1 Optical Absorption of Biological Tissues 14
2.2.2 Optical Scattering of Biological Tissues 14
2.3 Optical Imagery of Gold Nanoparticles as Biomarkers 15
2.3.1 Synthesis of Gold Nanoparticles 16
2.3.2 Optical Properties of Gold Nanoparticles 16
2.3.3 Biological Properties of Gold Nanoparticles 20
2.4 Overview 21

A scattering-based imagery and localization of nanometric gold particles conjugated to live biological cells is the main ambition of this thesis. When gold-labeled cells are optically investigated, the light interaction with such objects is mainly dominated by absorption and scattering processes. The scope of this chapter is to characterize this interaction for a better understanding of the light propagation in such complex media.
In the first section of this chapter, Section 2.1, we will present a review of the basic concepts that describes a general light-matter interaction. The optical and spectral properties of biological tissues are presented in Section 2.2. Section 2.3 addresses the physics behind gold nanoparticles : their optical detection is described and their unique properties as potential biological markers are presented.

2.1 Light-Matter Interaction : A Review

Our main interest is in the propagation and scattering characteristics of a wave in a biological media in the presence of nanometric-sized gold particles. The interaction of light with small particles depends strongly on the size, shape and composition of the particles, as well as on the composition of the medium in which the particles are embedded.

This section reviews the basic concepts that are needed to describe the propagation of light waves in such complex media.

2.1.1 The refractive index

The *refractive index* (or *index of refraction*) of a medium is a complex number noted $\tilde{n}$ with both a real and imaginary part. It describes the linear optical properties of the medium and its general form is given by :

$$\tilde{n}(\lambda) = n(\lambda) - i\,\kappa \tag{2.1}$$

The imaginary part encompasses the attenuation of a wave due to absorption (and scattering if the medium is heterogeneous) at a particular wavelength, thus the imaginary part is also called the extinction coefficient κ. The convention is to refer to the real part as the "refractive index" (as distinct from the "complex refractive index").

The real part, noted n, characterizes the phase velocity of the wave in the propagation medium and is expressed as a ratio of the speed of light in vacuum c (where $c \simeq 3 \cdot 10^8 m\,s^{-1}$) relative to that in the considered medium c_{med} :

$$n = \frac{c}{c_{med}} \tag{2.2}$$

$n_{vac} = 1$ and the wavelength of light in the medium λ_{med} is given in terms of the vacuum wavelength λ_{vac} as :

$$\lambda_{med} = \frac{\lambda_{vac}}{n_{med}} \tag{2.3}$$

Even though the phase speed and the wavelength of light depend on the refractive index, the wave frequency ν is always the same as in the vacuum :

$$\nu = \frac{c}{\lambda_{vac}} = \frac{c_{med}}{\lambda_{med}} \tag{2.4}$$

2.1.2 Scattering

When a light wave propagates in a medium and hits a localized structure with a different refractive index, a scattering process will occur : some of the incident light is redirected over a range of angles relative to the scattering structure. The scattering process depends on the size, morphology, and structure of the scattering object. In principle, the scattered radiation can be calculated if the refractive index of the medium where the light wave initially propagates, the refractive index of the scattering object, and the size and shape of the scatterer are known.

For a monochromatic wave that has a given intensity I_0 encountering the scattering object, some amount of power P_{scatt} gets spatially redirected (i.e. scattered). The ratio of the power scattered out of the wave to the incident intensity is called the *"scattering cross section"* σ_s .

$$\sigma_s = \frac{P_{scatt}}{I_0} \tag{2.5}$$

This parameter is used to quantify the scattering process.

A medium containing a uniform distribution of identical scatterers is characterized by the scattering coefficient μ_s :

$$\mu_s = \rho\,\sigma_s \tag{2.6}$$

where ρ is the density number of scatterers.
The scattering coefficient is essentially the cross-sectional area for scattering per unit volume of medium.

The appropriate expressions for calculation of the scattering cross section expressed above are provided from two theoretical frameworks : the theory of Rayleigh Scattering (after Lord Rayleigh) and the theory of Mie Scattering (after Gustav Mie).

2.1.2.1 Rayleigh Scattering Regime

When a light wave is scattered by non-absorbing structures much smaller than its wavelength, the corresponding scattering regime is called *"Rayleigh Scattering"* . The most important implication of the small size-to-wavelength ratio is that, at any moment in time, the scattering object sees only a spatially uniform electric field in the surrounding medium. In the electromagnetic wave description of light, this condition gives rise to a dipole moment yielding to a

redistribution of the charges in the scatterer. This dipole moment oscillates in time with the frequency of the incident field and, as a consequence, gives off dipole radiation [Bohren & Huffman 1983, Hulst 1981, Ishimaru 1978].

2.1.2.2 Mie Scattering Regime

Scattering of light by spherical objects is described by Mie theory [Mie 1908], which is in principle applicable at any size-to-wavelength ratio. In the intermediate size-to-wavelength ratio range, where the Rayleigh and geometric approximations are not valid, Mie theory is used [Bohren & Huffman 1983, Hulst 1981, Ishimaru 1978]. Thus a scattering process that occurs in this region where the scatterer size and wavelength are comparable is called the *"Mie scattering regime"*. Because the scatterer is on the order of the wavelength, it experiences a more complex field in the space around it at any moment in time, and thus the motion of charges in the scatterer in response to the field is also more complex. This results in a more complex angular dependence for the scattered light relative to the Rayleigh approximation. There can also be resonances and nulls due to the constructive and destructive interferences of the fields set up in the scatterer.

Because Mie scattering theory has no size limitations and converges to the limit of geometric optics for large particles, it may be used for describing most spherical particle scattering systems, including Rayleigh scattering.

The Mie scattering theory was specifically developed for spherical particles, although the label "Mie regime" is commonly used to refer to scattering from particles of arbitrary shape whose dimensions are on the order of or greater than the wavelength.

2.1.2.3 The Phase Function

The angular distribution for a single scattering event is described by the scattering phase function $p(\vec{s}, \vec{s}')$, where $\vec{s}$ is the direction of the incident light and $\vec{s}'$ is the direction of the scattered light as illustrated on Figure 2.1. The angle between directions $\vec{s}$ and $\vec{s}'$ is noted θ. If scattering is symmetric relative to the direction of the incident wave, then the phase function depends only on the scattering angle θ and is defined as the probability density function for scattering, in the direction $\vec{s}'$, of an incident light wave traveling in the direction $\vec{s}$ [Cheong *et al.* 1990] :

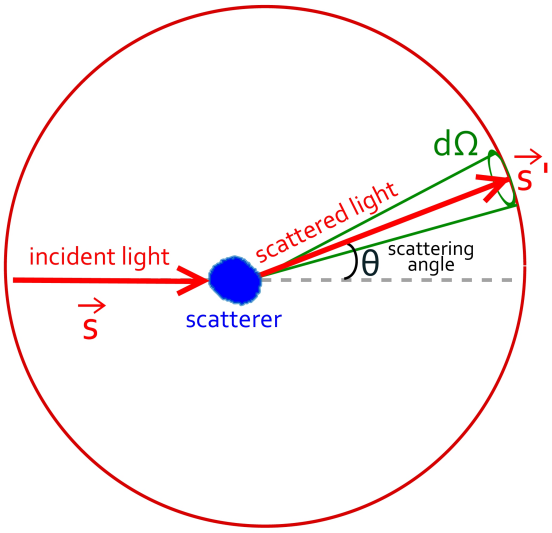

Figure 2.1: Scattering of a light wave by a localized scatterer

$$\int_{4\pi} p(\vec{s}, \vec{s}')\, d\Omega = 1 \tag{2.7}$$

where $d\Omega$ is the differential solid angle in the scattering direction $\vec{s}'$ as illustrated on Figure 2.1 .

The scattering phase function can be difficult to calculate, especially for complex scattering structures where detailed knowledge of the system is not possible. It is thus necessary to approximate this function.

2.1.2.4 The Anisotropy Factor

In order to approximate the scattering phase function, we introduce a new parameter, g , which is the average cosine of the phase function called the *anisotropy factor*. g is defined as the integral over all angles of the phase function (4π steradians for a complete circle) multiplied by the cosine of the scattering angle θ :

$$g = \int_{4\pi} p(\vec{s}, \vec{s}')\, (\vec{s} \cdot \vec{s}')\, d\Omega \tag{2.8}$$

g defines thus the mean cosine of the scattering angle θ .

The anisotropy factor g is a measure of the asymmetry of the single scattering pattern and its value defines the scattering regime and varies in the

range from 0 to ± 1 . A scatterer with $g > 0$ is more likely to forward-scatter a photon, while a negative g indicates a preference for backward scattering :

- when $g = 0$, light is scattered isotropically and this scattering process is called *isotropic scattering regime*
- when $g = 1$, light is scattered in the direction of the incident wave and the scattering process is a total *forward scattering regime*
- when $g =$ -1 , light is scattered completely backwards and the scattering process is a total *backward scattering regime*

2.1.3 Absorption

When a light wave propagates in a medium and hits a localized structure, an absorption process will occur : the absorbing structure extracts some energy from the incident light.
For a localized absorber, the *"absorption cross section"* σ_a, which is the ratio of the absorbed power to the incident intensity, can be defined in the same manner as for scattering :

$$\sigma_a = \frac{P_{abs}}{I_0} \tag{2.9}$$

where P_{abs} is the amount of power absorbed out of an initially uniform wave of intensity I_0 .

A medium with a uniform distribution of identical absorbing structures can be characterized by the *"absorption coefficient"* μ_a :

$$\mu_a = \rho\, \sigma_a \tag{2.10}$$

where ρ is the density number of absorbers.

For an absorber of thickness z, the transmitted intensity I_t is given by the Beer-Lambert law :

$$I_t = I_0\, e^{\mu_a \cdot z} \tag{2.11}$$

and the *transmission* T of the structure is thus defined as the ratio of the transmitted intensity I_t to the incident intensity I_0 :

$$T = I_t / I_0 \tag{2.12}$$

The attenuation, also called absorbance A or optical density OD, of a structure is given by :

$$A = OD = log_{10}(I_0/I_t) = -log_{10}(T) \tag{2.13}$$

2.1.4 Extinction

The total extinction of the incident light wave by the localized structure contains contributions of both scattering and absorption. The extincted energy is the sum of the absorbed and scattered energy. We can define thus the *"extinction cross section"* σ_e that is given by :

$$\sigma_e = \sigma_s + \sigma_a \tag{2.14}$$

2.2 Optical Imagery of Biological Media

Various photonic tools for probing, manipulating, and interacting with biological systems are provided by the electromagnetic spectrum of light. A great variety of electromagnetic phenomena are used in the field of biomedical photonics to detect and treat diseases and to contribute to the advancement of the scientific knowledge.
In this thesis, we are interested by the phenomenon of *propagation of "light"* in biological tissues labeled with gold nanomarkers, where the term "light" refers here to the visible and near infrared (NIR) portion of the electromagnetic spectrum.

The interaction of visible and NIR light with biological tissues is dominated by [Richards-Kortum & Sevick-Muraca 1996] :

- Absorption processes which are due to the presence of various chromophores such as hemoglobin, oxyhemoglobin, melanin, water, and lipids
- Scattering processes which are due to the cell membrane and cell structures such as the nucleus, mitochondria, lysosomes etc... that have heterogeneous refractive indices

Penetration of light in tissue is dependent on the extent of the two processes above and is low in the high-energy visible region of the spectrum. This is due to high absorption by hemoglobin and severe light scattering. In the wavelength regime between 600 nm and 1100 nm, absorption and

scattering losses are lower permitting high-light penetration. This is the so-called "optical imaging window" which is exploited for deep imaging in tissues [Richards-Kortum & Sevick-Muraca 1996].

2.2.1 Optical Absorption of Biological Tissues

The process of absorption in biological tissues is important for medical diagnostic and therapeutic applications :

- Diagnostic applications : Transitions between two energy levels of a molecule that are well defined at specific wavelengths could serve as a spectral fingerprint of the molecule for diagnostic purposes

- Therapeutic applications : Absorption of energy is the primary mechanism that allows light from a laser to produce physical effects on tissues (e.g., heating) for treatment purposes

The core of this thesis work is the scattering process, we will not thus focus on absorption.

2.2.2 Optical Scattering of Biological Tissues

In biological tissues, scattering interactions are often dominant mechanisms affecting light propagation. In biological tissues, scattering processes occurs because these objects are very heterogeneous structures and correspondingly have spatial variations in their optical properties. The spatial variation and density of these fluctuations make these tissues strong scatterers of light.

2.2.2.1 Coherent Scattering in Biological Tissues

Various cellular structures, such as mitochondria and nuclei, and extracellular components like collagen fibers have sizes on the order of hundreds of nanometers to a few microns, and are comparable in dimension to the photon wavelengths generally used in biomedical applications (0.5 to 1 μm). When monochromatic coherent sources of high coherence length are used to investigate biological structures, the scattered light exhibits incoherent properties and can also exhibit coherent properties since the size of the scatterers (cellular structures) is on the order of the excitation wavelength.

2.2.2.2 The Anisotropy Factor of Biological Tissues g_{bio}

Although the cellular structures are not necessarily spherical, their scattering behavior can be modeled reasonably well by Mie theory applied to spheres of comparable size and refractive index. Refractive index in tissues is of great importance for light-tissue interaction. Most tissues have refractive indices for visible light in the range from 1.335 to 1.62 [Tuchin 2007, Duck 1990].

We have seen in the previous section (Section 2.1), that the overall directional tendency of the scattered light is represented by the anisotropy factor g which characterizes the scattering phase function.

It is demonstrated that for biological tissues, this anisotropy factor g_{bio} is well characterized when the scattering phase function is approximated using the Henyey-Greenstein function [Prahl 1988, Yoon 1988, Vo-Dinh 2003, Tuchin 2002, Jacques *et al.* 1987] :

$$p(\vec{s},\vec{s'}) = p(\theta) = \frac{1}{4\pi} \cdot \frac{1 - g_{bio}^2}{(1 + g_{bio}^2 - 2g_{bio}\cos\theta)^{3/2}} \tag{2.15}$$

In these approximation conditions, g_{bio} is given by :

$$g_{bio} = 1 - \mu_s'/\mu_s \tag{2.16}$$

where μ_s' is the reduced scattering coefficient that describes the random dispersion of scattered light in the tissues due to the strong scattering.

It is demonstrated experimentally that the anisotropy factor of biological cells g_{bio} varies in the range from 0.8 to 0.95 [Prahl 1988, Yoon 1988, Vo-Dinh 2003, Jacques *et al.* 1987, Cheong *et al.* 1990] i.e. close to one. This yields to a scattering that is strongly peaked in the forward direction.

2.3 Optical Imagery of Gold Nanoparticles as Biomarkers

Gold nanoparticles are spherical clusters of gold atoms with diameters typically between 1 and 100 nm. They are complex many-electron systems, where reduced sizes and quantum confinement of electrons and phonons give birth to fascinating new effects, potentially tunable with particle size and shape.

Gold nanoparticles have been broadly used in the field of biomedical imagery because they present a set of unique size and shape-dependent

optical and biochemical properties in addition to their easy synthesis in a wide size range.

This section presents a review about gold nanoparticles and their potential use as biological markers. In the first part of this section, the synthesis of nanometric-sized colloidal gold particle is reviewed. The optical properties of gold nanoparticles are presented in the second part of this section. In the last part, biochemical properties of gold nanoparticles, which makes them appealing biological markers, are presented.

2.3.1 Synthesis of Gold Nanoparticles

The synthesis of gold nanoparticles was first reported by Michael Faraday, who, in 1857 [Faraday 1857] , described the chemical process for the production of nanosized particles of gold from gold chloride and sodium citrate. Since then a number of different methods have been developed to synthesize colloidal gold with controllable size [Daniel & Astruc 2004].

The most commonly used method of preparing gold nanoparticles, dispersed in water, is the citrate reduction of HAuCl4 in water method that was first proposed by Turkevich et al. in 1951 [Turkevich *et al.* 1951] and then was developed by Frens in 1973 [Frens 1973] : Gold salt and citrate are stirred in water, while the temperature, the ratio of gold to citrate, and the order of addition of the reagents control the size distribution of the generated gold nanospheres.

2.3.2 Optical Properties of Gold Nanoparticles

The confinement of electrons and phonons causes the physical properties of nanometer-sized objects to depart from those of bulk solids. In nanoscience, these deviations are exploited in order to tailor the properties of nanoparticles through their sizes and shapes.

The surface plasmon resonance of colloidal gold nanoparticles, which is a collective oscillation of the conduction electrons, governs their strong interaction with light : the strongly enhanced surface plasmon resonance of AuNps at optical frequencies makes them excellent scatterers and absorbers of visible light [Kreibig & Vollmer 1995, Jain *et al.* 2006] . The surface plasmon resonance of nanometric spherical gold particles in water is observed at about 520 nm [Van Dijk *et al.* 2006] .

In addition to their high scattering efficiencies, gold nanoparticles are immune to photobleaching and photoblinking [Cognet *et al.* 2003].

There have been several reports [Link & El-Sayed 1999, Alvarez *et al.* 1997, Bohren & Huffman 1983] on the optical properties of metal nanoparticles, including gold nanospheres and well-established theoretical tools based on the Mie theory method have been readily exploited for a quantitative study of the nanoparticle optical properties [Bohren & Huffman 1983].

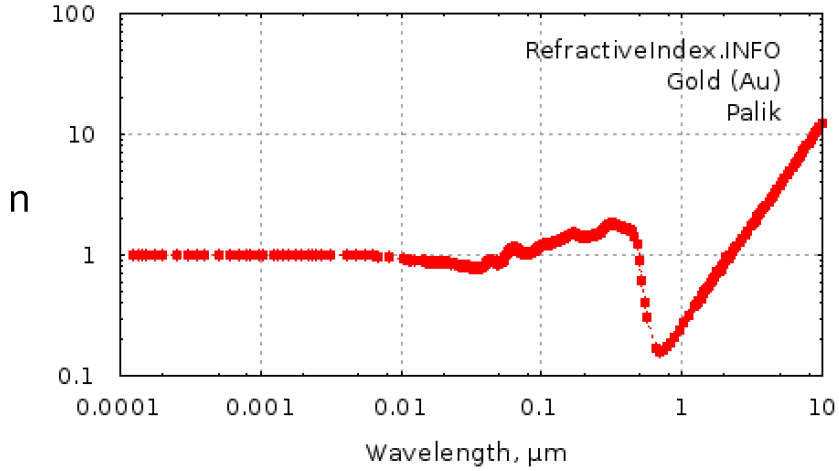

Figure 2.2: Real part of the refractive index of gold in function of the wavelength. Data measured by Palik [Palik 1991]

2.3.2.1 Complex Refractive Index and Dielectric Constant of Gold

Optical properties of gold nanoparticles can be presented in terms of the complex refractive index $\tilde{n}$. Another representation that describes very well these properties, apart from a small correction for particles with a radius a below 5 nm [Link & El-Sayed 1999, Kreibig & Vollmer 1995], is in terms of the complex dielectric constant ε.
Assuming the material is not magnetic, the dielectric constant and the complex refractive index are related by [Doremus 1964] :

$$\varepsilon = \tilde{n}^2 \tag{2.17}$$

The complex refractive indices and the dielectric constants of most noble metals are known from experiments, mostly done in the 1960's and 1970's [Johnson & Christy 1972]. For gold, values of the real part n of the complex

refractive index in function of the wavelength, that we used in this thesis and that were obtained by Palik [Palik 1991] , are plotted in Figure 2.2 . Values of the imaginary part κ are plotted in Figure 2.3 .

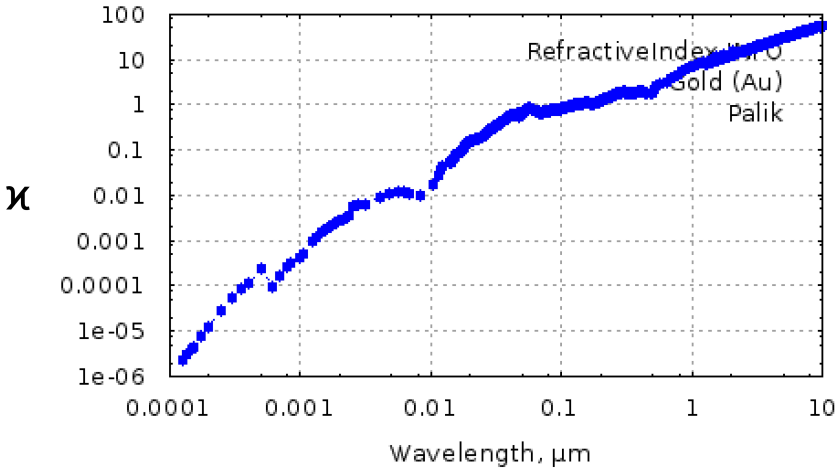

Figure 2.3: Imaginary part of the refractive index of gold in function of the wavelength. Data measured by Palik [Palik 1991]

2.3.2.2 Scattering of AuNps

Solving the problem of light scattering by a small particle involves solving Maxwell's equations with the correct boundary conditions. For spherical particles, this problem is exactly solvable. This was first shown in 1908 by Gustav Mie [Mie 1908]. A complete derivation of Mie theory is given by Bohren & Huffman and Hulst [Hulst 1981, Bohren & Huffman 1983]. From Mie theory scattering matrices can be derived, from which information about, for example, the direction and polarization dependence of the scattered light can be extracted.

Scattering Cross Section σ_s of AuNps

An important parameter that can be calculated with Mie theory is the scattering cross section σ_s described in Section 2.1 of this chapter :

$$\sigma_s = \frac{\lambda^2}{2\pi} \sum_{n=1}^{\infty} (2n+1)(|a_n^2| + |b_n^2|) \tag{2.18}$$

Coefficients a_n and b_n describe the amplitudes of the scattered electric and magneti fields respectively and are given by :

$$a_n = \frac{m\psi_n(mx)\psi_n^{'}(x) - \psi_n(x)\psi_n^{'}(mx)}{m\psi_n(mx)\zeta_n^{'}(x) - \zeta_n(x)\psi_n^{'}(mx)} \tag{2.19}$$

$$b_n = \frac{\psi_n(mx)\psi_n^{'}(x) - m\psi_n(x)\psi_n^{'}(mx)}{\psi_n(mx)\zeta_n^{'}(x) - m\zeta_n(x)\psi_n^{'}(mx)} \tag{2.20}$$

where ψ and ζ are Ricatti-Bessel functions of order n (they are related to Bessel and second-order Hankel functions respectively) [Bohren & Huffman 1983], $x = k\,a$ is a size parameter, a is the radius of the particle and $m = \sqrt{\varepsilon_{Au}/\varepsilon_{med}}$ is the square root of the ratio of the dielectric constant of the gold particle and of the medium where the particle is embedded and k is the modulus of the wave vector in that medium.
The prime indicates a derivation to the parameter in parentheses.

Using the experimentally determined real and imaginery parts of the refractive index of gold, plotted respectively on the graphs of Figure 2.2 and Figure 2.3 in Section 2.3.2.1, the dielectric constant of gold ε_{Au} can be calculate using Equation 2.17 . Equation 2.18 thus provides the scattering of the nanoparticle as functions of the particle radius a, the refractive index of the particle and the refractive index of the medium n_{med} in which it is embedded.

It is shown that the scattering cross section of a small gold nanoparticle varies as a^6 [Hulst 1981, Van Dijk *et al.* 2006] :

$$\sigma_s = \frac{128\pi^5}{3\lambda^4}\, a^6 \left|\frac{m^2-1}{m^2+2}\right|^2 \tag{2.21}$$

Anisotropy Factor g_{Au} of AuNps

By performing scattering calculations based on Mie theory, the anisotropy factor of a scattering gold nanoparticle embedded in a medium can be calculated (check `http://omlc.ogi.edu/calc/mie_calc.html`) . Parameters like the real refractive index of the particle, the imaginary refractive index of the particle, the refractive index of the medium where the particle is embedded, the diameter of the particle etc... , should be defined in order to complete the calculations.

The anisotropy factor g_{Au}, calculated for a gold nanoparticle, is tiny and can be considered as null. Consequently, gold nanoparticles scatters light isotropically without any directional tendency.

2.3.2.3 Absorption of AuNps

Similarly to scattering, the absorption of gold nanoparticles can be characterized by Mie theory. In fact, we have seen in Section 2.1.4 of this chapter that the absorbtion cross section σ_a is related to the scattering cross section σ_s and to the extinction cross section σ_e (see Equation 2.14) .

From Mie theory [Bohren & Huffman 1983], the extinction cross section σ_e is given by :

$$\sigma_e = \frac{\lambda^2}{2\pi} Re(a_n + b_n) \tag{2.22}$$

Using Equation 2.22 and Equation 2.14, the absorption cross section σ_a can be deduced.

It is shown that the absorption cross section of a gold nanoparticle varies as a^3 : [Hulst 1981, Van Dijk *et al.* 2006]

$$\sigma_a = -\frac{8\pi^2}{\lambda} a^3 \, Im\left(\frac{m^2 - 1}{m^2 + 2}\right) \tag{2.23}$$

2.3.3 Biological Properties of Gold Nanoparticles

There is an enormous interest in exploiting nanoparticles in various biomedical applications since their size scale is similar to that of biological molecules (for example : proteins, DNA etc...) and structures (e.g., viruses and bacteria). Furthermore, useful properties can be incorporated into the design of the nanoparticles for manipulation or detection of biological structures and systems.

2.3.3.1 Cytotoxicity of AuNps

Cells exposed to gold nanoparticles will incorporate the particles or will interact with them. Hence biocompatibility issues have to be considered.
Gold nanoparticles are composed of an inert material and thus acute cytotoxicity has not been observed so far. AuNps are regarded as **biocompatible** and it may be applicable to use gold nanoparticles as a reference nanoparticle for low toxicity [Lewinski *et al.* 2008, Sperling *et al.* 2008, West *et al.* 2006].

2.3.3.2 Bioconjugation of AuNps

Gold nanoparticles are surrounded by a shell of stabilizing molecules. With one of their ends, these molecules are either adsorbed or chemically linked to

the gold surface, while the other end points towards the solution and provides colloidal stability.
Biological molecules can be attached to the particles in several ways. If the biological molecules have a functional group which can bind to the gold surface (like thiols or specific peptide sequences), the biological molecules can replace some of the original stabilizer molecules when they are added directly to the particle solution. In this way molecules like oligonucleotides, peptides or PEG can be readily linked to AuNps and subsequent sorting techniques even allow particles with an exactly defined number of attached molecules per particle to be obtained. Alternatively, biological molecules can also be attached to the shell of stabilizer molecules around the Au particles by bioconjugate chemistry [Sperling *et al.* 2008].

Molecules coated on gold colloids retain their native structure without denaturation, which allows further application of those bio-modified nanoparticles [Pasquato *et al.* 2004].

With related strategies almost all kinds of biological molecules can be attached to the surface of gold nanoparticles.

2.4 Overview

In this chapter, we have first reviewed the basic concepts that governs light-matter interaction for a better characterization of the light propagation in complex biological media in the presence of AuNps. Complex refractive index, is thus defined as well as absorption and scattering cross sections. Moreover we have seen that the overall directional tendency of the scattered light is represented by the anisotropy factor g .

Then, we have specifically described the interaction of light waves with biological tissues that are characterized as strong light scatterers because their structure is very complex and heterogeneous. In fact, their structure consists of several organelles and cellular elements of different sizes and refractive indices. Additionally, we have seen that the anisotropy factor of biological tissues g_{bio} is close to one yielding to a scattering that is peaked in the forward direction.

We have also described the interaction of light waves with spherical gold nanoparticles. Based on Mie theory, we have seen that the scattering cross section of a gold nanoparticle (radius a), varies as a^6, while its absorption

cross section varies as a^3 only. Therefore, for very small particles, absorption is dominant, and thus their detection, using scattering-based methods, is challenging. Furthermore, we have seen that the anisotropy factor of AuNps g_{Au} is almost zero yielding to an isotropic scattering regime.

Finally, we have discussed about the unique properties of gold nanoparticles that makes them appealing objects for biological labeling : it is easy to synthesize gold particles in a wide size range, it is easy to functionalize them with a variety of small molecules, they have potential light extinction efficiencies in the visible (and NIR) region of the spectrum due to their surface plasmon resonance, they do not suffer from photobleaching and photoblinking and are inert yielding to low cytotoxic effects.

Chapter 3

Holography : the principles

Contents

3.1 Historical Introduction 23

3.2 Physical basis of Holography 25

3.2.1 Wave Theory of Light 26

3.2.2 Interference Theory 29

3.2.3 Coherence Requirements 31

3.2.4 Diffraction Theory 35

3.3 Theory of Classic Holographic Imaging 36

3.4 Digital Holography 44

3.4.1 Digital Recording of Holograms 44

3.4.2 Numerical Reconstruction Approaches 50

3.1 Historical Introduction

Holography, a technique employed to make three-dimensional images, originates from the work of the British-Hungarian physicist Prof. Dennis Gabor (Figure 3.1), while trying to improve the resolution of his electron microscope in 1947 by recording a diagram of the amplitude and the phase of the wave at the same time. Gabor, influenced by the work of Sir Lawrence Bragg, proposed a two-step process : illuminating the samples with electron beams and using white light to read out the recordings. It should be noted that the concept of separating the recording from the reconstruction was first proposed and used by Ernest Abbe.

Gabor's drawing of his setup, as published in his article 'A New Microscopic Principle'([Gabor 1948]), is depicted in Figure 3.2. A diverging reference wave (primary wavefront) illuminates an object. Part of the wave is scattered by the object. This secondary wave interferes with the reference wave, and the interference pattern, named *hologram* (from Greek : holos = whole, graphein

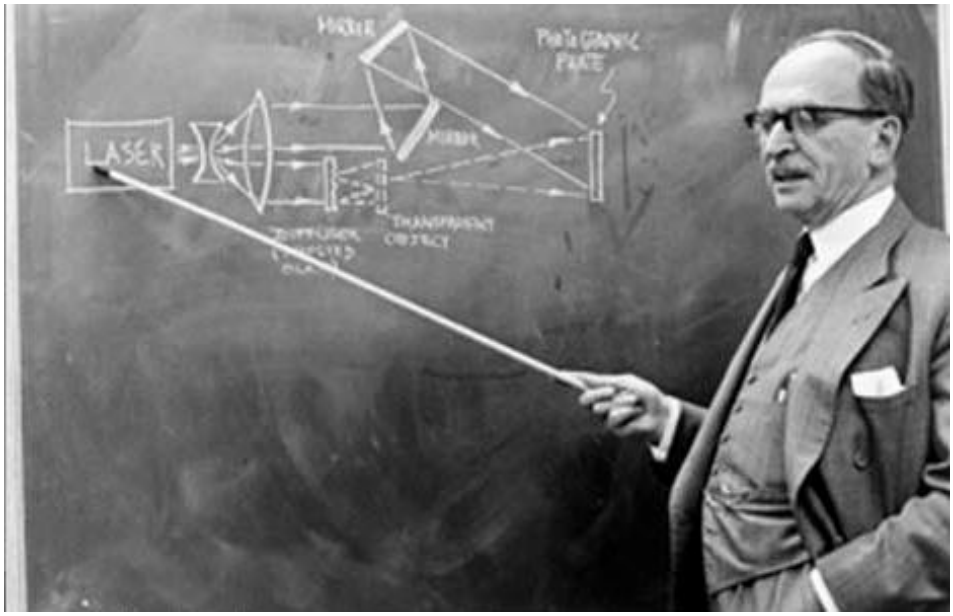

Figure 3.1: Dennis Gabor

= to write), is recorded on a photographic plate. All 3D information of the imaged object is contained in one single recorded hologram. For reconstructing the image, the photograph is first developed by reversal and then illuminated with an optical imitation of the electronic wave.
The method was named "*Microscopy by reconstructed wavefronts*" ([Gabor 1949]) that becomes, throughout the years, "*holography*".
In 1971 Dennis Gabor was rewarded the Nobel prize "for his invention and development of the holographic method'. Yet the success and progress of holography did no come overnight because of two main limiting factors :

- The origin of holography traces back to a time when lasers were not yet invented and, a the time, coherent light sources consisted of a mercury lamp used with a combination of a pinhole and color filters. Light sources, used in holography, suffer thus from weak intensity and low temporal coherence resulting in poor quality distorted holograms.

- The reconstructed images contains, in addition to the original object's image, a second image of the object (named twin image) and a coherent background that results from the directly transmitted beam. Those two last terms disturbs the reconstructed relevant image leading to a poor image quality. This overlapping of the different diffraction orders was not solved at the time.

The invention of the laser by Dr. T.H. Maiman in 1960 [Maiman 1960] marked a new era in holography : monochromatic and coherent lights obtained from lasers made it possible to produce distortion free holograms of high quality.
Moreover, Emmeth Leith and Juris Upatnieks in late 1962 ([Leith & Upatnieks 1962, Leith & Upatnieks 1963]) presented a solution for the overlapping of the different diffraction orders on the reconstructed images, by introducing the "*off-axis holography*", a modified configuration of Gabor's initial setup. In this configuration, the object beam is spatially separated from the reference beam, resulting in image and twin image sufficiently far apart from each other and from the reference beam.
Consequently, an important step was done toward the developing of holography as an imaging technique.

The lasers at the time had poor temporal coherence and mode stability, and their holograms where degraded by reflections and noise. With the development of laser and availability of high coherent lasers the holographic technique is now possible for different applications.

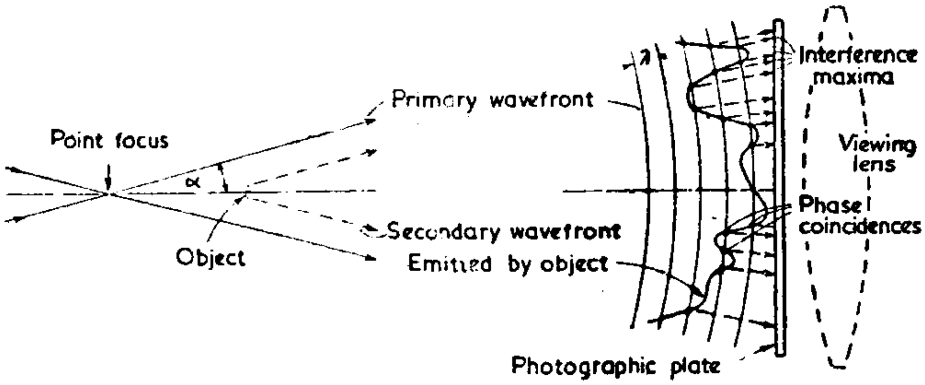

Figure 3.2: Dennis Gabor initial experimental holographic setup

3.2 Physical basis of Holography

Since ancient antiquity, two controversial competing theories describing the nature of light exists. The first theory, called the *wave theory of light* mainly conducted by Christiaan Huygens and later confirmed by Thomas Young and Augustin-Jean Fresnel, describes light as a propagating wave. While the second theory, called the *corpuscular theory of light* mainly conducted by Isaac Newton, describes light as a current of particles called photons. Both theories

contradict each other, but are necessary to describe the full spectrum of light phenomena.
In practice, the theory to be referred to depends on the experimental situation itself ; taking into account the *coherence* requirements, holography is essentially an ingenious combination of *Interference* and *Diffraction*, two phenomena based on the wave nature of light and are thus perfectly described by the wave theory, which is based on the theory of classical electromagnetism formulated by James Clerk Maxwell.

3.2.1 Wave Theory of Light

Light is a transverse electromagnetic wave, propagating at the constant speed of light c, characterized by two oscillating components, the electric field and the magnetic field $\vec{B}$.

As formulated in the classical electromagnetic theory, the electric and magnetic fields are coupled through Maxwell's equations [Kreis 2005] :

$$\left.\begin{aligned} \nabla \cdot \vec{E} &= \frac{\rho}{\varepsilon_0} \\ \nabla \cdot \vec{B} &= 0 \\ \nabla \times \vec{E} &= -\frac{\partial \vec{B}}{\partial t} \\ \nabla \times \vec{B} &= \mu_0 \vec{J} + \mu_0 \varepsilon_0 \frac{\partial \vec{E}}{\partial t} \end{aligned}\right\} \quad \text{Maxwell's Equations} \tag{3.1}$$

$\nabla\cdot$ is the divergence operator defined as : $\nabla\cdot = \frac{\partial}{\partial x} + \frac{\partial}{\partial y} + \frac{\partial}{\partial z}$

$\nabla\times$ is the curl operator defined as [1] : $\nabla \times \vec{A} = \begin{pmatrix} \frac{\partial A_z}{\partial y} - \frac{\partial A_y}{\partial z} \\ \frac{\partial A_x}{\partial z} - \frac{\partial A_z}{\partial x} \\ \frac{\partial A_y}{\partial x} - \frac{\partial A_x}{\partial y} \end{pmatrix}$

ε_0 is the permittivity of free space, μ_0 is the permeability of free space, ρ is the total charge density and $\vec{J}$ is the total current density.

Light propagation is described by the wave equation, which follows from Maxwell's equations. The wave equation in vacuum is :

$$\nabla^2 \vec{E} - \frac{1}{c^2} \frac{\partial^2 \vec{E}}{\partial t^2} = 0 \tag{3.2}$$

[1] Here, $\vec{A}$ is an arbitrary vector

where ∇^2 is the Laplace operator defined as :

$$\nabla^2 = \frac{\partial^2}{\partial x^2} + \frac{\partial^2}{\partial y^2} + \frac{\partial^2}{\partial z^2} \tag{3.3}$$

and c is the propagation speed of light in vacuum :

$$c = 299792458\, m\, s^{-1} \backsimeq 3 \cdot 10^8 m\, s^{-1} \tag{3.4}$$

(x, y, x) are the Cartesian spatial coordinates and t denotes the temporal coordinate.

In many applications, the wave vibrates only in a single plane. Such light wave is called linearly-polarized light. For a linearly-polarized light wave, propagating in the z-direction, it is sufficient to consider the scalar wave equation :

$$\frac{\partial^2 \vec{E}}{\partial z^2} - \frac{1}{c^2}\frac{\partial^2 \vec{E}}{\partial t^2} = 0 \tag{3.5}$$

The most important solution of the wave equation is the harmonic plane wave described in real notation by :

$$E(x, y, z, t) = a\, \cos(\omega t - \vec{k}\vec{r} - \varphi_0) \tag{3.6}$$

a is the real amplitude of the wave and the spatially varying term :

$$\varphi = -\vec{k}\vec{r} - \varphi_0 \tag{3.7}$$

is the phase, with φ_0 a phase constant.
$\vec{r}$ is a position vector defined as : $\vec{r} = x\hat{x} + y\hat{y} + z\hat{z}$
The symbol $\hat{}$ signifies a unit vector.

The *wave vector* $\vec{k}$ describes the propagation direction of the wave :

$$\vec{k} = \begin{pmatrix} k_x \\ k_y \\ k_z \end{pmatrix} \tag{3.8}$$

$$\vec{k} = k(k_x\hat{x} + k_y\hat{y} + k_z\hat{z}) \tag{3.9}$$

The modulus of $\vec{k}$, named *wave number*, is calculated by :

$$\|\vec{k}\| = k = \frac{2\pi}{\lambda} \tag{3.10}$$

the wave vector is thus :

$$\vec{k} = \frac{2\pi}{\lambda}(k_x\hat{x} + k_y\hat{y} + k_z\hat{z}) \tag{3.11}$$

The angular frequency ω is related to the frequency ν of the light wave by :

$$\omega = 2\pi\nu \tag{3.12}$$

Frequency ν and wavelength λ of the light wave are related by :

$$\nu = \frac{c}{\lambda} \tag{3.13}$$

Using the Euler's formula that relates the trigonometric functions and the complex exponential :

$$e^{i\alpha} = \cos\alpha + i\sin\alpha \tag{3.14}$$

where $i = \sqrt{-1}$ is the imaginary unit, equation 3.6 can be written in complex form :

$$E(x, y, z, t) = a\, Re\{e^{i(\omega t - \vec{k}\vec{r} - \varphi_0)}\} \tag{3.15}$$

Since only the real part of the complex field $E(x, y, z, t)$ represents the physical wave, the "Re" notation can be omitted, and thus the harmonic wave in complex notation is :

$$E(x, y, z, t) = a\, e^{i(\omega t - \vec{k}\vec{r} - \varphi_0)} \tag{3.16}$$

Using the complex notation of 3.16, we can separate the spatial and temporal parts of the wave :

$$\begin{aligned} E(x, y, z, t) &= a\, e^{i\omega t}\, e^{i(-\vec{k}\vec{r} - \varphi_0)} \\ E(x, y, z, t) &= a\, e^{i\omega t}\, e^{i\varphi} \end{aligned} \tag{3.17}$$

In optics calculations, only the spatial distribution of the wave is of interest. So by dropping the time dependence, only the spatial part of the electric field, named complex amplitude, has to be considered :

$$E(x, y, z) = a\, e^{i\varphi} \tag{3.18}$$

$E(x, y, z)$ as given by Equation 3.18 represents thus the complex amplitude of the electric field. Equation 3.18 is valid for plane waves and in general for any three-dimensional wave whose amplitude a and phase φ may be functions of x, y and z.

Intensity

The only directly measurable quantity is intensity I, which is defined as the time average of the amount of energy which crosses in unit time a unit area perpendicular to the direction of the energy flow :

$$I = \varepsilon_0 c \langle E^2(x,y,z) \rangle_t = \varepsilon_0 c \lim_{T \to \infty} \int_{-T}^{T} E^2(x,y,z)\, dt \tag{3.19}$$

In complex notation and for a plane wave, the intensity is simply calculated by taking the square of the modulus of the complex amplitude :

$$I(x,y,z) = E(x,y,z) \cdot E(x,y,z)^* = |E(x,y,z)|^2 = a^2 \tag{3.20}$$

3.2.2 Interference Theory

The term *Interference* describes the superposition of two or more waves in space. The idea was first introduced by Thomas Young in 1803 in the context of water waves. The interference phenomenon is the basis of holography and holographic interferometry.
In the following, we consider the interference of two monochromatic waves, emitted by the same source.
In order to interfere, the two electromagnetic waves must be coherent, have very nearly the same frequency, and the superposition principle must apply [Schnars & Jueptner 2005] :

- Coherence will be described in details in the next section (Section 3.2.3).
- The superposition principle is automatically fulfilled because of the linearity of the differential wave equation : since each individual wave of the two interfering waves, described by $E_j(\vec{r},t)$ is a solution of the wave equation, the superposition of those two waves is itself a solution two. This superposition is given by :

$$E(\vec{r},t) = \sum_{j=1}^{2} E_j(\vec{r},t) \tag{3.21}$$

The result of adding two waves of the same frequency depends on the value of the phase of the wave at the point in which the waves are added.
The complex amplitude of the two interfering monochromatic waves are respectively :

$$E_1(x,y,z) = a_1\, e^{i\varphi_1} \tag{3.22}$$
$$E_2(x,y,z) = a_2\, e^{i\varphi_2} \tag{3.23}$$

Because the two interfering waves are identically polarized, the scalar approach can be considered here and the resulting complex amplitude E is then calculated by adding the individual complex amplitudes :

$$E(x,y,z) = E_1(x,y,z) + E_2(x,y,z) \tag{3.24}$$

From Equation 3.20, the intensity of the interference is[2] :

$$\begin{aligned} I &= |E_1 + E_2|^2 && (3.25)\\ I &= (E_1 + E_2)\,(E_1 + E_2)^* && (3.26)\\ I &= (a_1\, e^{i\varphi_1} + a_2\, e^{i\varphi_2})\,(a_1\, e^{i\varphi_1} + a_2\, e^{i\varphi_2})^* && (3.27) \end{aligned}$$

By developing the complex exponentials and using the following trigonometric identities[3] :

$$\begin{aligned} 2\cos\zeta\cos\eta &= \cos(\zeta-\eta) + \cos(\zeta+\eta) && (3.28)\\ 2\sin\zeta\sin\eta &= \cos(\zeta-\eta) + \cos(\zeta+\eta) && (3.29) \end{aligned}$$

we get :

$$I = \underbrace{a_1{}^2}_{I_1} + \underbrace{a_2{}^2}_{I_2} + 2a_1a_2\cos\underbrace{(\varphi_1-\varphi_2)}_{\Delta\varphi} \tag{3.30}$$

and finally :

$$I = I_1 + I_2 + 2\sqrt{I_1\,I_2}\cos\Delta\varphi \tag{3.31}$$

where I_1 and I_2 are the individual intensities and $\Delta\varphi$ is the phase difference between the two waves.

The resulting intensity consists of one part that is the addition of the individual intensities and another part, the interference term $2\sqrt{I_1\,I_2}\cos\Delta\varphi$ which depends on the phase difference between the two interfering electromagnetic waves. It can be easily demonstrated, that in the case of orthogonally polarized waves, interference is not possible and thus the interference term do not appear. Consequently, the result of their superposition consists only on the addition of the individual intensities.
Constructive interference is achieved when the condition :

$$\Delta\varphi = 2n\pi, n = 0,1,2,... \tag{3.32}$$

is fulfilled yielding to a maximum of intensity (I_{max}), whereas points corresponding to

$$\Delta\varphi = (2n+1)\pi, n = 0,1,2,... \tag{3.33}$$

[2]The "(x,y,z)" notation in the equations is dropped for clarity and simplicity
[3]Here, ζ and η are arbitrary functions

conduct destructive interference where the intensity reaches its minimum (I_{min}). Parameter n is an integer and refers to the interference order.
As a consequence, an interference pattern composed of an alternation of bright and dark fringes is obtained. When the interfering waves have equal or nearly equal amplitudes, their superposition gives complete constructive and destructive interference yielding to the clearest interference pattern with maximum fringes' contrast. The visibility of the interference pattern refers to the contrast of the fringes and is described by :

$$V = \frac{I_{max} - I_{min}}{I_{max} + I_{min}} \tag{3.34}$$

3.2.3 Coherence Requirements

Coherence, in the context of interference, is an important property of the superposing waves. It defines the correlation between the phases of the individual waves and is, consequently, a direct measure of the interference ability of light waves : two waves should be mutually coherent in order to interfere. For this reason, interference is described as a *coherent superposition* of electromagnetic waves.

When two interfering waves are mutually coherent, their phase difference, defined by the term $\Delta\varphi = \varphi_1 - \varphi_2$ introduced in Equations 3.30 and 3.31, is constant in time. However, when $\Delta\varphi$ varies randomly or rapidly in time, the average value of the $\cos\Delta\varphi$ term is zero and the waves are mutually incoherent. Subsequently, interference is not achieved and only a pure addition of the individual intensities is observed : this is called *incoherent superposition*

The general concept of coherence includes two intrinsic aspects which are *temporal coherence* and *spatial coherence*[Kreis 2005].

3.2.3.1 Temporal Coherence

Temporal coherence of light waves is commonly revealed by a typical Michelson interferometric experiment illustrated on Figure 3.3 : a beam splitter (BS) splits the light of an emitting source into two waves that travel to mirrors M_1 and M_2 (M_1 is a fixed mirror while M_2 is a translating mirror) were they are back-reflected into their initial incident directions. Both beams cross again the beam splitter and a detector discloses their superposition in the form of an interference pattern. The optical path length from BS to M_1 and back to BS is noted d_1 and the optical path length from BS to M_2 and back to BS is noted d_2 . Since M_2 is a translating mirror, d_2 can be experimentally

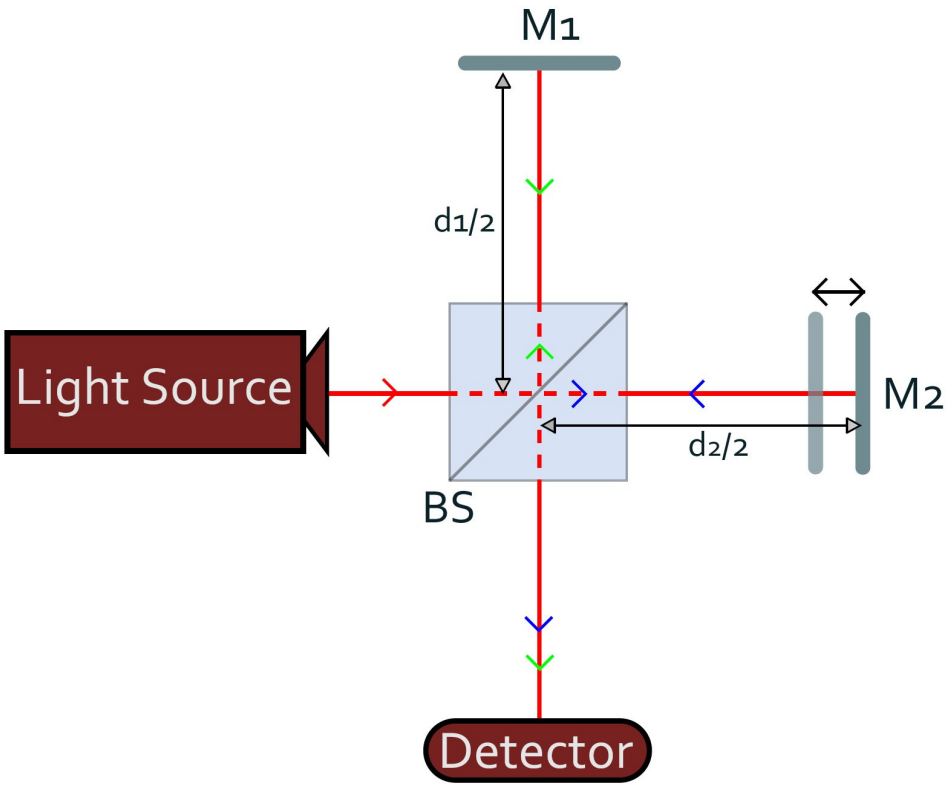

Figure 3.3: Michelson's interferometer

controlled. An interference is observed only when the optical path length difference between the two superposing waves δd, where $\delta d = d_1 - d_2$, does not exceed a certain length ℓ_c . When δd exceeds this limit, a vanishing of the interference fringes on the superposition pattern is observed, revealing that interference hasn't occurred.

This critical length ℓ_c is named *coherence length* and the corresponding emission time for the wave train is named *coherence time* :

$$\tau_c = \frac{\ell_c}{c} \tag{3.35}$$

This time interval τ_c , that describes the temporal coherence of a light wave is the time required for the train-wave to traverse, when traveling in vacuum, the coherence length ℓ_c which is the greatest distance between two points for which there is a phase difference that remains constant in time.

Temporal coherence thus describes the correlation of a wave with itself at different instants in time and is related to the finite *spectral bandwidth* of the

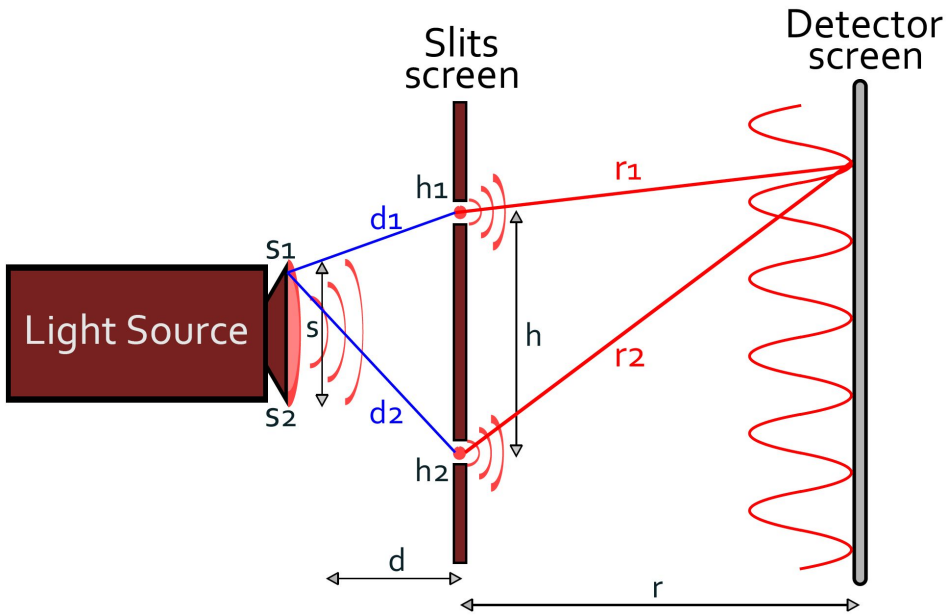

Figure 3.4: Young's double slit interferometer

emitting source $\Delta\nu$ ($\tau_c = \infty$ in the ideal case of pure monochromatic waves) :

$$\tau_c = \frac{1}{\Delta\nu} \tag{3.36}$$

The coherence length is therefore a measure of the spectral bandwidth of the light source :

$$\ell_c = \frac{c}{\Delta\nu} \tag{3.37}$$

3.2.3.2 Spatial Coherence

Spatial coherence depicts the mutual correlation of different parts of the same wavefront. It is commonly revealed by a typical Young's double slit interferometer illustrated on Figure 3.4 : a screen with two transparent slits (h_1 and h_2) is mounted between a light source and a detection screen. The slits' screen is placed at a distance d from the initial light source. h denotes the distance between h_1 and h_2. Light waves pass through the slits and interfere on a detection screen placed at distance r in front of them. In reality, a light source is never an ideal point source but an extended source that emits light from different points (source points s_1 and s_2 on the illustration of Figure 3.4 were the distance between s_1 and s_2 is noted s). The distances between the source points and the slits are noted d_1 and d_2 , those between the slits and the detection point are r_1 and r_2 .

If the phase between s_1 and s_2 is fluctuating randomly, interference is not observed on the detection screen and we get only a sum of the individual intensities. However, in order to obtain an interference pattern similar to the one obtained from and ideal one-point source, a fixed phase relation between s_1 and s_2 should exists. The path shift should be thus less than a half-fringe spacing :

$$|s_1 - s_2| < \frac{\lambda}{2} \tag{3.38}$$

This condition should be fulfilled for every point of the extended light source.
For the edges' points s_1 and s_2 , the following relations are valid :

$$s_1 = \sqrt{d^2 + \frac{h-s}{2}} \tag{3.39}$$

$$s_2 = \sqrt{d^2 + \frac{h+s}{2}} \tag{3.40}$$

Since $h \ll d$ and $s \ll d$, we get :

$$|s_1 - s_2| \approx \frac{h\,s}{2d} \tag{3.41}$$

Combining 3.38 and 3.41, we get :

$$\frac{h\,s}{2d} < \frac{\lambda}{2} \tag{3.42}$$

Consequently, the *spatial coherence length*, noted h_s, is given by :

$$\frac{h_s\,s}{2d} = \frac{\lambda}{2} \tag{3.43}$$

From Equation 3.43 we can see that the spatial coherence does not depend only on the intrinsic properties of the light source itself (λ), but depends also on the geometry of the optical arrangement (s and d).
In the context of holography, the spatial coherence of the used laser sources is associated with the transverse mode structure of their resonance cavities. For lasers resonating in the lowest order transverse mode (TEM_{00} mode), all points on the wavefront essentially have the same phase, therefore they have extremely good spatial coherence.

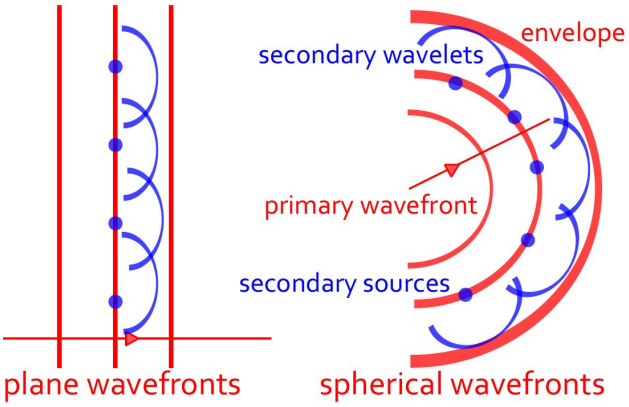

Figure 3.5: Huygens' principle

3.2.4 Diffraction Theory

Diffraction of light was first finely characterized by Francesco Maria Grimaldi in 1665. The term originates from the Latin word *"diffringere"* that means 'to break into pieces'. Diffraction, which is commonly described as the bending of a lightwave from its rectilinear propagation direction, occur whenever a portion of the wavefront is obstructed in some way. For example, a light wave illuminates an opaque screen with a small transparent hole, and the result is examined on a screen on the other side. From geometrical optics, one would expect a uniformly bright spot of the size of the hole surrounded by shadow. A closer look however reveals a pattern of bright and dark regions. This effect is due to diffraction.

The Huygens' principle, illustrated on Figure 3.5, brings out a **qualitative** explanation of this diffraction phenomenon by which wavefronts of propagating waves bend when they are obstructed : *every point of a wavefront can be considered as a new source point for 'secondary' spherical wavelets. Hence, the primary wavefront, at a later instant, is the 'envelope' of these wavelets* [Hecht 2001].

A **quantitative** description is given by the Fresnel-Kirchhoff integral [Schnars & Jueptner 2005] :

$$\Gamma(x,y,z) = \frac{1}{i\lambda}\iint_{-\infty}^{+\infty} A(x',y')\frac{e^{ik\rho'}}{\rho'}\cos\Theta\, dx'dy' \tag{3.44}$$

This integral can be derived from the Kirchhoff-Helmholtz integral theorem, as shown in [Born *et al.* 1999] .

$A(x', y')$ is the complex amplitude of the wave in the aperture plane. ρ' is the distance between a point in the aperture plane and a point in the observation plane. Since according to Huygens' principle, every point (x',y') within the hole in the aperture is a source of a spherical wave, the wavefront Γ at any point (x,y) in the observation plane is the superposition of all those spherical waves. This superposition is expressed by the integral. The amplitude of each spherical wave is proportional to the amplitude A(x',y') of the original wave at the aperture plane. The inclination factor $\cos\Theta$ is introduced to exclude the propagation of the secondary spherical waves back in direction towards the source.

Diffraction is the second optical phenomenon that forms, together with interference, the basis of holography. While interference is associated with the recording of holograms, diffraction is implicated in the second facet of the holographic technique : the reconstruction of wavefronts. Indeed, holographic reconstruction can be described as an evaluation of the propagating field received at a certain distance when obstructed by the recorded interference holograms. The scene is very well elucidated by the diffraction theory of waves.

In this section, we have presented a brief review of the main results of scalar diffraction theory as they are needed in what follows. A rigorous treatment of the theory leading to the diffraction formulas can be found in References [Born *et al.* 1999, Hecht 2001, Goodman 1968] .

3.3 Theory of Classic Holographic Imaging

Optical wave fields consists of an amplitude distribution as well as a phase distribution. However, in most conventional optical imaging techniques, the phase of a recorded optical wave field is lost in the recording process since all detectors or recording material (photographic films, CCD detectors etc...) have only the possibility to register intensities. The unique characteristic of holography is the idea of recording both the phase and the amplitude of light waves by converting the phase information into variations of intensity.

A hologram is defined as the recorded interference pattern between a coherent object wave, transmitted or reflected by an object, and a reference wave which interferes directly with this wave at the recording medium. The hologram contains information about the entire three-dimensional object field (amplitude and phase) which is encoded in the form of interference fringes. In

classical holography, holograms are usually recorded on a photographic plate using a coherent illumination of the object. The recorded object field is then reconstructed optically by illuminating the chemically processed hologram with an optical replica of the reference wave. This produces a reconstructed object which is indistinguishable from the original object and contains the 3D information, both amplitude and phase.

In this section, we will start first by describing the classic holographic recording procedure. We will describe then the holograms optical reconstruction process.

3.3.0.1 Holographic Recording

Holograms, in classic holography, are recorded on a photographic plate using a coherent illumination of the object (complex field $E_{obj}(x, y, z)$) and introducing, as shown in Figure 3.6 , a reference beam (complex field $E_R(x, y, z)$) derived from the same source. The photographic film records the interference pattern (the "*Hologram*") produced by this reference beam and the light waves scattered by the object.

We have seen in Section 3.2.3 that if two waves of the same frequency interfere, the resulting intensity distribution is temporally stable and depends on the phase difference $\Delta\varphi$. This is used in holography where the phase information is coded by interference into a recordable intensity. Clearly, to get a temporally stable intensity distribution, at least as long as the recording process, $\Delta\varphi$ must be stationary, which means the wave fields must be mutually coherent.

The intensity of the interference ($I(x, y, z_{det})$) of E_{obj} and E_R is recorded at the detector plane ($z = z_{det}$) and is given by :

$$\begin{aligned} I(x, y, z_{det}) &= |E_R(x, y, z_{det}) + E_{obj}(x, y, z_{det})|^2 \\ I(x, y, z_{det}) &= [E_R(x, y, z_{det})) + E_{obj}(x, y, z_{det})]\,[E_R(x, y, z_{det}) + E_{obj}(x, y, z_{det})]^* \end{aligned} \tag{3.45}$$

where * symbolizes the complex conjugate. The expression of this interference can be decomposed in three terms :

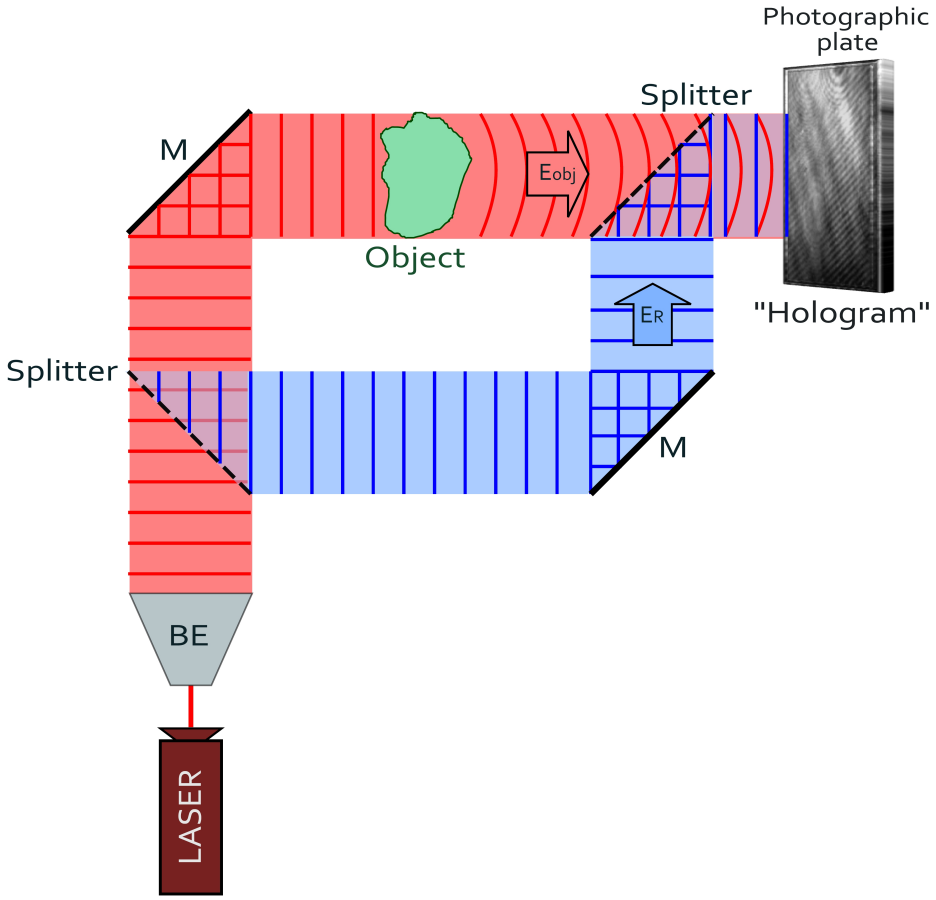

Figure 3.6: Schematic drawing of the hologram recording procedure in classic holography. The initial beam partly illuminates the object and partly forms the reference beam. The light scattered by the object forms the object beam E_{obj} . E_{obj} interferes with the reference beam E_R on the photographic plate, yielding the hologram

$$\begin{aligned} I(x,y,z_{det}) &= E_R(x,y,z_{det})\,E_R^*(x,y,z_{det}) + E_{obj}(x,y,z_{det})\,E_{obj}^*(x,y,z_{det}) \\ &+ E_R(x,y,z_{det})\,E_{obj}^*(x,y,z_{det}) \\ &+ E_R^*(x,y,z_{det})\,E_{obj}(x,y,z_{det}) \end{aligned} \tag{3.46}$$

using :

$$I_R = E_R(x,y,z_{det})\,E_R^*(x,y,z_{det}) = |E_R(x,y,z_{det})|^2 \tag{3.47}$$

$$I_{obj} = E_{obj}(x,y,z_{det})\,E_{obj}^*(x,y,z_{det}) = |E_{obj}(x,y,z_{det})|^2 \tag{3.48}$$

the interference equation can be rewritten as :

$$\begin{aligned} I(x,y,z_{det}) &= I_{obj} + I_R \\ &+ E_R\,E_{obj}^* \\ &+ E_R^*\,E_{obj} \end{aligned} \tag{3.49}$$

The spatial coordinates are omitted for the sake of readability.

The first term in Equation 3.49 , corresponds to the sum, at the detector plane z_{det} of the intensity scattered by the object I_{obj} and the intensity I_R of the reference wave. This term doesn't holds any phase information and thus do not allow the reconstruction of the illuminated object. The second term in Equation 3.49 , is proportional to the object's field and the third term to its complex conjugate. Accordingly, these two last terms are useful for the reconstruction of the object.

At the end of the recording process, the photographic plate is chemically processed and the "hologram" of the investigated object is thus obtained. Each point (x,y) of this hologram is proportional to the recorded intensity $I(x,y,z_{det})$ of the interference between the reference wave and the object's scattered wave.

3.3.0.2 Optical Reconstruction

To reconstruct the object, the recorded hologram is illuminated, at the initial position of the photographic plate, with the same original reference wave E_R as illustrated on Figure 3.7. The complex field, behind the hologram, will be thus the sum of the three terms of the interference expression of Equation 3.49

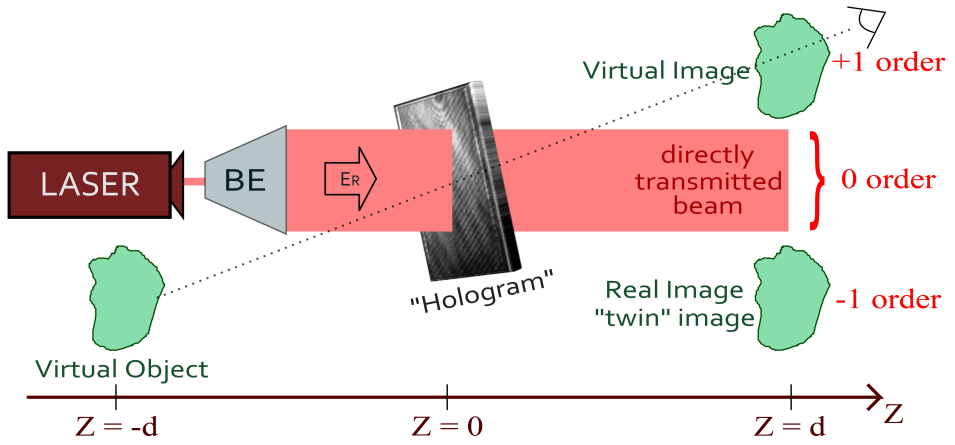

Figure 3.7: Optical reconstruction in classical holography

multiplied by the reconstruction wave E_R , yielding to the reconstructed field E_r :

$$\begin{aligned} E_r &= (I_{obj} + I_R)\, E_R + E_R\, E_{obj}^*\, E_R + E_R^*\, E_{obj}\, E_R \\ E_r &= \underbrace{(I_{obj} + I_R)\, E_R}_{0} + \underbrace{{E_R}^2\, E_{obj}^*}_{-1} + \underbrace{I_R\, E_{obj}}_{+1} \end{aligned} \tag{3.50}$$

From Equation 3.50 , three terms in the formation of the reconstructed holographic image can be identified :

- The first term represents the reference wave modulated by the intensities I_R and I_{obj} . It is called the *zero diffraction order*.
- The second term contains the conjugate complex of the object wave and produces a real image located on the other side of the hologram. Since this term is formed by the conjugate of the object wave the depth is inverted and can thus be imagined as the time-reversed original object wave E_{obj}. It is called the *-1 diffraction order*.
- The third term contains the desired information about the object. This term is the reconstruction of the object wave E_{obj} where the multiplication with the amplitude factor I_R can be viewed as an amplification of the reconstructed signal. It forms the virtual image located at the position initially occupied by the object. It can be viewed through the hologram. This term is called the *+1 diffraction order*.

In this way, a method is found to preserve the whole complex amplitude of a wave in a two-dimensional image.

It must be noted that the resulting reconstructed wavefront is an overlay of the three terms described above. Only the +1 order is of interest for the reconstruction of the object's field. Consequently, this term should be isolated from the other overlapping terms. In fact, using a proper design of the reference wave and recording geometry, the 0 and -1 terms are suppressed or will, spatially, not affect the desired virtual image. The spatial separation of the three diffraction order components can be achieved using the off-axis configuration. Off-axis holography will be described in details in the next section of this chapter. Moreover, the 0 and -1 terms can be completely suppressed using phase-shifting holography. This last technique will be described, in details, in the next chapter of this thesis (Chapter 4).

3.3.0.3 Off-axis configuration in classic holography

Leith and Upatnieks succeeded, since 1962, in spatially separating the three terms that occur in the reconstruction procedure [Leith & Upatnieks 1962, Leith & Upatnieks 1964]. Their idea was to introduce a sufficient angle θ between the propagation direction of the reference wave and of the object wave as illustrated on Figure 3.8. The increase in the angle between the two interfering waves increases the spatial distance between the 0 order and the two holographic terms which is desired so that one can easily extract the relevant information for the holographic image.

The **recording reference plane wave** travels in the (x,z) plane at an angle θ with respect to the z-axis and is recorded by the photographic plate in an off-axis configuration. This reconstruction wave can be written as :

$$E_R(x, y, z_{det} = 0) \propto A_R \, e^{-ikx \sin\theta} \tag{3.51}$$

where A_R is a real constant.

The **reconstruction reference wave** is a plane wave that travels in the propagation direction of the object wave and can be written as :

$$E_R(x, y, z) \propto A_R \tag{3.52}$$

From Equation 3.50, the wave scattered by the hologram becomes [Saleh *et al.* 1991] :

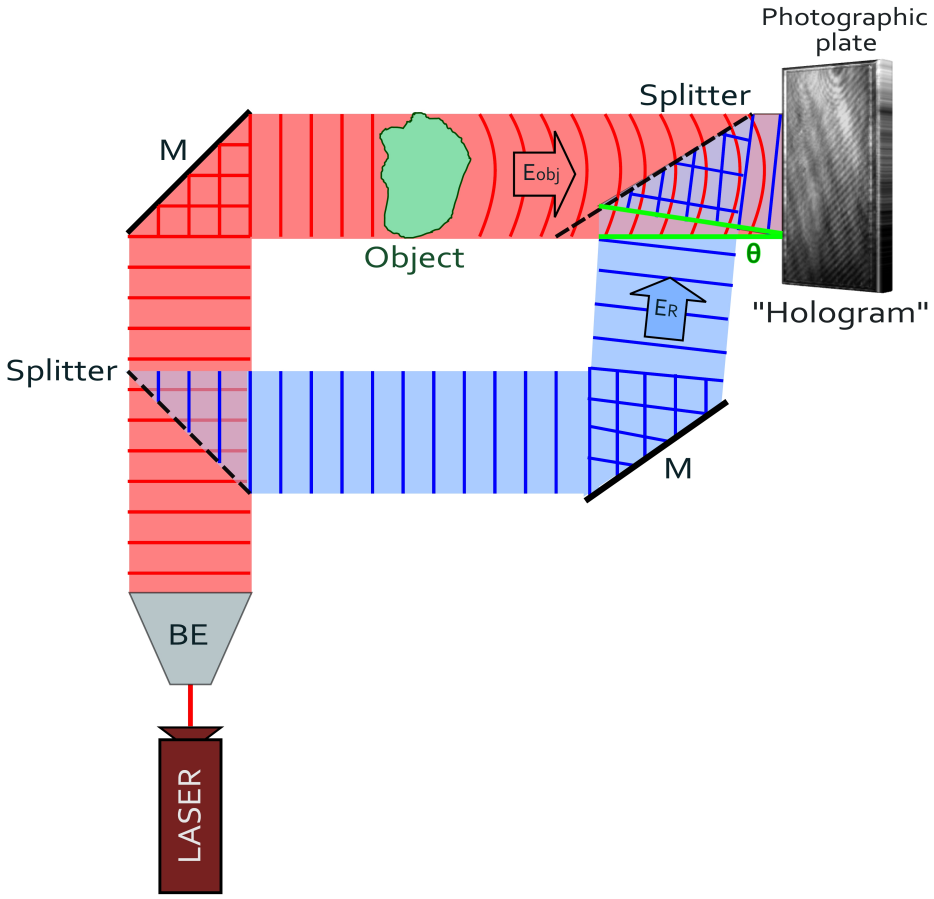

Figure 3.8: Schematic drawing of the hologram recording procedure in off-axis classic holography. The initial beam partly illuminates the object and partly forms the reference beam. The light scattered by the object forms the object beam E_{obj} . E_{obj} interferes with the reference beam E_R on the photographic plate, yielding the hologram

$$\begin{aligned} E_r \quad \propto \quad & A_R^3 \\ & + A_R (E_{obj}\, {E_{obj}}^*) \\ & + A_R^2\, {E_{obj}}^*\, e^{ikx \sin\theta} \\ & + A_R^2\, E_{obj}\, e^{-ikx \sin\theta} \end{aligned} \tag{3.53}$$

The first term is the source term which is a plane wave traveling in z-direction and the last term is the reproduced object wave. The third term contains the phase-inverted image of the object. This wavefront propagates in a direction including an angle -θ with the z-axis. If the angle θ is chosen large enough, these three terms are now well-separated [Saleh *et al.* 1991].

The second term can be neglected, if the object is small enough. If this is not the case, this term produces a halo surrounding the reference wave with approximately twice the angular spread θ_S of the object [Goodman 1968]. So the angle θ has to be large enough to ensure the separation of the waves : this is satisfied for $\theta \geq 3\theta_S$ [Saleh *et al.* 1991].
As we will see in the next section of this chapter when we consider digital holography, this constraint on the off-axis tilt angle imposes a lower limit on the camera resolution.

3.3.0.4 Overview for classic holography

In classical holography, holograms are recorded on photographic films that consists of very fine photographic emulsion (usually silver halide crystals) suspended in gelatin. Because the grain size of the emulsion is tiny, holograms are recorded with a high resolution allowing high resolution reconstructions of the investigated objects. However, photographic film holography suffers from a main experimental limitation which is the chemical processing necessity of the holographic films.

In digital holography, which is an alternative method to classic holography, this experimental limitation does not exists since holograms are recorded on digital devices that consists of pixels' arrays. Holograms acquisition is thus faster than in classic holography. However the resolution in digital holography is lower than the one achieved in film holography since the grain size of the photographic emulsion is much smaller than a digital pixel.

The next section of this chapter is a review of digital holography.

3.4 Digital Holography

Digitization in the context of holography concerns the two main steps of this imaging technique : the recording of holograms and the reconstruction of the object. Accordingly, the physical and chemical recording processes are replaced with electronic ones. Moreover, the optical reconstruction process is replaced with a numerical computation of the object field.

First digitization attempts have been done in 1967 by J.W. Goodman et R.W. Laurence[Goodman & R.W. 1967]. But it is until 1994 that digital holography gained its wide spread when U. Schnars and W. Jüptner [Schnars & Jüptner 1994] replaced the photographic plate with a CCD (Coupled Charge Device) camera that records the interference of the reference field and the object field as illustrated on Figure 3.9.

In this section, we will present first the numerical recording procedure of digital holograms. Then, we will describe how objects fields can be restituted numerically in digital holography.

3.4.1 Digital Recording of Holograms

Similarly to classic holography, holograms can be recorded in-line or off-axis. The hologram recording procedure in in-line digital holography is illustrated on Figure 3.9 and the digital off-axis configuration is sketched on Figure 3.10 . The recording principle is exactly the same as in film holography, but the photographic plate is replaced here with a CCD camera : an initial coherent laser beam partly illuminates the object and partly forms the reference beam. The light scattered by the object forms the object beam E_{obj} . E_{obj} interferes with the reference beam E_R on the digital camera, yielding the hologram. The intensity of this interference is directly recorded on the detector of the CCD device since this intensity induce an photoelectric current that is proportional to the number of incident photons.

The expression of the digital holographic field is exactly the same as the expression obtained in classic holography (Equation 3.49) :

$$I = \underbrace{I_{obj} + I_R}_{I_0} + \underbrace{E_R\, E^*_{obj}}_{I_{-1}} + \underbrace{E^*_R\, E_{obj}}_{I_{+1}} \tag{3.54}$$

Where :

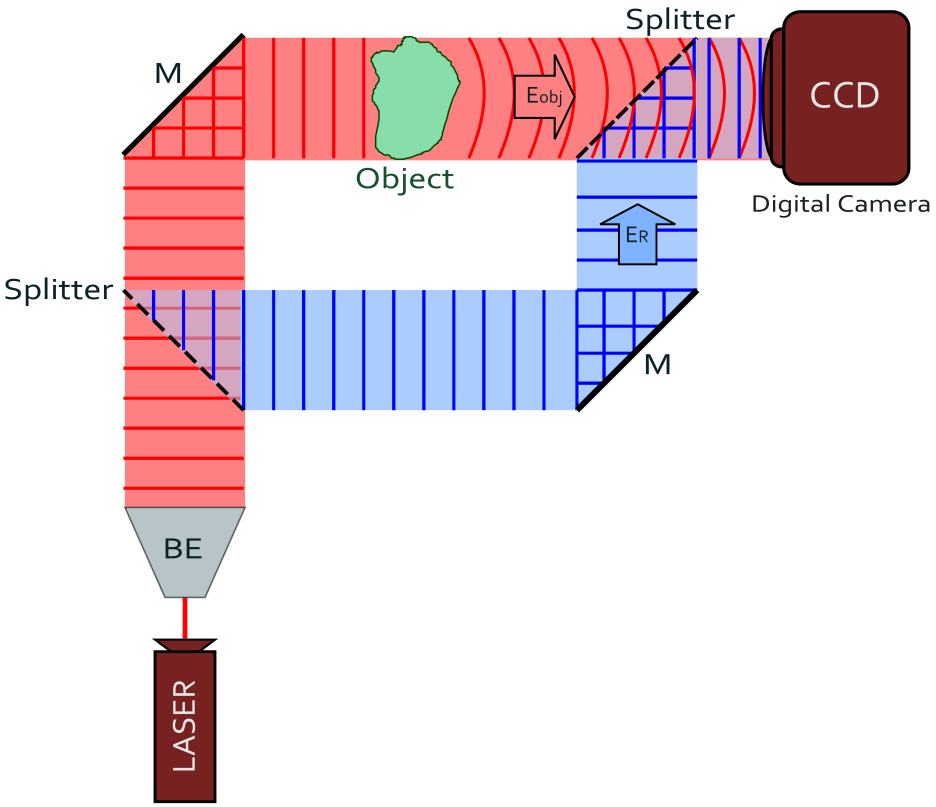

Figure 3.9: Schematic drawing of the hologram recording procedure in in-line digital holography. The initial beam partly illuminates the object and partly forms the reference beam. The light scattered by the object forms the object beam E_{obj} . E_{obj} interferes with the reference beam E_R on the digital camera, yielding the hologram.

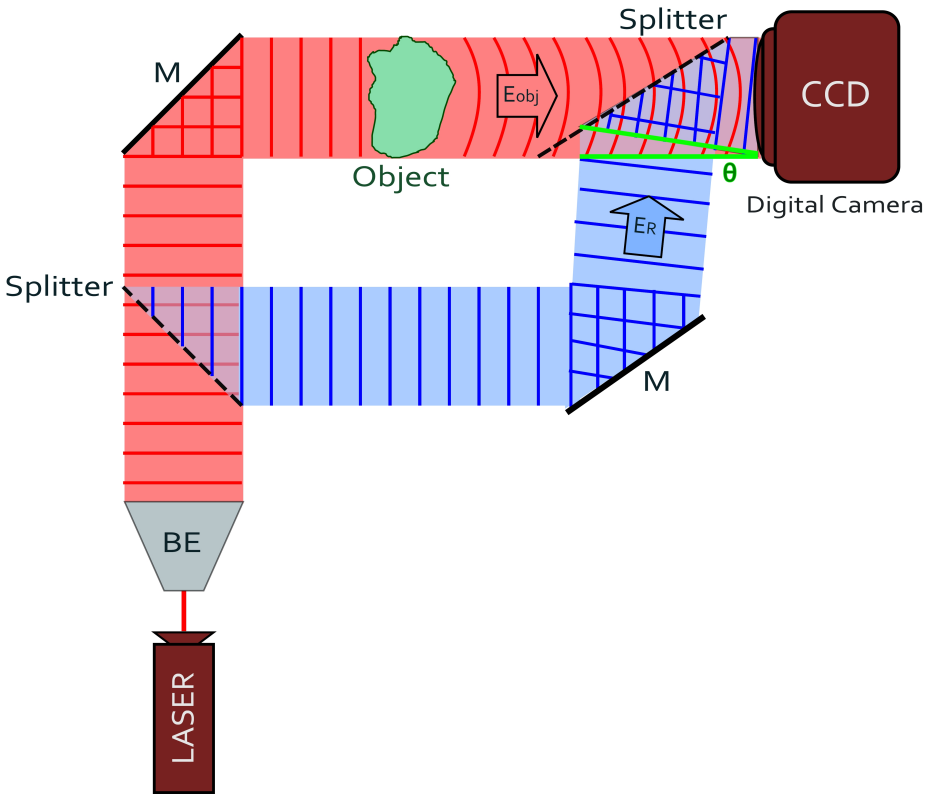

Figure 3.10: Holograms Off-axis recording in digital holography

- I_0 is the 0 diffraction order term and corresponds to the directly transmitted wave
- I_{-1} is the -1 diffraction order term and gives the real image or twin image
- I_{+1} is the $+1$ diffraction order and gives the desired virtual image of the object

Figure 3.11 shows an image, in the Fourier space, of a holographic signal recorded by a CCD camera in an off-axis geometry. The sample that we imaged here consists of 40 nm Gold Nanoparticles in a water and agarose solution. It should be noted here that Figure 3.11 is a reconstructed image of the specimen at an intermediate plane and not at the object's plane (it is in fact a reconstructed image at the microscope objective rear aperture plane as it will be explained in Chapter 5 of this manuscript). On this image, the three terms of the interference are spatially separated, thanks to the off-axis angle, and can be clearly depicted : I_0 is the centered structure with a halo, the blurry structure corresponds to the twin image I_{-1} and the sharp circular structure, symetrical to I_{-1} corresponds to I_{+1} .

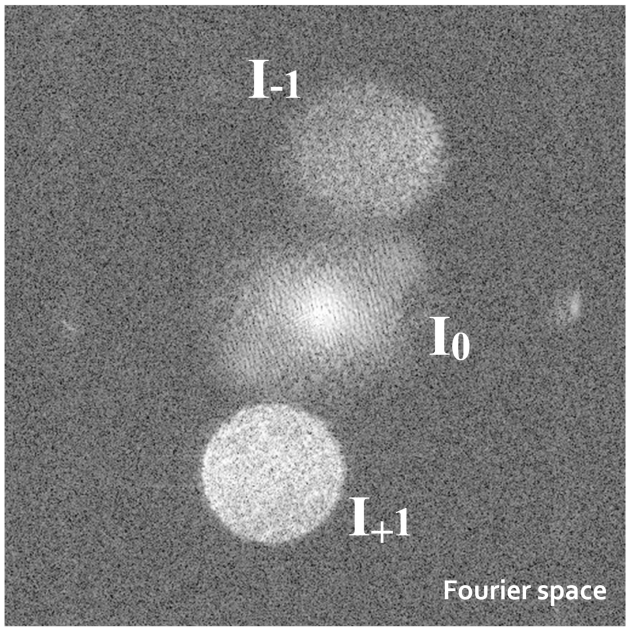

Figure 3.11: Off-axis holographic signal recording by a CCD device. The three interference terms can be clearly depicted

The signal that corresponds to I_{+1} is the interesting signal that is used to reconstruct the object's field. In digital holography, only this signal is con-

served while the two other terms, I_0 and I_{-1}, are completely filtered out using an appropriate numerical spatial filtering technique exhaustively described in Chapter 5 of this manuscript. It is also possible, as we have mentioned before, to directly obtain genuine holograms that contain only the interesting I_{+1} term using phase shifting holography [Yamaguchi & Zhang 1997] described in details in the next chapter (Chapter 4).

Spatial Frequency Requirements for Hologram Recording

In digital holography, the interference pattern is formed by the superposition of the object wave with the reference wave is recorded by a digital device (CCD camera). Spatial resolution of an imaging device describes the ability of this device to resolve image details. The main parameters which determine spatial resolution are pixel size and pixel number. We use CCD cameras whose detectors are rectangular arrays of light sensitive pixels organized in N lines and M rows. The center-to-center spacing of the pixels, the pixel pitch, is p_ξ and $p\eta$ in the two orthogonal directions (see Figure 3.12).

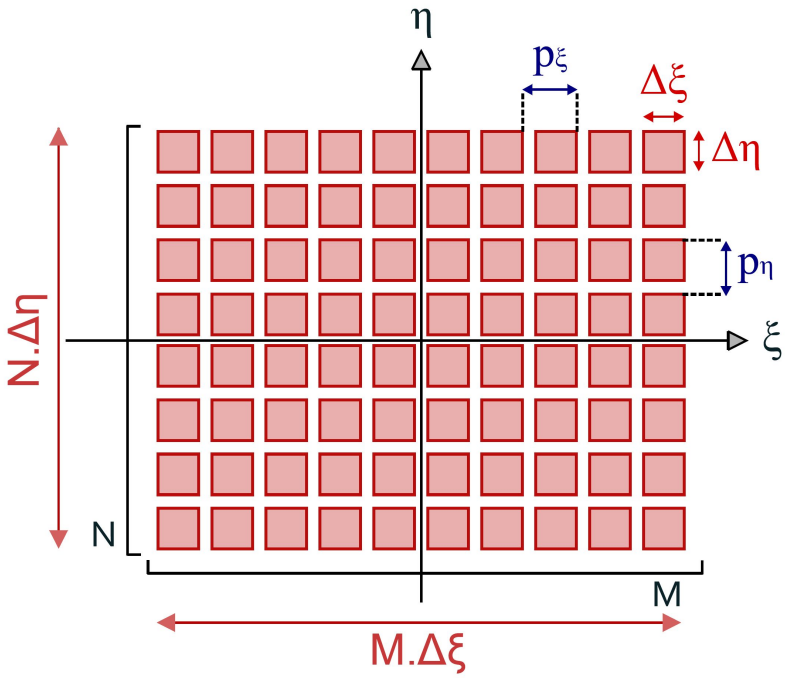

Figure 3.12: CCD array architecture

According to the Shannon-Nyquist sampling theorem, a correct acquisition of a hologram by a CCD camera requires that the sampling frequency (Nyquist frequency) must be at least twice as high as the highest signal frequency.

This means that the recorded signal can be reproduced faithfully from data recorded by the array up to spatial frequencies :

$$f_{N_\xi} = \frac{1}{2p_\xi} \tag{3.55}$$

$$f_{N_\eta} = \frac{1}{2p_\eta} \tag{3.56}$$

were f_{N_ξ} and f_{N_η} are the Nyquist frequencies.

This requires that the angle between the object and reference waves must be sufficiently small.

In practice,the CCD devices that we use are composed of square pixels with identical spacing in vertical and in horizontal directions :

$$\Delta\xi = \Delta\eta = d_{px} \tag{3.57}$$

Pixel pitches are also equal and the interspace distance between two consecutive pixels is too small that it can be neglected.

$$p_\xi \approx \Delta\xi = d_{px} \tag{3.58}$$

$$p_\eta \approx \Delta\eta = d_{px} \tag{3.59}$$

Thus, the Nyquist frequencies are equal :

$$f_{N_\xi} = f_{N_\eta} = f_N = \frac{1}{2d_{pix}} \tag{3.60}$$

Moreover, the sampling theorem states that every interferometric fringe of the hologram has to be sampled by at least two pixels of the CCD array to resolve the fringe frequency : the interference fringe spacing d_f should be at least twice the CCD pixels spacing d_{px}

$$\frac{1}{d_f} = \frac{1}{2d_{px}} \tag{3.61}$$

The maximal inter-fringe distance d_f, determines the maximum spatial frequency of the recorded signal f_N which needs to be resolved, for the wavelength λ and is given by the maximum angle between the reference and the object waves θ_{max} :(see figure 3.13) :

$$d_f = \frac{\lambda}{2\sin\frac{\theta_{max}}{2}} \tag{3.62}$$

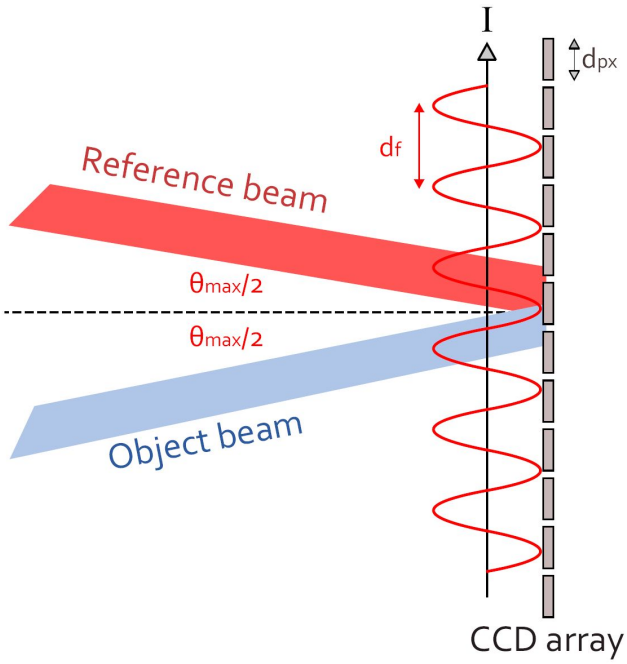

Figure 3.13: Interfringe distance

Using the small-angle approximation :

$$\sin\theta \approx \theta \tag{3.63}$$

and combining equations 3.61 and 3.62, the maximum angle is given by :

$$\theta_{max} = \frac{\lambda}{2d_{px}} \tag{3.64}$$

Since the size of the CCD pixels is fixed, the spatial sampling cannot be increased. The only way to obey the sampling theorem, in order to create good recording conditions, is to correctly adapt θ which is the off-axis angle between the object and the reference beams ; θ should not exceeds the maximum angle θ_{max} :

$$\theta \leq \frac{\lambda}{2d_{px}} \tag{3.65}$$

3.4.2 Numerical Reconstruction Approaches

As described previously, to optically reconstruct the image from a hologram, the hologram is illuminated with the reference wave E_R. The complex amplitude behind the hologram is given as established by Equation 3.50 , and

the wavefront propagates as described by the Fresnel-Kirchhoff formula. In digital holography, the complex amplitude of the wave is calculated from the digital hologram, and the propagation of the wave is computed numerically. Numerical reconstruction has a major advantage compared to the optical method : since it is the complex amplitude which is computed, not only the intensity of the wave can be calculated, but also the phase.

Mathematically, the reconstruction process reduces to the calculation of the Fresnel-Kirchhoff diffraction integral. If one treats the digital holographic system as a coherent imaging system, then the reconstruction algorithm functions like the lens in an optical system. All computer calculations can be performed based on the Fresnel-Kirchhoff diffraction formula, however, using this formula directly is often time consuming. There are a number of computationally efficient numerical methods available to calculate the holographic diffraction [Kreis *et al.* 1997]. The most commonly applied method has been the discrete *Fresnel Transform* where the approximation of spherical Huygens wavelet by a parabolic surface allows the calculation of diffraction integral using a single Fourier transform. In the *Convolution Method*, the diffraction integral is calculated without such approximation using three Fourier transforms through the convolution theorem [Demetrakopoulos & Mittra 1974, Kreis 2002]. On the other hand, the *Angular Spectrum Method* involves two Fourier transforms, plus simple filtering of the angular spectrum [Yu & Kim 2005]. In this thesis work, we are interested by the **Fresnel Transform** and the **Angular Spectrum** methods. We review thus here these two methods.

3.4.2.1 Reconstruction by the Fresnel Transformation

In this section we confine ourselves to the Fresnel approximation of the Fresnel-Kirchhoff diffraction integral which is feasible due to the sufficient distance between the object and the CCD device.

Fresnel Transformation : the formula

Figure 3.14 describes the coordinate system used for the numerical reconstruction : a CCD device records the hologram $E_H(x, y, 0)$ and the field at the image plane $E'(\xi', \eta', z_r)$, situated at a distance d'_r behind the CCD plane, is reconstructed.
In classic holography, the field at a plane situated behind the hologram (real or virtual image) is reconstructed by diffracting the same reference beam that is used to record the hologram, onto the holographic plate. However, in dig-

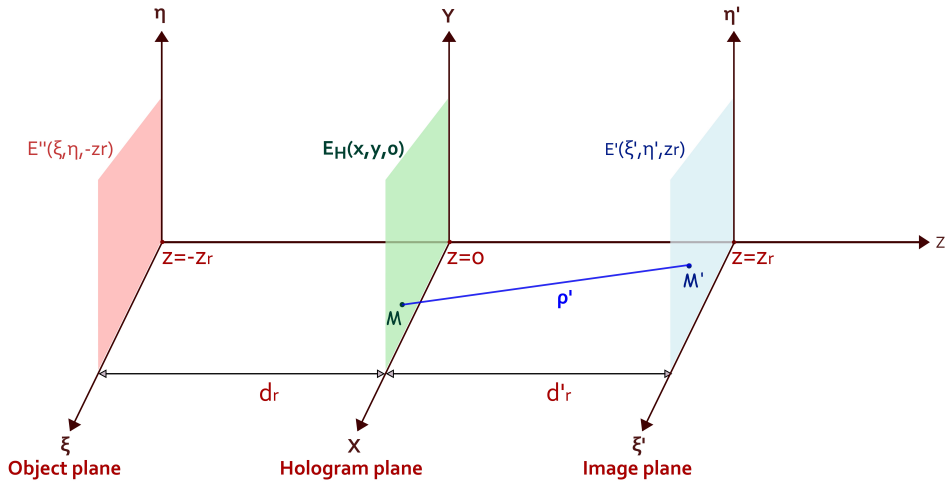

Figure 3.14: Coordinate system for digital holography

ital holography, the hologram is recorded on a digital CCD detector and the diffraction needed for the reconstruction is not performed optically but is "numerically simulated".
This diffraction is described by the Fresnel-Kirchhoff integral based on the Huygens-Fresnel principle, as introduced in Section 3.2.4 . The diffraction pattern, which gives the reconstructed image in the image plane $E'(\xi', \eta', z_r)$, is thus given by the Fresnel-Kirchhoff diffraction formula which states that a wave field, which is known in a given plane, can be calculated in any other plane in the three-dimensional space :

$$E'(\xi', \eta', z_r) = \frac{1}{i\lambda} \iint_{-\infty}^{+\infty} E_H(x, y, 0) E_{R_d}(x, y, 0) \frac{e^{ik\rho'}}{\rho'} \cos\Theta \, dxdy \qquad (3.66)$$

where ρ' is the distance between a point in the hologram plane M and a point in the reconstruction plane M' and E_{R_d} is a digital replica of the optical reference wave E_R that is used to record hologram $E_H(x, y, 0)$. As described in Section 3.4.1, only the virtual I_{+1} relevant term is of interest. The hologram field that is used for the reconstruction $E_H(x, y, 0)$ includes thus only this I_{+1} term : $E_H(x, y, 0) = E_R^*(x, y, 0)\, E_{obj}(x, y, 0)$.

According to Figure 3.14 , ρ' is defined as :

$$\begin{aligned} \rho' &= |MM'| \\ &= \sqrt{{d'_r}^2 + (x - \xi')^2 + (y - \eta')^2} \end{aligned} \qquad (3.67)$$

Due to the small angles between the hologram normal and the rays from the hologram to the image points, the obliquity factor can be set to $\cos\Theta = 1$ Since the values of x, y, ξ' and η' are small compared to the distance d'_r between the reconstruction plane and the CCD device, the expression in Equation 3.67 can be expanded to a Taylor series which is limited to the linear and quadratic terms :

$$\rho' \approx d'_r + \frac{(x-\xi')^2}{2{d'_r}^2} + \frac{(y-\eta')^2}{2{d'_r}^2} \tag{3.68}$$

The reconstructed image, using an additional approximation of replacing the denominator ρ' in Equation 3.66 by d'_r , is thus expressed as :

$$E'(\xi', \eta', z_r) = \frac{e^{ikd'_r}}{i\lambda d'_r} \iint_{-\infty}^{+\infty} E_H(x, y, 0) E_{R_d}(x, y, 0) e^{ik[(x-\xi')^2+(y-\eta')^2]/2d'_r}\, dxdy \tag{3.69}$$

By developing the exponential in Equation 3.69 , we get :

$$\begin{aligned} E'(\xi', \eta', z_r) \quad = \quad & \frac{e^{ikd'_r}}{i\lambda d'_r} \iint_{-\infty}^{+\infty} E_H(x, y, 0) E_{R_d}(x, y, 0)\, e^{ik(x^2+y^2)/2d'_r} \cdot \\ & e^{ik(\xi'^2+\eta'^2)/2d'_r} e^{-ik(x\xi'+y\eta')/d'_r}\, dxdy \end{aligned} \tag{3.70}$$

This equation is named *Fresnel transformation*. The Fresnel transformation enables the reconstruction of the wave field in a plane behind the hologram. It states that the reconstruction distance z is sufficiently larger than the size of the diffracting obstruction (here the obstruction is the hologram). The Fresnel transformation is quite similar, as we will see later on, to a traditional Fourier Transform : it is essentially the Fourier transform of the diffracting hologram multiplied by the phase factor of the light waves at the hologram.

For digitization of the Fresnel transform integral, the following spatial frequency terms are introduced :

$$k'_x = \frac{k\,\xi'}{2\pi d'_r} = \frac{\xi'}{\lambda\, d'_r} \tag{3.71}$$

$$k'_y = \frac{k\,\eta'}{2\pi d'_r} = \frac{\eta'}{\lambda\, d'_r} \tag{3.72}$$

Using these substitutions in the last exponential under the integral of Equation 3.70, we get :

$$E'(k'_x, k'_y, z_r) = \frac{e^{ikd'_r}}{i\lambda d'_r} \iint_{-\infty}^{+\infty} E_H(x, y, 0) E_{R_d}\, e^{ik(x^2+y^2)/2d'_r} \cdot e^{ik(\xi'^2+\eta'^2)/2d'_r}\, e^{-i2\pi(x\,k'_x + y\,k'_y)}\, dxdy \quad (3.73)$$

In practice, the reference wave $E_{R_d}(x, y, z)$ is a uniform plane wave that is simply given by its real amplitude :

$$E_{R_d}(x, y, z) \propto a_{R_d} \quad (3.74)$$

a_{R_d} is constant, the multiplication with the digital reference wave E_{R_d} can thus be omitted in the calculations. Equation 3.73 is thus ($E_H \equiv E_H(x, y, 0) \equiv E_R^*(x, y, 0)\, E_{obj}(x, y, 0) \equiv {E_R}^* E_{obj}$) :

$$E'(k'_x, k'_y, z_r) = \underbrace{\frac{e^{ikd'_r}}{i\lambda d'_r}}_{1} \iint_{-\infty}^{+\infty} E_H\, e^{ik(x^2+y^2)/2d'_r} \underbrace{e^{ik(\xi'^2+\eta'^2)/2d'_r}}_{2} e^{-i2\pi(x\,k'_x + y\,k'_y)}\, dxdy \quad (3.75)$$

The term, $e^{ikd'_r}/i\lambda d'_r$, noted "1" in Equation 3.75, is a constant term, independent of the position (ξ', η') in the reconstruction plane z_R, and depends only on the wavelength λ of the wave and on the reconstruction distance d'_r, that are both fixed . Moreover, the term, $e^{ik(\xi'^2+\eta'^2)/2d'_r}$, noted "2" in Equation 3.75, shows that, in reality, the reconstruction is not performed over plane (x, y, z_r) but over a spherical surface of radius d'_r and centered in point $z = 0$.

The phase factor $e^{ikd'_r}/i\lambda d'_r$ is constant and thus do not intervene. Phase factor $e^{ik(\xi'^2+\eta'^2)/2d'_r}$ also do not intervene because, here, only the intensity is of interest. Consequently, these two phase factors can be neglected. Equation 3.75 can thus be rewritten as :

$$E'(k'_x, k'_y, z_r) = \iint_{-\infty}^{+\infty} E_H(x, y, 0)\, e^{ik(x^2+y^2)/2d'_r} e^{-i2\pi(x\,k'_x + y\,k'_y)}\, dxdy \quad (3.76)$$

A comparison of equation 3.76 with the definition of the two-dimensional direct Fourier transform :

$$\mathscr{F}\{f(x, y)\} = \iint_{-\infty}^{+\infty} f(x, y) \cdot e^{-i2\pi(k_x x + k_y y)} dx\, dy \quad (3.77)$$

shows that the reconstructed field $E'(k'_x, k'_y, z_r)$, obtained by the Fresnel transformation, up to a neglected spherical phase factor

$e^{ikd'_r/i\lambda d'_r} \cdot e^{ik(\xi'^2+\eta'^2)/2d'_r}$, is proportional to a two-dimensional Fourier transform of the digital hologram $E_H(x, y, 0)$ multiplied by a quadratic phase term $e^{ik(x^2+y^2)/2d'_r}$ that accounts for the curvature of the wave fronts.

It is also demonstrated, that this quadratic phase factor $e^{ik(x^2+y^2)/2d'_r}$ is equal to the transmission function of a lens with focal length $f = d'_r$ [Schnars & Jueptner 2005].

Discretization of the Fresnel Transformation integral

In practice, the hologram is recorded by a CCD detector which is a two-dimensional matrix of pixels as illustrated on Figure 3.12. The hologram's field $E_H(x, y, 0)$ is thus sampled on a $M \times N$ pixel array with steps $(\Delta\xi, \Delta\eta)$ along both the horizontal and vertical directions. The continuous formulas are transferred into finite discrete algorithms which can be implemented in digital image processing systems : the Fresnel transformation integral is discretized by replacing the double integral with a double summation $(\sum_{k=0}^{N-1} \sum_{l=0}^{M-1})$ and the continuous variables x and y at the hologram plane are now described as discrete coordinates :

$$(x, y) = (k\Delta\xi, l\Delta\eta) \tag{3.78}$$

where k and l are integers varying in the range of $0 \leq k \leq M-1$ and $0 \leq l \leq N-1$.

Similarly, the continuous frequency variables k'_x and k'_y are converted into discrete variables too :

$$(k'_x, k'_y) = (m\Delta k'_x, n\Delta k'_y) \tag{3.79}$$

where m and n are integers varying in the range of $0 \leq m \leq M-1$ and $0 \leq n \leq N-1$.

The maximum frequency is determined by the sampling interval in the spatial domain :

$$k'_{x\,max} = M\Delta k'_x = \frac{1}{\Delta\xi} \tag{3.80}$$

$$k'_{y\,max} = N\Delta k'_y = \frac{1}{\Delta\eta} \tag{3.81}$$

with the condition :

$$-k'_{x,y_{max}}/2 < k'_{x,y} < -k'_{x,y_{max}}/2 \tag{3.82}$$

The pixel' size in the hologram $(\Delta\xi\,, \Delta\eta)$ and the pixel' size in the reconstructed image plane $(\Delta\xi'\,, \Delta\eta')$ are not equal. Relations between them is deduced from the previous equations [Schnars & Jueptner 2005] (Equations 3.71 ,3.72 ,3.80 ,3.81) as following :

$$\Delta\xi = \frac{\lambda d'_r}{M\Delta\xi'} \tag{3.83}$$

$$\Delta\eta = \frac{\lambda d'_r}{N\Delta\eta'} \tag{3.84}$$

From Equation 3.83 and Equation 3.84 , we can see that the pixel' size $(\Delta\xi', \Delta\eta')$ of the reconstructed image, which is determined directly from the Fresnel transform, vary as a function of the reconstruction distance d'_r. Therefore the reconstructed image changes in size according to the reconstruction distance.

$$\Delta\xi' = \frac{\lambda d'_r}{M\Delta\xi} \tag{3.85}$$

$$\Delta\eta' = \frac{\lambda d'_r}{N\Delta\eta} \tag{3.86}$$

Equation 3.85 and Equation 3.86 give the horizontal and vertical diameters of the Airy disk in the image plane and set thus the diffraction limited resolution of the optical system.

Limitations

Highly diffusive objects

In order to conserve the accuracy of the Fresnel approximation, the value of the integral in Equation 3.70 should remains undisturbed. Hence, it is necessary that the higher order terms of the Taylor expansion remains negligible.

Although the Fresnel diffraction formula can still give an accurate reconstruction for smooth and slowly varying objects where the Fresnel approximation is not strictly satisfied, it cannot correctly reconstruct near wave-fields for more diffractive objects, where the higher-order terms in the Taylor expansion of the Fresnel approximation are more significant.

Reconstruction distance requirements

The Fresnel transform also requires that the distance between the object and the hologram plane be sufficiently large in comparison to the size of the object or the hologram. This sets the minimum reconstruction distance $d_{r_{min}}$

Size of the reconstructed image

A deep examination of the reconstructed image, obtained from the reconstructed field $E'(k'_x, k'_y, z_r)$, shows that the image coordinates correspond to the components(k_x, k_y) of the wave vector $\vec{k}$ which is oriented along the varying reconstruction point M'. Hence, dimensions of the reconstructed image directly depends on the chosen reconstruction distance z_r

Overview of the reconstruction with the Fresnel transformation

From the the hologram's field $E_H(x, y, 0)$ recorded at the CCD plane, the field $E'(\xi', \eta', z_r)$ of a plane situated at any distance d'_r behind the CCD can be reconstructed using the Fresnel Transformation which consists of two steps :

The first step consists of multiplying the initial wave field at the CCD plane $E_H(x, y, 0)$ by a phase factor $e^{ik(x^2+y^2)/2d'_r}$ that accounts for the curvature of the wavefronts, which is also equivalent to the transfer function of a lens with a focal length d'_r.

The second step consists of performing a Direct Fourier Transformation (DFT) of the obtained function that will yield to the field $E'(\xi', \eta', z_r)$ at the reconstruction plane.

$$E'(\xi', \eta', z_r) = E(k'_x, k'_y, z_r) = DFT\{E_H(x, y, 0)e^{ik(x^2+y^2)/2d'_r}\} \tag{3.87}$$

In practice, holograms are recorded on discrete numerical CCD detectors and calculations are carried out on discrete processors, we use the discrete version of the Fresnel transform integral and thus the Fourier transforms are done using the Fast Fourier Transforms algorithms (FFT).

3.4.2.2 Reconstruction by the Angular spectrum method

The *angular spectrum* method of calculating holographic optical fields is noted to have several advantages over the more commonly used Fresnel transformation or Huygens convolution method : spurious noise and interference

components can be tightly controlled through the analysis and filtering of the angular spectrum. Moreover, the reconstruction distance does not have a lower limit, and the off-axis angle between the object and reference wave can be lower than that of the Fresnel requirement, while still allowing the zero-order background to be cleanly separated.

The angular spectrum reconstruction method is formulated in a framework that closely resembles the theory of linear, invariant systems were the complex wave field is expanded into a summation of infinite number of plane waves. The technique can predict a field distribution over a plane, based upon knowledge of the field distribution at a parallel plane. In fact, if the complex field distribution of a monochromatic disturbance is Fourier-analyzed across any plane, the various spatial Fourier components can be identified as plane waves traveling in different directions away from that plane. The field amplitude at any other point, or across any other parallel plane, can be calculated by adding the contributions of these plane waves, taking into account the phase shifts they have undergone during propagation.

Definition of the Angular Spectrum

Suppose that, due to some unspecified system of monochromatic sources, a wave is incident on a transverse $(x, y, 0)$ plane and traveling with a component of propagation in the positive z direction. Let the complex field across that $z = 0$ plane be represented by $E_0(x, y, 0)$; our ultimate objective is to calculate the resulting field $E_r(x, y, z_r)$ that appears across a second, parallel plane (x, y, z) at a distance $z = z_r$ to the right of the first plane as illustrated on Figure 3.15 [4].

By the use of the generalized form of the two-dimensional direct and inverse Fourier transforms :

$$\mathscr{F}\{f(x,y)\} = F(u,v) = \iint_{-\infty}^{+\infty} f(x,y) \cdot e^{-i2\pi(ux+vy)} dx\, dy \tag{3.88}$$

$$\mathscr{F}^{-}\{F(u,v)\} = f(x,y) = \iint_{-\infty}^{+\infty} F(u,v) \cdot e^{i2\pi(ux+vy)} du\, dv \tag{3.89}$$

across the $z = 0$ plane, the function E_0 ($E_0 \equiv E_0(x, y, 0)$) has a two-dimensional Fourier transform given by [Goodman 1968] :

[4] the notation "r" is used to refer to "reconstruction"

$$\mathscr{F}\{E_0\} = A_0(f_x, f_y; 0) = \iint_{-\infty}^{+\infty} E_0 \cdot e^{-i2\pi(f_x x + f_y y)} dx\, dy \tag{3.90}$$

The inverse Fourier transform of A_0 ($A_0 \equiv A_0(f_x, f_y; 0)$ is :

$$\mathscr{F}^{-}\{A_0\} = E_0 = \iint_{-\infty}^{+\infty} A_0 \cdot e^{i2\pi(f_x x + f_y y)} df_x\, df_y \tag{3.91}$$

To give physical meaning to the functions in the integrand of the above integral, consider the form of a simple plane wave $E(x, y, z)$ propagating with wave vector $\vec{k}$ as formulated in the beginning of this chapter. Such a plane wave has a complex representation of the form:

$$E(x, y, z) = e^{i\varphi} = e^{i\vec{k}\vec{r}} \tag{3.92}$$

writing the dot product of vectors $\vec{k}$ and $\vec{r}$ out fully, we get :

$$E(x, y, z) = e^{i\frac{2\pi}{\lambda}(k_x x + k_y y)} e^{i\frac{2\pi}{\lambda}k_z z} \tag{3.93}$$

The coordinates of $\vec{k}$ are interrelated through:

$$k_z = \sqrt{k^2 - k_x^2 - k_y^2} \tag{3.94}$$

Thus across the plane $z = 0$, the complex-exponential function $e^{i2\pi(f_x x + f_y y)}$ may be regarded as representing a plane wave propagating with :

$$\vec{k} = \begin{pmatrix} k_x = 2\pi\, f_x \\ k_y = 2\pi\, f_y \\ k_z = \sqrt{k^2 - k_x^2 - k_y^2} \end{pmatrix} \tag{3.95}$$

In the Fourier decomposition of E, the complex amplitude of the plane-wave component with spatial frequencies (f_x, f_y) is simply $A_0(f_x, f_y, 0)\, df_x\, df_y$, evaluated at $(f_x = k_x/2\pi, f_y = k_y/2\pi)$

For this reason, the function $A_0(k_x, k_y, 0)$ is called the angular spectrum of the disturbance $E_0(x, y, 0)$:

$$A_0(k_x, k_y; 0) = \iint_{-\infty}^{+\infty} E_0(x_0, y_0, 0) \cdot e^{-i(k_x x + k_y y)} dx\, dy \tag{3.96}$$

$$E_0(x_0, y_0, 0) = \iint_{-\infty}^{+\infty} A(k_x, k_y; 0) \cdot e^{i(k_x x + k_y y)} dk_x\, dk_y \tag{3.97}$$

Propagation of the Angular Spectrum

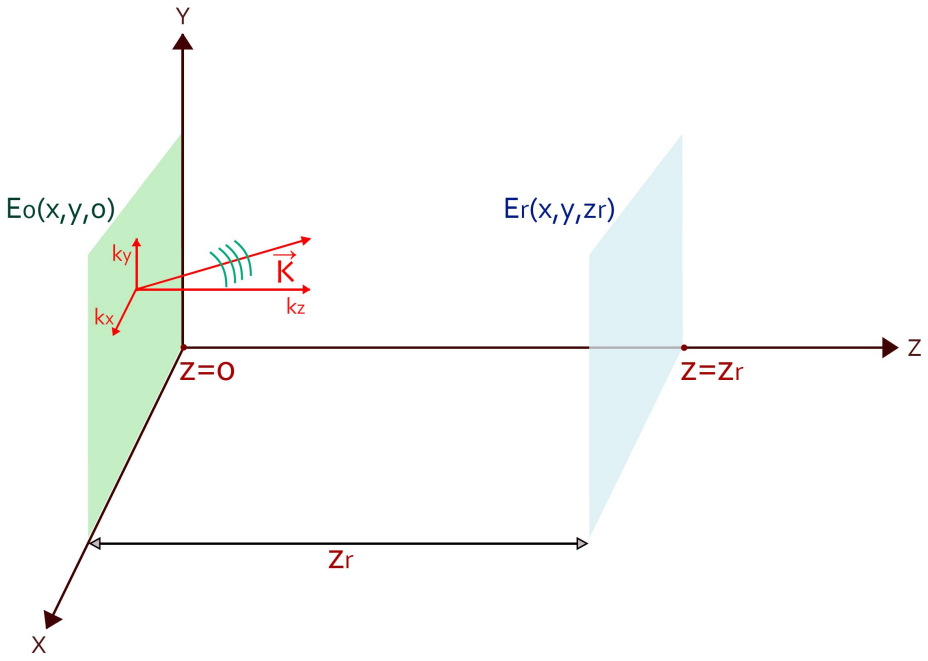

Figure 3.15: Coordinate system of the angular spectrum propagation

We will consider now the angular spectrum of the disturbance E across a plane parallel to the (x, y) but at a distance z_r from it. The coordinate system is sketched on figure 3.15.

The function $A_r(k_x, k_y; z_r)$ represents the angular spectrum of $E_r(x, y, z_r)$:

$$A_r(k_x, k_y; z_r) = \iint_{-\infty}^{+\infty} E_r(x, y, z_r) \cdot e^{-i(k_x x + k_y y)} dx\, dy \tag{3.98}$$

$$E_r(x, y, z_r) = \iint_{-\infty}^{+\infty} A_r(k_x, k_y; z_r) \cdot e^{i(k_x x + k_y y)} dk_x\, dk_y \tag{3.99}$$

In order to determine the effect of wave propagation on the angular spectrum of the disturbance, the relation between $A_0(k_x, k_y; 0)$ and $A_r(k_x, k_y; z_r)$ should be determined.

The complex amplitude of any monochromatic optical wave propagating in free space must satisfy the Helmholtz equation. Hence, $E_r(x, y, z_r)$ must obey :

$$\nabla^2 E_R + k^2 E_R = 0 \tag{3.100}$$

Consequently, A_r ($A_r \equiv A_r(k_x, k_y; z_r)$) must thus satisfy the following differential equation :

$$\frac{d^2}{dz_r^2} A_r + \frac{2\pi}{\lambda}[k^2 - k_x^2 - k_y^2]\, A_r = 0 \tag{3.101}$$

An elementary solution of this equation is :

$$A_r(k_x, k_y; z_r) = A_0(k_x, k_y; 0) e^{i\sqrt{k^2 - k_x^2 - k_y^2} \cdot z_r} \tag{3.102}$$

$$A_r = A_0\, e^{ik_z \cdot z_r} \tag{3.103}$$

Equation 3.103 establishes thus the relation between the angular spectrum $A_0(k_x, k_y; 0)$ at the $(x, y, 0)$ plane and the new angular spectrum $A_r(k_x, k_y; z_r)$ at the propagation plane (x, y, z_r).

It is thus interesting to introduce the notion of "*optical transfer function*". Equation 3.103 can be rewritten as :

$$\frac{A_r}{A_0} = e^{ik_z \cdot z_r} \tag{3.104}$$

By writing $k_z = \sqrt{k^2 - k_x^2 - k_y^2}$ and switching to the spatial frequencies, equation 3.104 gives :

$$\frac{A_r(f_x, f_y; z_r)}{A_0(f_x, f_y; 0)} = H(f_x, f_y) = e^{i2\pi\sqrt{(\frac{1}{\lambda})^2 - f_x^2 - f_y^2} \cdot z_r} \tag{3.105}$$

where $H(f_x, f_y)$ is called *optical transfer function* and characterizes the system's propagation phenomenon in the frequency domain :

$$H(f_x, f_y) = \begin{cases} e^{i2\pi\sqrt{(\frac{1}{\lambda})^2 - f_x^2 - f_y^2}} \cdot\ z_r & \text{if } f_x^2 + f_y^2 < \frac{1}{\lambda^2}, \\ 0 & \text{elswhere} \end{cases} \tag{3.106}$$

The propagation phenomenon can be considered as a low-pass filter, whose transmittance is equal to zero outside of a circular region of radius $\frac{1}{\lambda}$ in the frequency plane. Inside this circular domain, the transfer function modulus is equal to 1 , but a phase shift dependent on (f_x, f_y), λ and z_r is introduced. In other words, the effect of a propagation over a distance z_r is simply a change of the relative phase of the various components of the angular spectrum.

For simplification in what follows, the optical transfer function in equation 3.105 can be rewritten as :

$$H(f_x, f_y) = e^{i\frac{2\pi}{\lambda}\sqrt{(1 - (\lambda f_x)^2 - (\lambda f_y)^2} \cdot z_r} \tag{3.107}$$

We make a Taylor expansion of the square root term in equation 3.107 and we obtain :

$$\begin{aligned}\sqrt{(1-(\lambda f_x)^2-(\lambda f_y)^2} &= [(1-(\lambda f_x)^2-(\lambda f_y)^2]^{\frac{1}{2}} \\ &\simeq 1-\frac{\lambda^2}{2}(f_x^2+f_y^2) \end{aligned} \tag{3.108}$$

By substituting equation 3.108 in equation 3.107, we get :

$$H(f_x,f_y) = \underbrace{e^{i\frac{2\pi}{\lambda}\cdot z_r}}_{constant\ phase} \quad e^{-i\pi\lambda(f_x^2+f_y^2)\cdot z_r} \tag{3.109}$$

The first term in equation 3.109 is a constant phase term and can thus be omitted in what follows.
By substituting (f_x, f_y) in equation 3.109 with $(\frac{k_x}{2\pi}, \frac{k_y}{2\pi})$, we get :

$$H(k_x,k_y) = e^{-i\frac{(k_x^2+k_y^2)}{2\,k}\cdot z_r} \tag{3.110}$$

yielding finally to :

$$\begin{aligned} A_r(k_x,k_y;z_r) &= A_0(k_x,k_y;0)\,e^{ik_z\cdot z_r} \\ &= A_0(k_x,k_y;0)\,e^{-i\frac{(k_x^2+k_y^2)}{2\,k}\cdot z_r} \end{aligned} \tag{3.111}$$

Equation 3.111 describes the propagation effect of the angular spectrum A from the plane $z = o$ to the plane $z = z_r$: this propagation can be simply performed by multiplying the angular spectrum of the primary plane (A_0) by a phase factor, which is the exponential term $e^{ik_z\cdot z_r} = e^{-i\frac{(k_x^2+k_y^2)}{2\,k}\cdot z_r}$.
We can notice that this phase factor is quadratic in k_x and k_y and linear in z.

Reconstruction by propagation of the Angular Spectrum

In practice, holographic experiments are performed using a CCD detector which is a 2D matrix of discrete pixels $(N \times N)$. Consequently, a discrete formulation of the Angular Spectrum is considered in the following discussion.

An optical field $E_i(x, y, z_i)$ created at an initial plane (x, y, z_i) propagates along the z direction. The disturbance created by this propagating field can be evaluated at any later $z = z_r$ distance by reconstructing the resulting optical field $E_r(x, y, z_r)$ at this desired parallel plane (x, y, z_r). The geometrical

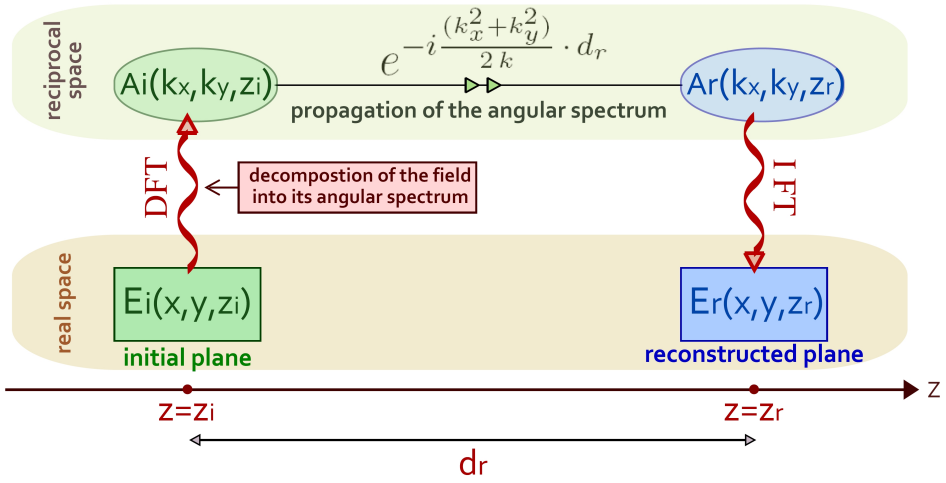

Figure 3.16: Numerical reconstruction by the angular spectrum method

distance between the two planes is noted d_r . The reconstruction method is a 3-steps process that involves two Fourier transforms. The full procedure is illustrated on figure 3.16.

The first step consists of decomposing the initial field $E_i(x, y, z_i)$ into its two-dimensional angular spectrum of plane waves $(A_i(f_x, f_y; z_i))$. As demonstrated in the previous paragraph, the angular spectrum is the Fourier transform of the field distribution. Hence, the angular spectrum decomposition process is, in practice, equivalent to a two-dimensional Direct Fourier Transform (DFT) :

$$A_i(k_x, k_y; z_i) = \iint_{-\infty}^{+\infty} E_i(x, y, z_i) \cdot e^{-i(k_x x + k_y y)} dx\, dy \tag{3.112}$$

The second step consists of propagating, in the reciprocal space, the initial angular spectrum $(A_i(k_x, k_y; z_i))$ to the desired reconstruction plane (x, y, z_r) in order to get its angular spectrum $(A_r(k_x, k_y; z_r))$. The propagation of the angular spectrum has been exhaustively described in the previous paragraph. It consists of a simple multiplication of the primary angular spectrum by a phase factor (or propagation term) which accounts for the phase change that each plane wave of the spectrum will undergo on its journey from the initial plane to the reconstruction plane :

$$A_r(k_x, k_y; z_r) = A_i(k_x, k_y; i)\, e^{-i\frac{(k_x^2+k_y^2)}{2\,k}\cdot d_r} \tag{3.113}$$

The angular spectrum $A_r(k_x, k_y; z_r)$ at the reconstruction plane is thus

obtained.

The third and last step of the reconstruction procedure allows the obtention, from the new resulting angular spectrum A_r , of the optical field E_r over the desired reconstruction plane (x, y, z_r). The field disturbance is the inverse Fourier transform of its angular spectrum : E_r is thus obtained from A_r by applying a two-dimensional Inverse Fourier Transform (IFT) :

$$E_r(x, y; z_r) = \iint_{-\infty}^{+\infty} A_r(k_x, k_y; z_r) \cdot e^{i(k_x x + k_y y)} dk_x \, dk_y \tag{3.114}$$

At the end of this chapter, it should be noted that, although we have described the basic processes in holography using the theoretical continuous variables definitions, in real experiments, holograms are recorded on discrete digital pixel arrays with finite pixels' number and size. The continuous double integrals that were used to describe the Fourier transformation operations are in practice discretized with discrete double summations and the corresponding discrete Fourier transforms were computed using the Fast Fourier Transform (FFT) algorithms.

Chapter 4

Heterodyne Digital Holography

Contents

4.1 Phase-Shifting Digital Holography 66

4.1.1 Phase-Shifting using a mirror mounted on a Piezoelectric Transducer 67

4.1.2 Phase-Shifting using a pair of Acousto-Optic Modulators 68

4.2 Holography at Ultimate Shot-Noise 73

4.3 Application for the Imagery of Vibrating Objects . . 74

In this thesis work, a system of heterodyne phase-shifting digital holography was elaborated. This system was basically used for the acquisition of all experimental holograms that are mainly presented in Chapters 5, 6 and 7 of this manuscript. This chapter is dedicated for the description of the adopted heterodyne detection-based holographic system while showing some possible direct applications. A detailed description of the holographic detection system is presented in Section 4.1 of this chapter. In Section 4.2 we will discuss about shot-noise in heterodyne holography. An application of phase-shifting heterodyne digital holography for the imagery of vibrating objects is presented in the last section of this chapter (Section 4.3).

We have seen in Chapter 3, that isolation of the third term in the interference (Equations 3.54), which is denoted +1 term or "complex interference" term, is a major issue in holography. This complex term is given by :

$$I_{+1} = E_R^* \, E_{obj}$$

The off-axis technique introduced by Leith and Upatnieks [Leith & Upatnieks 1962], which was described previously in this manuscript in Section 3.3.0.3 of Chapter 3, ensures the spatial separation, in the frequency domain, of the three different interference terms (0, -1 and +1), but I_{+1} is not straightforwardly isolated on the hologram captured by the CCD device. Accordingly, several methods have been developed for removal of the two disturbing terms from off-axis holograms. These methods are essentially

based on numerical filtering procedures [Kreis 2005].

In the case of in-line holography, the three terms overlap spatially making the isolation of I_{+1} much more complicated.

An effective technique of producing straightforward "pure" holograms where only I_{+1} is conserved is the *Phase-shifting digital holography*.

4.1 Phase-Shifting Digital Holography

Phase-Shifting holography was first introduced in 1997 by Yamaguchi and Zhang [Yamaguchi & Zhang 1997, Zhang & Yamaguchi 1998] and has attracted widespread interest. This technique works well for off-axis holography as well as for in-line holography and can be applied in both configurations. The basic principle of Phase-shifting holography emanates from the following observation [Mertz 2010] : the arbitrary phase between the reference and object waves, which is omitted when it is assumed to be fixed, can play quite a significant role when it is varied in a controlled manner. In the phase-shifting technique, the 0 and -1 terms are retrieved through multi-exposure holographic recording while shifting the phase of the reference wave by an integer fraction of 2π between two consecutive captured CCD images.

Taking into account the spatial and the temporal dependence, the complex notation of the reference field, where the wave is assumed to be traveling in the z-direction, is given by :

$$\begin{aligned} E_R(x,y,z,t) &= a_R\, e^{i\omega_L t}\, e^{i(-k\,z-\varphi_0)} \\ E_R(x,y,z,t) &= a_R\, e^{i\,2\pi\,f_L t}\, e^{i(-k\,z-\varphi_0)} \end{aligned} \tag{4.1}$$

where : $f_L = 2\pi/\omega_L$ is the frequency of the initial Laser source.
From Equation 4.1, we can see that two experimental approaches are possible for shifting the phase of the reference wave :

1. Modulating the optical path z of the reference wave : this is performed using a reflective mirror mounted on a piezoelectric transducer (PZT) [Yamaguchi *et al.* 2001, Yamagushi 2006]

2. Modulating the frequency of the reference wave using a pair of Acousto-Optic Modulators (AOMs) [LeClerc *et al.* 2000]

Both approaches will be described, but we will focus on the second method that performs frequency modulation using two AOMs in the context of this thesis.

4.1.1 Phase-Shifting using a mirror mounted on a Piezoelectric Transducer

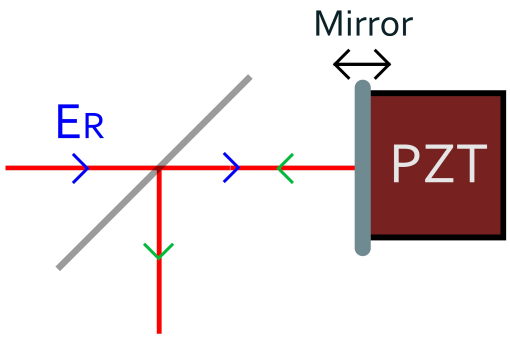

Figure 4.1: Phase-Shifting of the reference wave using a mirror mounted on a Piezoelectric Transducer

In a holographic experiment, the object wave and the reference wave are interfering at the surface of a CCD detector. In the phase-shifting technique that we are describing here, a phase shifting device is employed : the phase of the reference wave is shifted, relative to that of the object wave, by means of a mirror mounted on a piezoelectric transducer as shown in Figure 4.1. The piezo-crystal is controlled electrically. A mirror shift of $\lambda/8$ corresponds to a path-length change of $2\pi/8$ and due to the double pass results in a phase shift of $\pi/2$ in the reflected reference wave.

This is the most commonly used phase-shifting method. However, because of the non linearity of piezoelectric transducers, it is hard to achieve an equal accurate $\pi/2$ phase-shift between each two consecutive acquired images. Thus, we used another method that involves two acousto-optic modulators to achieve a better accuracy on the desired phase-shift thanks to the ability of AOMs to shift the frequency of a laser light beam by a precise and stable amount, which is crucial for the holographic experiments.

4.1.2 Phase-Shifting using a pair of Acousto-Optic Modulators

In this phase-shifting technique, a heterodyne method is used to generate the phase shift on the reference beam. The technique makes use of a *frequency shift* : a continuous phase change can be produced by inserting two acousto-optic modulators into the experimental arrangement.

We will first briefly present a review about Acousto-Optic Modulators. Then we will describe in details how heterodyne phase-shifting holography is achieved experimentally and we will describe the heterodyne detection method. Finally we will present the demodulation method that we used to extract I_{+1} from the several acquired phase-shifted holograms.

4.1.2.1 Acousto-Optics Modulators

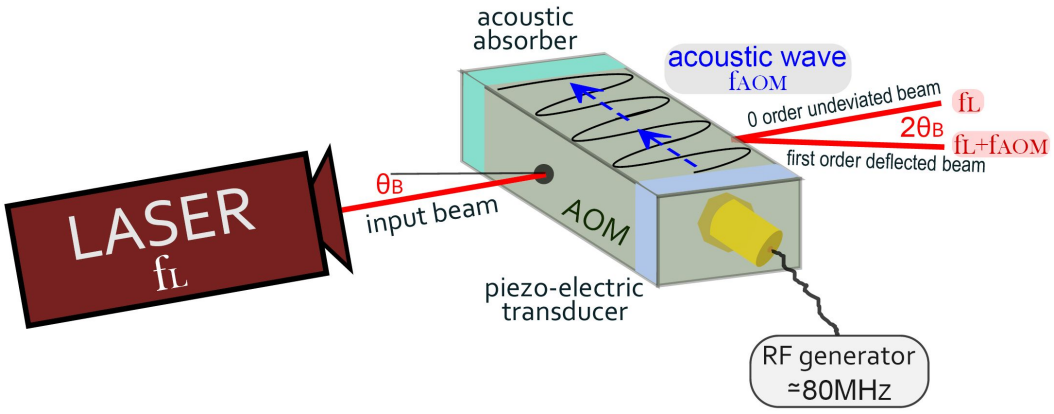

Figure 4.2: Acousto-Optic Modulator or Bragg Cell

An acousto-optic modulators, also called a Bragg cell, uses the acousto-optic effect, i.e. the modification of the refractive index by the oscillating mechanical pressure of a sound wave, to diffract and shift the frequency of an incident laser light. The commonly used sound waves are usually at radio-frequency.

The key element of an AOM is a transparent crystal through which the light propagates. A piezoelectric transducer attached to the crystal is used to excite a sound wave with a frequency of the order of 100 MHz. This acts like a "phase grating", traveling through the crystal at the acoustic velocity of the material and with an acoustic wavelength λ_{AOM} dependent on the

frequency of the used RF signal (see Figure 4.2). Light can then experience Bragg diffraction at the traveling periodic refractive index grating generated by the sound wave; therefore, AOMs are also called Bragg cells. Several diffraction orders can be observed(± 1, ± 2 ...) in addition to to undiffracted 0 order. However at one particular incidence angle θ_B, only one diffraction order with a maximum intensity is produced. This critical Bragg angle is given by :

$$\theta_B = \frac{\lambda_L}{2\lambda_{AOM}} \tag{4.2}$$

This first order diffracted beam is deviated by an angle which is equal to $2\theta_B$. The change in direction is small since the wavelength of the incident laser beam is very small compared with that of the sound wave. Furthermore, the diffracted beam is frequency shifted by Doppler effect. The frequency shift can be varied within the RF bandwidth of the Acousto-optic device by tuning the input RF carrier frequency and this shift δf is given by :

$$\delta f = \pm f_{AOM} \tag{4.3}$$

The light beam will be upshifted ($\delta = +f_{AOM}$) when the sound wave have a component of motion toward the incident beam, and downshifted ($\delta = -f_{AOM}$) when the sound wave have a component of motion away from the incident light beam. In this thesis, the upshifted first diffracted order is of interest, accordingly, the laser beam, after passing through the AOM, has a total frequency of $f_L + f_{AOM}$ (see Figure 4.2).

The frequency and direction of the scattered beam can be controlled via the frequency of the sound wave, whereas the acoustic power is the control for the optical powers. For sufficiently high acoustic power, more than 50% of the optical power can be diffracted and in extreme cases, even more than 95%.

4.1.2.2 Experimental Configuration for Heterodyne Phase-Shifting Holography

In our holographic experiments, a CCD camera detects the interference of the object and reference beams. Detection is only possible when the frequency of the resulting interference falls in the bandpass of the detection camera. In practice, CCD cameras have bandpass ranges limited to typically few tens of Hertz. It is thus impossible to acquire holograms where the reference beam was modulated by an AOM that operates in the domain of radio frequencies (80 MHz in our experiments). A heterodyne detection is thus needed in order to transpose the energy of the spectrum towards low frequencies to fall in

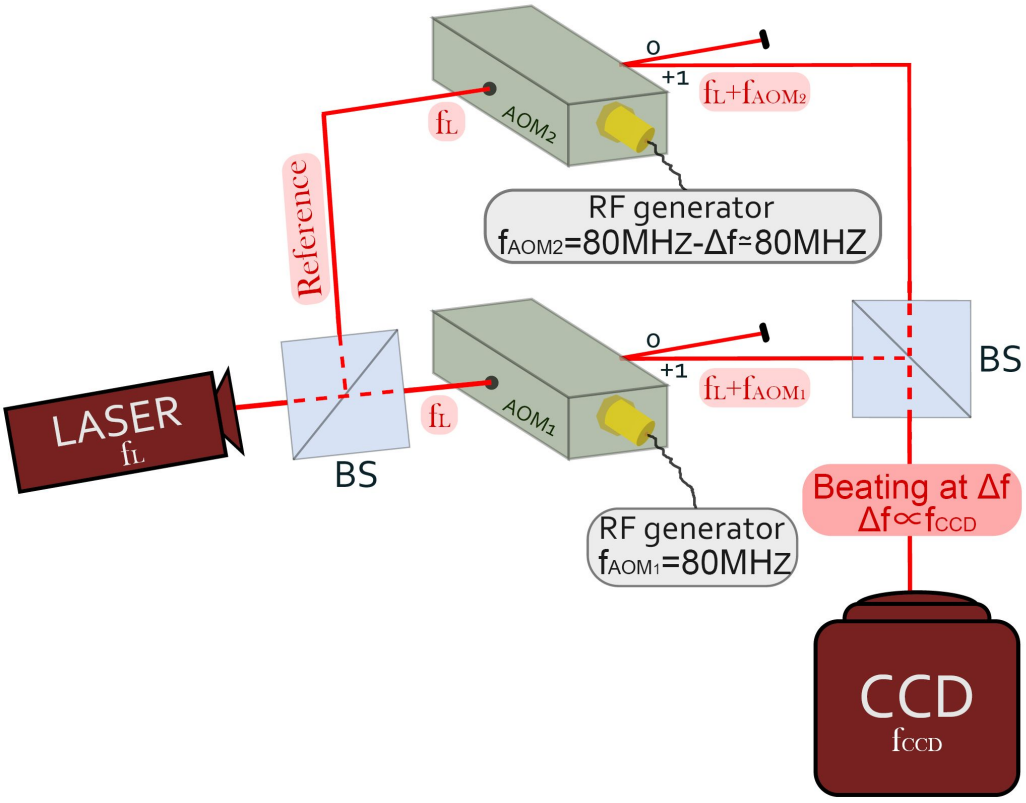

Figure 4.3: Arrangement for holographic heterodyne detection using two Acousto-Optic Modulators

the bandpass of the camera. Consequently, the modulated reference beam needs to be mixed with the object beam that is set to a close-by frequency before the final detection. This is achieved by shifting, as well, the object beam using a second AOM. This is why we have previously evoked that this phase-shifting technique requires the use of a pair of AOMs.

Figure 4.3 shows the typical arrangement that we adopted to perform holographic heterodyne detection using two AOMs.

The initial beam of the laser source (frequency f_L) is splitted into a reference beam (frequency f_L) and an object beam (frequency f_L). To perform temporal heterodyning, two AOMs were used.

AOM_1 is implemented on the object arm and is driven at frequency $f_{AOM_1} \equiv f_{AOM} = 80MHz$. Using an iris, we select the upshifted first order that is diffracted by the AOM. This diffracted beam is now the new object beam and its complex field is given by :

$$E_{obj} \simeq a_{obj}\, e^{i\,2\pi\, f_{obj} t} \tag{4.4}$$

where :

$$f_{obj} = f_L + f_{AOM_1} = f_L + f_{AOM} \tag{4.5}$$

AOM_2 is implemented on the object arm and is driven at frequency $f_{AOM_2} = f_{AOM} - \Delta f = 80MHz - \Delta f$. Using an iris, we select the first order that is diffracted by the AOM. This diffracted beam is now the new reference beam and its complex field is given by :

$$E_R \simeq a_R\, e^{i\,2\pi\, f_R t} \tag{4.6}$$

where

$$f_R = f_L + f_{AOM_2} = f_L + f_{AOM} - \Delta f \tag{4.7}$$

and Δf is the heterodyne beating frequency and is chosen to be in the bandpass of the detection CCD device. Δf is thus tuned to be proportional to the frame rate frequency f_{CCD} of the camera.

In this manner, heterodyne detection is achieved : the two optical waves (E_{obj} and E_R) are mixed after being set at a close-by frequency. The outcome is an intensity distribution oscillating with the beat frequency, which is the

introduced slight difference frequency Δf, that still carries the interesting information of the original high frequency signal but is now oscillating at a lower more easily processed carrier frequency.

Combining Equations 4.4, 4.5, 4.6 and 4.7 the interference of the obtained E_{obj} and E_R is given by :

$$\begin{aligned} I &= (E_R + E_{obj})(E_R + E_{obj})^* \\ I &= \underbrace{I_R + I_{obj}}_{0order} + \underbrace{E_R\, {E_{obj}}^*\, e^{i\,2\pi\,\Delta f\, t}}_{-1order} + \underbrace{{E_R}^*\, E_{obj}\, e^{-i\,2\pi\,\Delta f\, t}}_{+1order} \end{aligned} \tag{4.8}$$

In Equation 4.8, the 0 order term constitutes the homodyne part of the detected signal which is the self-beating term :

$$I_{hom} = I_R + I_{obj} \tag{4.9}$$

The -1 and $+1$ terms of Equation 4.8 constitutes the heterodyne part :

$$I_{het} = E_R\, {E_{obj}}^*\, e^{i\,2\pi\,\Delta f\, t} + {E_R}^*\, E_{obj}\, e^{-i\,2\pi\,\Delta f\, t} \tag{4.10}$$

The second term of Equation 4.10, is the relevant term that constitutes our holographic signal. A demodulation method is then used to eliminate the 0 and -1 terms and isolate the $+1$ term.

4.1.2.3 Four phases Demodulation

From the complex structure of Equation 4.8, we can perceive that if a four phases demodulation is executed using a sequence of M different holograms (where M is a multiple of 4) with the same frequency shift Δf but captured at different instants with a relative phase shift $\Delta\varphi = 2\pi\Delta f\, t = \pi/2$ between two consecutive frames, 0 and -1 terms automatically cancel. Thus, the acquisition of a sequence of M different holograms with the same frequency shift Δf on the reference wave but with different phase-states ($\Delta\varphi$) is necessary :

$$\Delta\varphi = \frac{\pi}{2} = 2\pi\frac{\Delta f}{f_{CCD}} \tag{4.11}$$

The frame rate frequency of the camera f_{CCD} should thus be 4 times larger than the frequency shift Δf :

$$\Delta f = f_R - fobj = f_{AOM_1} - f_{AOM_2} = f_{CCD}/4 \tag{4.12}$$

Along these lines, a sequence of M holograms is recorded by the CCD camera (H_1,...,H_M), each individual hologram having a phase-shift of $\Delta\varphi_j = j\frac{\pi}{2}$. Parameter j defines the index of each individual recorded hologram $j = 1,...,M$. Each hologram is defined as :

$$H_j = I_R + I_{obj} + E_R {E_{obj}}^* e^{i\frac{\pi}{2}j} + {E_R}^* E_{obj} e^{-i\frac{\pi}{2}j} \quad (4.13)$$

$$H_j = I_R + I_{obj} + E_R {E_{obj}}^* i^j + {E_R}^* E_{obj} (-i)^j \quad (4.14)$$

The total demodulated complex field at the CCD plane E_{CCD} is the sum of all the Hj holograms :

$$E_{CCD} = \sum_{j=1}^{M} i^j H_j \quad (4.15)$$

Combining Equation 4.14 and Equation 4.15, we get :

$$E_{CCD} = \sum_{j=1}^{M} i^j (I_R + I_{obj}) + \sum_{j=1}^{M} (-1)^j E_R {E_{obj}}^* + \underbrace{\sum_{j=1}^{M} (+1)^j {E_R}^* E_{obj}}_{+1\, order} \quad (4.16)$$

The two first terms of Equation 4.16 automatically cancel during the summation. A pure hologram, containing only the +1 term is thus generated :

$$E_{CCD} = M \cdot {E_R}^* E_{obj} \quad (4.17)$$

4.2 Holography at Ultimate Shot-Noise

We have seen in the previous section that our heterodyne technique used in an off-axis holographic configuration allows to record holograms with optimal sensitivity since the technical noise (the 0 order term), mainly related to the reference beam, is fully filtered-off. The only limiting noise, is the shot noise on the reference beam. Consequently, holographic imagery can be achieved at very low object's signal levels. The exhaustive review, that includes a comparative theoretical and experimental study, published as a book chapter [Joud *et al.* 2010a], is totaly out of scope of this thesis and can be found in Appendix B.3.

4.3 Application for the Imagery of Vibrating Objects

A possible direct application of phase-shifting heterodyne digital holography is the imagery of vibrating objects. More specifically, we have considered a vibrating clarinet reed that is excited by a sound wave produced by a loudspeaker. Since the reed is vibrating, the backscattered optical field is phase-modulated and is consequently expanded into carrier and sideband components. We have shown, that by a proper tuning of the frequency-shift induced by the AOMs, holographic imagery can be performed not only at the carrier frequency but also selectively at the vibration sidebands' frequencies. This is called sideband digital holography. Sidebands orders up to 120 have been observed allowing the characterization of oscillation amplitudes that are significantly larger than the optical wavelength. By this way, the vibration shape of the reed is reconstructed.

Since this application is not in the essence of this thesis work, we have decided to include in this section the journal paper, published in Optics Express [Joud *et al.* 2009a], that describes the experiment in details for interested readers. For information, another complementary paper [Joud *et al.* 2009b], published in Optics Letters, is included in Appendix B.4 of this manuscript.

Imaging a vibrating object by Sideband Digital Holography

F. Joud[1], F. Laloë[1], M. Atlan[2], J. Hare[1] and M. Gross[1].

[1] *Laboratoire Kastler Brossel – UMR 8552 École Normale Supérieure, UPMC, CNRS 24 rue Lhomond ; 75231 Paris Cedex 05 ; France*

[2] *Département de Biologie Cellulaire — Institut Jacques Monod, UMR 7592, CNRS, Univ. Paris 6 and 7 — 2 Place Jussieu ; 75251 Paris Cedex 05; France*

gross@lkb.ens.fr

Abstract: We obtain quantitative measurements of the oscillation amplitude of vibrating objects by using sideband digital holography. The frequency sidebands on the light scattered by the object, shifted by n times the vibration frequency, are selectively detected by heterodyne holography, and images of the object are calculated for different orders n. Orders up to $n = 120$ have been observed, allowing the measurement of amplitudes of oscillation that are significantly larger than the optical wavelength. Using the positions of the zeros of intensity for each value of n, we reconstruct the shape of vibration the object.

OCIS codes: (090.1760) Computer holography; (200.4880) Optomechanics; (040.2840) Heterodyne; (100.2000) Digital image processing.

References and links

1. R. Powell and K. Stetson, "Interferometric vibration analysis by wavefront reconstruction," J. Opt. Soc. Am **55**, 1593–1598 (1965).
2. P. Picart, J. Leval, D. Mounier, and S. Gougeon, "Time-averaged digital holography," Opt. Lett. **28**, 1900–1902 (2003).
3. F. Zhang, J. Valera, I. Yamaguchi, M. Yokota, and G. Mills, "Vibration Analysis by Phase Shifting Digital Holography," Opt. Rev. **11**, 297–299 (2004).
4. A. Asundi and V. Singh, "Time-averaged in-line digital holographic interferometry for vibration analysis," Appl. Opt. **45**, 2391–2395 (2006),.
5. V. Singh, J. Miao, Z. Wang, G. Hegde, and A. Asundi, "Dynamic characterization of MEMS diaphragm using time averaged in-line digital holography," Opt. Commun. **280**, 285–290 (2007).
6. N. Demoli and D. Vukicevic, "Detection of hidden stationary deformations of vibrating surfaces by use of time-averaged digital holographic interferometry," Opt. Lett. **29**, 2423–2425 (2004).
7. N. Demoli, "Real-time monitoring of vibration fringe patterns by optical reconstruction of digital holograms: mode beating detection," Opt. Express **14**, 2117–2122 (2006).
8. C. C. Aleksoff, "Temporally modulated holography," Appl. Opt. **10**, 1329–1341 (1971).
9. F. LeClerc, L. Collot, and M. Gross, "Numerical Heterodyne Holography Using 2D Photo-Detector Arrays," Opt. Lett. **25**, 716–718 (2000).
10. F. Pinard, B. Laine, and H. Vach, "Musical quality assessment of clarinet reeds using optical holography," J. Acoust. Soc. Am. **113**, 1736–1742 (2003).
11. M. Facchinetti, X. Boutillon, and A. Constantinescu, "Numerical and experimental modal analysis of the reed and pipe of a clarinet," J. Acoust. Soc. Am. **113**, 2874–2883 (2003).
12. I. Yamaguchi and T. Zhang, "Phase-Shifting digital holography," Opt. Lett. **22**, 1268–1270 (1997).
13. M. Atlan, M. Gross, and E. Absil, "Accurate phase-shifting digital interferometry," Opt. Lett. **32**, 1456–1458 (2007).
14. E. Cuche, P. Marquet, and C. Depeursinge, "spatial filtering for zero-order and twin-image elimination in digital off-axis holography," Appl. Opt. **39**, 4070–4075 (2000).
15. M. Gross and M. Atlan, "Digital holography with ultimate sensitivity," Opt. Lett. **32**, 909–911 (2007).

#104040 - $15.00 USD Received 12 Nov 2008; revised 6 Feb 2009; accepted 8 Feb 2009; published 11 Feb 2009

16. M. Gross, M. Atlan, and E. Absil, "Noise and aliases in off-axis and phase-shifting holography," Appl. Opt. **47**, 1757–1766 (2008).
17. U. Schnars and W. Jüptner, "Direct recording of holograms by a CCD target and numerical reconstruction," Appl. Opt. **33**(2), 179–181 (1994).

Holographic imaging is based on interferences between a signal optical field and a reference beam; it provides an accurate method to image the vibration of various objects. Powell and Stetson [1] have shown that the *time-averaged* hologram of an harmonically vibrating object involves the Bessel function $J_0(z)$, where z is the phase modulation amplitude. In the backscattering geometry, $z = 4\pi A/\lambda$ where A is the mechanical amplitude of vibration and λ the optical wavelength. Image reconstruction then provides a direct mapping of the amplitude A at various points of the object, in the form of dark fringes appearing around points where $J_0(z)$ is zero.

Picard et al. [2] have simplified the processing of the data by performing Time Averaged Digital Holography (TADH) with a CCD camera, leading to numerous recent developments [3, 4, 5, 6, 7]. Nevertheless, the quantitative measurement of vibration amplitudes remains limited to situations where fringes can be counted, which implies that the amplitudes of vibration must be relatively small; otherwise, it becomes difficult to count many narrow fringes, and even impossible when they are smaller than the optical resolution.

In this letter, we show how Sideband Digital Holography (SDH) can overcome the problem. Sideband holography was already demonstrated in 1971 by C.C. Aleksoff, in a pioneering experiment [8] where the reference beam was frequency-shifted by an ultrasonic diffraction cell; selecting a given frequency resulted in a selection of a given sideband of the signal backscattered by the object. The experiment was done with holographic plates. Here, we use digital heterodyne holography [9]; both reference and illumination laser beams are frequency shifted, and the selection of one sideband is obtained by a proper detuning of one of the beams followed by heterodyne detection on a CCD camera; this technique provides much more flexibility and leads to accurate quantitative measurements. As a demonstration, inspired by the work described in [10, 11] we perform an experiment where the vibrating object is the reed of a clarinet; in addition to the intrinsic interest of such an object, with its possible musical implications, a reed provides a test system that is particularly well adapted to our purposes, with typical vibration

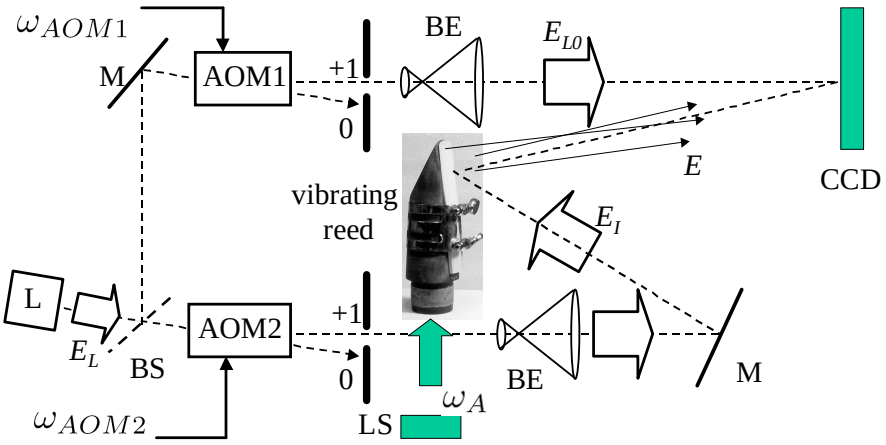

Fig. 1. Setup. L: main laser; AOM1, AOM2: acousto-optic modulators; M: mirror; BS: beam splitter; BE: beam expander; CCD: CCD camera; LS: loud-speaker exiting the clarinet reed at frequency $\omega_A/2\pi$.

#104040 - $15.00 USD Received 12 Nov 2008; revised 6 Feb 2009; accepted 8 Feb 2009; published 11 Feb 2009

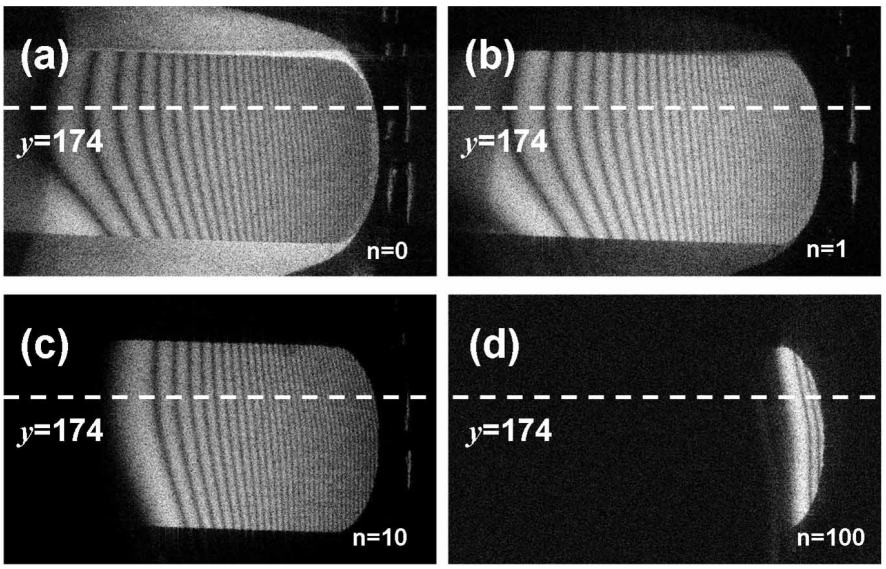

Fig. 2. Reconstructed holographic images of a clarinet reed vibrating at frequency $\omega_A/2\pi =$ 2143 Hz perpendicularly to the plane of the figure. Fig. (a) shows the carrier image obtained for $n = 0$; Fig. (b)-(d) show the frequency sideband images respectively for $n = 1$, $n = 10$, and $n = 100$. A logarithmic grey scale has been used.

amplitudes of the order of 0.1 mm. We will see that, even with smaller amplitudes, there is no difficulty in obtaining holographic images corresponding to the n^{th} sideband with n up to 100 or more.

The experimental setup is schematically shown in Fig. 1. A laser beam, with wavelength $\lambda \simeq 650$ nm (angular frequency ω_L) is split into a local oscillator beam (E_{LO}) and an illumination beam (E_I); their angular frequencies ω_{LO} and ω_I are tuned by using two acousto-optic modulators (Bragg cells with a selection of the first order diffraction beam) AOM1 and AOM2: $\omega_{LO} = \omega_L + \omega_{\text{AOM1}}$ and $\omega_I = \omega_L + \omega_{\text{AOM2}}$ where $\omega_{\text{AOM1,2}}/2\pi \simeq 80$ MHz. The clarinet reed is attached to a clarinet mouthpiece and its vibration is driven by a sound wave propagating inside the mouthpiece, as in playing conditions, but in our experiment the sound wave is created by a loudspeaker excited at frequency ω_A and has a lower intensity than inside a clarinet; no attempt has been made to reproduce the mechanical effect of the lip of the player. The excitation frequency is adjusted to be resonant with the first flexion mode (2143 Hz) of the reed. The phase of the field E backscattered by any element of the reed is then phase modulated at frequency ω_A, so that E can be expanded into carrier (E_0) and sideband components (E_n) as:

$$E(t) = \mathscr{E} e^{j\omega_I t} e^{jz\sin(\omega_A t)} = \sum_{n=-\infty}^{\infty} E_n(t) \tag{1}$$

$$E_n(t) = \mathscr{E} J_n(z) e^{j\omega_L t} e^{j(\omega_{AOM2} + n\omega_A)t} \tag{2}$$

where $\mathscr{E}$ is the complex field of the object in the absence of modulation, $z = 4\pi A/\lambda$ is the phase modulation amplitude, A the amplitude of vibration of the particular element, and J_n is the n-th order Bessel function of the first kind (with $J_{-n}(z) = (-1)^n J_n(z)$ for integer n and real z).

To selectively detect the n^{th} sideband we use 4 phase shifting holography [12] and adjust the

#104040 - $15.00 USD Received 12 Nov 2008; revised 6 Feb 2009; accepted 8 Feb 2009; published 11 Feb 2009

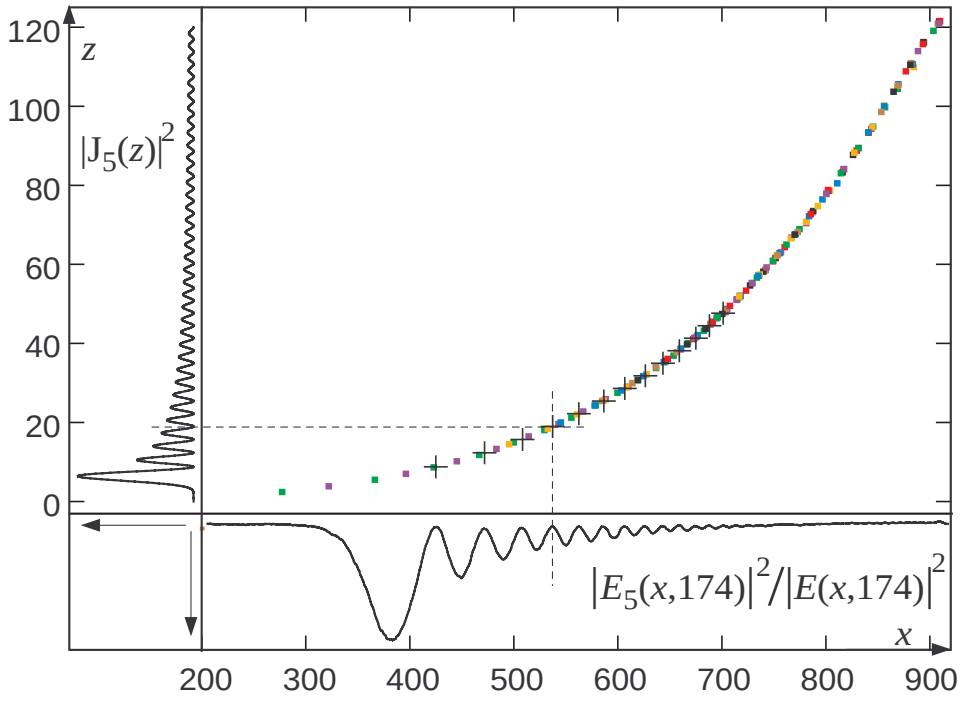

Fig. 3. A slice of the data along the $y = 174$ line is used in this figure; the x horizontal axis gives the pixel index (100 pixels correspond to 3.68 mm.), the vertical axis the phase modulation amplitude z. The lower part of the figure shows the normalized signal $|E_n(x)|^2/|E(x)|^2$ for a particular sideband order $n = 5$, with a downwards axis; the left part shows the corresponding square of the Bessel function $|J_5(z)|^2$ with a leftward axis. The zeroes of the two curves are put in correspondence, which provides the points in the central figure; a different color is used for each harmonic order $n = 0, 1, 5, 10...100$; the crosses correspond to $n = 5$. The juxtaposition of the points for all values of n gives an accurate representation of the amplitude of vibration A as a function of x.

frequency ω_{AOM1} to fulfil the condition:

$$\omega_{\mathrm{AOM2}} - \omega_{\mathrm{AOM1}} - n\,\omega_A = \omega_{\mathrm{CCD}}/4 \tag{3}$$

where ω_{CCD} is the CCD camera frame frequency and n is a (positive or negative) integer; the phase of the modulated signal is then shifted by 90° from one CCD image to the next [13]. The sideband complex hologram signal H_n provided by each pixel of the camera, proportional to the local sideband complex field, is obtained by 4-phase demodulation:

$$H_n = (I_0 - I_2) + j(I_1 - I_3)\ , \tag{4}$$

where $I_0, \cdots I_3$ are 4 consecutive intensity images digitally recorded by the CCD camera (Pike: Allied vision Technology Inc, 12 bits, $\omega_{\mathrm{CCD}}/2\pi = 10$ Hz, exposure time 100 ms, 1340×1024 pixels). The LO beam is slightly angularly shifted ($\sim 1°$) with respect to the beam originating from the reed; in this way, the zero order and twin-image aliases [14] can be suppressed and an ultimate detection sensitivity can be reached [15, 16].

From the complex holograms, the images of the reed are reconstructed by the standard convolution method [17]. To simplify the Fourier transform calculation, the 1340×1024 pixels

#104040 - $15.00 USD Received 12 Nov 2008; revised 6 Feb 2009; accepted 8 Feb 2009; published 11 Feb 2009

data are truncated to 1024×1024. Because of the angular shift, the image of the reed lies in the upper side of the reconstruction grid. In Fig. 2, for pixels ranging from 200 to 1023 along the x axis and 0 to 511 on the y axis, we show the reconstructed images for different sideband orders n; only the square modulus of the complex signal is retained (the phase coming from $\mathscr{E}$ is ignored), so that we obtain intensity images, proportional to $|E_n|^2$ for each different sideband.

Figure 2(a) is obtained at the unshifted carrier frequency ($n = 0$). The left side of the reed is attached to the mouthpiece, and the amplitude of vibration is larger at the tip of the reed on the right side; in this region the fringes become closer and closer and difficult to count. The mouthpiece is also visible, but without fringes since it does not vibrate. Similar images of clarinet reeds have been obtained in [10, 11], with more conventional techniques and lower image quality. Figures 2(b)-2(d) show images obtained for three sideband frequencies. As expected, the non-vibrating mouthpiece is no longer visible. Figure 2(b) shows the $n = 1$ sideband image, with J_1 fringes that are slightly shifted with respect to those of J_0. Figure 2(c) shows the order $n = 10$ and (d) the order $n = 100$ (e). The left side region of the image remains dark because, in that region, the vibration amplitude is not sufficient to generate these sidebands, $J_n(z)$ being evanescent for $z < n$.

We have performed cuts of the reconstructed images signal $|E_n(x,y|^2$ obtained for different sideband orders n along the horizontal line $y = 174$ (this value has been chosen because it corresponds to a region where the fringes are orthogonal to the y axis). To reduce the effect of speckle fluctuations, the intensity signal $|E_n(x, y = 174)|^2$ has been averaged over 20 pixels in the y direction ($y = 164 \ldots 184$). Moreover, since the illumination of the reed is not uniform, we have normalized the sideband signal by the reconstructed image intensity $|E|^2$ obtained at the carrier frequency ($n = 0$) without mechanical excitation of the reed (loud-speaker off). One example of the normalized signals $|E_n|^2/|E|^2$ along the cut is shown for $n = 5$, in the lower part of Fig. 3, with a downwards intensity axis. In this case, and for many other values of n, we have checked that the normalized curves vary as the square of Bessel functions, with a first fringe that moves to higher values when n increases (it occurs when $z \simeq n$ and the amplitude of vibrations increases with x). For instance, for $n = 0$, which corresponds to standard TADH, the variations of $|J_0(z)|^2$ show a large number of nodes and anti-nodes, with decreasing visibility for increasing x; above $x = 700$, the fringes are no longer visible. For $n = 20$, the first fringe, which corresponds to $z \simeq n = 20$, is located near $x \simeq 560$. Going to $n = 60$ pushes the first fringe to $x \simeq 755$, where the counting of fringes with TADH would no longer be possible. In a more general way, the first fringe on the n^{th} sideband image provides a convenient marker for the region $z \simeq n$.

For a more precise treatment of the data, we use the position of the antinodes, which is insensitive to inhomogeneities of illumination; no normalization is then required. To build the central part of Fig. 3, a similar linear cut at $y = 174$ is processed, for the values $n = 0, 1, 5, 10, \ldots 100$. The x locations of the successive minima of the signal $|E_n(x)|^2$ are plotted against the zeros of the corresponding $|J_n(z)|^2$. To illustrate the way the points are obtained, we show in the left part of the Fig. 3 the expected signal $|J_5(z)|^2$, to be compared to the signal in the lower part. For all observed sideband order n ranging from 0 to 100, all the points displayed on Fig. 3 fall on a well defined curve, which provides the vibration amplitude z as function of the location x. The excellent consistency of the overlapping data sets demonstrates the validity of expansions Eq. 1 for any order n. Therefore the figure provides a direct and accurate visualization of the map of the maximal elongations of the reed, from the left part clamped on the mouthpiece to the tip on the right; here, the maximum amplitude is $z \simeq 120$ radians, corresponding to $A \simeq 6.2\ \mu$m.

To conclude, recording separately different sideband Fourier components of the light back-scattered by a vibrating object gives access to a large amount of information; this can be used to remove ambiguities and inaccuracies in measurements of large modulation amplitude. Using

#104040 - $15.00 USD Received 12 Nov 2008; revised 6 Feb 2009; accepted 8 Feb 2009; published 11 Feb 2009

large sideband order n actually makes the calibration of the vibration amplitude z straightforward: the first fringe of a high order image can be used as a marker. This marker is easy to locate since it corresponds to a fast transition from zero signal, and moreover is brighter and broader. Performing sideband holography with many orders n gives a direct and accurate access to the shape of the vibration amplitude and its position dependence. Figure 3 shows only a representation of a slice of the data along one given axis, but more information is available if one changes the value of y or chooses another direction, for instance parallel to y to accurately map the transverse variations of the amplitude A. Sideband digital holography therefore opens up a variety of new possibilities in holography.

The authors acknowledge the support of French National Research Agency (ANR-05-NANO-031) and the "Centre de compétence NanoSciences Île de France" (C'nano IdF).

#104040 - $15.00 USD Received 12 Nov 2008; revised 6 Feb 2009; accepted 8 Feb 2009; published 11 Feb 2009

Chapter 5

Interferometric Heterodyne Digital Holographic Microscopy

Contents

5.1 Optical Apparatus and General Reconstruction Scheme 82

5.1.1 Optical Apparatus for the Holographic Microscope . . 82

5.1.2 Optical Arrangement for Reconstruction in Holographic Microscopy 83

5.1.3 The principle of the Reconstruction In Heterodyne Holographic Microscopy 85

5.2 First Step of The Reconstruction : Reconstruction of the Conjugate Image 86

5.2.1 Determination of the lens, tilt and magnification parameters by a proper calibration of the setup 86

5.2.2 Determination of the lens, tilt and magnification factor by reconstructing the image of the MO exit pupil . . . 93

5.3 Second Step : 3D Reconstruction of the Object by propagation of the Angular Spectrum 102

5.4 Abberations 105

5.4.1 Propagation kernel for large Numerical Aperture MO . 106

5.4.2 Specimen maintained in a culture medium and imaged with an air MO 107

5.4.3 Specimen uncovered with a coverslip and imaged with a cover glass corrected MO 109

5.5 Overview of the Reconstruction procedure in Holographic Microscopy 112

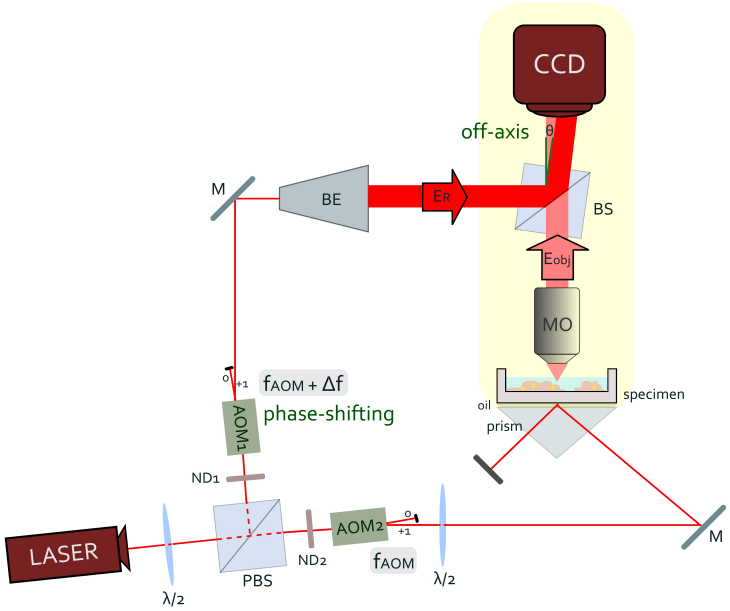

Figure 5.1: General Experimental setup for Heterodyne Digital Holographic Microscopy

5.1 Optical Apparatus and General Reconstruction Scheme

This section is reserved to the general description of the optical apparatus used for holographic microscopy. The optical arrangement that is considered for the reconstruction process is also described here.

5.1.1 Optical Apparatus for the Holographic Microscope

The optical apparatus of digital holographic microscopy is illustrated on Figure 5.1. It is a modified Mach-Zehnder interferometer were a laser is used as a coherent illumination source. A polarizing beam splitter cube, noted PBS, is used to split the original illumination laser light into two beams, a reference beam and an object illumination beam. The complex field of the reference wave is noted E_R and its frequency f_R. Similarly, the complex field of the illumination wave is noted E_{obj} and its frequency f_{obj}. Those beams form thus the two arms of the Mach-Zehnder interferometer. A combination of two neutral density filters (ND_1, ND_2) is used to prevent the saturation of the detector by controlling the optical power traveling in each arm. Two acousto-optic modulators AOM1 and AOM2, driven around 80 MHz with a selection of the first order of diffraction, shift both frequencies at respectively f_{AOM1}

and f_{AOM2}. Acousto-optic modulators are driven at f_{AOM1} and f_{AOM2} using two synchronized numerical waveform synthesizers allowing thus to finely control f_{AOM1} and f_{AOM2} and consequently the frequency (and the phase) of the reference wave :

$$f_R = f_{obj} + (f_{AOM1} - f_{AOM2}) \tag{5.1}$$

The object beam illuminates the sample in total internal reflection (TIR) and a microscope objective (MO) collects the light scattered from the sample. A beam splitter BS is then used to combine the scattered object wave and the reference wave which is slightly angularly tilted ($\theta \sim 1°$) with respect to the propagation axis of the object wave in an off-axis configuration. In order to fulfill optimal interference conditions, the polarization of the two interfering waves is controlled using the two half wave plates ($\lambda/2$) that are implemented on the optical apparatus. The interference of E_R and E_{obj} is detected by the sensor of a CCD camera that records a sequence of M (M is an integer) intensity frames (or holograms) H_{CCD_j} (j is the frame index, varying from 1 to M), where each frame corresponds to a given phase state of the reference wave.

Typical experiments are made in phase-shifting recording configuration with a relative phase-shift $\Delta\varphi = \pi/2$ between two consecutive frames. As described in Chapter 4, this 4-phases configuration corresponds to :

$$f_R = f_{obj} + f_{CCD}/4 \tag{5.2}$$

and this is achieved when $f_{AOM1} - f_{AOM2} = f_{CCD}/4$, where f_{CCD} is the camera frame frequency. The complex field at the CCD plane E_{CCD} is given by :

$$E_{CCD}(x, y, z_{CCD} = 0) = \sum_{j=1}^{M} i^{\,n} H_{CCD_j} \tag{5.3}$$

with $i^2 = -1$

5.1.2 Optical Arrangement for Reconstruction in Holographic Microscopy

The different steps of the reconstruction process are based on a specific adopted optical arrangement. Thus, in order to explain the reconstruction algorithm, we should first start by describing this specific arrangement. We focus on the yellow-highlighted part of the general experimental setup of figure 5.1, which is the main part of the holographic microscope. This part of the optical apparatus is illustrated in details on figure 5.2.

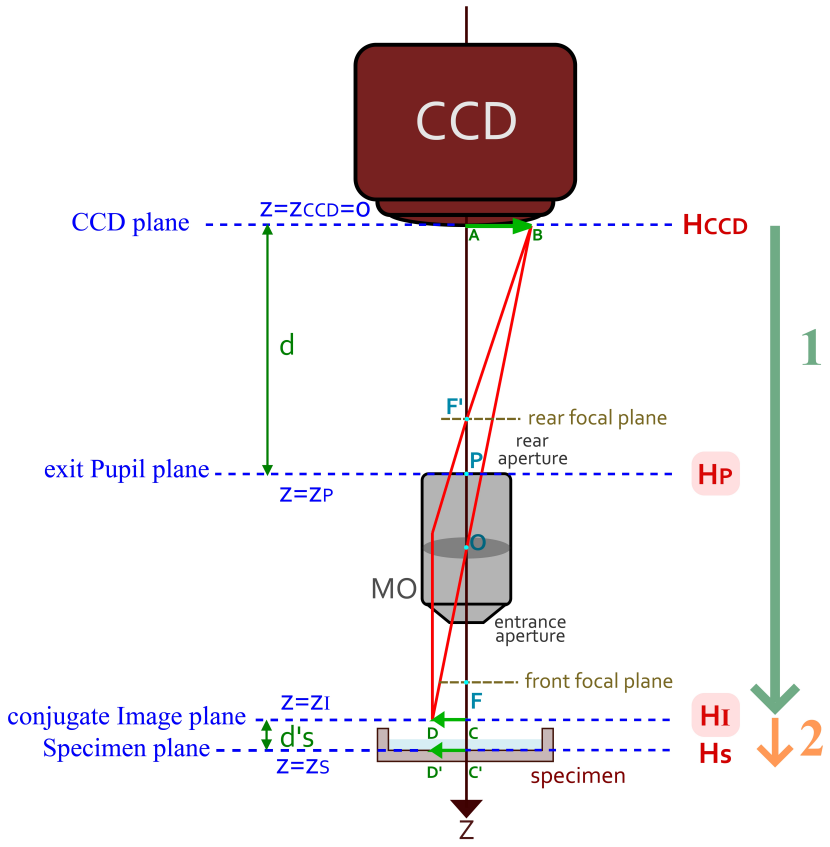

Figure 5.2: Optical arrangement for reconstruction in Digital Holographic Microscopy

The CCD camera, the microscope objective and the specimen are aligned along a vertical axis which defines the optical axis z of the holographic microscope. The position of the CCD sensor along axis z defines the CCD plane with coordinates $(x, y, z = z_{CCD} = 0)$. The hologram that is recorded by the CCD camera, at this plane, is denoted H_{CCD}. The position of the specimen along along axis z defines the specimen plane with coordinates $(x, y, z = z_S)$. The hologram at the specimen plane is noted H_S.

F is the front (or principal) focal point of the microscope objective lens and defines thus the front focal plane. F' is the rear (or back) focal point of the objective and defines thus the rear focal plane. Point P defines the z-position of the rear aperture of the microscope objective tube, and thus the corresponding plane is called the exit pupil plane with coordinates (x, y, z_P). The hologram at this plane is noted H_P .

The image of H_{CCD} through the microscope objective is formed at $z = z_I$. This position defines the conjugate image plane with coordinates (x, y, z_I).

In the illustration of figure 5.2, d is the distance between the CCD plane and the exit pupil plane, while d'_S denotes the distance between the conjugate image plane and the specimen plane.

5.1.3 The principle of the Reconstruction In Heterodyne Holographic Microscopy

The optical arrangement described above is the basis of the reconstruction algorithm that we used to reconstruct all our experimental data. Green arrow 1 and orange arrow 2 on Figure 5.2 briefly shows, in parallel with the corresponding optical arrangement, the general adopted reconstruction process.

Two important observations have drawn the main lines of our reconstruction method :

- It's easy to obtain the conjugate image from the CCD hologram : H_I is the conjugate of H_{CCD} which is, indeed, on focus on the CCD sensor.
- The conjugate image plane and the specimen plane are located in the same half-space. Hence, the propagation from H_I to H_S is a free space propagation that carry the great advantage of keeping the pixels size constant while propagating. Images obtained by free space propagation are thus undistorted.

Accordingly, the reconstruction process is performed in two steps. First, the hologram of the conjugate image, which is the image through the MO of the hologram recorded by the CCD device, is reconstructed (green arrow 1 in Figure 5.2). This hologram is then used to reconstruct the object by free space propagation (orange arrow 2 in Figure 5.2).

5.2 First Step of The Reconstruction : Reconstruction of the Conjugate Image

As we have introduced above, the easiest way to reconstruct the object field is to start first by reconstructing the conjugate image, that is located in the near vicinity of the object and in the same half space. We should also note that the conjugate image plane is situated nearby the front focal plane (F) of the MO.

5.2.1 Determination of the lens, tilt and magnification parameters by a proper calibration of the setup

The calculation of H_I from H_{CCD} seams to be not very complicated, since the corresponding intensity images are identical : $|H_I| = |H_{CCD}|$. Nevertheless, three main optical and experimental considerations (called : *lens*, *tilt* and *magnification*) should be taken into account in order to obtain properly the complex field :

1. *Lens*: The specimen is imaged through a microscope objective. Consequently, recorded holograms present phase curvatures and eventually phase distortions that are related to the microscope objective. Thus, before computing the field E_I at the conjugate image plane, a lens phase correction factor, noted ϕ_ℓ must be added to the phase of the complex field E_{CCD} of the recorded hologram in order to compensate this curvature.

2. *Tilt*: This is an experimental consideration related to the off-axis recording geometry of the considered holographic microscope. The off-axis tilt effect on the recorded CCD hologram should be compensated by adding a phase correction factor ϕ_t to E_{CCD}.

3. *Magnification*: Due to the magnification effect of the microscope objective, pixels' size in the conjugate image plane d'_{px} and in the CCD image plane d_{px} are not equal but interrelated through the transverse magnification factor G of the MO.

$$d'_{px} = d_{pix}/G \tag{5.4}$$

   Hence, pixel's size should be properly corrected.

Many research papers [Ferraro *et al.* 2003] discuss about the correction of these phase effects, in particular from the C. Depeursinge

Group [Montfort *et al.* 2006, Colomb *et al.* 2006a, Colomb *et al.* 2006c, Colomb *et al.* 2006b].

One must notice that many of the paper listed above discuss about microscope objective abberations. In most cases, this is an improper use of the term "abberation" since, as we will see, the phase corrections would be the same with an ideal objective free of abberation. In some cases, nevertheless, abberations play a significant role and can be compensated in holography [Nicola *et al.* 2002, Colomb *et al.* 2006b].

The correction of these phase effects, which is essential in order to get a proper reconstruction of the conjugate image, is not very eased because each correction factor should be calculated separately and added to the phase of the CCD hologram. Colomb et al. have proposed an automatic procedure to perform these corrections *in situ* [Colomb *et al.* 2006a], but this procedure (as most of the works done by the C. Depeursinge group) implicitly consider phase-contrast holographic microscopy [Marquet *et al.* 2005]. This means that the sample exhibit flat phase regions, where a phase reference can be easily measured.

In our experiments where gold nanoparticles are targeted, the illumination is made in Total Internal Reflection (TIR) configuration and there is no way to get a phase reference, because, approximately, the detected signal corresponds only to the gold nanoparticles. The Colomb et al. *in situ* calibration cannot be thus used. To reconstruct the images of the gold particles, it is thus necessary to determine the correction parameters by another way. The best way is to perform a proper calibration of the setup.

The purpose of this calibration is to compensate the lens and tilt effects by multiplying the CCD recorded hologram H_{CCD} by the proper lens and tilt phase maps (ϕ_ℓ and ϕ_t). By this way, the phase of hologram H_I becomes flat for a flat-phase sample.

$$H_I(x,y) = H_{CCD}(x,y)\ e^{-i\phi_\ell(x,y)}\ e^{-i\phi_t(x,y)} \tag{5.5}$$

A simple way to get a flat-phase sample is to consider a NULL sample illuminated by a plane wave (see Figure 5.3). This means that one records a hologram without a sample $H_{CCD,0}$, and with plane wave illumination. The phase of this plane wave is zero in any plane located in front of the MO entrance aperture, in particular in the conjugate plane $z = z_I$.

One can then directly measure the phase of $H_{CCD,0}(x,y)$ getting by this way the phases $\phi_\ell + \phi_t$ needed to execute the phase corrections as described in Equation 5.5.

$$[\phi_\ell + \phi_t](x,y) = \arg(H_{CCD,0}(x,y)) \tag{5.6}$$

This method is very simple but can be troublesome if $H_{CCD,0}$ is measured in noisy conditions.

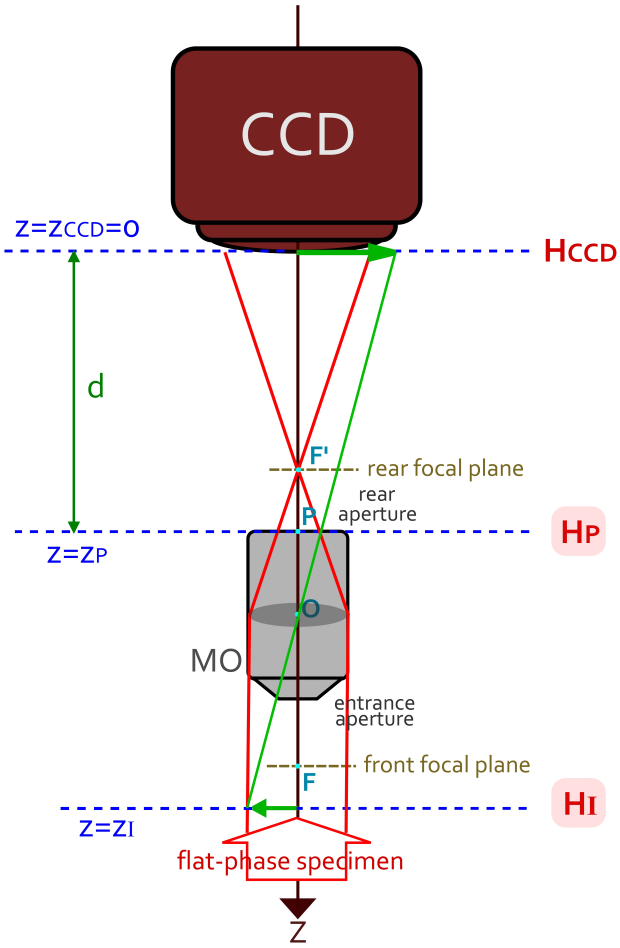

Figure 5.3: Holograms of a flat phase object in the CCD image conjugate plane ($z = z_I$), in the rear focal plane $z \simeq z_p$ and in CCD plane $z = z_{CCD}$.

A better calibration is to perform a Zernike polynomial development of $H_{CCD,0}$ in order to remove the noise. The phase correction $\phi_\ell + \phi_t$ is then extracted from that development.

5.2.1.1 The lens phase correction

One can notice that the plane wave is focused by the microscope objective MO in the rear focal point F'. This point F' becomes a point source, which emits a spherical coherent wave. For this reason, the hologram of the flat-phase sample is uniform in amplitude and has the phase of a spherical wave with a curvature $R = |\text{F'A}| \simeq d$ (see Figure 5.3). We have thus :

$$E_{CCD}(x, y, z_{CCD}) \propto e^{ik(x^2+y^2)/2d} \tag{5.7}$$

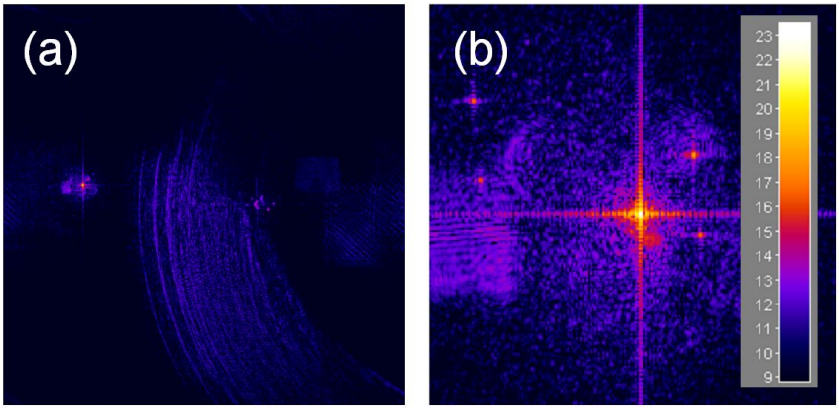

Figure 5.4: Reconstructed image of the MO rear focal plane with plane wave illumination and without sample : image (a) and zoom of the bright point in the left hand side of the image (b). Display is made in colored logarithmic scale for $|H_{F'}|^2$ (see scale bar).

where $k = |\vec{k}| = \lambda/2\pi$ is the modulus of the wave vector $\vec{k}$. To establish Equation 5.7, we have made the small angle approximation that yields a quadratic phase. This approximation is valid, since the detector size (< 1 cm) is much smaller than the pupil to CCD distance d (20 cm or larger in typical microscopic experiments).

Case of a plane wave reference field E_R

If the **reference field** on the CCD detector is uniform in amplitude and **flat in phase**, we have

$$E_R(x, y, z_{CCD}) = E_{R,0} \tag{5.8}$$

The interference pattern recorded by the CCD (i.e. the hologram H_{CCD}) exhibit then the same phase factor than the field $E_{CCD,0}$ recorded without sample

$$H_{CCD} = [E_{CCD,0}E_R^*](x, y) = E_{CCD,0}E_{R,0}^* e^{ik(x^2+y^2)/2d} \tag{5.9}$$

The CCD conjugate image hologram H_I is thus obtained by multiplying the CCD recorded hologram H_{CCD} by the inverse phase factor $e^{-ik(x^2+y^2)/2d}$, and the lens phase correction is simply :

$$\phi_\ell(x, y) = k(x^2 + y^2)/2d \tag{5.10}$$

A possible method to determine ϕ_ℓ is to measure d by performing the holographic reconstruction of the holographic signal in the MO rear focal plane ($H_{F'}$) using the Schnars et al. reconstruction method

[Schnars & Jüptner 1994] (see Figure 5.4). This reconstruction is made by multiplying H_{CCD} by the factor $e^{-ik(x^2+y^2)/2d}$ (where d is the reconstruction distance), and by performing a Fourier transformation. This is equivalent to a Fresnel transformation as described in Chapter 3 of this manuscript. One can than adjust d in order to get, on the reconstructed image, a bright point as sharp as possible. This bright point is visible on the left hand side of Figure 5.4(a), and on Figure 5.4(b). It corresponds to the F' field source, while the black background corresponds to the other points of the MO rear focal plane. One can notice that the reconstruction phase factor $k(x^2+y^2)/2d$ is equal to the lens correction factor ϕ_ℓ, which is determined by this way.

Case of a spherical reference field E_R

This result remains valid if the hologram is recorded with a spherical reference field E_R.

$$E_R(x, y, z_{CCD}) = E_{R,0} e^{ik(x^2+y^2)/2d'} \tag{5.11}$$

The field E_R is then emitted from a point source M, and d' is the M to CCD distance. In this case, Equation 5.9, which gives the phase of the hologram recorded without sample, must be replaced by :

$$H_{CCD} = E_{CCD} E_R^* \propto E_{CCD}(x, y, z_{CCD}) \propto e^{ik(x^2+y^2)d''} \tag{5.12}$$

where

$$\frac{1}{d''} = \frac{1}{d} - \frac{1}{d'} \tag{5.13}$$

The lens phase correction becomes

$$\phi_\ell(x, y) = k(x^2 + y^2)/2d'' \tag{5.14}$$

The Schnars et al. [Schnars & Jüptner 1994] reconstruction is also affected by the sphericity of E_R, and, to reconstruct F' on focus, H_{CCD} must be multiplied by $e^{-ik(x^2+y^2)/2d''}$, where d'', given by Equation 5.13 is the rear focal plane apparent reconstruction distance.

In both cases (plane reference wave and spherical reference wave), the lens phase correction ϕ_ℓ can be obtained by recording a hologram without sample, and by adjusting the Schnars et al. [Schnars & Jüptner 1994] reconstruction distance d or d'' in order to get in the reconstructed image a bright point as sharp as possible that corresponds to F'.

One must notice that this calibration do not depends on the exact location of the object, but only on the CCD detector to MO back focal point F' reconstruction distance d or d''. This means, that the calibration of the set-up can be made once, and remains valid if the CCD detector to microscope objective distance d is not modified, which is generally the case.

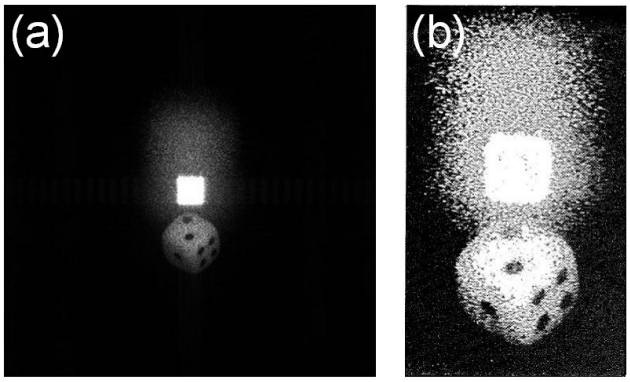

Figure 5.5: Example of an off-axis reconstructed holographic image: image from [Schnars & Jüptner 2002] (a) and zoom from [Schnars & Jüptner 1994] (b)

5.2.1.2 The off-axis Tilt phase correction

We have seen in the description of our optical apparatus, that the reference wave interferes with the object illumination wave in an off-axis geometry. This off-axis geometry is used in order to separate spatially the three interference terms [Cuche *et al.* 1999] preventing by this way the overlapping of the self beating term and twin image term with the relevant image term in the frequency domain of the recorded holograms.

The off-axis tilt effect can be clearly seen on the reconstructed image of the object on Figure 5.5 from the Schnars historical papers [Schnars & Jüptner 1994, Schnars & Jüptner 2002]. The image of the object is visible slightly off axis in the bottom. The zero-order and twin images [Cuche *et al.* 1999] correspond respectively to the white blurred square in the center of Figure 5.5, and to the the totally blurred white zone in the top.

The off-axis tilt effect is also seen on the rear focal plane image of Figure 5.4 : we can see that image of F' is not situated in the center of the image but is slightly translated to the left hand side of the image. To correct the tilt effect, one must multiply H_{CCD} by $e^{i\phi_t}$, with :

$$\phi_t = k_{t,x}x + k_{t,y}y \tag{5.15}$$

By choosing the correct values for $k_{t,x}$ and $k_{t,x}$, the bright point that corresponds to F' is shifted back in the center of the reconstructed image. Using this method the tilt phase ϕ_t can be adjusted very accurately.

Here again, we must notice that the off-axis tilt calibration do not depends on the exact location of the object. It nevertheless depends on the illumination direction of the reference hologram recorded without a sample.

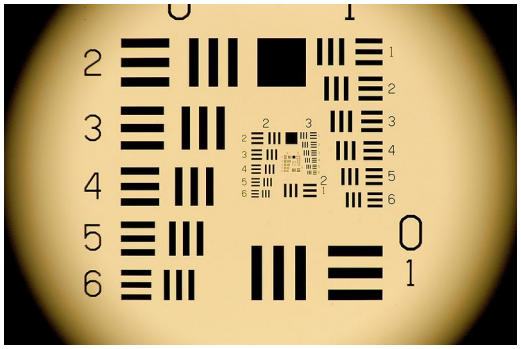

Figure 5.6: Standard USAF resolution target

This direction defines here the optical axis in the object half space of the microscope objective.

5.2.1.3 The MO transfer magnification factor G

The transfer magnification factor G defines the relation between the pixels' size in the CCD image plane d_{px} and in the conjugate image plane d'_{px} :

$$G = \frac{d_{px}}{d'_{px}} \tag{5.16}$$

In order to calculate factor G, the most commonly used method is the use of a standard USAF 1951 Test Target shown in Figure 5.6. This standard test object is composed of horizontal and vertical three-bar patterns in the form of a reflecting chromium coating set on a glass substrate. These patterns are specifically arranged into groups of six elements where each element is composed of three equal longitudinal bars and three equal horizontal bars. The vertical bars are used to calculate horizontal resolution and the horizontal bars are used to calculate vertical resolution. Each one of these bars are very well calibrated and each bar of each element in each group have well defined dimensions and frequency. USAF targets are provided with the corresponding calibration chart.

According to Figure 5.2, the transverse magnification factor G of the microscope objective is the ratio of the sizes of the CCD image (segment AB) and of the conjugate image (segment CD). G is also the ratio of the distance between the center of the imaging lens (O) and the CCD image plane $z = z_{CCD}$ versus the distance between O and the conjugate image plane $z = z_I$.

$$G = \frac{AB}{CD} = \frac{OA}{OC} \tag{5.17}$$

Moreover, the transfer magnification factor G is defined as the ratio of the distance between the back focal point F' of the MO and the CCD image $z = z_{CCD}$, versus the focal length f_l of the microscope objective MO :

$$G = \frac{F'A}{F'O} = \frac{d}{f_l} \tag{5.18}$$

The focal length f_l of the used microscope objective is known. In order to calculate G, parameter d must be determined. Since d is the reconstruction distance needed to reconstruct properly the rear focal point F', the distance d and thus the transfer magnification factor G can be calculated from the hologram recorded with the plane wave and no sample. One must nevertheless notice, that this measurement must be done with a known curvature reference field E_R that is, in practical situations, a **plane wave reference beam** E_R.

5.2.1.4 Spatial Filtering

Although our experiments are predominantly carried out by acquiring a sequence of M phase-shifted holograms (M is an integer multiple of 4), and performing a four-phases demodulation method in order to retrieve the relevant grating order +1 term only, reconstructions based on a single acquired hologram are sometimes needed, especially in the case of fast object-tracking experiments. In this last case were the four-phases demodulation is not performed, the self beating terms (zero grating order image) and the twin images (-1 grating order) persists on the recorded holograms.

It is thus necessary to remove the zero and -1 grating order signals. This is generally done by spatial filtering in the Fourier space [Cuche *et al.* 1999]. One must notice that in our nanoparticle experiments, the nanoparticles signal can be extremely week, since it is roughly proportional to the 6^th power of the particle diameter a ($\propto a^6$). It is thus important to optimize the spatial filtering process in order to remove the parasitic grating orders 0 and -1 totally, while keeping all the useful information of the relevant grating order +1. This spatial optimization problem has been discussed in details by Li et al. [Li *et al.* 2010] for free space holography.

5.2.2 Determination of the lens, tilt and magnification factor by reconstructing the image of the MO exit pupil

We have seen that in order to execute a proper reconstruction, the three correction parameters (lens, tilt and magnification) should be accurately determined using a plane wave calibration of the optical setup. However, in some

cases, this calibration has not been made, or has been lost. In this section, we will see that, by performing a very convenient alternative calibration process based on the reconstruction of the microscope objective exit pupil plane, it is nevertheless still possible to determine the lens, tilt and magnification factors.

We will thus present an ingenious *in situ* method (that do not require flat phases regions of the sample) and that can be applied in almost all experimental situations. In this method, the complex field $E(x, y, z_P)$ at the exit pupil plane of the MO is reconstructed from the recorded CCD hologram H_{CCD}.

5.2.2.1 Lens parameter

In our experiments, and more generally in most of bio-imagery applications, specimens are imaged using high magnification microscope objectives. In practice, high magnification objectives have very short working distances, typically less than one millimeter. Yet, working distances of low magnification objectives are more significant. Since in our application we use high magnifying objectives (typically 50×) with short working distance, the distance PF' between the back focal plane of the MO (given by point F' on Figure 5.2) and its back aperture plane (given by point P) is tiny. We can thus consider that both planes are coincident. This is only true for objectives with magnifying powers going from 40× and above.

In most experimental situations, investigated specimens scatter some light in all directions yielding enough light in the rear pupil plane allowing thus the reconstruction of the MO exit pupil's image. By adjusting the reconstruction distance d'' until the reconstructed image of the pupil present sharp edges as illustrated on Figure 5.7, one can measure the MO pupil $z = z_P$ to CCD detector $z = z_{CCD}$ distance.

Similarly to the calibration with plane wave illumination without a sample (see Section 5.2.1.1), the distance d'', that produces a sharp image, may differ from the real CCD to pupil distance d. This is in particular the case if the reference beam is a spherical wave that is emitted from a point source located at distance d' from the CCD, since in that case we have (see Equation 5.13)

$$\frac{1}{d''} = \frac{1}{d} - \frac{1}{d'}$$

Nevertheless, whatever the sphericity of the E_R field is, the measured distance d'' is very close to the distance that must be used to calculate the lens phase

Figure 5.7: Reconstructed intensity image of a microscope objective exit pupil in a gray logarithmic scale

correction.

$$\phi_\ell(x,y) \simeq k(x^2+y^2)/2d'' \tag{5.19}$$

One can thus approximates ϕ_ℓ. This is sufficient in most cases. If one needs to get a better estimation of ϕ_ℓ, one can measure the distance between the rear pupil ($z = z_P$) and the rear focal point F', and add to ϕ_ℓ, given by the above equation, the numerical lens that shifts the image of the rear pupil plane $z = z_P$ into the rear focal plane F'. This correction corresponds to few millimeters and is not very significant especially when compared with d ($d \sim 20$ cm in typical experiments).

5.2.2.2 The tilt parameter and Spatial filtering

Although spatial filtering approaches are confronted to significant difficulties (mainly due to the irregularity distributions of the spectrums to be treated), the spatial filtering is especially easy in the presented reconstruction method, since the relevant term obtained by the reconstruction of the MO rear aperture (plane $z = z_P$), is presented as a bright disk with sharp edges as illustrated on Figure 5.8 (a). Figure 5.8 (a) is thus a reconstruction of hologram H_P and gives consequently the field $E_P(x,y,x_P)$. On H_P, the useful signal that brings information on the investigated sample is included within the bright disk, while parasitic signals and the noise are out of the disk. A genuine numerical spatial mask, that accurately matches the well defined circular geometric shape of the bright disk, can thus be easily applied as illustrated on Figure 5.8 (b). By this way, optimal spa-

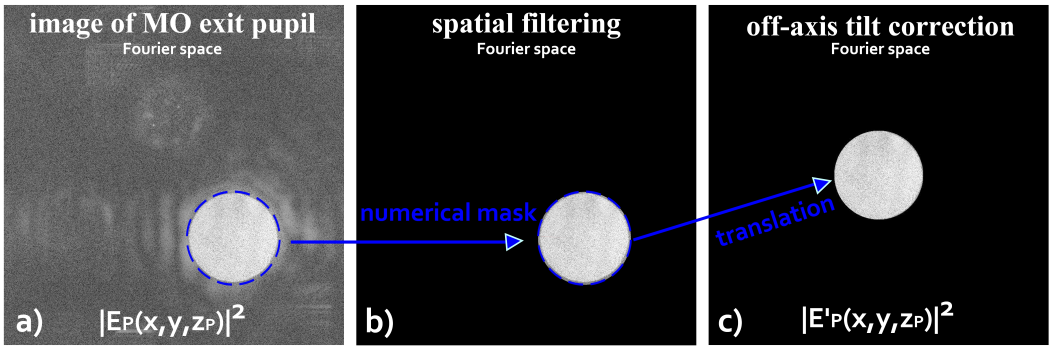

Figure 5.8: (a) Reconstructed hologram H_P in the MO objective rear aperture plane $z = z_P$. The specimen consists of 80 nm gold nanoparticles in a water and agarose solution. The hologram H_{CCD} is recorded with 4 phases phase shifting method. (b) Same hologram filtered with a numerical mask. (c) Same hologram filtered and corrected for the off-axis tilt. Images are displayed in gray logarithmic scale for $|E_P|^2$ and $|E'_P|^2$

tial filtering is performed and only the relevant holographic signal is conserved.

The filtered signal can now be translated to the center of the calculation grid correcting by this way the off-axis tilt as illustrated on Figure 5.8 (b). The off-axis tilt effect can be clearly seen on the reconstructed image of the MO exit pupil, since the obtained bright disk is not located at the center of the reconstructed image but is spatially shifted. The translation is chosen in such a way that the center of the selected zone coincide with the center of the calculation grid. With this choice, the optical axis becomes coincident with the experimental optical axis (which corresponds to the line drawn from the center of the MO pupil to the center of the CCD zone that is used to record the holographic data). This off-axis tilt compensation procedure, based on the reconstruction of the MO rear pupil, is effortless. In many situations, and in particular with our samples of gold nanoparticles coupled to live cells, the light scattered by the nanoparticles and by the cells is sufficient to visualize the disk that corresponds to the MO rear pupil. It is thus possible to perform the spatial filtering and to correct the off-axis tilt in situ, i.e. from the investigated sample's holographic data without the need of a calibration with an extra reference hologram recorded without sample.

At the end of this filtering and translation procedure, a corrected hologram is obtained H'_P (complex field $E'_P(x, y, x_P)$) at the MO rear pupil plane.

5.2.2.3 The magnification parameter G

The magnification factor G can be calculated from the experimental parameters that are manifested during the reconstruction process of the MO exit pupil plane, without the need of a previous calibration with a USAF test target. In fact, as explained in a previous section of this Chapter, G can be determined if the physical distance d between the CCD and the rear focal point F' is known.

It is possible, indeed, to measure d from any recorded hologram, whatever the curvature of the reference beam E_R is. This can be achieved by imaging the microscope objective's exit pupil and by extracting quantitative information from the rear pupil's reconstructed image.

If the reference beam E_R is a plane wave, the distance d'' that makes the pupil image sharp is equal to the CCD to pupil plane distance d. In this case, d is thus determined. $|AF'|$ can also be determined after performing the small pupil to F' correction. Finally, as explained in Section 5.2.1.3 , G is obtained using Equation 5.17.

If the reference beam E_R is not a plane wave, or if the experimental details have been lost, one can nevertheless determine d, and thus G, from the size in pixels of the image of the rear pupil. The detailed procedure will be described in the following, but we must first point out that the reconstructed hologram H_P, and thus the size of the reconstructed exit pupil do not depend on the reference field's sphericity.

This can be proven by considering the two following experimental situations and comparing their corresponding results :

- Situation 1 : a plane wave reference beam E_R is used. The reconstruction distance d and the physical distance between the CCD and P (where $P \equiv F'$) are thus equal.

- Situation 2 : a spherical reference beam E_R is used. The reconstruction distance d'' is not equal to the physical distance d.

To reconstruct H_P, H_{CCD} is multiplied by the reconstruction phase factor $e^{jk(x^2+y^2)/2d}$, then a direct Fourier transform is executed :

- For situation 1, E_R is a flat field (i.e. $E_R = E_{R,0}$) , we get thus :

$$\begin{aligned} H_{CCD}e^{jk(x^2+y^2)/2d} &= E_{CCD}E_R^* e^{jk(x^2+y^2)/2d} \\ &= E_{CCD}E_{R,0}^* e^{jk(x^2+y^2)/2d} \end{aligned} \tag{5.20}$$

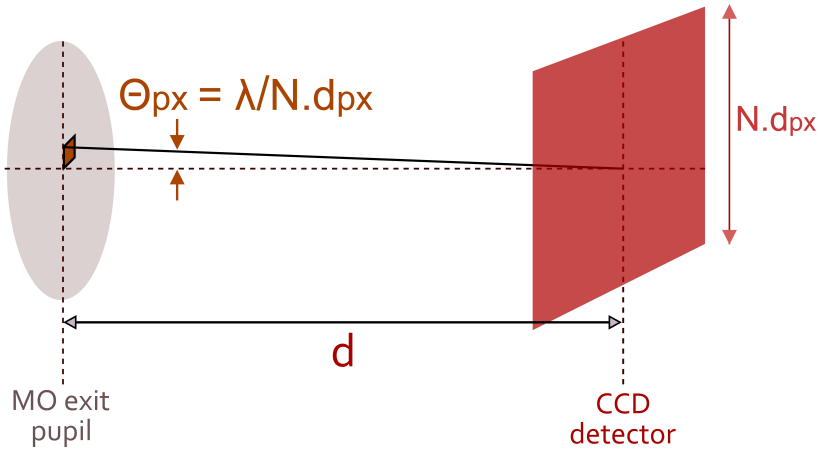

Figure 5.9: Size of the pixels in the MO pupil plane

- For situation 2, E_R is a spherical wave field ($E_R = E_{R,0}e^{-jk(x^2+y^2)/2d'}$):

$$\begin{aligned} H_{CCD}e^{jk(x^2+y^2)/2d''} &= E_{CCD}(x,y)E_R^*(x,y)e^{jk(x^2+y^2)/2d''} \\ &= E_{CCD}E_R^*e^{jk(x^2+y^2)/2d''}e^{-jk(x^2+y^2)/2d'} \\ &= E_{CCD}E_{R,0}^*e^{jk(x^2+y^2)/2d} \end{aligned} \tag{5.21}$$

Equation 5.20 and Equation 5.21 show that the complex matrix that is transformed to the Fourier space in order to get H_P is the same whatever the reference field sphericity is. The reconstructed hologram H_P do not thus depends on the sphericity of E_R.

As we will see, one can extract, from H_P, the CCD to pupil distance d (i.e. the distance between the CCD and the rear focal point F' which is $\simeq d$), and get thus G using Equation 5.18. Let us consider the Fourier transformation that yields H_P. The hologram H_{CCD} is a matrix of complex numbers where each pixel of the matrix corresponds to the physical pixels of the CCD camera. For example, for one of the cameras that we used (PixelFly: PCO Inc.), the number of pixels is 1280×1024 and the pixel size is $d_{px}\times d_{px} = 6.7\times6.7\mu\text{m}^2$. To make easier calculations, the 1280×1024 matrix that is measured is truncated to $N\times N = 1024\times1024$ where $N = 1024$ is a power of 2. By this way, we can perform the reconstruction with efficient Fast Fourier Transformation (FFT).

Let us calculate the size in pixels Units of the MO exit pupil image in the Fourier space (see Fig.5.9). H_P has been obtained by multiplying the recorded CCD hologram H_{CCD} by a phase factor and applying then a FFT [Schnars & Jüptner 1994]. The Fourier space coordinates are (k_x, k_y). For each point J of the pupil plane, we can introduce $\vec{k}_J = (k_x, k_y, k_z)$ with:

$$\vec{k}_J = k\,\vec{u}_J \tag{5.22}$$

where $k = 2\pi/\lambda$ is the modulus of the optical wave vector, and where $\vec{u}_J = \vec{OJ}/|OJ|$ the Units vector that points from the center of the CCD detector into point J. The Fourier coordinates (k_x, k_y) of J in wave vector Units correspond thus to the transverse coordinates of the optical wave vector $\vec{k}_J$ parallel to $\vec{u}_J$.

For H_{CCD}, in the "real space", we have $N \times N$ pixels of size $d_{px} \times d_{px}$. For H_P, in the "Fourier space", we have $N \times N$ pixels of size $k_{px} \times k_{px}$. Because H_P and H_{CCD} are interrelated through a FFT, the pixel sizes in real and Fourier space are interrelated by :

$$N d_{px} k_{px} = 2\pi \tag{5.23}$$

The pixels size $\theta_{px} = \frac{k_{px}}{k}$ in angular Units **viewed from the CCD** is then :

$$\theta_{px} = \frac{\lambda}{N d_{px}} \tag{5.24}$$

Lets consider now the MO pupil. Its diameter can be measured in length Units (D_P), in angular Units **viewed from the CCD** (θ_P) or in pixels Units (N_P) for the reconstructed images. These tree measures (D_P,D_P and N_P) are interrelated through :

$$\begin{aligned} \theta_P &= D_P/d \\ N_P &= \theta_P/\theta_{px} \end{aligned} \tag{5.25}$$

We get from Equation 5.24 and Equation 5.25

$$d = \frac{D_P}{\theta_P} = \frac{D_P}{N_P \theta_{px}} = \frac{D_P}{N_P} \frac{N d_{px}}{\lambda} \tag{5.26}$$

This last equation gives the CCD to MO pupil distance $d = z_{CCD} - z_P$ from the ratio D_P/N_P of the pupil diameter in length Units (D_P) and in pixels Units (N_P). The pupil diameter D_P is known, since it is related to the MO focal length f_l and MO numerical aperture NA by :

$$D_P = f_l \cdot NA \tag{5.27}$$

Another possible way of determining d can be achieved by measuring, experimentally, the MO objective exit pupil's diameter D_P from the reconstructed image of H_P. d can thus be calculated from Equation 5.26. Finally, knowing d (and f_l), the magnification factor G can be deduced using Equation 5.18.

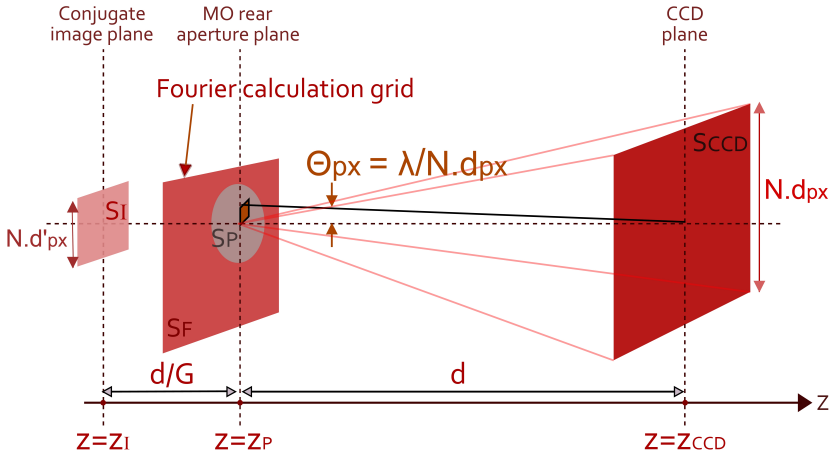

Figure 5.10: Etendue for the holographic signal collection

5.2.2.4 The Optical Etendue

A simple mnemonic method to get the size of the reconstructed pixels is to introduce the etendue (http://en.wikipedia.org/wiki/Etendue) for the holographic signal collection (see Figure 5.10). The etendue is the volume of the phase space that is equal to the product of an area S by a solid angle Ω.

The holographic microscopic signal passes through the MO exit pupil aperture and is collected by the CCD camera. The collection etendue $S\Omega$ is thus equal to the product of the CCD area S_{CCD} by the pupil solid angle **viewed from the CCD** ($\Omega_P = S_P/d^2$). It is also equal to pupil area S_P times the CCD solid angle **viewed from the pupil** ($\Omega_{CCD} = S_{CCD}/d^2$).
We have thus :

$$\begin{aligned} S\Omega &= S_P\Omega_{CCD} \\ &= S_{CCD}\Omega_P \\ &= \frac{S_P\ S_{CCD}}{d^2} \end{aligned} \tag{5.28}$$

Note that we can also consider the etendue of the CCD image with respect to the MO entrance pupil aperture. The etendue $S\Omega$ is then equal to the area of the imaged region $S_I = S_{CCD}/G^2$ times the MO solid angle Ω_{MO} **viewed from the imaged region**, which is directly related to the MO numerical aperture (NA).

The collection etendue must be compared to the etendue $[S\Omega]_{px}$ that corresponds to 1 reconstructed pixel. This etendue is equal to the pixel solid angle θ_{px}^2 times the CCD area S_{CCD} or to the reconstructed pixel area $(\theta_{px}d)^2$

times the CCD solid angle $\Omega_{CCD} = S_{CCD}/d^2$. We get:

$$[S\Omega]_{px} = \theta_{px}^2 \; S_{CCD} = \left(\frac{\lambda}{N d_{px}}\right)^2 \times \left(N^2 d_{pix}\right)^2 = \lambda^2 \tag{5.29}$$

For one pixel of the Fourier space, the optical etendue is thus simply equal to λ^2 and do not thus depends on the geometry (i.e. on the CCD to MO distance d) and on the characteristics of the objective MO (focal length f_l or Numerical Aperture NA). This result is quite general and means that the etendue of coherent detection on a single pixel detector is λ^2.

One can thus define the number of modes, channels, speckles of a system that transport energy through waves as being the optical etendue in λ^2 Units [Imry 1986, Scheffold & Maret 1998, Feng & Lee 1991, Scheffold & Maret 2001].

For example, if one wants to calculate a thermal energy radiated by a black body of temperature T using the Plank's law (http://en.wikipedia.org/wiki/Planck%27s_law), one gets that the energy W radiated in a time t within a bandwidth $1/t$ is equal to 2 (because radiation can occurs in 2 orthogonal polarizations) times the Bolzmann energy $h\nu/(e^{h\nu/kT} - 1)$ (that is equal to kT for $kT \gg h\nu$) times the number of modes (that is $S\Omega/\lambda^2$) :

$$W = 2\frac{h\nu}{e^{h\nu/kT} - 1} \times \frac{S\Omega}{\lambda^2} \tag{5.30}$$

In holographic microscopy, the number of modes N_{modes} that collects the signal corresponds to the etendue sustained by the pupil, and the CCD. We have thus :

$$N_{modes} = \frac{S_P S_{CCD}}{d^2 \lambda^2} \tag{5.31}$$

N_{modes} is also equal to the number of pixels of the exit pupil image. It represents also the number of independent pixels of information that describes the complex field that passes through the MO pupil and that reaches the CCD detector.

One can also calculates the etendue sustained by the CCD and the Fourier calculation grid, whose area is S_F. This etendue corresponds to N^2 modes, i.e. to the number of pixels of the CCD detector, since we have :

$$N^2 \frac{S_F S_{CCD}}{d^2 \lambda^2} \tag{5.32}$$

N^2 is thus the maximum number of modes that can be detected by holography.

Since the area of the MO pupil S_P is smaller than the area of the Fourier calculation grid S_F, we have :

$$N_{modes} < N^2 \tag{5.33}$$

This means that the CCD camera oversample the field collected by the microscope objective and that reaches the CCD camera. The N_{modes} pixels of information of the imaged zone are thus collected by the microscope objective and by the CCD camera without losses.

5.3 Second Step : 3D Reconstruction of the Object by propagation of the Angular Spectrum

From the first step of the reconstruction process, a corrected field in the CCD image plane $z = z_I$ is obtained. This field is corrected for the aberrations, introduced by the imaging lens, and for the off-axis tilt. The obtained field is also filtered from all parasitic noise. Moreover, the magnification factor G of the MO that is used to calculate the new pixels' size has been determined.

Here, we present the second step of the reconstruction process, which consists of reconstructing the image at the object plane from the conjugate image plane.

In the previous section, we have shown that the lens phase correction of the conjugate image field $E_I(x, y, z_I)$ is performed by multiplying the field at the CCD plane $E_{CCD}(x, y, z_{CCD})$ by the lens phase factor $e^{jk(x^2+y^2)/2d}$ (where d is the CCD to MO pupil distance). The spatial filtering and the tilt corrections are made then in the Fourier space. This means that we have calculated the Fourier transform of $E_{CCD}e^{jk(x^2+y^2)/2d}$, which yields to E_P, since the performed operations are similar to the ones performed for the reconstruction of field E_P in the pupil plane by the Schnars method [Schnars & Jüptner 1994]. The spatial filtering and the tilt correction (translation) are thus made in the Fourier space, i.e. on E_P. We get then the corrected pupil field E'_P. To get back the corrected image field E'_I, we have to make a reverse Fourier transformation. We have thus :

$$\begin{array}{ccc} E'_P & \overset{\text{FFT}^{-1}}{\longrightarrow} & E'_I \\ E'_I & \overset{\text{FFT}^{+1}}{\longrightarrow} & E'_P \end{array} \tag{5.34}$$

The sample field $E_S(x, y, z)$ is then calculated from the corrected image field $E'_I(x, y, z_I)$ by free space propagation using the angular spectrum method that involves two Fourier transformations. The corrected image field E'_I is thus the starting point for this second reconstruction step. It should be pointed out that E'_P is the Fourier transform of E'_I. We will thus consider that the first

Fourier transformation of the angular spectrum propagation is already made, and we start the propagation from E'_P.

The specimen, in most of the cases, is a thick volume object that is expanded on the optical axis over a relatively broad range of $z-$positions that are defined according to their relative position to z_I . Each $z-$position of the specimen, is defined by :

$$z_{S_n} = z_I + d'_n \, \delta z \tag{5.35}$$

where n is an integer varying from 0 to $R-1$, R is the number of the desired object reconstruction planes around the conjugate image plane and d'_n is the distance between the conjugate image plane and each z_{S_n} plane of the specimen that is given by :

$$d'_n = (n - \frac{R}{2}) \, \delta z \tag{5.36}$$

δz defines the step between two consecutive $z-$positions of the imaged specimen: it is thus the sectioning step of the specimen. In practice, δz is defined by the user and depends on the application. It is typically chosen in the order of 100 nm.

The angular spectrum method is a very advantageous reconstruction method because it has no minimal reconstruction distance requirement and it keeps constant the pixels' size. The pixels' size do not vary with the variation of reconstruction distance, resulting images are thus undistorted. The principles of this method have been described in details in Chapter 3 of this manuscript.

The reconstruction scheme is mainly composed of three steps that involves two Fourier transforms. An exhaustive illustration of the complete process is illustrated on Figure 5.11.

1. The determined field $E'_I(x, y, z_I)$ is decomposed into its two-dimensional angular spectrum components $A_I(k_x, k_y, z_I)$. These components are calculated from $E'_I(x, y, z_I)$ by a two-dimensional Direct Fast Fourier Transform (FFT^{+1}) :

$$E'_I(x, y, z_I) \overset{\mathrm{FFT}^{+1}}{\longrightarrow} A_I(k_x, k_y, z_I) \tag{5.37}$$

   As noticed above (see Equation 5.34), this Fourier transformation is not needed since $A_I \equiv E'_P$ and E'_P have already been determined in the first step of the reconstruction (from the reconstruction of the MO exit pupil plane).

2. The angular spectrum A_I is then propagated in free space to the desired reconstruction plane z, by multiplying each point in the spectrum by a

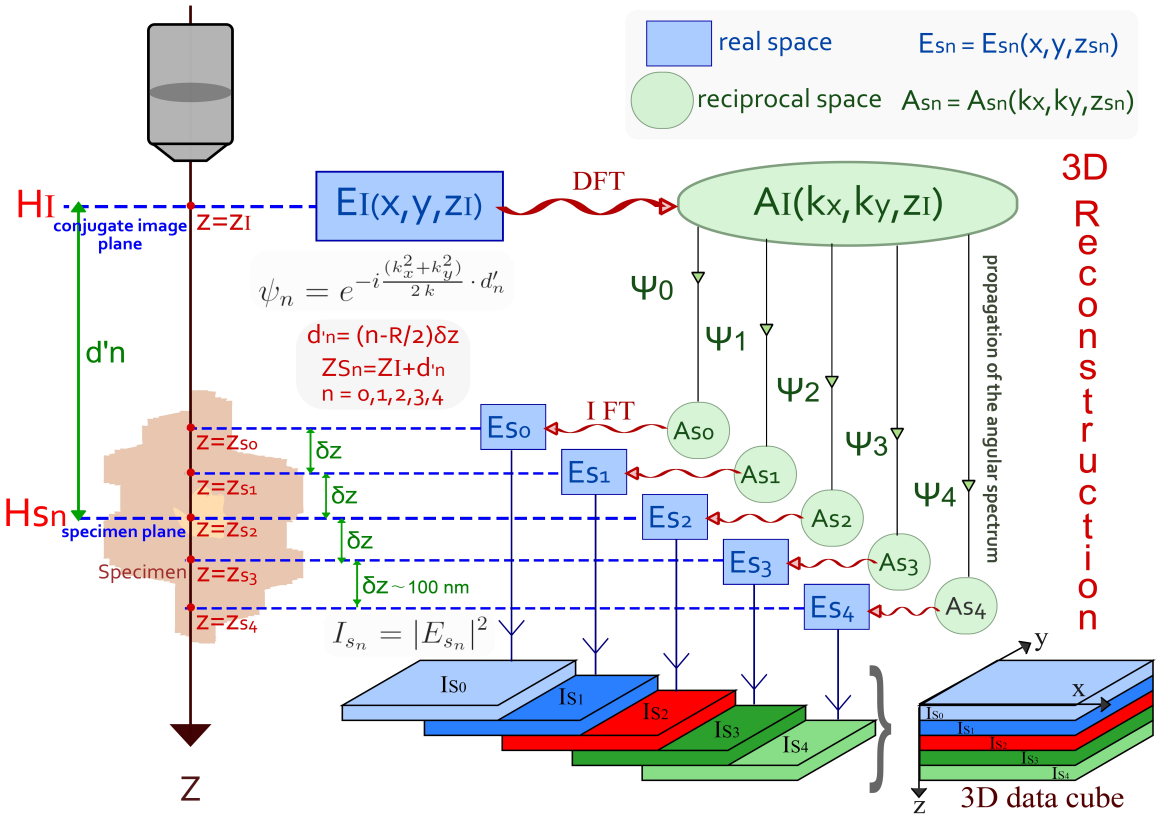

Figure 5.11: Second step of the reconstruction by free space propagation of the Angular Spectrum

propagation term which accounts for the phase change that each plane wave will undergo on its journey to the reconstruction plane.

In order to perform a 3D reconstruction of the entire volume object, the angular spectrum A_I must be propagated to each z_{S_n} specimen reconstruction plane. A_I is thus multiplied, for each reconstruction plane, by the corresponding propagation term ψ_n that is given by :

$$\psi_n(k_x, k_y) = e^{-id'_n(k_x^2+k_y^2)/2k} \tag{5.38}$$

The Angular spectrum $A_{S_n}(k_x, k_y, z_{S_n})$ at each plane $z = z_{S_n}$ of the specimen is thus obtained :

$$A_{S_n}(k_x, k_y, z_{S_n}) = A_I(k_x, k_y, z_I)\, e^{-id'_n(k_x^2+k_y^2)/2k} \tag{5.39}$$

3. The last step of the reconstruction process consists of performing a two-dimensional IFFT (Inverse Fast Fourier Transform) for every A_{S_n} to get the reconstructed field $E_{S_n}(x, y, z_{S_n})$ of each intrinsic object plane.

$$A_{S_n}(k_x, k_y, z_{S_n}) \overset{\text{FFT}^{-1}}{\longrightarrow} E_{S_n}(x, y, z_{S_n}) \tag{5.40}$$

In order to obtain a full 3D mapping of the entire reconstructed object field, intensity images can be calculated for every reconstructed object field E_{S_n} :

$$I_{s_n} = |E_{s_n}|^2 \tag{5.41}$$

For simplification, in the illustration of Figure 5.11, we have considered only five reconstruction planes of the specimen :

$$n = \{0, 1, 2, 3, 4\} \tag{5.42}$$

5.4 Abberations

Reconstructed holographic images can exhibit spherical aberrations if the imaging microscope objective is used in an improper mode :

- Generally, in the field of biological imagery, specimens are investigated while maintained in a nutritive medium, that consists mainly of water, to ensure cell survival. Consequently, if such specimens are imaged with an air microscope objective (and not an immersion microscope objective), spherical aberrations are introduced.

- Generally, in the field of microscopic imagery, specimens are mounted on a microscope glass slide covered with a glass cover slip. Accordingly, most of microscope objectives are tailored with a fixed-thickness or adjustable-thickness cover glass correction. Consequently, if the specimen is prepared without a cover slip and imaged with a cover glass corrected MO, spherical aberrations are introduced.

Abberations may not be very significant if the imaging microscope objective has a small Numerical Aperture since not all the distorted light is collected. However, these aberrations become significant when large Numerical Aperture microscope objectives are used. It is thus interesting to compensate these aberrations by performing reconstructions using the proper propagation term.

We will start first by describing this proper propagation kernel, then we will discuss more about the two introduced possible aberrations' modes.

5.4.1 Propagation kernel for large Numerical Aperture MO

When holograms have been recorded with a large Numerical Aperture (NA) microscope objective, holographic images that are reconstructed with the propagation kernel $\psi_n(k_x, k_y)$ of Equation 5.38 exhibit spherical aberrations. We will analyze these abberation effects, and show that it is possible to compensate them using the proper propagation kernel $\Psi_n(k_x, k_y)$.

When the Numerical Aperture of the microscope objective is large, the quadratic propagation kernel $\psi_n(k_x, k_y)$ given by Equation 5.38, that is used to propagate the field from z_I to z_{S_n}, is not valid anymore. This quadratic kernel is only valid in the case of small angles (or small Numerical Apertures). In our experiments, we used a microscope objective with a Numerical Aperture NA=0.5. The propagation in the object half space of the microscope objective involves thus field components whose wave vector $\vec{k}$ makes an angle up to arcsin $0.5 = \pi/6$ with respect to the propagation axis. The small angle approximation, that allowed the calculation of the propagation kernel $\psi_n(k_x, k_y)$ given by Equation 5.38, is thus not completely accurate. Consequently, it is more efficient to use the unapproximated exhaustive propagation kernel :

$$\Psi_n(k_x, k_y) = e^{-id'_n(\sqrt{k^2-k_x^2-k_y^2}-k)} \tag{5.43}$$

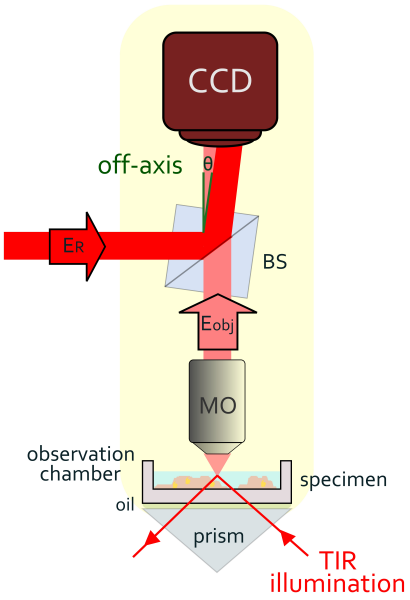

Figure 5.12: Gold nano particles on cell membranes in Petri dish imaged with Total Internal Reflexion (TIR) illumination.

5.4.2 Specimen maintained in a culture medium and imaged with an air MO

In this thesis, we are mainly interested by the imagery of gold nanoparticles in live cell environments (see Figure 5.12). As we will describe in Chapter 6 and Chapter 7, during the holographic experiments cells are maintained in a nutritive culture medium that consists mainly of water and glucose. There are observed from the top with an air microscope objective. Specimens are illuminated in dark field configuration from the bottom by provoking Total Internal Reflection (TIR) on the medium-air interface. With such an optical setup, the signal scattered by the sample, travels through different media (water and air) of different refractive indexes. Abberations are thus induced. These induced abberations are significant especially when the signal is collected by a large Numerical Aperture microscope objective.

This microscopic imaging system exhibits thus spherical abberations that are similar to common abberations obtained when an air microscope objective is used without a proper correction for the cover glass thickness (see `http://www.microscopyu.com/tutorials/java/aberrations/correctioncollar/`). Since the culture medium mainly consists of water, its refractive index is $n = 1.33$. Its height in the observation chamber is $h \sim 1$mm. The refractive index of a standard microscopy glass coverslip is

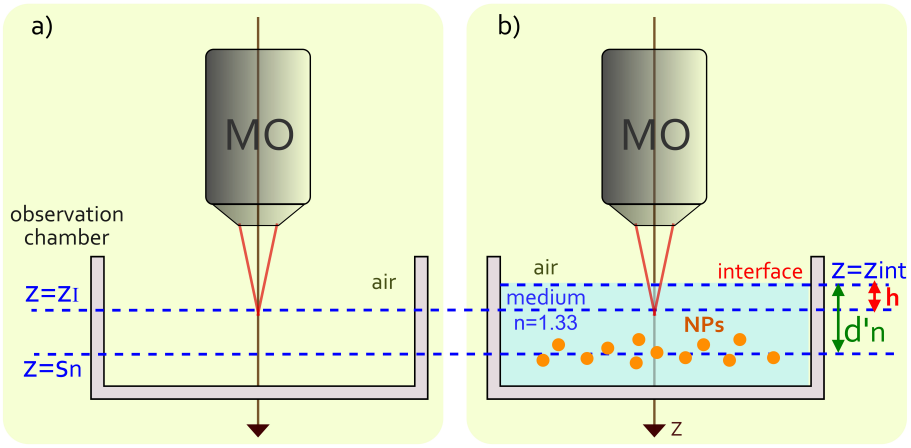

Figure 5.13: Zoom of the TIR setup without (a) and with (b) culture medium and gold particles

$n = 1.515$ and its thickness is $h = 0.17$. Since n and h of the culture medium differs largely from the refractive index and thickness of standard microscopy cover glasses, the objective adjustable or fixed cover glass correction cannot work properly. It is thus necessary to perform the correction using another method. As we will see, it is possible to make this correction by performing the holographic reconstruction with the proper exhaustive propagation kernel $\Psi_n(k_x, k_y)$.

To simplify the discussion we will consider a microscope objective without cover glass correction that image gold nanoparticles immersed in a medium (see Fig.5.13). The CCD conjugate plane $z = z_I$ is located (if imaged in air) at a depth h below the medium-air interface $z = z_{int}$. The reconstruction is performed in plane $z = z_{S_n}$ located at a depth d'_n below the interface. The reconstruction in plane $z = z_{S_n}$ is made in two steps.

1. First, we propagate the field in **air** from the image plane $z = z_I$ to the interface plane $z = z_{int}$ getting by this way the field E_{int} at the interface. We have thus :

$$E_{int}(k_x, k_y) = e^{+ih\left(\sqrt{k_{\mathbf{air}}^2 - k_x^2 - k_y^2} - k_{air}\right)} E'_I(k_x, k_y) \tag{5.44}$$

   Here, since the propagation occurs in the z^- direction, the exponential has a "+" sign contrarily to Equation 5.43 where the exponential has a "−" sign.

2. We propagate then the field in the **medium** from the image plane $z = z_{int}$ to the sample plane $z = z_{S_n}$. We have:

$$E_{z_{S_n}}(k_x, k_y) = e^{-d'_n\left(\sqrt{k_{\mathbf{med}}^2 - k_x^2 - k_y^2} - k_{liq}\right)} E'_I(k_x, k_y) \tag{5.45}$$

Here, since the propagation occurs in the medium, the wave vector $\vec{k}$ in air, must be replaced by the wave vector in the medium k_{med}. Wave vectors in the air and in the medium are interrelated through the refractive index $n = 1.33$ of the culture medium :

$$\begin{aligned} k_{air} &= k \\ k_{med} &= n\,k \end{aligned} \tag{5.46}$$

The proper propagation term for a medium of height h and that consists of water is thus :

$$\begin{aligned} \Psi_n(k_x, k_y) &= e^{-id'_n\left(\sqrt{k_{med}^2 - k_x^2 - k_y^2} - k_{liq}\right)} e^{+ih\left(\sqrt{k_{air}^2 - k_x^2 - k_y^2} - k_{air}\right)} \\ &= e^{-id'_n\left(\sqrt{n^2k^2 - k_x^2 - k_y^2} - nk\right)} e^{+ih\left(\sqrt{k^2 - k_x^2 - k_y^2} - k\right)} \end{aligned} \tag{5.47}$$

5.4.3 Specimen uncovered with a coverslip and imaged with a cover glass corrected MO

5.4.3.1 Abberations introduced by an improper glass coverslip correction

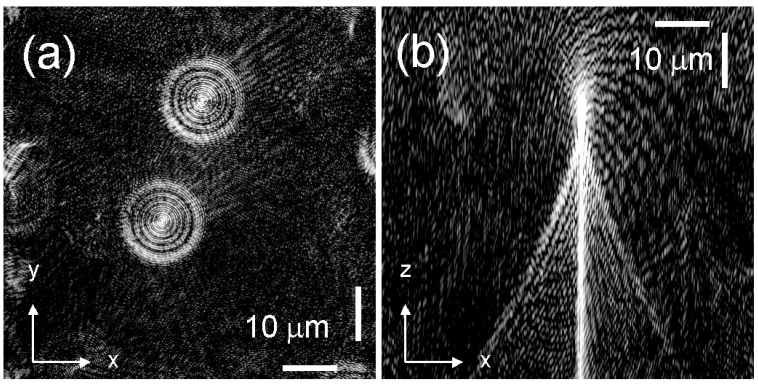

Figure 5.14: Reconstructed images of 200 nm gold particles from the holographic data of [Atlan *et al.* 2008]. The 3D reconstruction is performed on a 512×512 calculation grid (x, y axis) for $n = 0...512$ different reconstruction distances d'_n (z axis). Displayed images correspond to 2D cuts of the 3D reconstructed data along the xy (a) and zx (b) plane

In the first experiments on gold nanoparticles carried in our group in the Laboratoire Kastler Brossel [Atlan *et al.* 2008], particles were spin coated on a glass slide, illuminated in Total Internal Reflection using a green laser and

Olympus UPLFLN 60X MO	
Numerical Aperture	0.90
Focal Number	26.5
Working Distance	0.2 mm

Table 5.1: Specifications of the Olympus UPLFLN 60X MO

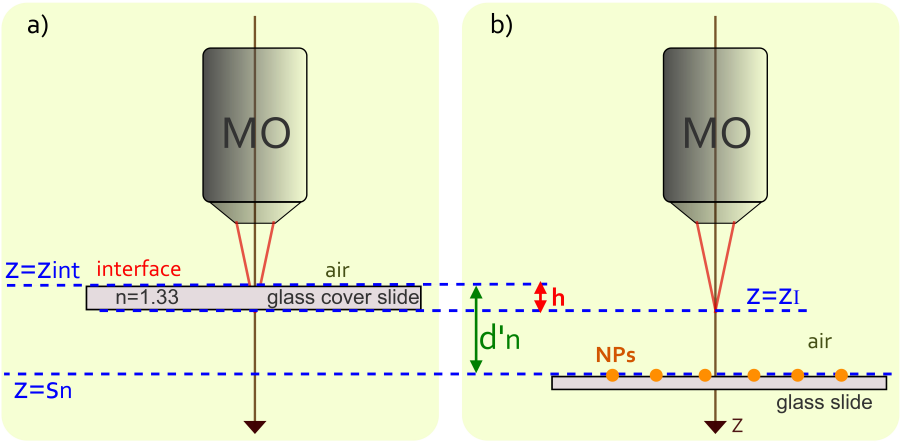

Figure 5.15: Zoom of gold nanoparticles imaging setup with an improper cover glass thickness compensation. (a) Setup with cover glass. (b) Setup without cover glass and with particles at the surface of a glass slide.

imaged with an air Olympus Microscope Objective UPLFLN 60X whose characteristics are given in Table 5.1.

Since the Numerical Aperture (NA=0.90) is high, the objective is provided with the ability of correcting the cover glass thickness h. This correction can be performed and adjusted for a cover glass thickness going from $h = 0.11$ to $h = 0.23$ mm using a MO correction ring.

Holograms of the spin coated nanoparticles are thus recorded with a proper cover glass correction. However, in practice, specimens of gold nanoparticles are prepared without adding a glass cover slide on the top. Consequently, huge spherical abberations are introduced. These abberations yield to the rings that convolute the nanoparticles as seen on the image of Figure 5.14 (a). The unsymmetrical triangular shape of the xz image of Figure 5.14 (b) is also an effect of these aberrations.

5.4.3.2 Abberations correction : the principle

The compensation of the improper cover glass correction can be performed similarly to the correction made in Section 5.4.2 using the proper propagation

kernel Ψ_n (see Figure 5.15). First, the field is back-propagated, in glass, from $z = z_I$ to $z =_{int}$ in order to remove the microscope objective cover glass correction (Figure 5.15 (a)). Here, h is a thickness equivalent to the thickness of the considered MO glass correction ring (h=0.11 to 0.23 mm). We propagate then the field, in air, from $z = z_{int}$ to the sample z_{S_n}. In this case, the proper propagation kernel Ψ_n is given by an equation similar to Equation 5.47, but here the propagation over h is performed in **glass**, and the propagation over d'_n is performed in **air**. We obtain :

$$\begin{aligned} \Psi_n(k_x, k_y) &= e^{-id'_n\left(\sqrt{k^2_{\mathbf{air}}-k_x^2-k_y^2}-k_{air}\right)} e^{+ih\left(\sqrt{k^2_{\mathbf{glass}}-k_x^2-k_y^2}-k_{glass}\right)} \\ &= e^{-id'_n\left(\sqrt{k^2-k_x^2-k_y^2}-k\right)} e^{+ih\left(\sqrt{n^2k^2-k_x^2-k_y^2}-nk\right)} \end{aligned} \tag{5.48}$$

where n, here, is the refractive index of glass :

$$\begin{aligned} k_{air} &= k \\ k_{glass} &= n\,k \end{aligned} \tag{5.49}$$

5.4.3.3 Experimental results

Using the propagation kernel of Equation 5.48 that compensates equivalent glass thickness h of the MO correction ring, we have reconstructed images of gold particles from the holographic data of [Atlan *et al.* 2008]. Since the correction ring equivalent thickness h is unknown (this information has been lost), we have performed the reconstruction for different values of h. For each value of h, we have performed the reconstruction for $n = 1...512$ reconstruction distance d'_n getting by this way 3D data. Moreover, for each reconstruction distance d'_n, we have calculated the intensity $I_{max}(n)$ of the brightest point M_{max} on the intensity image $I(x, y) = |E(x, y, z = d'_n)|^2$, and we have plotted $I_{max}(n)$ for the different h values on Figure 5.17.

The shape of the curves on Figure5.17 (i.e. maxima, width and symmetry with respect to maxima) depends on the value of the thickness correction h. Without correction, i.e. for $h = 0.00$ mm, the maxima's intensity is low $I_{max}(n = 197) = 0.846 \times 10^9$, and the curve is broad and asymmetric. When corrections are applied, the maxima's intensity increases, the width of the curve increases and the curve becomes more symmetric. The best correction is obtained for a thickness $h = 0.20$ mm, which is within the range of the possible h values of the MO correction ring (h=0.11 to 0.23 mm). For $h = 0.20$ mm we get $I_{max}(n = 94) = 0.571 \times 10^9$. This corresponds to an improvement of the particle image's brightness by a factor of 6.75.

Figure 5.17 is a comparison of the reconstructed images of the gold particle without (a,b) and with (c,d) thickness correction. The brightness of the

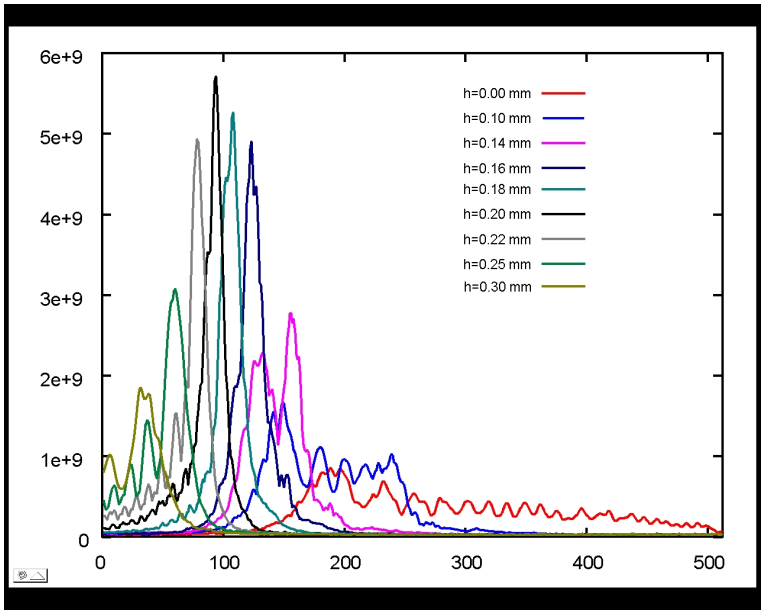

Figure 5.16: Plot of the intensity $I_{max}(n)$ of the brightest point M_{max} of the intensity image $I(x,y) = |E(x,y,z=d'_n)|^2$ of the 200 nm gold particles. The reconstruction is made from the holographic data of [Atlan *et al.* 2008] for different thickness corrections h. Vertical axis is $I_{max}(n)$ in arbitrary Units. Horizontal axis is the index n of the reconstruction distance d'_n.

holographic imaging system is highly improved when a glass coverslip thickness correction is applied. The resolution is also improved by approximately a factor of 3 in the xy direction, and by a factor of more than 10 in the z direction.

5.5 Overview of the Reconstruction procedure in Holographic Microscopy

In this section we will present an overview of the full reconstruction procedure in digital holographic microscopy which is schematically illustrated in Figure 5.18 .

First, the exit pupil plane of the microscope objective, is reconstructed, from the CCD hologram, by the Fresnel transform that requires one Fourier transform :

$$E_{CCD}(x,y,0)\ e^{ik(x^2+y^2)/2d} \overset{\mathrm{FFT}^{+1}}{\longrightarrow} E_P(x,y,z_P) \tag{5.50}$$

This method of reconstructing the MO exit pupil plane is an ingenious way to :

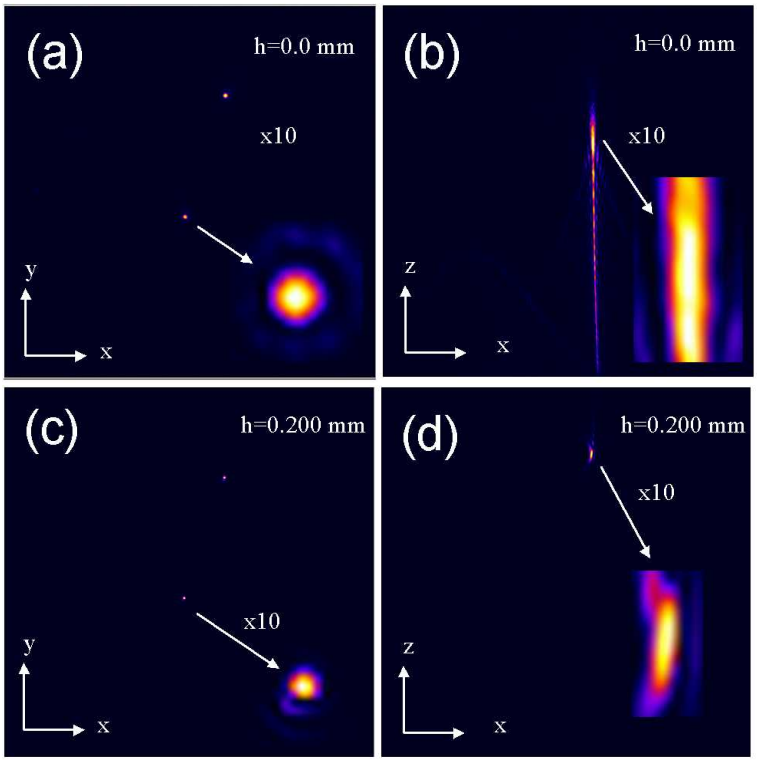

Figure 5.17: Reconstructed images of 200 nm gold particles from the holographic data of [Atlan *et al.* 2008]. 3D reconstruction is made on a 512×512 calculation grid (x, y axis) for $n = 0...512$ different reconstruction distances d'_n (z axis). The displayed images correspond to 2D cuts of the 3D reconstructed data along the xy (a,c) and zx (b,d) axis. Reconstruction is performed without (a,b) and with (c,d) glass coverslip thickness correction with $h = 0.20$ mm. Intensity images $I = |E|^2$ are displayed in a linear colored scale from $I = 0$ (black) to $I = I_{max} = 0.846 \times 10^9$ for images (a,b) and to $I = I_{max} = 0.571 \times 10^9$ for images (c,d) (white). A $\times 10$ zoom of the particle's image is displayed on the right hand bottom side of each image (a,b,c,d)

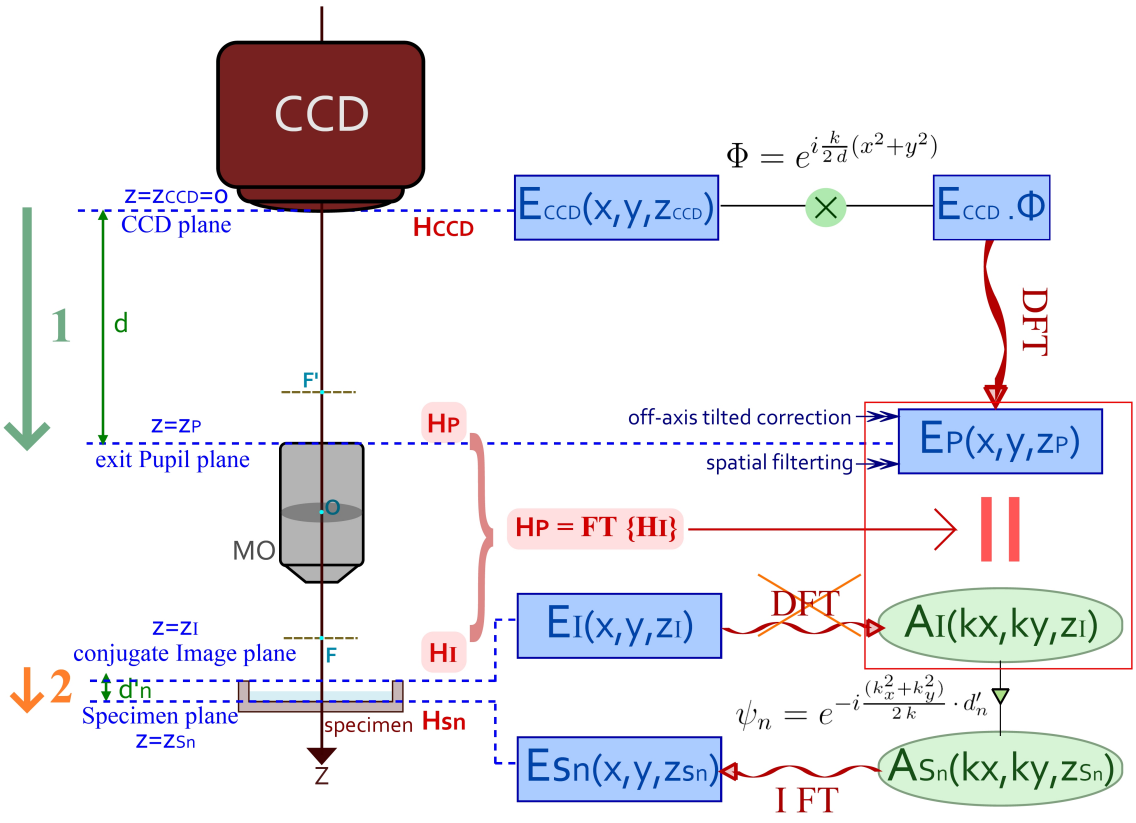

Figure 5.18: Overview of the reconstruction procedure in holographic microscopy

- easily correct the lens phase curvature ϕ_ℓ , which is exactly equal to the quadratic phase factor $\Phi = k(x^2 + y^2)/2d$ of the Fresnel transform formulation, and is thus automatically included.

- retrieve all the parasitic technical noise and undesired terms by applying a simple numerical spatial filter around the well defined relevant term obtained in the frequency domain of the reconstructed image, and compensate the off-axis tilt by a simple translation of the relevant term to the center of the image. These two operations can be symbolized by the $\mathcal{TSF}$ operator (Translation + Spatial Filtering). This operator transforms E_P into E'_P:

$$E_P \xrightarrow{\mathcal{TSF}} E'_P \tag{5.51}$$

- calculate the transverse magnification factor G of the microscope objective, that is needed to determine the new pixels'size d'_{px} of the conjugate image, directly from the experimental holographic data without any calibration of the optical system.

The corrected holographic field E'_P, at the MO exit pupil plane, is thus obtained. Because a high magnification MO is used, the distance between the back focal plane and the exit pupil plane of the MO is very small. Thus, the hologram at the exit pupil plane is the Fourier transform of the hologram E'_I at the conjugate image plane properly corrected and filtered. We have thus :

$$E'_P(x, y, z_P) \xrightarrow{\text{FFT}^{+1}} E'_I(x, y, z_I) \tag{5.52}$$

However, when a Direct Fourier Transform is applied to a complex field, it decomposes this field into its Angular Spectrum. We have thus :

$$E'_P \equiv E'_P(k_x, k_y, z_P) = FFT^{+1} E'_I(x, y, z_I) = A_I(k_x, k_y, z_I) \tag{5.53}$$

Since the reconstruction of $E'_P(x, y, z_P)$ automatically yields to the angular spectrum of the conjugate image $A_I(k_x, k_y, z_I)$, the Direct Fourier Transform of the angular spectrum reconstruction process, which is the second step of the all reconstruction procedure, is not needed.

The reconstructed field, at the exit pupil plane, is thus directly propagated, in free space, to the object plane. The propagation distance is defined by the distance between the conjugate image plane and the object plane. The angular spectrum of the field at the object plane is thus obtained :

$$A_{S_n}(k_x, k_y, z_{S_n}) = A_I(k_x, k_y, z_I) e^{-id'_n(k_x^2+k_y^2)/2k} \tag{5.54}$$

Finally, an Inverse Fourier Transform is applied to $A_{S_n}(k_x, k_y, z_{S_n})$, in order to get the reconstructed field at the specimen plane :

$$A_{S_n}(x, y, z_{S_n}) \xrightarrow{\text{FFT}^{-1}} E_{S_n}(x, y, z_{S_n}) \tag{5.55}$$

The combination of the all above presented equations gives finally :

$$E_{S_n}(x,y,z_{S_n}) = \mathrm{FFT}^{-1} e^{-id'_n(k_x^2+k_y^2)/2k}\ \mathcal{TSF}\ \mathrm{FFT}^{+1} e^{ik(x^2+y^2)/2d} E_{CCD}(x,y,0) \tag{5.56}$$

We have seen that holograms are calculated by four-phase demodulation method (see Equation 5.3) :

$$E_{CCD}(x,y,z_{CCD}=0) = \sum_{j=1}^{M} i\ {}^{n}H_j \tag{5.57}$$

We obtain finally :

$$E_{S_n}(x,y,z_{S_n}) = \mathrm{FFT}^{-1} e^{-id'_n(k_x^2+k_y^2)/2k}\ \mathcal{TSF}\ \mathrm{FFT}^{+1}\ e^{ik(x^2+y^2)/2d} \sum_{j=1}^{M} i\ {}^{n}H_{CCDj} \tag{5.58}$$

Chapter 6

Digital Holographic Microscopy of Gold Nanoparticles in living cells

Contents

6.1 Biological Context 117
6.2 Materials and Methods 118
6.2.1 Biological Specimen Preparation 118
6.2.2 Optical Methods 125
6.2.3 Reconstruction Procedure 131
6.3 Experimental Results 133
6.3.1 Gold Nanoparticles in live cells environments 134
6.3.2 Unlabeled 3T3 Cell 153
6.3.3 Free Gold Nanoparticles 156
6.4 Overview 165

6.1 Biological Context

The cell is the basic unit of every living organism. In nature, approximately 200 different types of cells exist. These cells forms biological tissues which constitutes the different organs. Biological processes, as well as the maintain of tissue cohesion, require the ability of cells to establish contacts with their surrounding environments, either with other neighboring cells or with protein complexes of the extracellular matrix (ECM) in the attempt of emitting and capturing signals and generating forces to move according the well defined paths. The presence of transmembrane cellular receptors promotes the establishment of these contacts since they can identify specific ligands that can be either adhesion proteins of a neighboring cell or proteins of the ECM. This specific "receptor-ligand" interaction is one of the most basic in all of biology, and defines the cellular adhesion. The cytoskeleton, a three-dimensional array of protein fibers, is the intracellular structure that

confers to the cell its shape and motility. The link between adhesion proteins and the cytoskeleton are mediated by a specific protein complex. Hence, the cell has the ability to form different adhesion zones whose properties differ depending on the implied adhesion proteins [Brevier].

Here we are interested in tight junctions that are responsible for the mechanical bonding of cells to either the ECM or to other neighboring cells. A cell bonds to its ECM via focal contacts that implicates membrane proteins of the family of *integrins* (the cadherins family is implicated in adherent junctions that connects two neighboring cells)[Liddington & Ginsberg 2002].

Fibronectin is quite an interesting prototype ligand since it can be pinpointed by the majority of the different existing cellular types via at least 10 membrane receptors of the *integrin* family. Consequently, fibronectin is involved in many different biological processes [Johansson *et al.* 1997].

Since we were interested by the study of the organization and dynamics of the individual integrin receptors and their response to stimuli, we have chosen to investigate these integrin receptors by exploiting the "integrin-fibronectin" interaction. Accordingly, nanometric-sized gold nanoparticles, conjugated to fibronectin, were used as biological markers for the integrin receptors. When cells meets the fibronectin-coated gold nanoparticles, the integrin receptors of the cells will recognize the fibronectin ligand and "integrin-fibronectin" interaction is promoted. We used our heterodyne digital holographic microscope to image and localize in 3D the gold nanoparticles that are conjugated to the integrin receptors in an attempt of characterizing these receptors.

6.2 Materials and Methods

6.2.1 Biological Specimen Preparation

We use NIH 3T3 mouse fibroblasts with integrin surface receptors labeled with 40 nm fibronectin-conjugated gold particles. Gold nanoparticles, precoated with streptavidin, were attached to the cell surface integrin receptors via biotin and fibronectin proteins. Streptavidin and biotin are two kinds of protein molecules that are very well known for their extraordinarily high mutual affinity [Green 1975], and fibronectin, an extracellular matrix protein, has the property of interacting specifically with cell surface receptors of the integrin family.

In the next subsections of this part we will describe, step by step, and in details the complete procedure that we used to prepare our biological specimens.

6.2.1.1 Cell Line

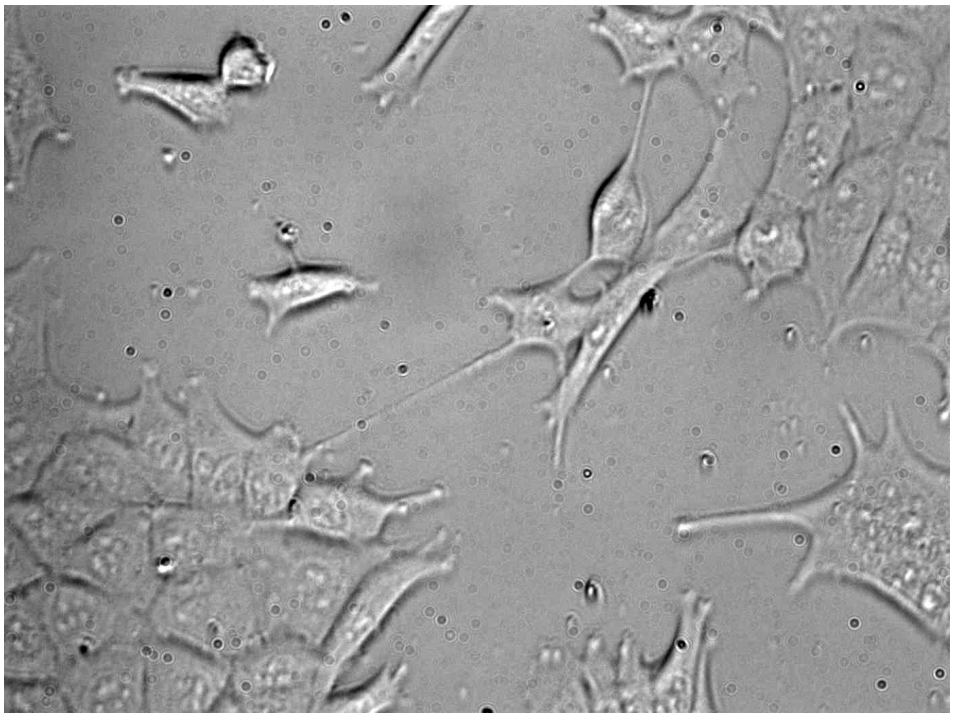

Figure 6.1: NIH 3T3 fibroblasts under bright-field microscopy (10X)

We use the NIH 3T3 standard fibroblast cell line originally obtained from **N**ational **I**nstitute of **H**ealth Swiss mouse embryo tissue at the School of Medicine of New York University in 1962 [Todaro & Green 1963]. **3T3** refers to the cell transfer and inoculation protocol for the line, and means "**3**-day **T**ransfer, inoculum $\mathbf{3} \cdot 10^5$ cells". Figure 6.1 is a 10 X image of a monolayer of the considered 3T3 cells obtained by bright-filed microscopy.

It should be pointed out that we have decided to work with NIH 3T3 fibroblasts because this cell line offers several advantageous properties :

- It is known than 3T3 Cells grow rapidly and can double every 18 hours. The become confluent at a density of approximately 40 000 cells/cm^2.
- 3T3 cells have a wide range of receptors and second messenger systems.
- This cell line is very common and can be found very easily.

- Culturing 3T3 cells is not very complicated and do not require elaborate growth conditions.
- 3T3 fibroblasts are relatively large cells (length $\sim 20 - 30\mu$m, width $\sim 5 - 10\mu$m).

6.2.1.2 Cells preparation

3T3 cells are seeded in 25 cm^2 tissue culture T-Flasks (from TPP) in 7.5 mL of Duelbecco's modified Eagle's medium (DMEM Gibco, Invitrogen, Carlsbad, CA) supplemented with 10% fetal calf serum (PAA Laboratories GmbH) at 37°C in a 5% CO2 atmosphere.

When cells reach a high density in their culture flask (when they are approximately 90% confluent), cell division stops. Hence, they should be passaged in order to be kept alive for extended periods of time.

Passaging

In their culture flasks cells are adherent to the surface of the flasks. In order to disperse the adherent cells, Trypsin treatment is used to break down the proteins responsible for surface adherence.

The complete subculturing protocol is described as follows :

1. The culture medium is totaly removed from the culture flasks and discarded.
2. Adherent cells are briefly rinsed with 1 mL Trypsin solution to remove all traces of serum that contains Trypsin inhibitor.
3. 2 mL of Trypsin solution is added to the culture flask and the flask is gently rocked so that the solution totaly covers the surface. The flask is then incubated at 37°C in a 5% CO2 atmosphere for 3-5 minutes until cells are detached from the surface.
4. The flask is taken out of the incubator. At this stage cells are totaly dispersed and do not adhere anymore to the flask's surface. 2 mL of fresh culture medium is added to the trypsinized cell suspension to block the effect of Trypsin. Media and cells are swished to obtain a better dissociation of the cells.
5. The trypsinized cell suspension is dispensed, at a density of $3 \cdot 10^5$ cells (which is, in practice, equivalent to approximately 2 drops of the

trypsinized cell suspension), into a new sterile culture flask containing 7.5 mL of complete growth medium. The new flask is lightly rocked to allow a better repartition of the cells. The freshly prepared flask is finally placed in the 5% CO2, 37°C incubator.

It should be noted that cells are passaged every 3 days and the passaging procedure is operated under a laminar flow hood and all materials that are used were previously sterilized.

Preparation of small culture dishes

Specimens of live cells should be prepared in adequate observation chambers for the holographic experiments, thus, fibroblasts are transported from their culture flask to a small sterilized 9.2 cm^2 culture dish (from TPP). Specimens are prepared 48 hours before performing the holographic experiment.

First, a sterilized 32 mm diameter optical quality glass coverslip is placed inside the culture dish in the bottom.

Second, the trypsinized cell suspension, obtained at step 4 of the passaging protocol, is dispensed, at a typical density of $3 \cdot 10^5$ cells onto the glass slide in the dish. Coverslips were coated, in advance, with fibronectin (fibronectin from bovine plasma, Sigma, St Louis, MO) to fulfil optimal cell growth conditions.

Finally, the culture dish is smoothly rocked in order to ensure an homogenous repartition of cells on the complete surface of the glass coverslip and is then placed overnight in the incubator to allow adherence and growing of cells on the glass slide. After 24 hours of incubation, cells in the prepared petri dish are ready to be labeled with gold nanoparticles. Labeled cells are then for another 24 hours before performing the experiment.

6.2.1.3 Preparation of Gold Conjugates

We have previously evoked that biological specimens that we used in our holographic experiments consist of 3T3 cells where their integrin surface cellular receptors are labeled with fibronectin-functionalized gold nanoparticles. Based on the very well known strong mutual affinity of streptavidin and biotin molecules, Fibronectin-functionalized gold conjugates were prepared, via biotin, from streptavidin-coated gold conjugates using a two-steps procedure :

1. Biotinylating fibronectin molecules
2. Conjugating biotinylated-fibronectin to the streptavidin-coated gold nanoparticles

Biotinylation of fibronectin

Fibronectin proteins (fibronectin from bovine plasma, Sigma, St Louis, MO) were labeled with biotin (Figure 6.2) by using EZ-Link®Sulfo-NHS-LC-Biotin according to the provider protocol (Pierce, Rockford, IL). The biotinylation procedure is relatively complicated and time consuming. The complete protocol can be found in Appendix A.1 . The final concentration of biotinylated-fibronectin solution was 0.447 mg/mL.

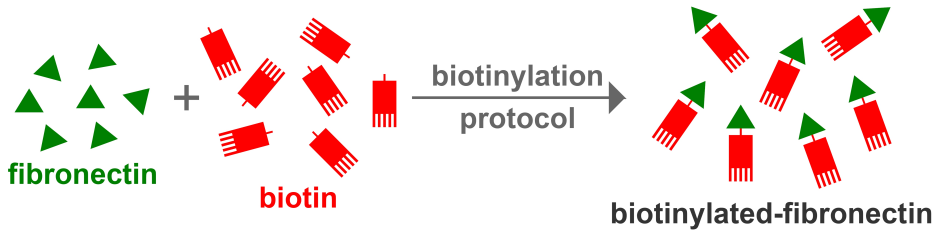

Figure 6.2: Biotinylation

The efficiency of the biotinylation protocol is verified by measuring the level of biotin incorporation on an HABA [2-(4' -Hydroxyazobenzene) Benzoic Acid)] quantitation assay according to the provider's protocol (Pierce, Rockford, IL) that can be found in Appendix A.1 . Average number of biotin molecules obtained per fibronectin is 2.5.

Coating gold nanoparticles with biotinylated-fibronectin

We used a solution of 40 nm average diameter gold conjugates pre-coated with streptavidin (from BioAssay, Gentaur-France) shown on Figure 6.3. The concentration of the initial gold solution is 15 OD (Optical Density).

Gold nanoparticles were functionalized with biotinylated-fibronectin (Figure 6.4) using the following protocol :

1. The streptavidin dressed gold conjugates were rinsed twice with 1X PBS (Phosphate Buffered Saline) (pH = 7.25) in order to eliminate free sterptavidin molecules from the solution : 10 μL of the 40 nm streptavidin-dressed gold solution is mixed with 1,5 mL 1X PBS in a 2 mL Eppendorf

centrifuge tube. The tube, containing the mixture, is then vortexed and centrifuged at 3000 rpm (round per minute) for 1 minute. After centrifuging, the supernatant is carefully removed from the tube using a Pasteur pipette and only the pellet is kept. The supernatant is discarded.

2. The obtained pellet is suspended into a tube containing 990 μL of 1X PBS buffer : a 1 mL dilute streptavidin-coated gold solution is thus obtained.

3. 50 μL of the previously prepared biotinylated-fibronectin solution was added to the tube containing the dilute gold solution. The mixture is vortexed at 700 rpm during four hours at room temperature to allow streptavidin-biotin bonding. Streptavidin and biotin have a strong mutual affinity and the streptavidin-biotin interaction is one of the strongest non-covalent interactions known in nature.

Figure 6.3: Streptavidin-coated Gold Nanoparticles solution from BioAssay Works

At the end of step 3, a solution of 40 nm fibronectin-functionalized gold colloids is obtained. This prepared solution was stored at 4°C and used within 24 hours after preparation in order to ensure maximum functionality.

6.2.1.4 Gold-Cells conjugation

After 24 hours of incubation under 5% CO2 and 37°C atmosphere, the culture dish, prepared as described in Section 6.2.1.2 is retrieved from the incubator

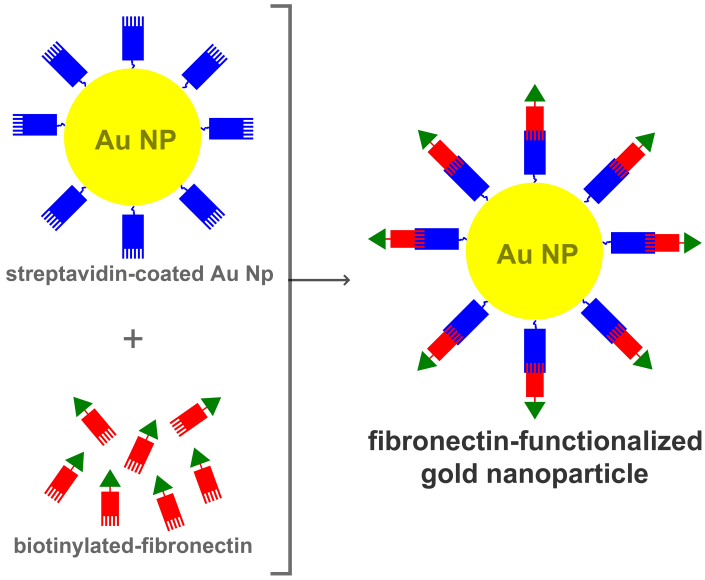

Figure 6.4: Fibronectin-functionalized gold nanoparticles

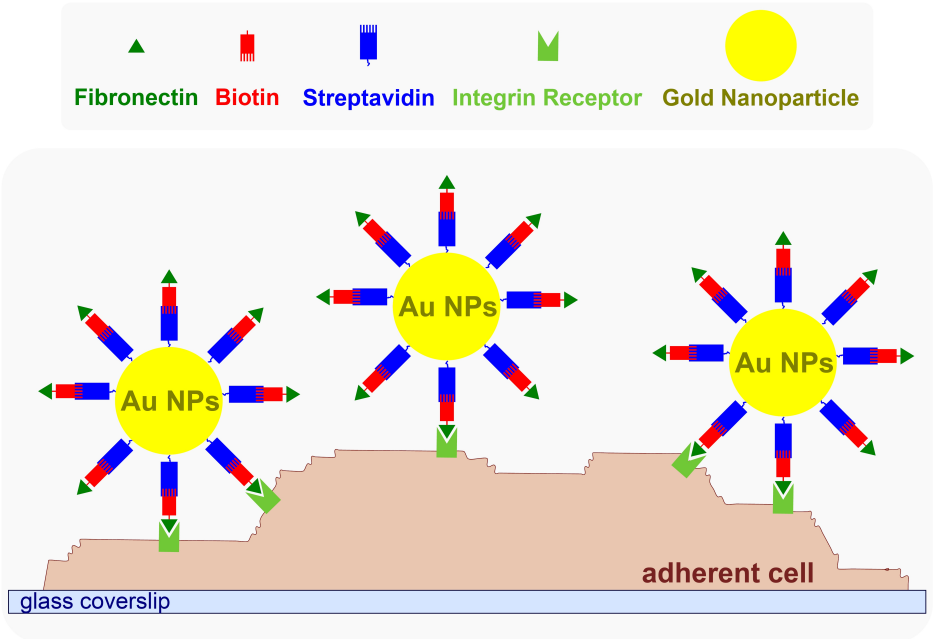

Figure 6.5: Labeled Cell

and placed under the laminar flow hood in order to perform the coupling with the prepared gold nanoconjugates. The dish contain a monolayer of 3T3 cells on the glass coverslip immersed in 2 mL of DMEM medium. The culture medium contained in the dish is aspirated and replaced by a solution composed of 2 mL DMEM plus 500 μL of the functionalized gold colloids solution prepared as described in 6.2.1.3. The integrin-fibronectin link is created at this level allowing the cells to attach, on their surface, the functionalised gold nanoparticles (see Figure 6.5). It should be noted that the functionalized gold solution was sonicated before being added to the culture dish.The culture dish, containing now fibroblasts and functionalized gold solution, is gently rocked in order to ensure a good repartition of the gold beads. The dish is then reinserted in the incubator for another 24 hours prior to the envisaged experiment.

6.2.1.5 Specimen in the Observation Chamber

24 hours after the conjugation process, the holographic experiment was performed. Hence, the culture dish was taken out of the incubator and the glass slide containing adherent 3T3 cells tagged with 40 nm gold nanoparticles was extracted. The glass slide was mounted on a specific observation chamber. The observation chamber that we used in the experiments presented in this chapter is shown on Figure 6.6.
To ensure optimum cell survival conditions during the observation, coverslips were kept in a special DMEM-F12 observation medium from PAA Laboratories (DMEM-F12 without Phenol red, B12 vitamin, Riboflavin, 0.5% fetal calf serum) that is supplemented with L-Glutamine and 20 mM of HEPES [(4-(2-hydroxyethyl)-1-piperazineethanesulfonic acid)], which is a buffering agent that maintains the physiologic pH conditions. In order to prevent the observation medium from leaking, a plastic well is mounted on the observation chamber.

6.2.2 Optical Methods

6.2.2.1 Experimental Apparatus

The experimental apparatus is basically a modified Mach-Zehnder interferometer.Figure 6.7 is a schematic representation of the optical setup.
A coherent laser source is used as the illumination source. The initial illumination laser light is splitted, using a polarizing beam splitter cube (PBS), into two beams, a reference beam (complex field E_R, frequency f_R) and an object illumination beam (complex field E_o, frequency f_o) forming the two arms of the Mach-Zehnder interferometer. A combination of a half wave

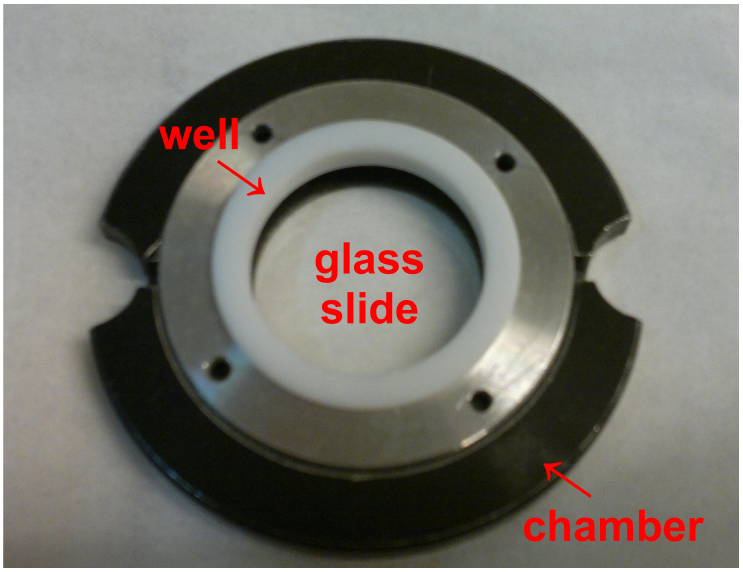

Figure 6.6: Observation chamber for live biological specimens

plate ($\lambda/2$) and two neutral density filters, ND_1 and ND_2, is used to prevent the saturation of the detector by controlling the optical power traveling in each arm. Two acousto-optic modulators, AOM1 and AOM2, driven around 80 MHz with a selection of the first order of diffraction, shift both frequencies at respectively f_{AOM1} and f_{AOM2}.
The object beam illuminates the sample, prepared as described in Section 6.2.1, in a dark field arrangement in order to prevent direct illumination light from entering the system. The illumination wave is scattered by the specimen and this scattered wave (complex field E_{obj}) is collected by a microscope objective (MO). A beam splitter (BS) is then used to combine the scattered object wave E_{obj} and the reference wave E_R which is slightly angularly tilted ($\theta \sim 1°$) with respect to the propagation axis of the object wave in an off-axis configuration. The half wave plate on the object illumination arm aligns the polarization of the corresponding beam ensuring its optimal interference with the reference beam. A CCD camera detects the interference pattern (hologram H_{CCD}).

Laser source

In the experiments presented in the current chapter, the laser source that we used is a DL7140-201S single-mode near infrared Sanyo Laser diode, emitting at λ=785nm. The laser is operated at 90 mA current and the optical output power is 80 mW.

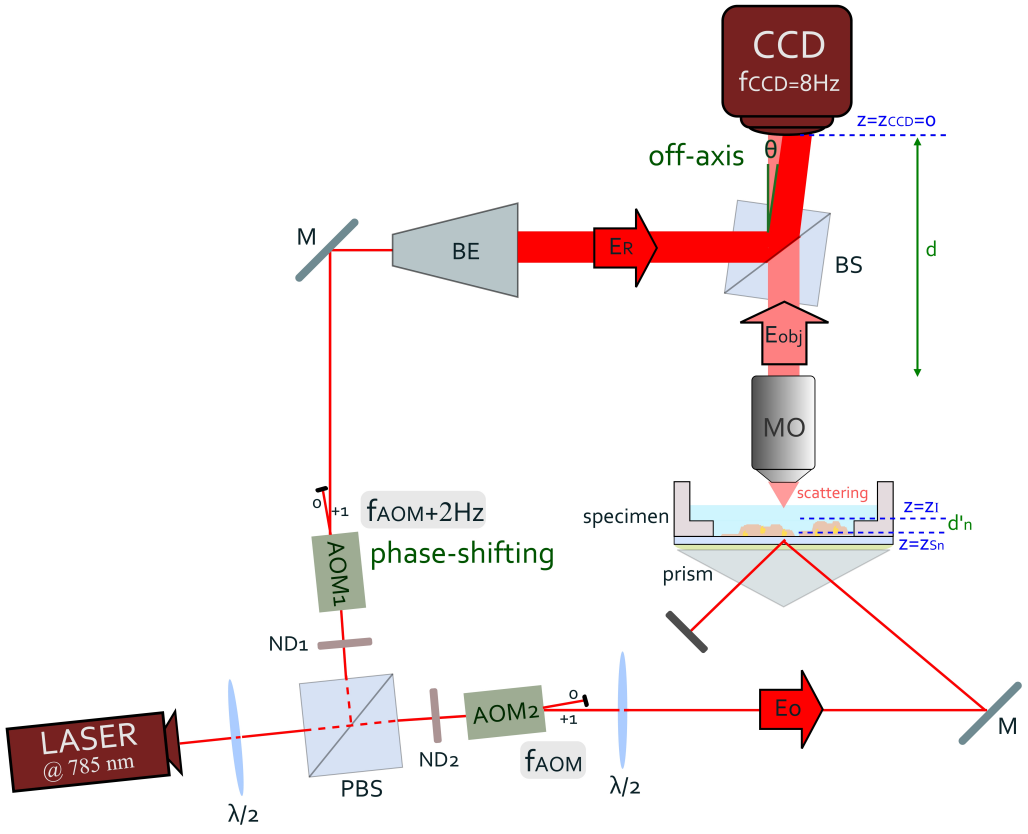

Figure 6.7: Optical apparatus for DHM in total internal reflection

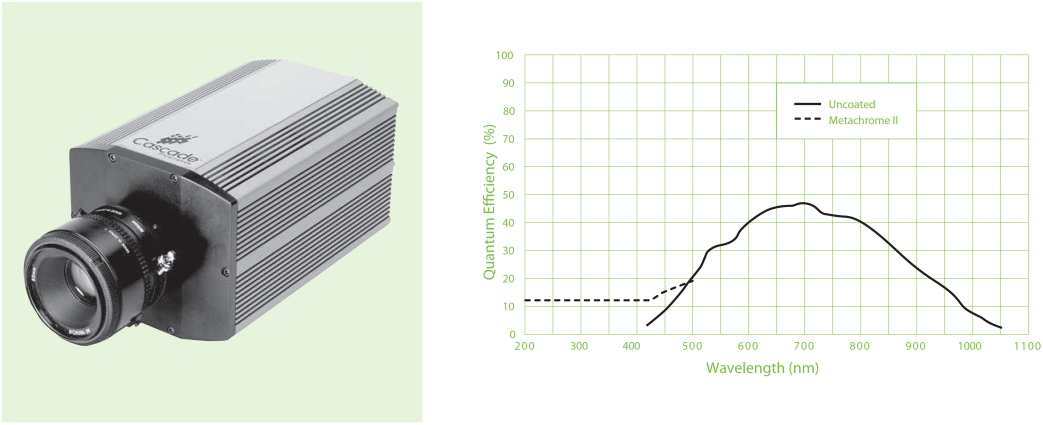

(a) Photo of the Roper CCD camera

(b) Quantum efficiency graph of the Roper camera in function of the wavelenght

Figure 6.8: Roper cascade 512F CCD camera

CCD Camera

The CCD camera that we used is a Roper Cascade 512F (see Figure 6.8) with a detector composed of 512×512 square pixels and 8.2×8.2 mm optically centered imaging area. The physical size of the pixels is $d_{px} = 16\mu m$. The frame rate frequency of the camera is $f_{CCD} = 8$ Hz.

Microscope Objective

In our experiments, we used an Olympus LMPLFLN air microscope objective. The specifications of this objective are presented in table 6.1 :

Olympus LMPLFLN 50X MO	
Numerical Aperture	0.5
Focal Length	3.6 mm
Working Distance	10.6 mm

Table 6.1: Specifications of the Olympus LMPLFLN 50X MO

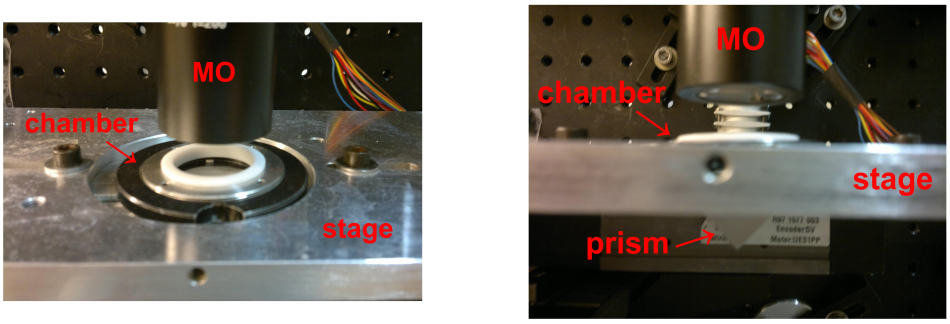

(a) Top view (b) Front view

Figure 6.9: Specimen microscopy stage

6.2.2.2 Sample Illumination

We used dark field illumination, by performing total internal reflection (TIR) using a 90° prism, in order to prevent the direct light from entering the system and thus collecting only the light scattered by the specimen using the full dynamic range of the detector. For this purpose, the observation chamber containing the biological specimen, immersed in the observation medium and prepared as described in Section 6.2.1.5, is mounted on a specific customized X-Y translation motorized stage. The stage is specifically designed to allow a facilitated positioning of the prism in its center in such a way to establish a direct contact between the surface of the prism and the specimen's glass slide contained in the bottom of the observation chamber as shown on Figure 7.6. An index-matching material is applied at the contact surface of the prism and the glass slide.
The object's laser beam illuminates the specimen by provoking total internal reflection at the medium-air interface (see Figure 6.10). A total laser power of 70 mW illuminates a region which is approximately 200 micrometers in diameter, with an optical power density of 56 $W.cm^{-2}$. This is 5 orders of magnitude lower than the power densities of several $MW.cm^{-2}$ used on living cells in earlier works (e.g. [Cognet *et al.* 2002]), and can therefore be assumed to be well below their damage threshold.
The illumination wave is scattered by the beads and by the local change of refractive index within the cells yielding a propagating scattered wave, which

is collected by the microscope objective.
This illumination configuration has been chosen because it holds back most of the directly transmitted illumination light preventing from reaching the detection system. Additionally, using this configuration, less strain is executed on the living cells. However, the TIR illumination arrangement constrains the usage of high working distance microscope objectives which are known to have limited numerical apertures (NA=0.5 typically), limiting consequently the reachable resolution of the reconstructed images.

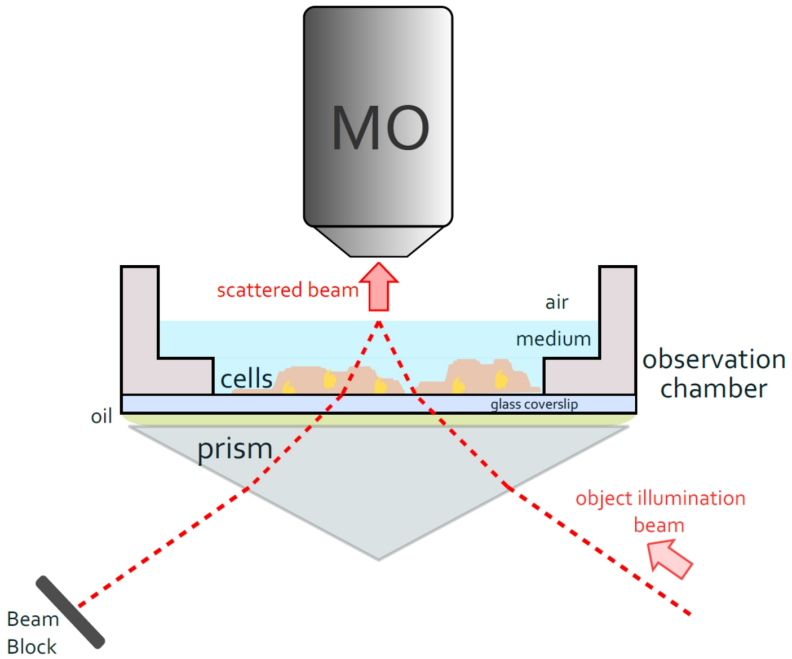

Figure 6.10: Dark field illumination of the specimen in Total Internal Reflection

6.2.2.3 Holograms Acquisition

We used phase-shifting digital holography in order to directly obtain pure clean holograms were only the relevant +1 term (virtual image) is procured. Accordingly, it is necessary to record several phase-shifted digital holograms with a relative phase shift $\Delta\varphi = \pi/2$ between two consecutive frames. In the experiments presented in this chapter, the CCD camera records a sequence of 32 frames H_0,...,H_{31} with an acquisition time equal to 100 ms per acquired hologram.

As we have exhaustively described in Chapter 4, we used a heterodyne method to generate the phase shift on the reference beam by inserting two acousto-optic modulators into the reference arm. To get an accurate phase shift [Atlan *et al.* 2007, Verpillat *et al.* 2010, Joud *et al.* 2010a], the reference wave is frequency-shifted by tuning the two acousto-optic modulators AOM1 and AOM2 [LeClerc *et al.* 2000], so that the heterodyne beating frequency is:

$$\Delta f = f_{AOM1} - f_{AOM2} = \frac{f_{CCD}}{4} = 2Hz \tag{6.1}$$

where f_{CCD} =8Hz for the Roper camera that we used.

The complex distribution of the field is then obtained from the recorded sequence of CCD holograms using the M-phases demodulation method, described in Chapter 4.
The object field E_{CCD} on the CCD plane ($z = z_{CCD} = 0$) is given by:

$$E_{CCD}(x, y, z = 0) = \sum_{j=1}^{M} i^n \, H_{CCDj} \tag{6.2}$$

where $i^2 = -1$ is the imagery unit, and M is an integer defining the number of frames used for the reconstruction, which is equal either to 1 or to 32 in the experiments we present in this chapter. In Equation 6.2), the coordinates x, y (with $0 < x, y < 511$ for the used Roper camera) are integers, which represent the pixel location within the CCD plane. The pixel size is then the physical CCD pixel size, i.e., 16 μm.

6.2.3 Reconstruction Procedure

We have described in details the full reconstruction procedure that we used in all our experiments. It consists, briefly, of two steps :

First, the field is calculated at the conjugate image plane $z = z_I$ by a pioneer reconstruction of the MO exit pupil plane (plane $z = z_P$) using the one Fourier transform Fresnel transformation method [Schnars & Jüptner 1994]. This reconstruction of the MO exit pupil plane allows the correction of the phase curvature related to the presence of the imaging lens [Colomb *et al.* 2006c] and also the correction of the off-axis phase tilt.

Second, the object field $E_{S_n}(x, y, z_{S_n})$ is calculated in the vicinity of the conjugate image plane $z = z_I$ (i.e. for $z_{S_n} \simeq z_I$) by free space propagation using the angular spectrum method, which requires two Fourier transforms

[Mann *et al.* 2005, LeClerc *et al.* 2000, LeClerc *et al.* 2001, Yu & Kim 2005]. Before performing the angular spectrum propagation, the magnification factor of the conjugate image plane was measured by imaging, on the same setup, a USAF target (see Figure 6.11). Since pixels of the CCD detector of the Roper camera are square pixels, horizontal and vertical pixel sizes in the conjugate image plane ($\Delta\xi'$ and $\Delta\eta'$) are equal. The obtained pixel size in the conjugate image plane is $d'_{px} = \Delta\xi' = \Delta\eta' = 177$ nm.
Knowing d'_{px}, the angular spectrum propagation is performed with the proper compensation of the enlargement factor related to the presence of the magnifying imaging lens. This reconstruction method is specifically chosen because pixels' size are kept constant during the propagation independently of the reconstruction distance d'_n.

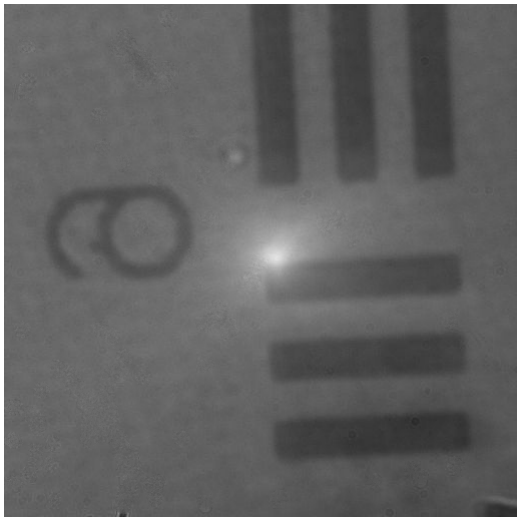

Figure 6.11: White light direct image of a USAF chart for calibrating the MO

We should point out that, as described in Chapter 5, the magnification factor G is given by :

$$G = \frac{d_{px}}{d'_{px}} = \frac{d}{f_l} \tag{6.3}$$

Since the physical pixel size, the pixel size in the conjugate image and the focal length of the MO (see Table 6.1) are known quantities ($d_{px} = 16\mu m$, $d'_{px} = 177nm$ and $f_l = 3.6mm$), d which is the CCD to the MO output aperture distance can be deduced :

$$d = \frac{d_{px} \cdot f_l}{d'_{px}} = 32.5cm \tag{6.4}$$

The obtained d distance calculated by Equation 7.3 is consistent with the experimentally measured distance $d_{exp} \simeq 32cm$.

Combining the two steps of the reconstruction procedure, the object field $E_{S_n}(x, y, z_{S_n})$ is thus obtained by :

$$E_{S_n}(x, y, z_{S_n}) = \mathrm{FFT}^{-1} e^{-id'_n \frac{(k_x^2+k_y^2)}{2k}} \; \mathcal{TSF} \; \mathrm{FFT}^{+1} \; e^{ik\frac{(x^2+y^2)}{2d}} \sum_{j=1}^{M} i \; {}^{n}H_j \quad (6.5)$$

In order to reconstruct the entire volume object, the angular spectrum propagation was done for 512 different z_{S_n}-positions of the specimen. Accordingly, the reconstruction is done for 512 different reconstruction distances d'_n :

$$d'_n = (n - 256)\delta z \quad (6.6)$$

where n is an integer that defines the number of reconstruction planes. Here $n = 0...511$ since the reconstruction was done for 512 planes. δz defines the distance between two consecutive reconstruction planes z_{S_n} and $z_{S_{n+1}}$. δz is chosen as $\delta z = 177$ nm in order to get the same pixel's size ($\Delta\xi' = \Delta\eta' = \delta z = 177$ nm) in the 3 directions x, y and z.
The total reconstruction distance, which is the distance between the CCD camera plane where holograms are captured and the specimen plane is thus given by :

$$z_{S_n} = z_I + d'_n \quad (6.7)$$

where z_I is the z coordinate of the CCD conjugate image plane which is the plane that is directly imaged on the CCD without holographic reconstruction. From Equation 6.7 we can see that the specimen plane is calculate in the near vicinity of the conjugate image plane at a distance d'_n around the $z = z_I$ conjugate image plane.

On that account, we got 3D volume images composed of $512 \times 512 \times 512$ voxels, with the same pixel size laterally, transversally and in depth.

6.3 Experimental Results

To ensure a complete judicious study, we have investigated, in addition to the specimens of 40 nm gold-labeled 3T3 fibroblasts, two more varieties of specimens that consists of unmarked 3T3 fibroblasts and free 40 nm gold particles.

We will first start by presenting experiments of marked cells, then we will expose results obtained on unmarked cells. In the last part of this section, we will describe experiments performed on free 40 nm gold particles.

6.3.1 Gold Nanoparticles in live cells environments

In this section we will present experimental results obtained on biological specimens that consists of cells labeled with 40 nm gold particles. First we will consider a sample where cells were labeled with several gold conjugates. Then we will consider an extreme case were a 3T3 cell is labeled with a single gold nanoparticle to facilitate the quantitative analysis.

6.3.1.1 3T3 cells labeled with several gold particles

Figure 6.12 shows images of a first marked specimen, with two cells and several gold particles.

We have implemented on our optical holographic setup a tungsten lamp in a way to readily obtain, in the same conditions of the holographic manipulations, standard bright-field illumination images. Figure 6.12a shows a bright-field white light image of the considered specimen obtained by turning off the laser source and turning on the tungsten lamp only.
Figure 6.12b is a direct image of the same region of the specimen, but obtained by illuminating the cells with the object laser beam. The reference beam is blocked for this image.

Figure 6.12c is exactly the same as Figure 6.12b but we have turned on the tungsten lamp in order to clearly see the repartition of the specimen scattered light on the cells.

After performing the direct investigations of the considered specimen, it's time to perform the holographic experiment. The tungsten lamp is turned off, the reference beam is unblocked and the specimen is illuminated with the object beam. Figure 6.12d is a direct captured image of the interference between the reference beam and the object scattered beam that is recorded by the CCD camera.

All the images presented in this part consists of 512 pixels per side. From Section 6.2.3, we obtained that one pixel in the reconstructed images equals 177 nm. Hence, images are 90.6 μm wide.
Figure 6.13 shows the reconstructed holographic intensity image of the same

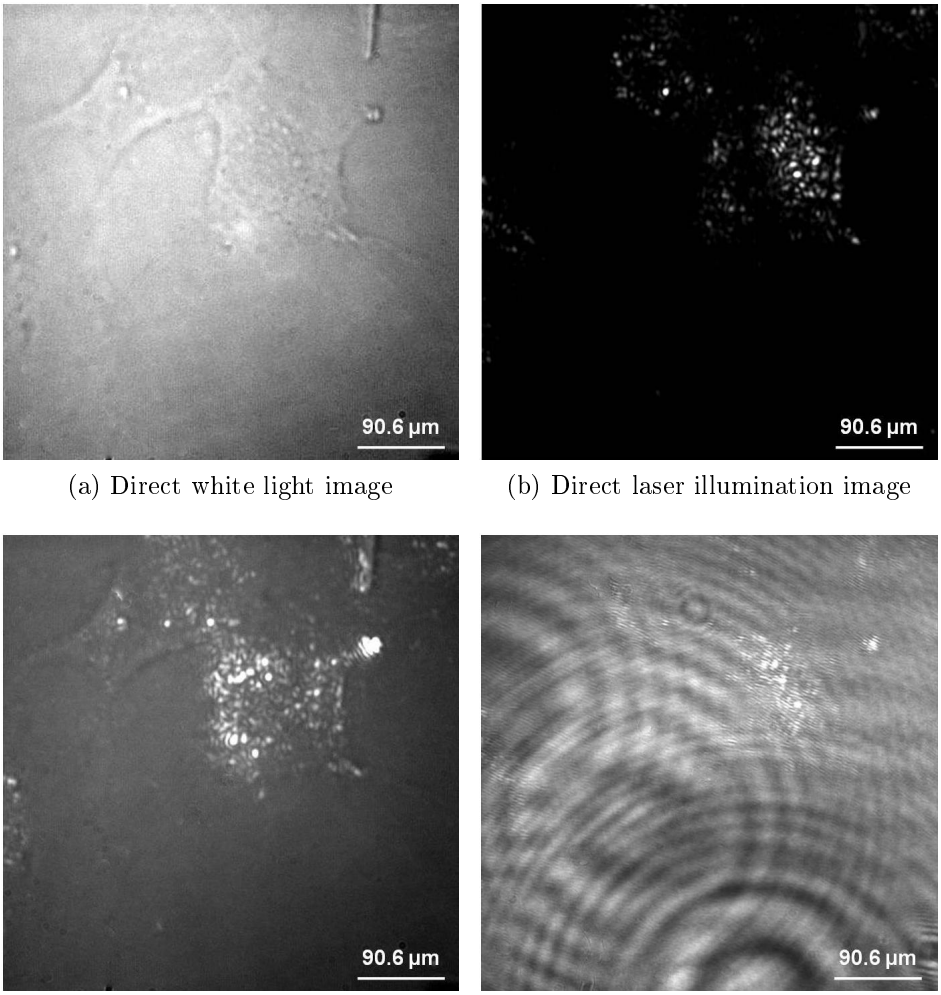

(a) Direct white light image

(b) Direct laser illumination image

(c) Direct white light and laser illumination image

(d) Hologram

Figure 6.12: Direct images of 3T3 fibroblasts labeled with several 40 nm Au Nps

region of the specimen that have been reconstructed for $n = 256$ and using $M = 32$ acquired frames. The display is made in a logarithmic color scale for the intensity $I = |E_{CCD}|^2$ were $5.9 \leq \ln I \leq 16.3$ Digital Counts (DC).

Because of the variation of the refractive index within the cells, the illumination light is diffracted yielding a speckle pattern that is superimposed with the particles' signal. This speckle is visible on Figure 6.13a, and, from the envelope of the speckled zone, one can assume the shape of the cells. We interpret the bright spots 1 and 2 of Figure 6.13a as being gold conjugates signals. However, bright spot 3 is considered as a hot spot and is basically related to a cellular structure and not to a gold conjugate. This assumption can be justified qualitatively and quantitatively.

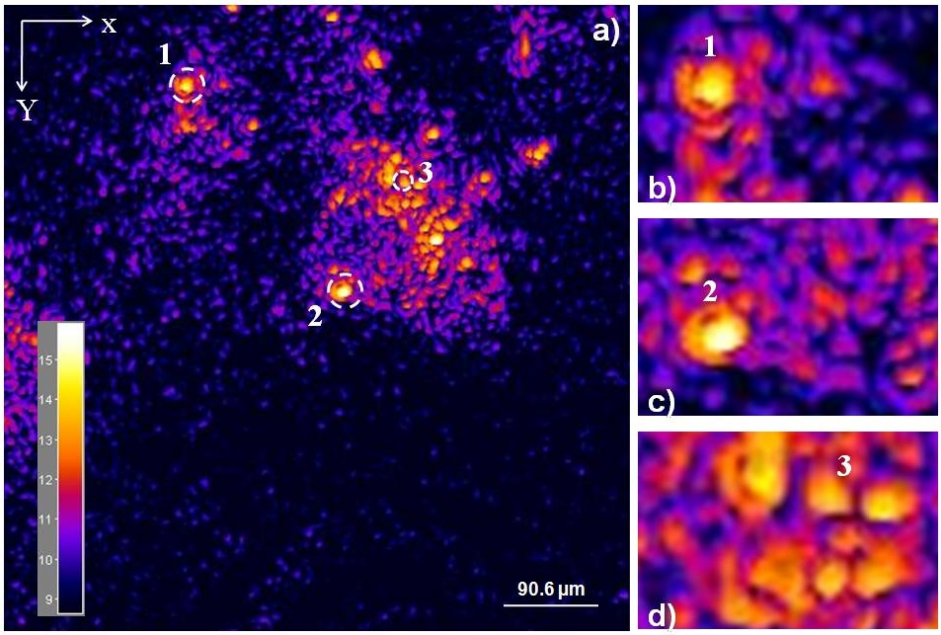

Figure 6.13: Reconstructed holographic intensity image of 3T3 cells labeled with several Au Nps

Qualitative Analysis

By comparing Figure 6.13a and Figure 6.13b which are 4X zooms of respectively spot 1 and 2 with Figure 6.13c which is a 4X zoom of spot 3. We can clearly see that spots 1 and 2 have a well defined bright circular shape that is consistent with the circular geometrical shape of colloidal particles. Nevertheless, the magnified image of spot 3 do not present any defined

consistent geometrical shape.

To better visualize the 40 nm gold particles, we have displayed, on Figure 6.14a, using the *Interactive 3D Surface Plot* plug-in of ImageJ software [Abramoff *et al.* 2004], a 3D linear surface plot of the region of the specimen that is displayed on Figure 6.13a. As seen, gold nanoparticles that correspond to sharp peaks can be easily visualized, but some ambiguity remains around the meaning of the lower peaks, which could be attributed either to particles, noises, or scattering by biological features of the cell.

Moreover, to illustrate the ability of our technique to localize the gold particle in 3D, we have reconstructed the full object field $E_{Sn}(x, y, z_{Sn})$ by reconstructing 512 different z_{Sn} planes for 512 different d'_n reconstruction distances. Then we have deduced the corresponding 512 intensity images $I_{Sn}(x, y, z_{Sn}) = |E_{Sn}(x, y, z_{Sn})|^2$ and we have displayed on Figure 6.14b a volume view of the $512 \times 512 \times 512$ reconstructed intensity image 3D data. The displayed 3D volume view was obtained using the *Volume Viewer* plug-in of ImageJ software.The bright light-bluish zones on the 3D volume image corresponds to the 40 nm gold particles signal

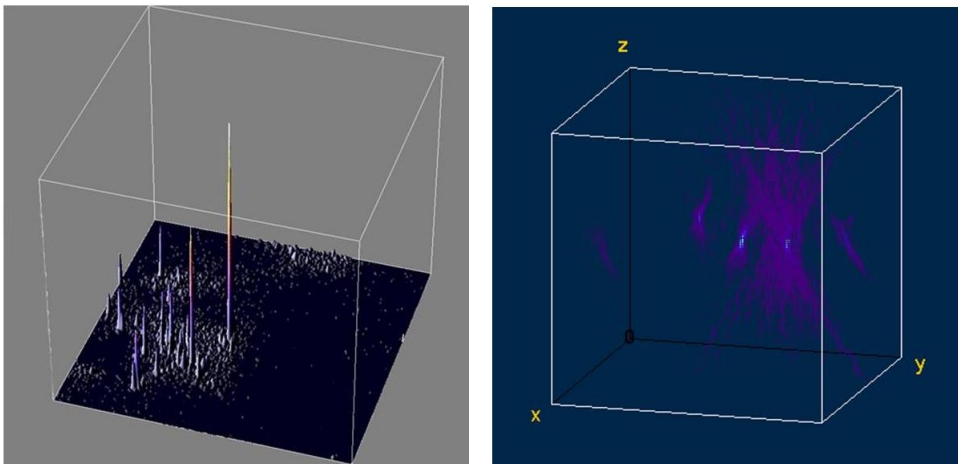

(a) 3D linear-scale surface plot of the reconstructed holographic intensity image of an unmarked 3T3 cell

(b) Volume view of the 3D reconstructed data

Figure 6.14: 3D visualizations of cells marked with several 40 nm Au Nps

Intensity and Cross Sections Analysis

In order to carry out a quantitative analysis of the data and provide thus a

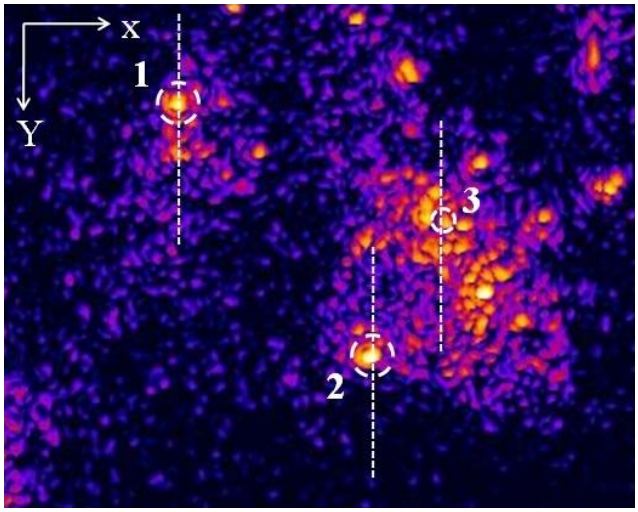

(a) x-sectioning on the reconstructed image

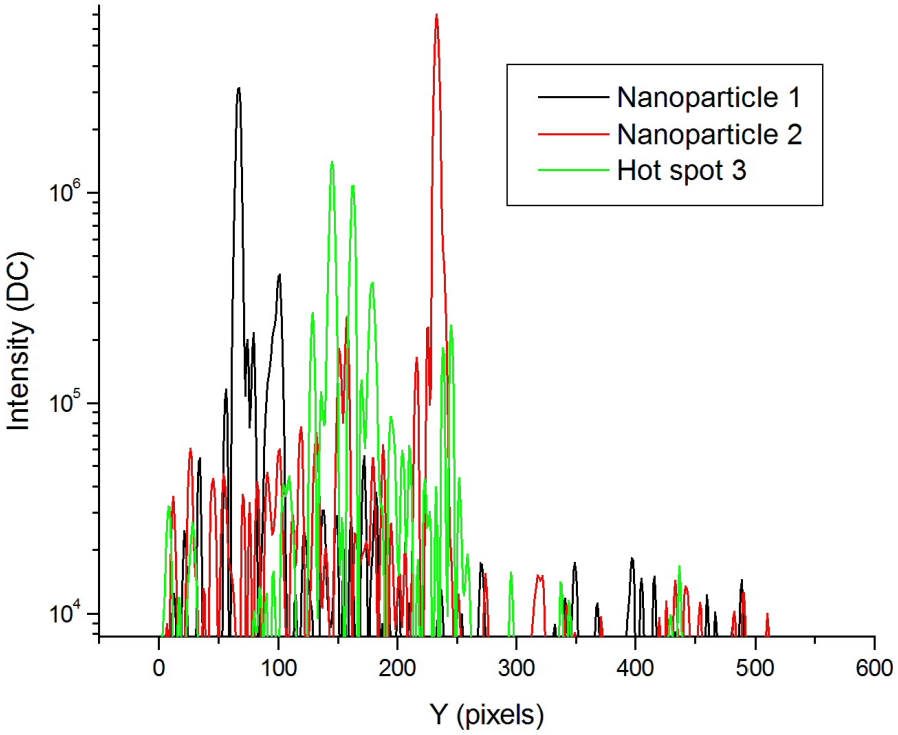

(b) Intensity cuts along x axis

Figure 6.15: Intensity cuts along x axis at positions of spots 1, 2 and 3 of the cells specimen marked with several Au Nps

quantitative argument of the presence of the gold nanoparticles, in addition to the previously described qualitative one, we have performed intensity cuts along the x axis at the positions of spots 1, 2 and 3 as illustrated on Figure 6.15a. The result of these cuts are displayed on the graph of Figure 6.15b. The black curve corresponds to nanoparticle 1, the red curve to nanoparticle 2 and the green curve to hot spot 3.

The following main outcomes can be pointed out from the observation of the graph of Figure 6.15b :

- We can clearly see that the scattering of the two gold nanoparticles, 1 and 2, is higher than the scattering of the considered hot spot 3.
- The scattering intensity of nanoparticle 2 is higher than the scattering intensity of nanoparticle 1, this can be explained by the following : since gold nanoparticles are attached the the integrine surface cellular receptors of the cells, their z-positions directly depends on the surface rugosity of the conjugate cell, thus all gold nanoparticles are not situated at the same z-position but are located at different depths. Accordingly, nanoparticle 1 and nanoparticle 2 are not situated at the same z-position, and thus the particle (which is here nanoparticle 2) that is located at exactly the same reconstruction plane of the considered reconstructed image is on focus on this image and gives thus a higher scattering intensity than the other particle that is not totaly on focus.
- Shapes and structures of the black and red curves, that corresponds to the nanoparticles, are very different from the shape and structure of the green curve that corresponds to the hot spot 3. Nanoparticles' curves present well defined peaks at the location of the corresponding particle, which is not at all the case for the hot spot's curve.
- Shapes and structures of the two nanoparticles' curves are very similar. This can lead to the conclusion that those two curves correspond to two objects of the same nature. This is another argument that proves that spot 1 and spot 2 corresponds well to gold nanoparticles' signals and not to cellular features.

For a better accuracy, we have carried out the same intensity cross sections but along the y axis as illustrated on Figure 6.16a. Results of these cuts are displayed on the graph of Figure 6.16b. The black curve corresponds to nanoparticle 1, the red curve to nanoparticle 2 and the green curve to hot spot 3. By observing the graph of Figure 6.16b, we can see that results are

perfectly consistent with the ones previously obtained for x intensity cuts.

Scattering Pattern's Shape Analysis

To go further, and to better characterize the Au particle's signal with respect to hot spots, we have analyzed the 3D images of the reconstructed object wavefield, obtained by performing the holographic reconstruction for the 512 different reconstruction distances, by performing cross sections in the attempt of exploring the shape of the different scattering patterns. For this purpose, we have used the Volume Viewer plug-in of ImageJ software who presents the functional ability of displaying cuts of 3D data cubes in arbitrary planes. Using this plug-in, we have performed cuts along the x axis to obtain reconstructed images in the (y, z) plane as illustrated schematically on Figure 6.17b.

Results of these cross sections are displayed on Figure 6.18.

Figure 6.18a shows the image of a cut made in the plane $x = 331$, that intersects the nanoparticle 1 of Figure 6.13a. The observed scattering pattern of particle 1 on the (y, z) cross image is presented as a bright straight pattern, located along the optical z axis with a limited extension.

Figure 6.18b shows the image of a cut made in the plane $x = 153$, that intersects the nanoparticle 2 of Figure 6.13a. The observed scattering pattern of particle 2 on the (y, z) cross image is also presented as a bright straight pattern, located along the optical z axis with a limited extension.

We can notice that, as expected, the nanoparticles' signals, on Figure 6.18a and Figure 6.18b are located at $z \simeq 256$ coordinate, which corresponds to the reconstruction plane of Figure 6.13a.

Figure 6.18c shows the image of a cut made in the plane $x = 281$, that intersects the hot spot 3 of Figure 6.13a. We can see that the cross images of nanoparticles 1 and 2 (Figure 6.18a and Figure 6.18b) have clearly outlined plainness planes and are quite different from this image (Figure 6.18c) where the plainness plane is ruffled.

We can see on Figure 6.13a that many bright points, other than the pointed ones (1, 2 and 3), are also visible on the reconstructed image, but it is not simple to determine, which spots correspond to gold nanoparticles, and which are speckle hot spots especially because several gold nanoparticles are conjugated to the cell thus bright spots are located in a close vicinity of each

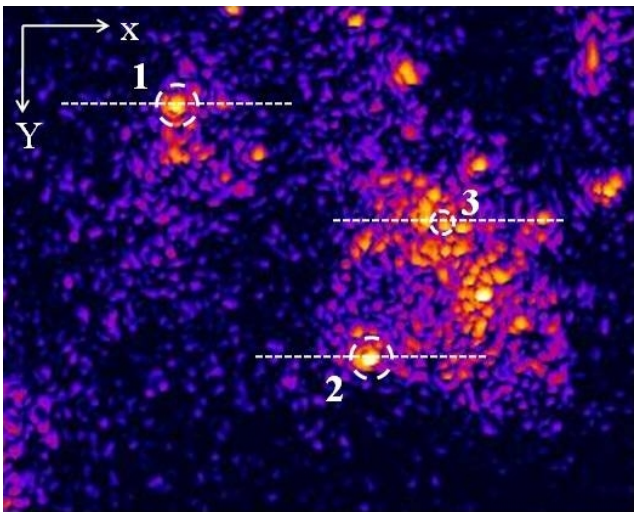

(a) y-sectioning on the reconstructed image

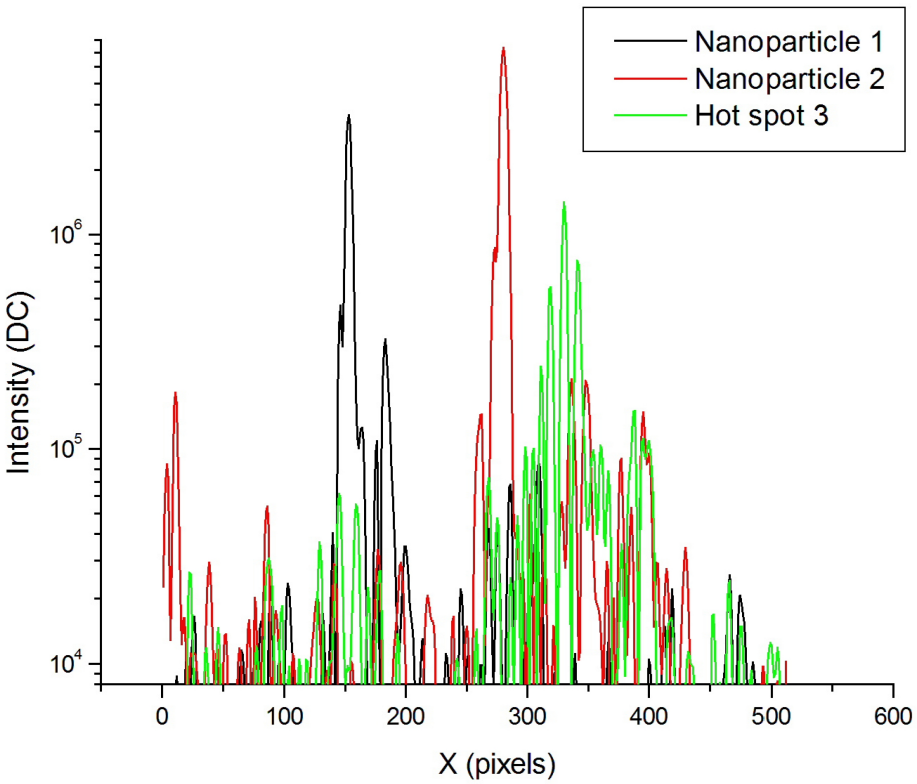

(b) Intensity cuts along y axis

Figure 6.16: Intensity cuts along y axis at positions of spots 1, 2 and 3 of the cells specimen marked with several Au Nps

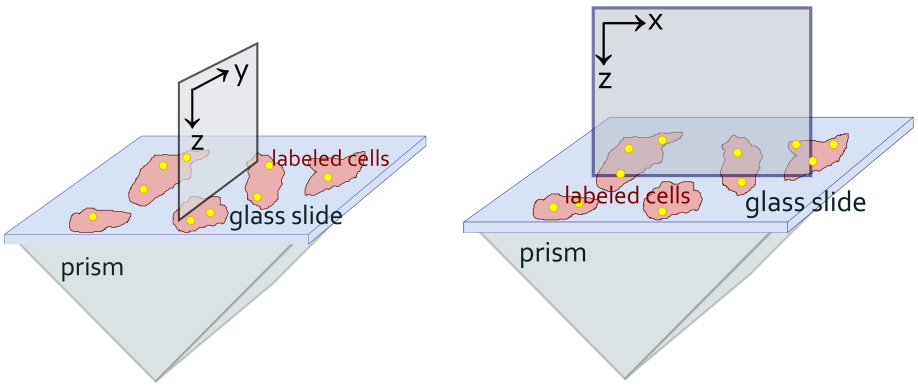

(a) (y,z) reconstruction plane (b) (x,z) reconstruction plane

Figure 6.17: Cross sections reconstruction planes of Au labeled cells

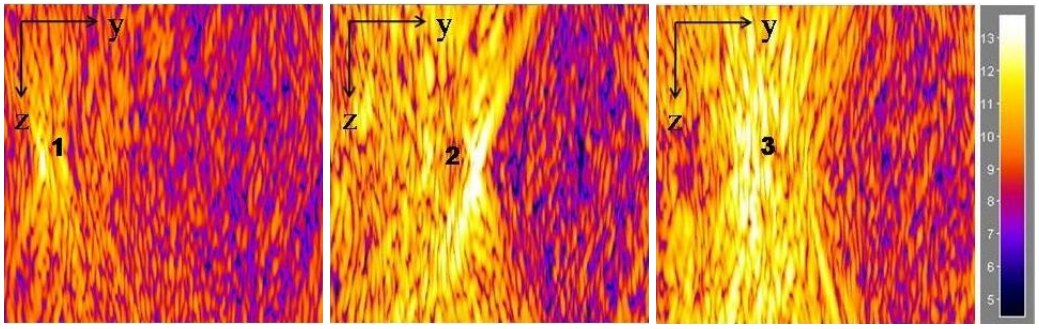

(a) (y,z) image of Np 1 (b) (y,z) image of Np 2 (c) (y,z) image of hot spot 3

Figure 6.18: Reconstructed images in the (y,z) plane obtained by performing a cut along x axis at the positions of the selected spots for the multi Au Nps marked 3T3 cell sample

other. Accordingly, we have chosen to work with a very low concentration of gold conjugates solution in order to be sure to have sufficiently few gold particles per cell to be able to discriminate easily the gold particles signal. Working at low concentration of gold conjugates allows also the interaction of few cellular receptors with the gold particle. Experimental investigations of a biological specimen with a single conjugated gold marker are presented in the next section (6.3.1.2).

6.3.1.2 3T3 cell labeled with a single gold particle

Volumes of gold solution and dilution buffers defined in Section 6.2.1.3 can be experimentally adjusted in order to get the desired concentration of the gold solution. Thus, in order to achieve a very low concentration of the gold conjugates solution in the goal of labeling a single cell with a single gold nanoparticle, we have sufficiently diluted the gold solution that is used for the conjugation.

Temporal resolution of an imaging system is an important issue, thus, it is important to minimize the total acquisition time of the holographic experiment. Hence, rather than manipulating using a sequence of $M = 32$ holograms, we have reconstructed 3D images of the sample using a single acquired CCD frame. We will see that this is sufficient for the localization of the gold marker on the living cell, but the Signal to Noise Ratio and the visibility of the marker are improved when the reconstruction is performed using the whole acquired sequence of 32 frames.

Reconstruction using a single acquired hologram

Figure 6.19a shows a direct image of the specimen, which is a 3T3 cell tagged with a single 40 nm gold particle, under white light illumination. While the cell is well defined on the left hand side of the image, the attached gold particle cannot be seen on this image.

Figure 6.19b is a direct image of the same region of the specimen, but obtained by illuminating the cells with the object laser beam and turning on the tungsten lamp. The reference beam is blocked for this image.

Figure 6.19c is a direct captured hologram.

Figure 6.19c shows the reconstructed holographic intensity image of the sample in a colored logarithmic scale ($6 < \ln(I) < 15$). The reconstruction

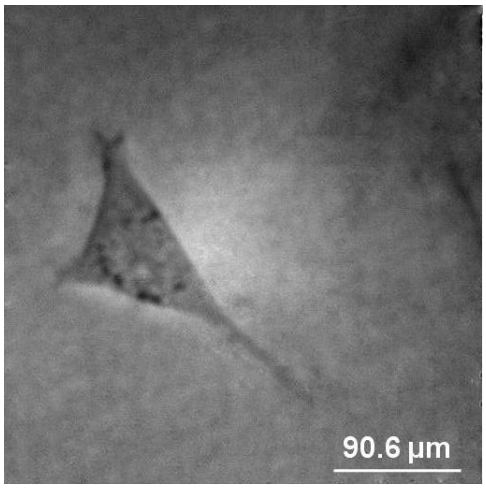

(a) Direct image under white light illumination

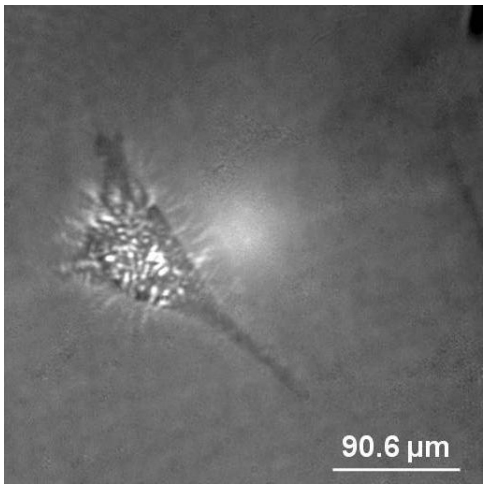

(b) Direct image under white light and Laser illumination

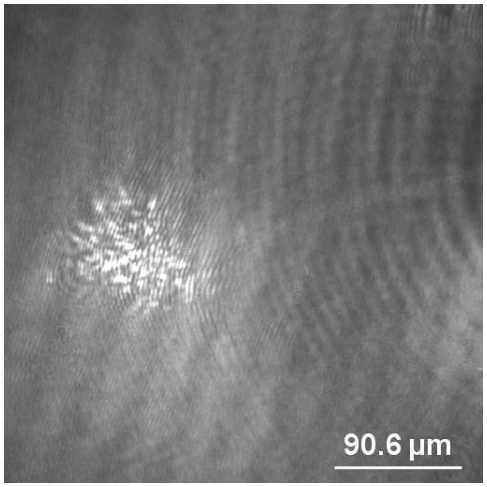

(c) Hologram

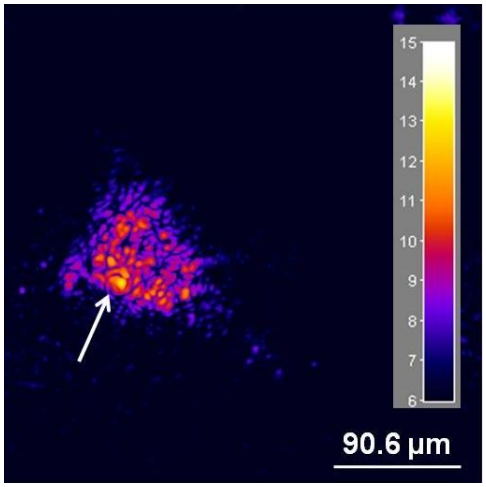

(d) Single frame reconstructed holographic intensity I image

Figure 6.19: Fibroblast cell tagged with a single 40 nm gold particle

is done using 1 CCD frame ($M = 1$) with an exposure time of 100 ms. The displayed reconstructed image is the plane where the brightest point is detected and is obtained for for $n = 325$. This means that this plane is situated at 12.2 μm above the conjugate image plane z_I.

The total reconstruction distance is thus : $z_{S325} = z_I + 12.2\ \mu$m.

The red and blue triangular structure with a few speckle yellow high spots, which correspond to the cell location on Figure 6.19a, is the holographic signal generated by the cell refractive index inhomogeneities, which scatter light. The gold particle corresponds to the brightest spot in Figure 6.19d. It is located on the left bottom of the cell, and marked with a white arrow.

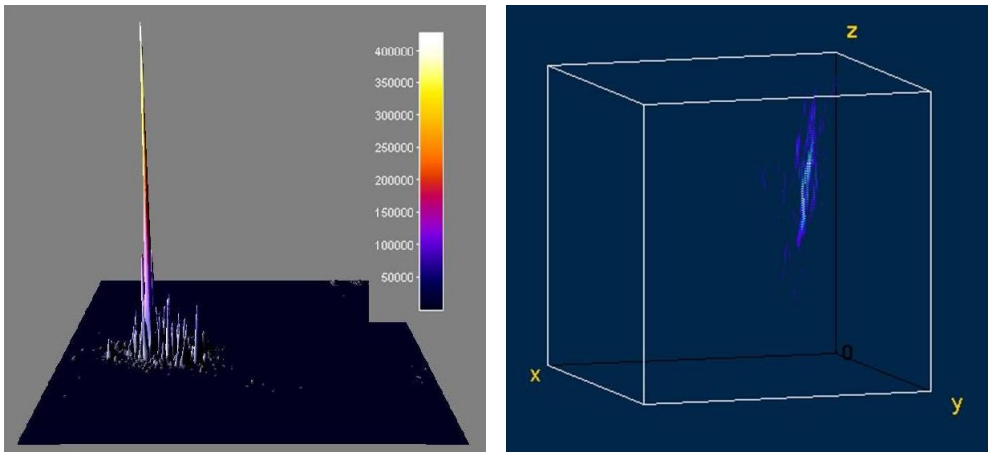

(a) 3D linear-scale surface plot of the intensity image reconstructed from a single frame.

(b) Volume view of the 3D reconstructed data

Figure 6.20: A fibroblast cell tagged with a 40 nm gold particle using 1 frame acquisition

To better visualize the 40 nm gold particle, we have displayed, on Figure 6.20a, a 3D linear surface plot of the corresponding logarithmic scale colored image of Figure 6.19d. As it can be seen, the gold particle signal is much higher than the signal generated by the cell refractive index inhomogeneities. The particle can thus be easily located.

Furthermore, and similarly to what we have done in the previous section where a specimen labeled with multiple nanoparticles was investigated, we have reconstructed the full object field $E_{Sn}(x, y, z_{Sn})$ by reconstructing

512 different z_{Sn} planes of the specimen for 512 different d'_n reconstruction distances and we have displayed on Figure 6.20b a volume view of the $512 \times 512 \times 512$ reconstructed intensity image 3D data in order to illustrate the ability of our technique to localize the gold particle in 3D. The bright light-bluish zone on the 3D image corresponds to the 40 nm gold particle signal. This wavefield has the shape of a cigar roughly oriented along the microscope objective axis (z axis).

To perform a quantitative analysis of the precision we expect in the 3D localization of the gold particle, we have considered the 3D volume intensity image of Figure 6.20b, and we have made cuts along the 3 axes (x, y and z) at the gold particle crossing point (i.e. where the three axis cross the highest intensity voxel of the 3D image). The intensity signals I along the 3 axes are plotted on Figure 6.21. Curves 1 (red), 2 (blue) and 3 (green) correspond to cross section along the x, y and z axis respectively. The horizontal dashed line indicates the half maximum of the curves.

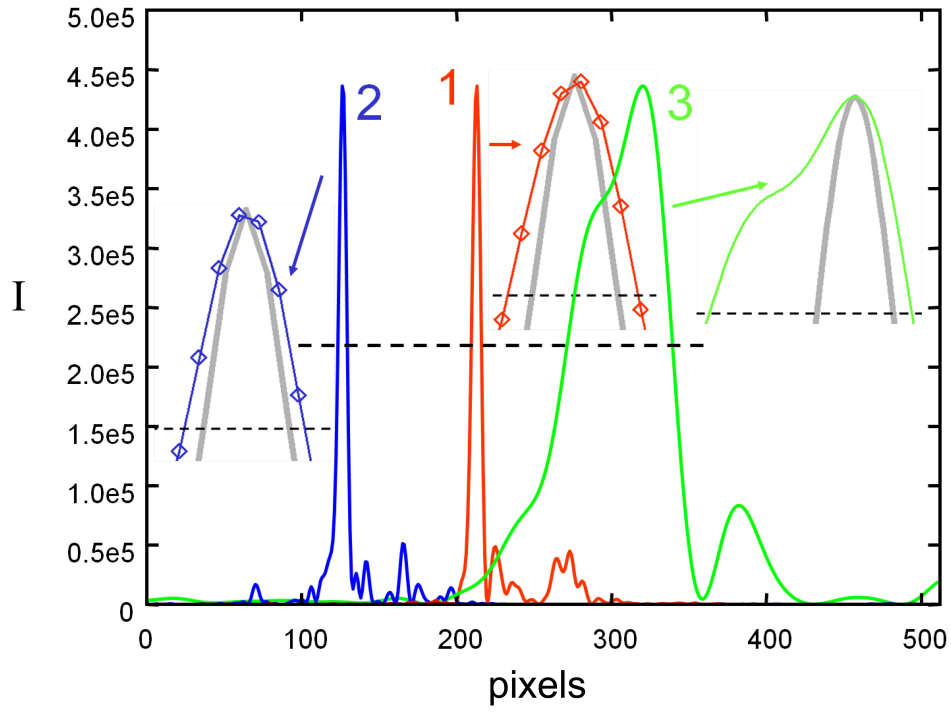

Figure 6.21: Experimental linear-scale plot of cuts made within the intensity signal I along the three axis x, y and z at the brightest voxel of Figure 6.20b corresponding to the gold nanoparticle location.

In order to measure the curves' widths, we have displayed zooms of the curves from maximum to half maximum. The individual pixels are visible on the zooms of curves 1 and 2 (cross section along the x and y axis). The Full Width at Half Maximum (FWHM) is about 6 pixels in the x and y directions ($6 \times 177 = 1060$ nm), and about 60 pixels in the z direction (10.6 μm).

To compare the resolution obtained here with the one expected from the NA of the microscope objective, we have computed the wavefield $E_I(x, y, z)$ that is expected in the ideal case for a 0.5 NA microscope objective, and we have made cuts along x, y and z directions of the $512 \times 512 \times 512$ ideal cube of data for $|E_I(x, y, z)|^2$. The corresponding theoretical cuts are plotted on Figure 6.21 with the zooms in heavy grey line. Similarly to the experimental cross section cuts, the horizontal axis, for the theoretical curves, displays the pixels' index. In the x and y directions, the obtained FWHM is close to the expected one. Yet, in the z direction the shape of the curve is not symmetric, and the measured FWHM is about 3 times larger than the expected FWHM in the ideal case. This is due to the holographic signal generated by the light scattered by the cell's structures, which adds to the nanoparticle signal.

Using a parabolic approximation for the local field, the location of the gold particle can be calculated by fitting the data points that are above half maximum with a parabola, and by considering that the particle is located on the parabola maximum.

The accuracy of the measurement obtained using this fitting method is ± 5 nm in the x and y directions (uncertainty given by the fit software Gnuplot). It corresponds also to the variation of the particle when the number of data points used for the fit is increased from 8 to 7. In the z direction, the measured curve is not perfectly symmetric, so the fit technique is not very accurate because the result of the fit strongly depends on the data points that are used in the calculation.

Reconstruction using 32 acquired holograms

In order to visualize the gold particle with a better Signal to Noise Ratio (SNR), we have also reconstructed the holographic images using a sequence of $M = 32$ acquired CCD frames. In this case, the total exposure time is 32×100 ms=3.2 s, while the measurement time is $32/f_{CCD} = 4$ s.

Figure 6.22a is the 32 frames reconstructed holographic intensity image of the sample in a colored logarithmic scale. The cell scattered signal, corresponding

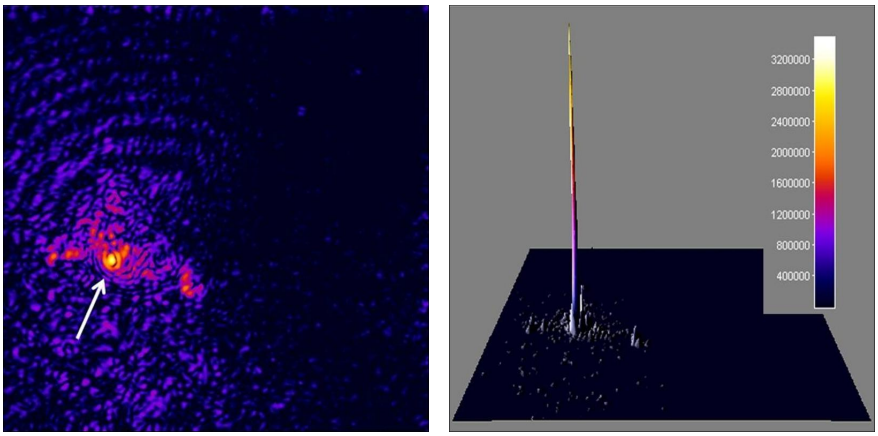

(a) 32 frames reconstructed holographic intensity I image

(b) 3D linear-scale surface plot of the 32 frames reconstructed holographic intensity image

Figure 6.22: A fibroblast cell tagged with a 40 nm gold particle using 32 frames acquisition

to the triangular bluish and reddish structure, is still visible. The particle signal in yellow is visible too (it is marked with a white arrow), but with a much better contrast than in Figure 6.19d.

Figure 6.22b shows the 3D linear surface plot of the reconstructed intensity image of Figure 6.22a. Here again, not only the gold particle signal is much higher than the light scattered by the cell, but the ratio of the particle's signal versus the light scattered by the cell is increased with respect to the ratio obtained for Figure 6.20a, and the visibility of the gold particle is improved. Indeed, we have observed that the light scattered by the live cell's refractive index inhomogeneities decorrelates faster than that of the gold particle. Therefore, the relative weight of the cell scattered signal is lower when averaging over 32 than over a single frame. Hence, when coherent holographic detection is performed using 32 images, the relative contribution of the light scattered by the cell to the total signal decreases and thus better z-resolution is obtained.

Similarly with the analysis presented in the previous part where a specimen of 3T3 cells labeled with several gold nanoparticles was considered, and in order to present a more detailed qualitative analysis of the obtained reconstructed images, we have pointed a hot spot on the reconstructed image of Figure 6.22a. As illustrated on Figure 6.23, this pointed hot spot is marked as spot 2 and the single nanoparticle is marked as spot1.

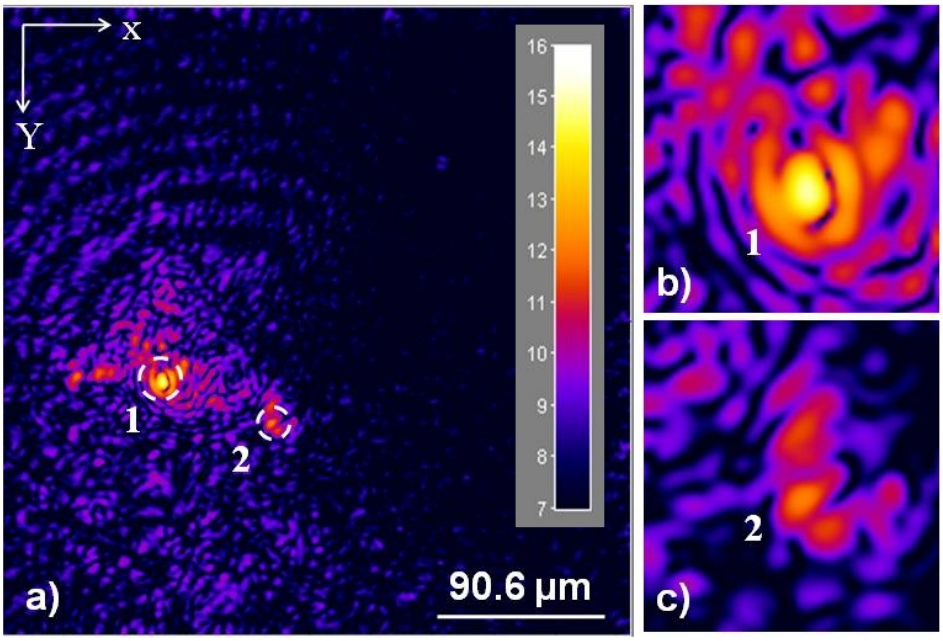

Figure 6.23: 32 frames reconstructed holographic intensity image of a 3T3 cell labeled with a single Au Np

By comparing Figure 6.23a and Figure 6.23b which are 4X zooms of respectively nanoparticle 1 and hot spot 2, we can clearly see that, similarly to Figure 6.13, spot 1 have a well defined bright circular shape that is consistent with the geometrical shape of colloidal particles. Nevertheless, the magnified image of spot 2do not present any defined consistent geometrical shape.

Figure 6.24 shows the cuts made along the 3 axes (x, y and z) obtained for the 32 frames reconstructed data. Here again, we have displayed zooms of the three cross sections from maxima to half maxima as well as zooms of the theoretical curves. These cross sections are similar to the cross sections obtained in the case of 1 frame acquisition, but in this case (32 frames) the heavy grey lines corresponding to the theoretical zoomed curves fits better with the experimental curves. In particular, in the z direction, the experimental curve is now in agreement with the theoretical one, because the relative weight of the cell-scattered signal is now lower, as seen by comparing Figure 6.22b with Figure 6.20a.

Here again, the location of the particle can be calculated by fitting the measured data point with a parabola. The accuracy is still ± 5 nm in the x

and y directions, but since the curve 3 is now roughly symmetric, the fit can also be performed in the z direction, and the particle can be located with an accuracy estimated to ±100 nm in the z direction.

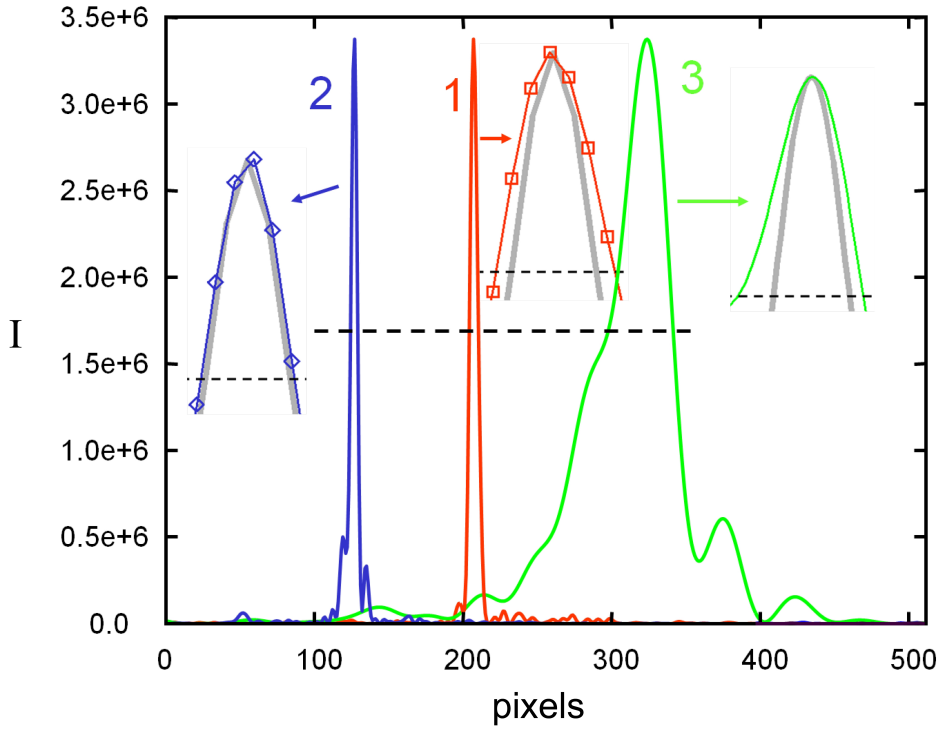

Figure 6.24: Experimental linear plot of cuts made within the intensity signal I along the three axis x, y and z at the brightest voxel of Figure 6.22a corresponding to the gold nanoparticle location

To go further, and to better compare the particle signal with respect to the light scattered by the cell, we plotted the intensity signal along x axis (which corresponds to curve 1 of Figure 6.24) in logarithmic scale on Figure 6.25. As seen, the particle' signal is 2 to 3 orders of magnitude larger than the cell scattered signal.

We plotted also (black curve 4 on Figure 6.25) the background signal obtained without illuminating the sample. This background corresponds to the ultimate sensitivity limit of the holographic detection [Atlan & Gross 2007], i.e. to the shot noise on the local oscillator beam. As seen, the shot noise background is about 100 times lower than the cell-scattered signal

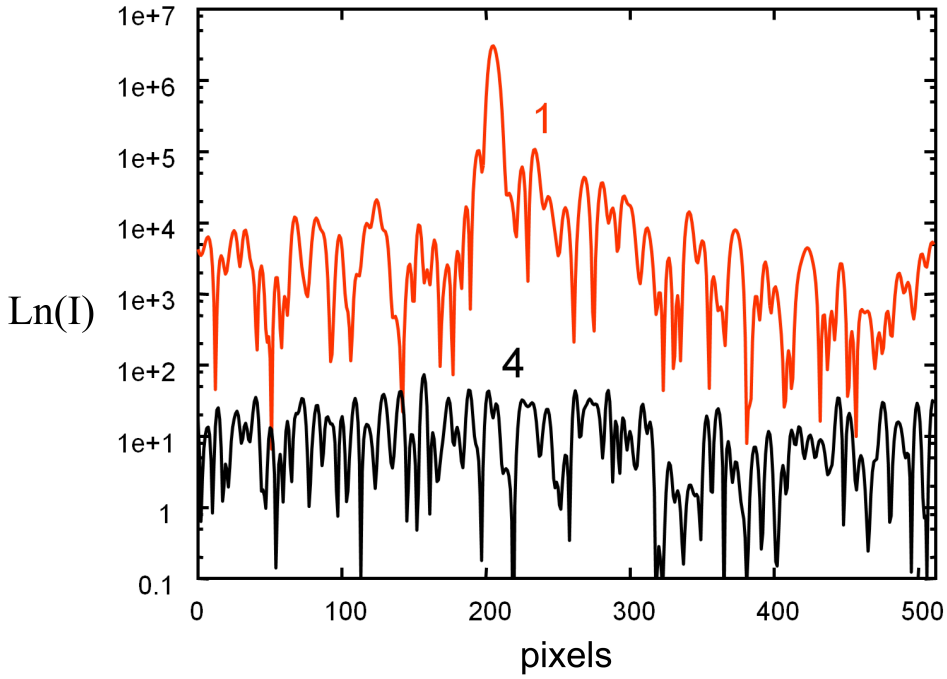

Figure 6.25: Intensity plot of the cut along the x axis in logarithmic scale : (1) at the nanoparticle location and (4) without illuminating the sample

Scattering Pattern's Shape Analysis

Here again, we we have performed cuts along the x axis to obtain reconstructed images in the (y, z) plane as illustrated schematically on Figure 6.17.

Results of these cross sections are displayed on Figure 6.26.

Figure 6.26a shows the image of a cut made in the plane $x = 128$, that intersects the nanoparticle 1 of Figure 6.23a. The observed scattering pattern of particle 1 on the (y, z) cross image, is presented as a well defined bright straight pattern, located, with a limited extension, along the optical z axis. The comparison of the scattering pattern of nanoparticle 1 of this specimen (Figure 6.26a) with those of nanoparticles 1 and 2 of the previous biological specimen (Figure 6.18a and Figure 6.18b) shows that the three patterns are similar and have a comparable structure.

Figure 6.26b shows the image of a cut made in the plane $x = 221$, that intersects the hot spot 2 of Figure 6.23a. Contrarily to the cross image of nanoparticle 1, the hot spot 2 scattering pattern's extension along the vertical

x axis is quite large. Moreover, the scattering pattern of the hot spot is angularly tilted in the (y, z) plane.
This introduced angular tilt effect can be simply interpreted by describing how the light propagation is governed in biological cells. Full details are provided in 2, we will review here some notions that are necessary for the analysis of the scattering images.

This propagation is dependant on the phase function inside the illuminated cell. Because biological tissues are inhomogeneous, the form of their phase function is not well defined and is thus characterized by the anisotropy coefficient g, which is the average cosine of the phase function. This parameter g describe the asymmetry of the single scattering pattern ; it is thus null when the scattering is isotropic, equals 1 for forward scattering and equals -1 in the case of backward scattering. In our experiments, the illuminated cells are maintained in DMEM medium that consists mainly of water. Since the refractive index of cells is close to that of water, the cell anisotropy factor g_{cell} is close to one ($g_{cell} \simeq 0.9$ in biological tissues as mentioned by [Cheong *et al.* 1990]). As a consequence, the light scattered by the cells mainly follows the forward scattering regime and the observed light scattering pattern appears to be tilted by approximately 45° since the incident illumination laser beam is initially tilted by approximately 45° in conformity with the TIR illumination geometry (see Figure6.10). In other words, the hot spot scattering signal keeps some memory of the illumination direction, and is thus angularly tilted in the (y, z) plane.

For a gold particle, the average cosine of the scattering phase function g_{Au} in water can be determined by Mie scattering calculations using the experimental parameters : the wavelength ($\lambda = 785$ nm), the particle diameter (40 nm), the complex refractive index of gold ($\tilde{n}_{Au} = 0.18 - i\,4.96$ at 785 nm) and the refractive index of water ($n_w = 1.33$). $\tilde{n}_{au}$ is determined from the graphs of Chapter 2. The obtained anisotropy factor is nearly null $g_{Au} < 10^{-3}$ (see `http://omlc.ogi.edu/calc/mie_calc.html`). This means that the gold particle scatters light isotropically. Consequently, no angular tilt effect are observed on the scattering patters of gold nanoparticles as observed in the cross sections images of Figure 6.18a and Figure 6.18b. The angular tilt was not observed on the cross section image of Figure 6.18c possibly because of the presence of several gold nanoparticles on the membrane of the considered cell that introduce several high interfering signals and will thus affect the clear detection of every single signal.
It should be pointed out that a similar angular tilt effect has been observed recently on the photothermal signal of 50 nm and 10 nm gold particles by

[Absil *et al.* 2010].

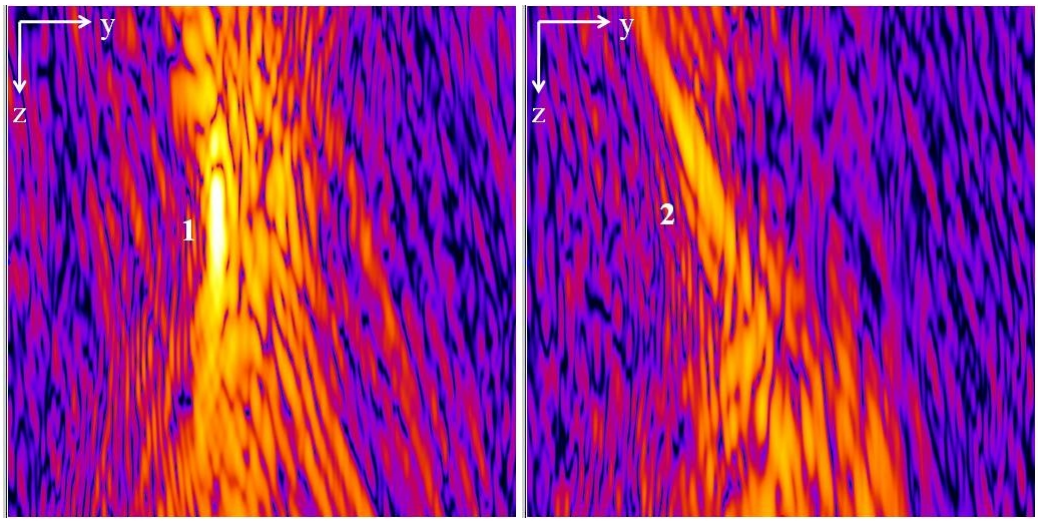

(a) (y,z) image of Np 1 (b) (y,z) image of hot spot 2

Figure 6.26: Reconstructed images in the (y,z) plane obtained by performing a cut along x axis at the positions of the selected spots for the single Au Np marked 3T3 cell sample

6.3.2 Unlabeled 3T3 Cell

Specimens of unlabeled 3T3 cells were prepared exactly as described in Section 6.2.1, but, obviously, no gold solution was added to the culture dishes.

The direct white light image of the considered unlabeled cell is shown on Figure 6.27a and a direct image obtained under white light and laser illumination is shown on Figure 6.27b.

Figure 6.28a displays the reconstructed holographic intensity image that shows the light scattered by the cellular features due to inhomogeneities of the corresponding refractive index. This scattered light, which has a speckle structure, exhibits several hot spots that correspond to bright spots on Figure 6.28a. Reconstruction is performed using $M = 32$ frames with exposure time of 100 ms per frame and the displayed reconstructed image is obtained for $n = 252$ and is specifically chosen because at this plane the maximum of the brightest spot is reached (5.85×10^5 DC). The reconstructed image is displayed on a color logarithmic scale ($5.80 \leq \ln I \leq 13.28$ DC). The

maximum intensity of the brightest hot spot of this specimen is much lower than the maximum intensities of the brightest spots of the labeled specimens that corresponds, indeed, to gold nanoparticles.

We have displayed on Figure 6.29 3D visualizations of the unlabeled cell. The 3D linear surface plot, shown on Figure 6.29a, does not provide any relevant information because the background noise is high. In fact, since this imaged specimen is unlabeled, no relevant high signals are detected and the background noise, consequently, visually appears higher than the one observed for labeled specimens. A volume view of the full $512 \times 512 \times 512$ reconstructed intensity 3D is shown on Figure 6.29b.

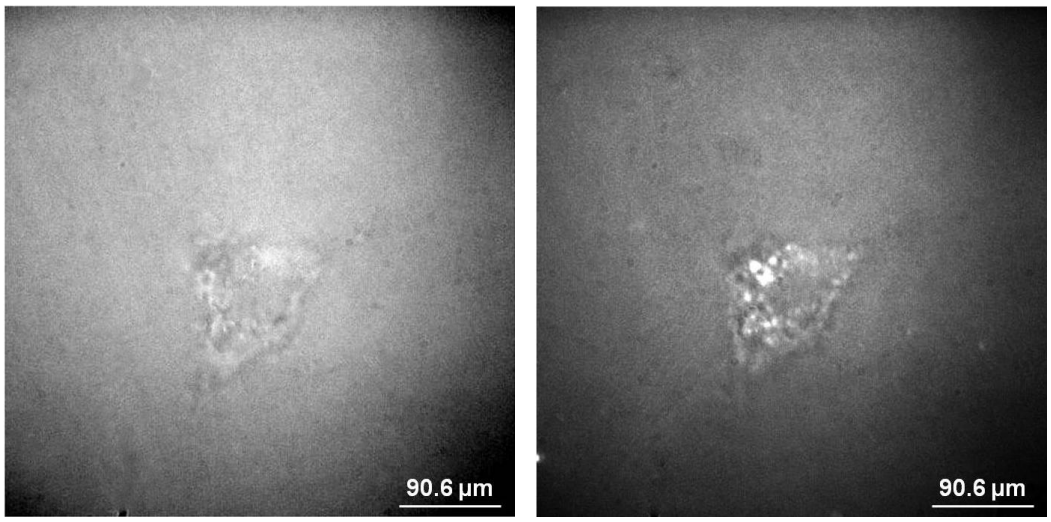

(a) Direct white light image

(b) Direct white light and laser illumination image

Figure 6.27: Direct images of an unmarked 3T3 fibroblast

The two brightest hot spots (hot spots 1 and 2) of Figure 6.28a were selected and their corresponding 4X zooms are respectively displayed on Figure 6.28b and Figure 6.28c. As observed, shapes of the magnified images of these pointed objects are not circular and do not have a defined geometrical shape. Their apparent shape clashes with the circular shape of nanoparticles 1 and 2 of the first biological specimen and nanoparticle 1 of the second biological sample, and resembles more to hot spot 3 of the first bilogical specimen and hot spot 2 of the second bilogical specimen.

Scattering Pattern's Shape Analysis

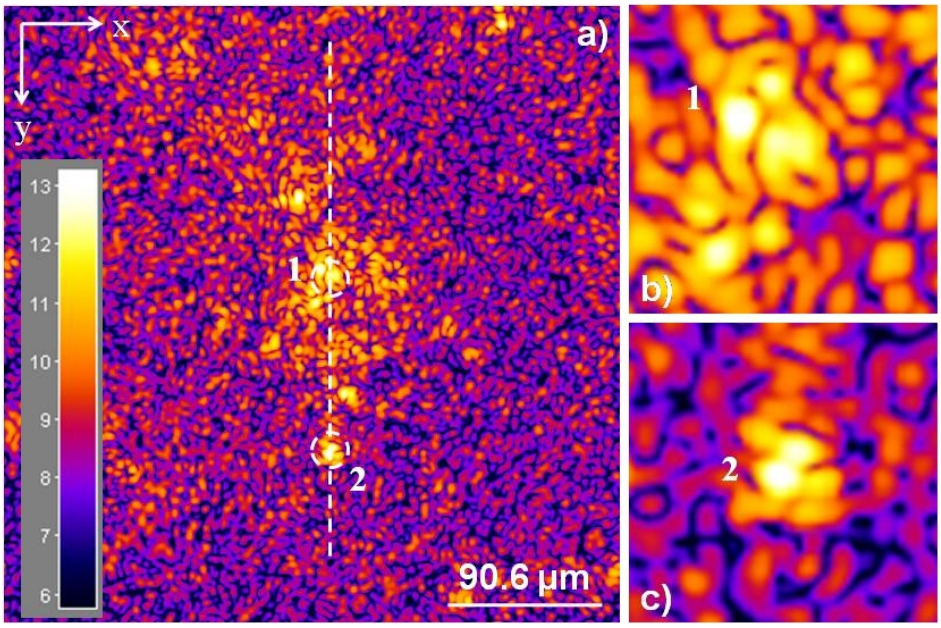

Figure 6.28: Reconstructed holographic intensity image of an unmarked 3T3 cell

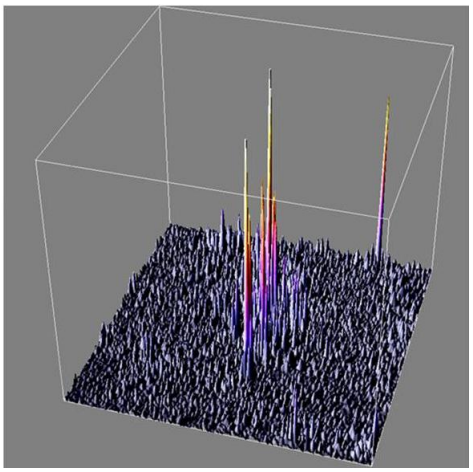

(a) 3D linear-scale surface plot of the reconstructed holographic intensity image of an unmarked 3T3 cell

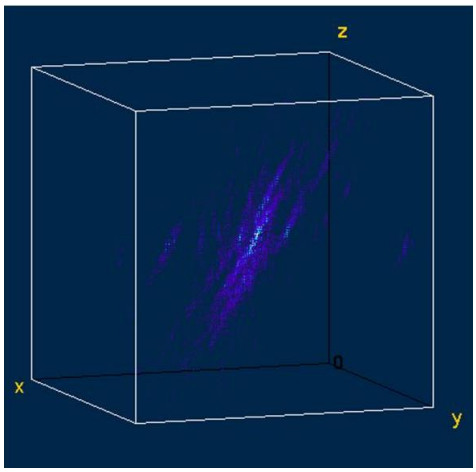

(b) Volume view of the 3D reconstructed data

Figure 6.29: 3D visualizations of an unlabeled fibroblast cell

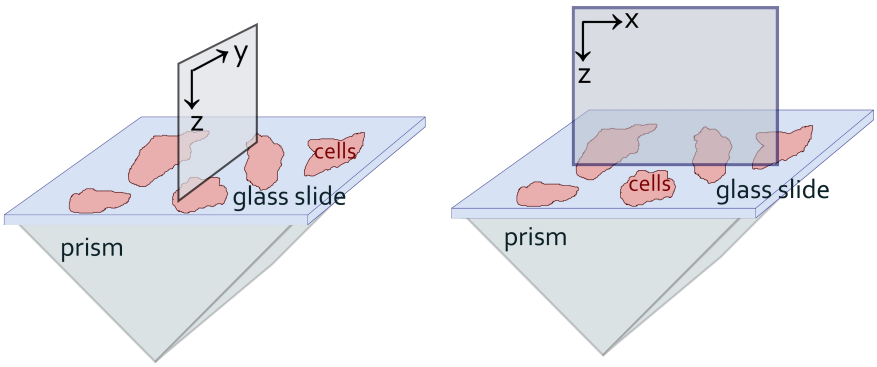

(a) (y,z) reconstruction plane (b) (x,z) reconstruction plane

Figure 6.30: Cross sections reconstruction planes of an unmarked 3T3 cell

This investigated specimen consists of an unlabeled cell. Bright spots on the reconstructed image Figure 6.28 are interpreted as hot spots that corresponds to cellular features and structures. Hence, corresponding scattering patterns on the (y, z) cross sections should appear angularly tilted similarly to Figure 6.26b. The obtained experimental images shows that this supposition is true, indeed.

We have performed a cut along the x axis to obtain the reconstructed image in the (y, z) plane as illustrated schematically on Figure 6.30b. Results of this cross section is displayed on Figure 6.31 that shows the (y, z) image obtained by performing a cut in the plane $x = 271$ that intersects the two bright hot spots (spots 1 and 2) of the investigated unlabeled sample. Images of hot spot 1 and hot spot 2 are obtained on the same (y, z) image because both spots are located on the same $x = 271$ plane. The observed (y, z) image is qualitatively different from (y, z) images of nanoparticles 1 and 2 of the multi labeled sample (Figure 6.18a and Figure 6.18b) and from the (y, z) image of nanoparticle 1 of the single nanoparticle labeled sample (Figure 6.26a). However, the signal is angularly tilted as in the (y, z) image of hot spot 2 of the single nanoparticle labeled sample (Figure 6.26b) and its extension in the vertical z direction is also large.

6.3.3 Free Gold Nanoparticles

Images of Figure 6.32 are obtained for a sample of free 40 nm gold particles (uncoupled to cells) in Brownian motion in a water and agarose suspension.

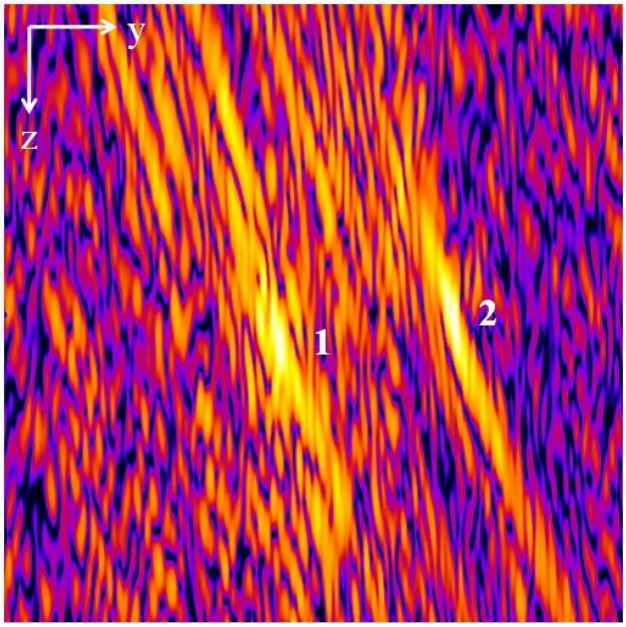

Figure 6.31: Reconstructed images in the (y,z) plane obtained by performing a cut along x axis at the positions of the selected spots for the unmarked 3T3 cell sample

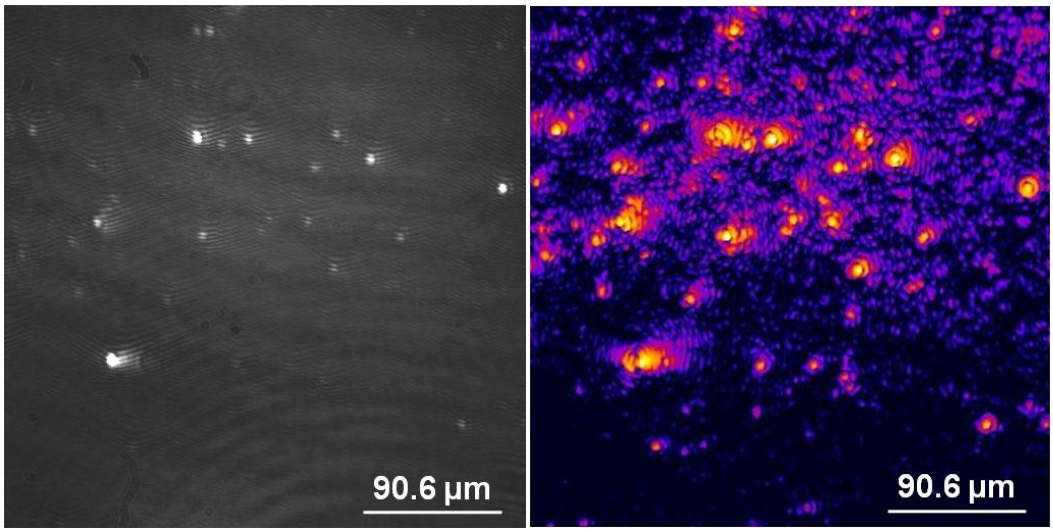

(a) Hologram of free 40 nm gold nanoparticles (b) Reconstructed image

Figure 6.32: Images of free 40 nm gold nanoparticles

Here, we used agarose to slow down the motion of the particles enough to make the displacement of the particles negligible during the time of acquisition of the sequence of $M = 32$ frames.
The free gold specimen is mounted in an observation that is quite similar to the one used for manipulating biological specimens.

Figure 6.32a is a direct captured hologram and Figure 6.32b shows the reconstructed holographic intensity image of the sample in a colored logarithmic scale. The reconstruction is done using 32 CCD frame ($M = 32$) with an exposure time of 100 ms per frame. The displayed reconstructed image is the plane where the brightest point is detected and is obtained for $n = 251$. Brightest points correspond to particles that are located within the reconstruction plane, while points of lower brightness are out of focus particles.

Qualitative Analysis

Similarly to what we have done in the previous sections, we have displayed on Figure 6.33a the reconstructed holographic intensity image (Figure 6.32b) in more details. Three bright spots (1, 2 and 3), that are assumed to be gold nanoparticles, were pointed and their corresponding 4X zooms are respectively displayed on Figure 6.33b, Figure 6.33c and Figure 6.33d.

These magnified images of the selected bright spots have well defined bright circular shape that is consistent with the geometrical shape of colloidal particles. Moreover, they are quite similar to the images of nanoparticles 1 and 2 of the first biological specimen and to nanoparticle 1 of the second biological sample. Yet, their shape differ largely from hot spot 3 of the first bilogical specimen, hot spot 2 of the second bilogical specimen and hot spots 1 and 2 of the third unmarked biological specimen.

To better visualize the 40 nm gold particles, we have displayed, on Figure 6.34, a 3D linear surface plot of the region of the specimen that is displayed on Figure 6.33a. As seen, gold nanoparticles correspond to sharp peaks and can be easily visualized. The intensity variations between the several observed gold particles is due to the different depth positions of these particles in the agarose suspension.

Intensity and Cross Sections Analysis

For a complete analysis we have performed intensity cuts along the x axis and the y axis at the positions of spots 1, 2 and 3 as illustrated respectively

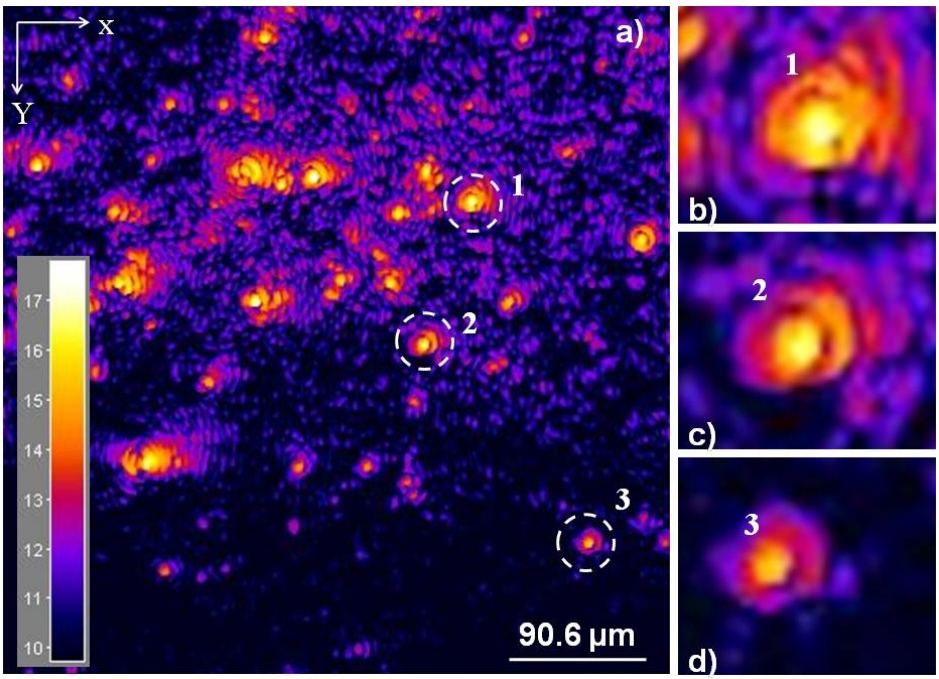

Figure 6.33: Reconstructed holographic intensity image of free 40 nm gold nanoparticles

on Figure 6.35a and Figure 6.36a. Results of these cuts are displayed on respectively on the graphs of Figure 6.35b and Figure 6.36b. Black color corresponds to nanoparticle 1, red color to nanoparticle 2 and green color to hot nanoparticle 3.
It is clearly seen on Figure 6.35b and Figure 6.36b that the curves are very similar : they have the same shape and sharp peaky structure at the corresponding pixel location of the considered nanoparticle. Additionally, the curves largely resembles the curves obtained on the assumed nanoparticles of the first considered biological specimen (Figure 6.15b and Figure 6.15b) and of the second biological specimen (Figure 6.25). Furthermore, the scattering intensities of these free gold nanoparticle have approximately the same order of magnitude as the scattering intensities obtained from the assumed gold nanoparticles of the two labeled biological specimens and are much higher than the scattering intensities of the hot spots of the all three biological specimens (the two labeled and the unlabeled specimens).

Scattering Pattern's Shape Analysis

This investigated specimen consists of free gold nanoparticles which scatters

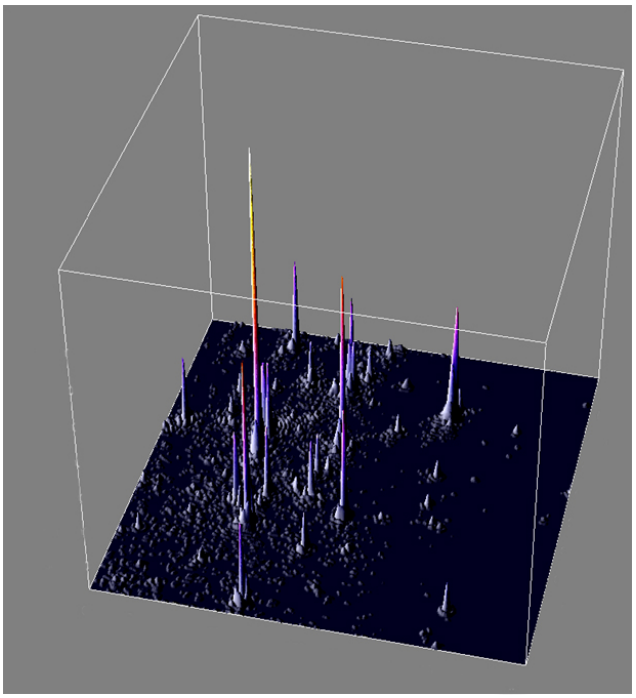

Figure 6.34: 3D linear-scale surface plot of the reconstructed holographic intensity image of free 40 nm gold nanoparticles

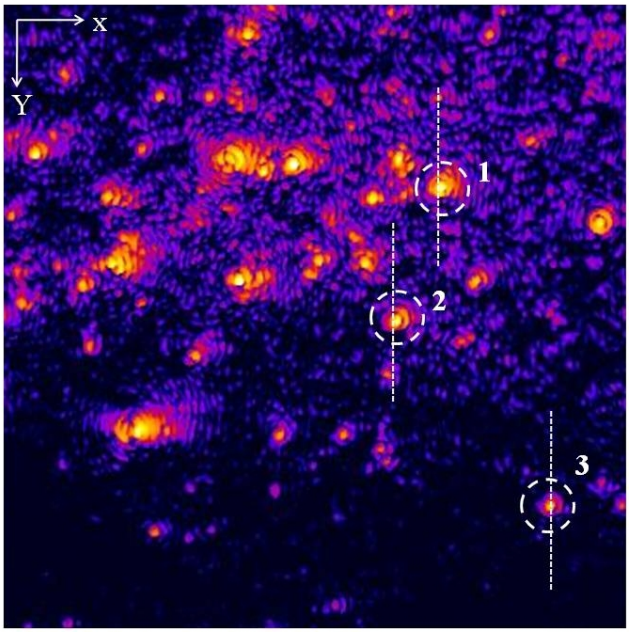

(a) x-sectioning on the reconstructed image

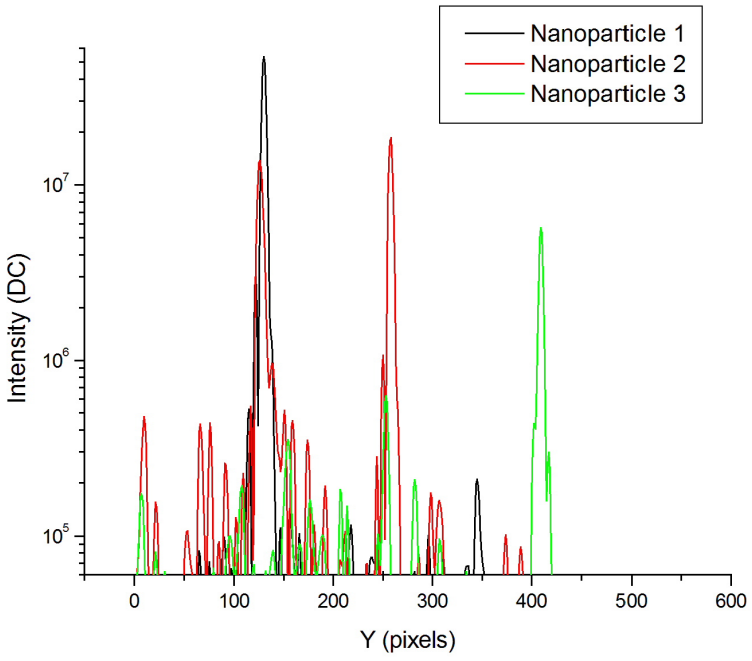

(b) Intensity cuts along x axis

Figure 6.35: Intensity cuts along x axis at positions of nanoparticles 1, 2 and 3 of the free 40 nm Au Nps

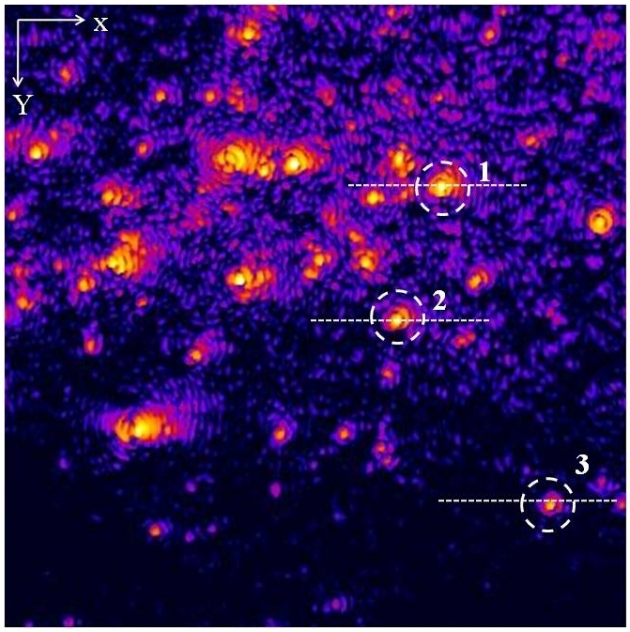

(a) y-sectioning on the reconstructed image

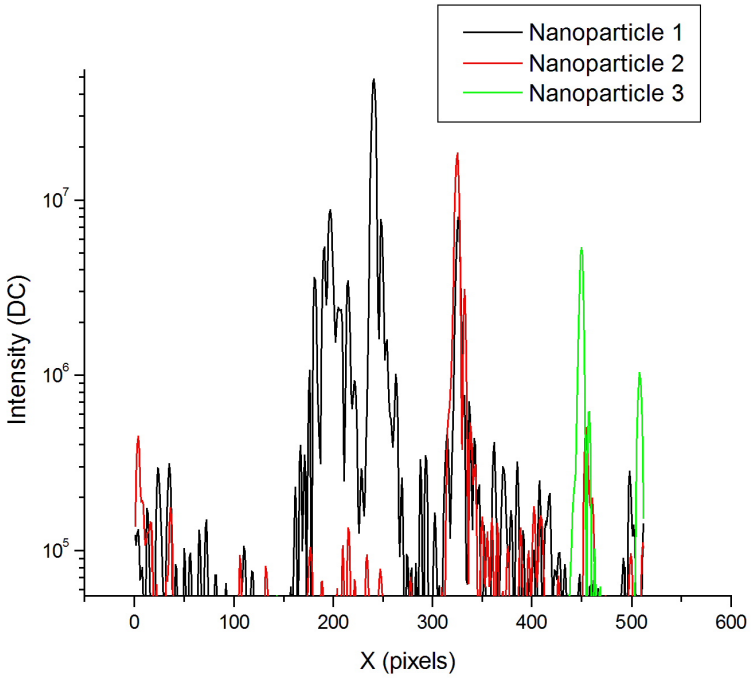

(b) Intensity cuts along y axis

Figure 6.36: Intensity cuts along y axis at positions of nanoparticles 1, 2 and 3 of the free 40 nm Au Nps

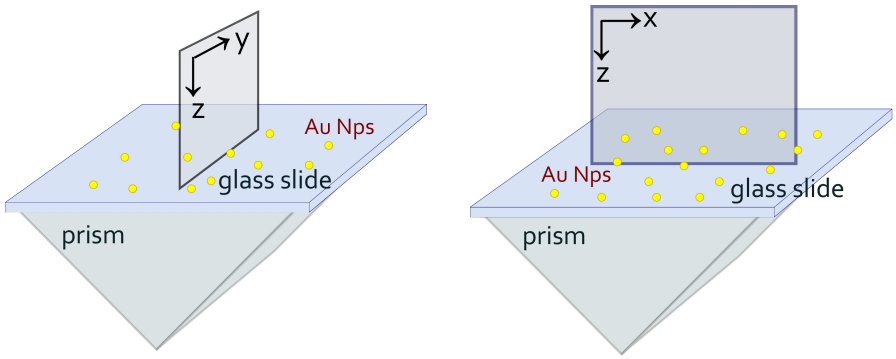

(a) (y,z) reconstruction plane (b) (x,z) reconstruction plane

Figure 6.37: Cross sections reconstruction planes of free gold nanoparticles

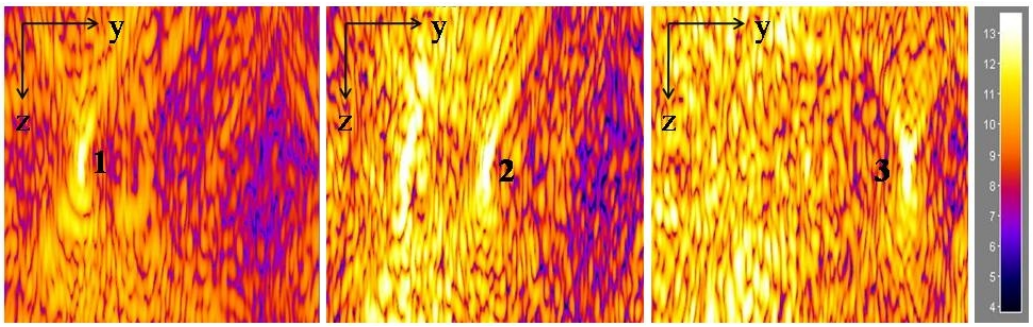

(a) (y,z) image of Np 1 (b) (y,z) image of Np 2 (c) (y,z) image of Np 3

Figure 6.38: Reconstructed images in the (y,z) plane obtained by performing a cut along x axis at the positions of the selected spots of the free Au Nps sample

light isotropically. Accordingly, the angular tilt effect of scattering patterns, observed on the previous biological specimens, should not appear here. The obtained experimental images shows that this supposition is true, indeed.

Similarly to the three previous sections, we have performed cuts along the x axis to obtain reconstructed images in the (y, z) plane as illustrated schematically on Figure 6.37b. Results of these cross sections are displayed on Figure 6.38 : Figure 6.38a shows the reconstructed image in the (y, z) plane obtained by performing a cut along the x direction at the position of nanoparticle 1. Figure 6.38b shows the reconstructed image in the (y, z) plane obtained by performing a cut along the x direction at the position of nanoparticle 2. Figure 6.38c shows the reconstructed image in the (y, z) plane obtained by performing a cut along the x direction at the position of nanoparticle 3.

The three observed scattering signals on the obtained (y, z) images are well defined straight bright patterns located along the vertical z axis and are qualitatively similar to the (y, z) images of nanoparticles 1 and 2 of the multi labeled sample (Figure 6.18a and Figure 6.18b) and to the (y, z) image of nanoparticle 1 of the single nanoparticle labeled sample (Figure 6.26a).

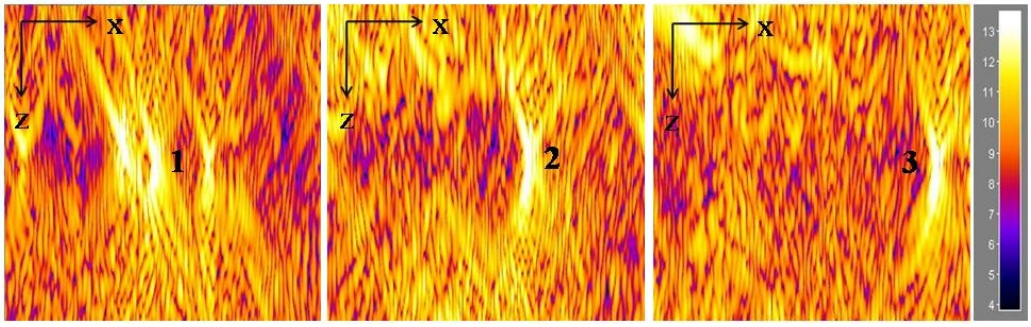

(a) (x,z) image of Np 1 (b) (x,z) image of Np 2 (c) (x,z) image of Np 3

Figure 6.39: Reconstructed images in the (x,z) plane obtained by performing a cut along x axis at the positions of the selected spots of the free Au Nps sample

Furthermore, and for a better accuracy of the results, we have performed cuts along the y axis as well to obtain reconstructed images in the (x, z) plane as illustrated schematically on Figure 6.37a. Figure 6.39a shows the reconstructed image in the (x, z) plane obtained by performing a cut along the y direction at the position of nanoparticle 1. Figure 6.39b shows the

reconstructed image in the (x, z) plane obtained by performing a cut along the y direction at the position of nanoparticle 2. Figure 6.39c shows the reconstructed image in the (x, z) plane obtained by performing a cut along the y direction at the position of nanoparticle 3.

Here again, and as expected, scattering patterns of the three gold nanoparticles have a small extension along the vertical z direction and do not exhibit the angular tilt that we have observed for hot spots in the different considered biological specimens (Figure 6.30b and Figure 6.26b.

This result confirms our interpretation of the angular tilt effect observed with the hot spots of the previous investigated specimens. As a consequence, the observed well defined bright scattering patterns that are not angularly titled and clearly located along the optical axis z, is a characterization of nanoparticles and is thus an unambiguous signature of the presence of gold biological nanomarkers, and validates the capability of digital holographic microscopy to discriminate them from background signals in live cells.

6.4 Overview

In this section, we will be giving an overview about the main relevant experimental results that we have presented in this chapter.

We have reported the detection and localization of 40 nm gold particles attached to the integrin surface receptors of live 3T3 fibroblasts using digital holographic microscopy. Specimens were illuminated in TIR configuration, and the imaging system detects scattered signals of both the cells and the gold markers. We have shown that the intensity of the signal scattered by gold nanoparticles is much larger than the signal scattered by the cell's structures and the obtained signal-to-noise ratio is about 100. This SNR is obtained when holographic images are reconstructed using a sequence of 32 camera frames with an exposure time of 100 ms per frame. However, we have shown that reconstructing using a single acquired image is still sufficient to localize in 3D the nanoparticle, but with a lower SNR and accuracy on the z-position estimation. Using 32 images, localization of the gold particle is obtained with a precision of 5 nm and 100 nm in the x,y and in the z directions respectively.
We have also shown that the detection of nanoparticles is not limited by the holographic detection noise since this inherent noise is about 2 orders of

magnitude lower than the cell scattered signal and 3 to 4 orders of magnitude lower than the particle scattered signal.
Additionally, 3D mapping of the entire sample' scattered field was achieved and the 3D exploration was performed within a relatively big volume $\sim (90 \times 90 \times 90)\ \mu m$.

We obtained also that relevant information can be derived not only from the intensity of the bright spots caused by the presence of gold particles, but also from the 3D shape of light scattering patterns, which are easily accessed using holography. In fact, in addition to a stronger scattering signal, gold particles induce a relatively isotropic scattering, whereas biological features are characterized by mostly forward scattering and thus keeps memory of the illumination direction. This dissimilarity in the scattering patterns, explained by the inconsistency of the refractive indexes and anisotropy parameters g, is easily accessed in holography. Accordingly, the shape of the scattered wavefield can thus be used as a signature that helps to discriminate the particles signal from the biological structures signal.

These experimental results have been confirmed by investigating different kind of specimens : non-labeled cells, free gold nanoparticles, cells labeled with high concentration gold conjugates and cells labeled with few gold conjugates. Experimental results obtained from these different specimens were quite coherent and thus allowed us to unambiguously discriminate gold nanoparticles from cellular features.

Chapter 7

Technical Developments

Contents

7.1 Preparation of Live Cells Specimens 168

7.1.1 Cell Culture and the Observation Chamber 168

7.1.2 Biological Specimen Preparation 169

7.1.3 Specimen in the Observation Chamber 172

7.1.4 Eliminating Uncoupled Gold Conjugates 172

7.2 Specimen Illumination Geometry 173

7.2.1 Slant Illumination Geometry 174

7.2.2 TIR Illumination Geometry 192

7.3 Experiments using a Short Coherence Length Laser . 199

7.4 Overview 201

In the previous chapter (Chapter 6), we have reported the detection and localization of gold nanomarkers down to 40 nm diameter in live cells environments using our evolved holographic microscope. Experiments, however, suffer from some experimental and technical limitations that originates mainly from the *biological and biochemical protocols* that are utilized to prepare the specimens, from the adopted *illumination geometry* and from the inherent *inhomogeneous structure of the investigated specimen* itself that exhibits high parasitic noise.

In the current chapter, we present some technical and experimental developments that tend to treat the limitations listed above. In the first section of this chapter (Section 7.1) , we will present the technical developments achieved for the biological preparation procedure of the specimens. In the second section (Section 7.2) , we tend to find an optimized alternative dark field illumination configuration. We will thus present experimental results obtained using the *Slant Illumination geometry*. A comparison with the TIR illumination geometry is also presented. The last section (Section 7.3) treats the problem

of the parasitic noise induced by the refractive index inhomogeneities in biological cells. Experimental results using a short coherence length laser source are thus presented.

Figure 7.1: Glass bottom cell culture dish from World Precision Instruments

7.1 Preparation of Live Cells Specimens

7.1.1 Cell Culture and the Observation Chamber

Cells are cultured using the standard commonly used method as described in Section 6.2.1.2 of Chapter 6 : Cells grow on a glass coverslip mounted inside a plastic culture dish. It is thus necessary prior to each holographic experiment to extract, using tweezers, the glass slide containing cells from the plastic dish and mount it on the specific observation chamber as described in the previous chapter in Section 6.2.1.5. This operation is delicate and increases the contamination probability of the biological specimen. Moreover, it is necessary to use a very adequate observation chamber (same diameter of the coverslip, leaking free, convenient thickness etc...) that should be well washed and sterilized thoroughly after each experiment.

To avoid this, we have chosen to prepare the cells directly in a convenient observation chamber. The existing standard glass petri dishes present several inconveniences : they are commercialized unsterilized, they are untreated for optimal cell growth and they are manufactured using thick bad optical property glass.

We found an excellent alternative solution which is to use the 35 mm Fluorodish glass-bottom cell culture dishes from World Precision Instruments (see Figure 7.1). Each fluorodish has in its bottom a 23.5 mm optical quality glass coverslip with a thickness of 0.17±0.01 mm that is attached, using a very low toxicity adhesive, to the bottom of a plastic culture dish that has a circular opening in its base. Dishes are commercialized sterilized, without a bottom edge and their cell culture surface is treated for optimal cell growth.

7.1.2 Biological Specimen Preparation

7.1.2.1 Preparation of Gold Conjugates

The functionalization procedure of gold nanoparticles (described in Section 6.2.1.3 of the previous chapter), is very long and relatively sophisticated. It should be performed with an expert in a biochemistry laboratory where specific equipments and products are needed.

An easier alternative customized solution is to conjugate the fibronectin directly to the gold nanoparticles without the previously used streptavidin and biotin system as illustrated on Figure 7.2

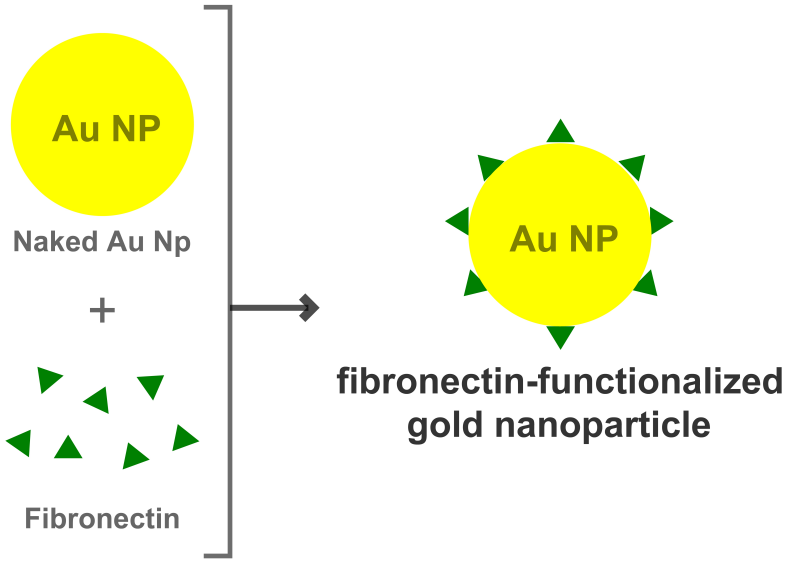

Figure 7.2: Fibronectin-functionalized gold nanoparticles

For this purpose, we purchased bovine plasma fibronectin from Sigma-Aldrich and we ordered this custom-made conjugation from BioAssay Systems (Hayward, CA - USA). Basically, the fibronectin was attached to the

gold nanoparticles using some of the sulphur components in the fibronectin molecule similarly to a traditional antibody-gold solution conjugation and the procedure was completed at neutral pH (7.0). The conjugation protocol follows BioAssay Gold-in-a-Box procedure and can be found in details in Appendix A.2 . An illustration of the steps, 1 through 6, described in the "Generic Procedure" part of the conjugation procedure (see Appendix A.2) can be found on Figure 7.3 .

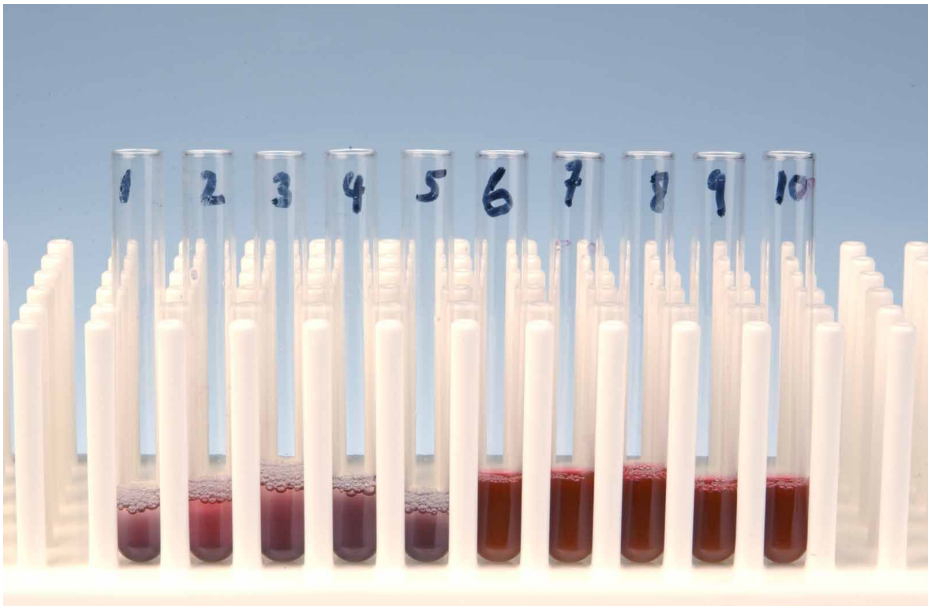

Figure 7.3: Glass bottom cell culture dish from World Precision Instruments

The fibronectin-gold conjugation is performed for 80, 60 and 40 nm diameter gold nanoparticles. 35 μg of fibronectin per mL of gold solution is used for the 40 nm conjugation, 25 μg of fibronectin per mL for the 60 nm conjugation and 17 μg of fibronectin per mL for the 80 nm conjugation. At the end of the conjugation there are approximately 210 fibronectin molecules on each 40 nm gold particle, 450 fibronectin molecules on each 60 nm gold particle and 800 fibronectin molecules on each 80 nm gold particle. The final concentration of the gold solution for the 40 nm , the 60 nm and the 80 nm fibronectin conjugates is 15 OD (see Figure 7.4).

7.1.2.2 Gold-Cells Conjugation

In the previous chapter, we have seen in Section 6.2.1.3 that, before each use, the gold solution should be rinsed with PBS in order to eliminate free protein molecules. Nevertheless, this is not necessary with this BioAssay

new conjugation process since the conjugation is performed slightly below the saturation point. The problem of free molecules is eliminated and a more complete coating of the gold is obtained yielding thus to optimized gold conjugates. Consequently, the gold conjugates can be used as supplied and only a dilution is needed.

After 24 hours of incubation under 5% CO2 and 37°C atmosphere, the glass-bottom culture dish, prepared as described in Section 6.2.1.2 is retrieved from the incubator and placed under the laminar flow hood in order to perform the coupling with the prepared gold nanoconjugates. The dish contains a monolayer of 3T3 cells immersed in 2 mL of DMEM medium. The culture medium contained in the dish is aspirated and replaced by a solution composed of 2 mL DMEM plus 500 μL of a PBS dilute fibronectin gold conjugates solution (2μL of the initial gold solution diluted in 1 ml PBS). The integrin-fibronectin link is created at this level allowing the cells to attach, on their surface, the functionalised gold nanoparticles (see Figure 7.5). The culture dish, containing now fibroblasts and functionalized gold solution, is gently rocked in order to ensure a good repartition of the gold beads. The dish is then reinserted in the incubator for another 24 hours prior to the envisaged experiment.

Figure 7.4: Glass bottom cell culture dish from World Precision Instruments

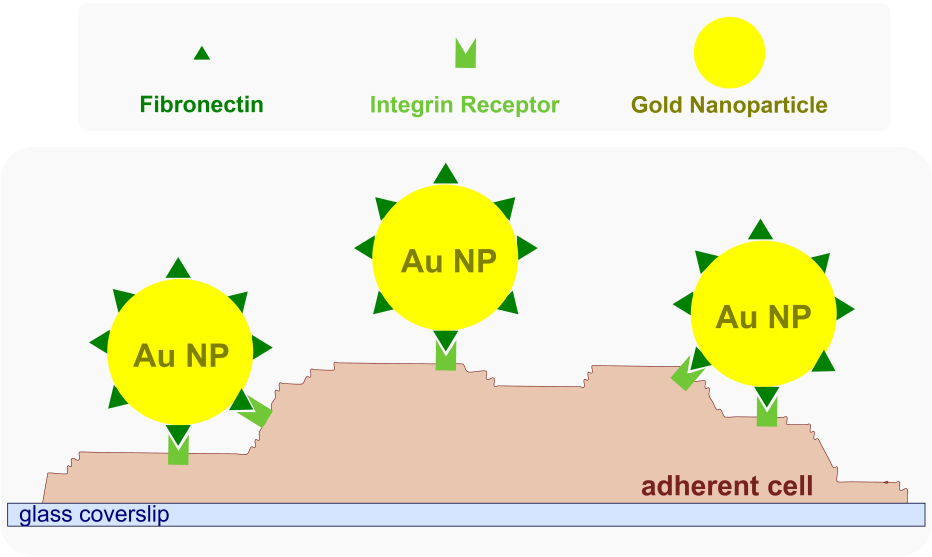

Figure 7.5: Labeled Cell

7.1.3 Specimen in the Observation Chamber

24 hours after the conjugation process, the holographic experiment was performed. Hence, the glass-bottom culture dish containing adherent 3T3 cells tagged with gold nanoparticles was taken out of the incubator and mounted directly on the experimental setup as illustrated on Figure 7.6.
To ensure optimal cell survival conditions during the observation, cells in glass-bottom dishes are observed in a special DMEM-F12 observation medium from PAA Laboratories (DMEM-F12 without Phenol red, B12 vitamin, Riboflavin, 0.5% fetal calf serum) that is supplemented with L-Glutamine and 20 mM of HEPES [(4-(2-hydroxyethyl)-1-piperazineethanesulfonic acid)], which is a buffering agent that maintains the physiologic pH conditions.

7.1.4 Eliminating Uncoupled Gold Conjugates

When cells are incubated with functionalized gold nanoparticles, some of the gold conjugates will bind to the cellular receptors with a certain protein-receptor interaction probability while others remain unattached to the cells. These free gold nanoparticles are still present in the observation medium and can consequently affect the quality of the detected holographic signal if they are present in the vicinity of the investigated part of the specimen. In order to remove any gold nanoconjugates that had not interacted with the cells, cells were washed with Hank's Balanced Salt Solution (HBSS) prior to each

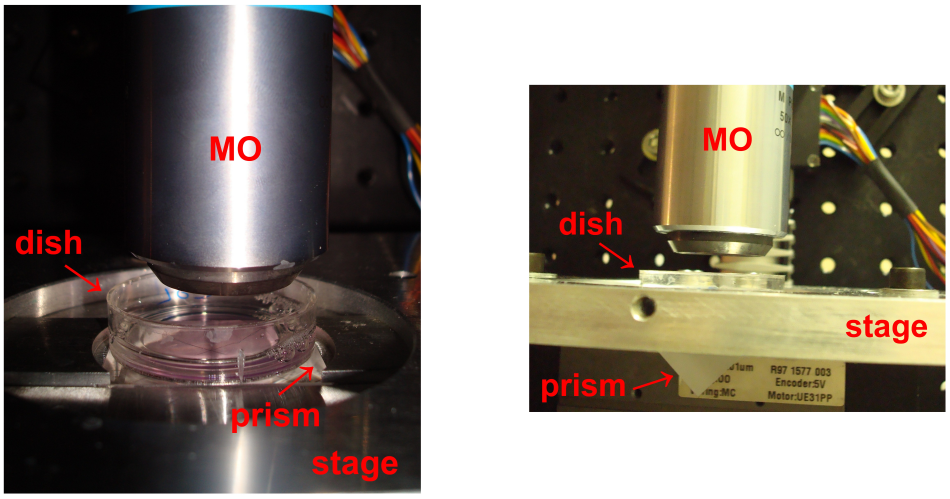

(a) Top view (b) Front view

Figure 7.6: Specimen microscopy stage

experiment.

7.2 Specimen Illumination Geometry

We have seen in the previous chapter that dark field microscopy is adopted in order to detect the relatively low scattering signal of gold nanomarkers coupled to live cells using the full dynamic range of the CCD detector. TIR illumination configuration is thus used to illuminate the specimen : by this way we eliminate most of the incident illumination light and we detect only the desired scattered light.
As described in the previous chapter (Figure 6.10) TIR is performed using a 90° prism. This configuration may present two limitations :

- The prism should be cleaned and sterilized before and after each experiment. Consequently, the prism should be frequently unmounted from the optical apparatus which may slightly alters the optical alignment.

- A problem of "Standing Waves" may be encountered especially if time-tracking experiments are carried out.

We tend to overcome these limitations by finding an optimized alternative dark field illumination configuration : the *Slant Illumination geometry*. We will first describe this new illumination geometry and show some experimental

results obtained using this configuration. Then, we will present a comparison with the TIR illumination geometry.

7.2.1 Slant Illumination Geometry

7.2.1.1 Materials and Methods

Experimental Apparatus

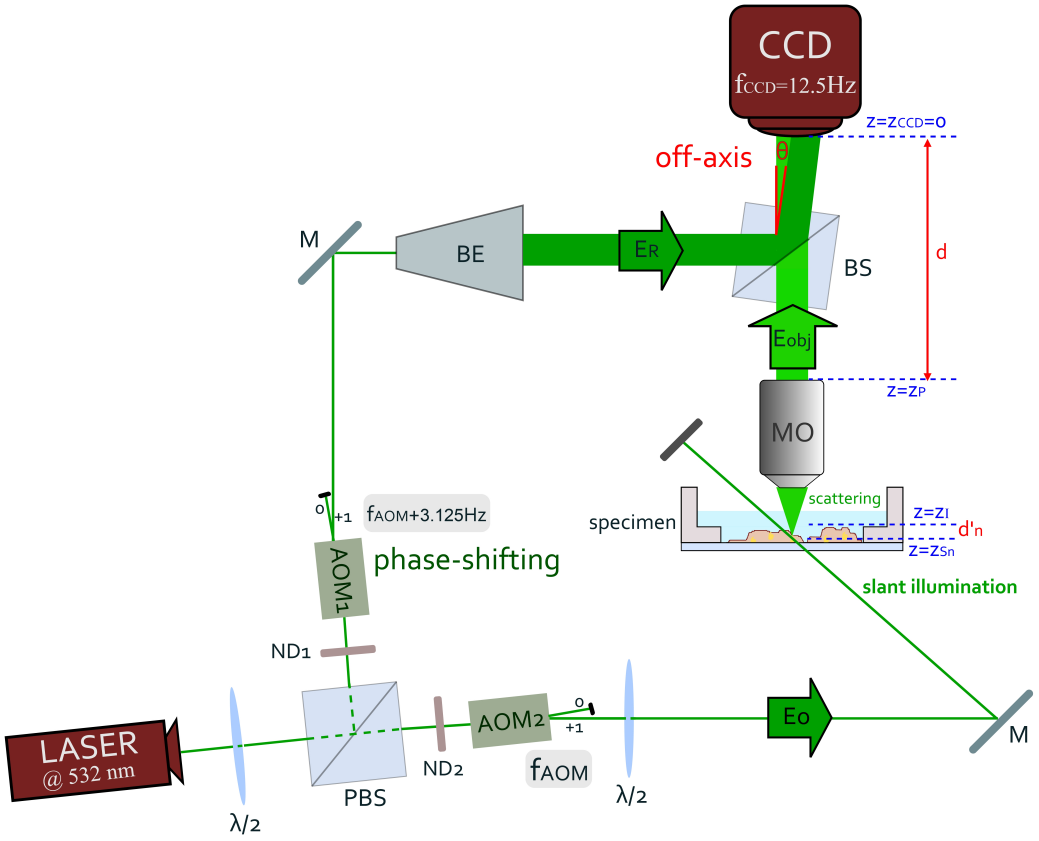

Figure 7.7: Optical apparatus for DHM in slant illumination geometry

The experimental apparatus is a modified Mach-Zehnder interferometer. It is basically the same apparatus that we used in the previous chapter. The only difference is in the specimen illumination geometry. Figure 7.7 is a schematic representation of this optical setup.
A coherent laser source is used as the illumination source. The initial illumination laser light is splitted, using a PBS cube, into two beams, a reference beam (complex field E_R, frequency f_R) and an object illumination beam

(complex field E_o, frequency f_o) forming the two arms of the Mach-Zehnder interferometer. A combination of a half wave plate and two neutral density filters, ND_1 and ND_2, is used to prevent the saturation of the detector by controlling the optical power traveling in each arm. Two acousto-optic modulators, AOM1 and AOM2, driven around 80 MHz with a selection of the first order of diffraction, shift both frequencies at respectively f_{AOM1} and f_{AOM2}.
The object beam illuminates the sample, in a dark field arrangement in order to prevent direct illumination light from entering the system. The illumination wave is scattered by the specimen and this scattered wave (complex field E_{obj}) is collected by a microscope objective (MO). A BS is then used to combine the scattered object wave E_{obj} and the reference wave E_R which is slightly angularly tilted ($\theta \sim 1°$) with respect to the propagation axis of the object wave in an off-axis configuration. The HWP on the object illumination arm aligns the polarization of the corresponding beam ensuring its optimal interference with the reference beam. A CCD camera detects the interference pattern (hologram H_{CCD}).

Laser source

In the experiments presented in the current section of this chapter, the main laser source that we used is a Diode Pumped Solid State (DPSS) Laser (Oxxius, single longitudinal mode, CW, 50 mW), emitting at $\lambda = 532$nm. This wavelength is chosen in order to excite the surface plasmon resonance of gold nanoparticles. The excitation of gold nanoparticles at their plasmon resonance results in a much higher scattering efficiency and thus in a gain in the detected intensity of the scattered light.

CCD Camera

The CCD camera that we used is a 12 bit PCO Pixelfly QE (see Figure 7.8) with a detector composed of 1280×1024 square pixels. The physical size of the pixels is $d_{px} = 6.45\mu m$. The frame rate frequency of the camera is $f_{CCD} = 12.5$ Hz.

Microscope Objective

In the experiments presented in this chapter, we used a Mitutoyo Plan Apo infinity corrected long working distace 50X air microscope objective. The specifications of this objective are presented in table 6.1 :
Specimen Illumination

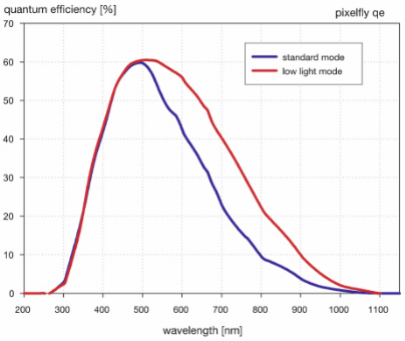

(a) Photo of the PCO CCD camera

(b) Quantum efficiency graph of the PCO camera in function of the wavelength

Figure 7.8: PCO Pixelfly QE CCD camera

Mitutoyo Plan Apo infinity corrected long WD 50X MO	
Numerical Aperture	0.55
Focal Length	4.0 mm
Working Distance	13.0 mm

Table 7.1: Specifications of the Mitutoyo 50X MO

We used dark field illumination, using a slant illumination configuration, in order to prevent the direct light from entering the system and thus collecting only the light scattered by the specimen using the full dynamic range of the detector. For this purpose, the glass-bottom dish filled with the observation medium and containing the biological specimen, is directly mounted on the X-Y translation motorized stage, without the prism.
The object's laser beam illuminates the specimen from the bottom using a slant geometry as illustrated on Figure 7.9.
The illumination wave is scattered by the nanoconjugates and by the local change of refractive index within the cells and this scattered wave is collected by the microscope objective. Since a long working distance microscope objective is used, the slant illumination angle is relatively high enough to let the incident light diagonally cross the specimen without entering the front aperture of the MO.
This illumination configuration is chosen because it holds back most of

the directly transmitted illumination light preventing it from reaching the detection system. Additionally, using this configuration, the 90° prism used in the TIR geometry is not needed here. This eliminates the need of frequently cleaning the prism and this eliminates also the possible problem of standing waves when long time-tracking holographic experiments are performed. However, similarly to the TIR configuration, the slant illumination arrangement constrains the usage of high working distance microscope objectives which are known to have limited numerical apertures (NA=0.5 typically), limiting consequently the reachable resolution of the reconstructed images.

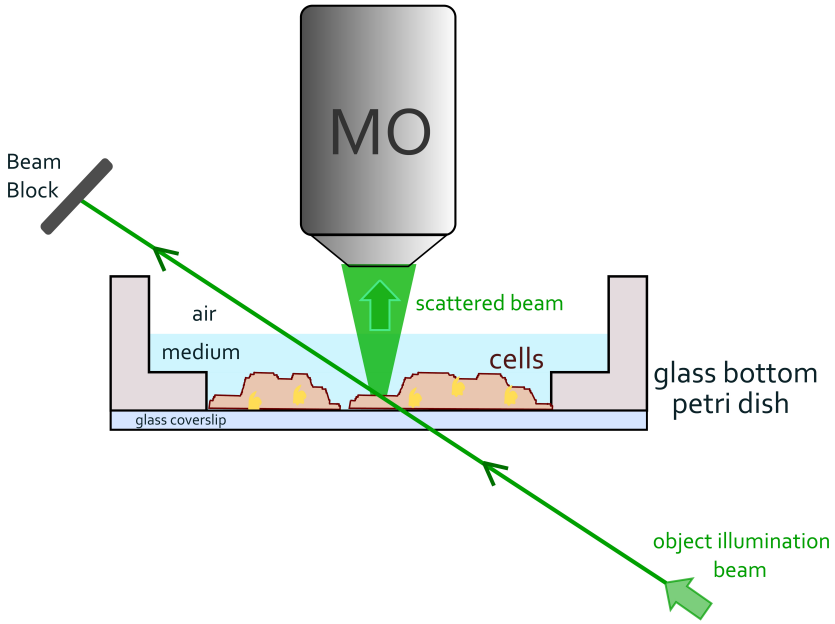

Figure 7.9: Slant illumination of the specimen for dark field microscopy

Holograms Acquisition

Similarly to the experiments presented in the previous chapter, we used here also phase-shifting digital holography in order to directly obtain alias-free holograms where only the relevant $+1$ term is procured. Accordingly, a sequence of M_{acq} phase-shifted holograms $H_0,...,H_{M_{acq}}$, with a relative phase shift $\Delta\varphi = \pi/2$ between two consecutive frames, are recorded. In the experiments presented in this chapter, holograms are recorded with an acquisition time $T = 1/f_{CCD} = 1/12.5 = 80\,\text{ms}$ per acquired hologram.

In the current experiments, the heterodyne beating frequency is :

$$\Delta f = f_{AOM1} - f_{AOM2} = \frac{f_{CCD}}{4} = 3.125Hz \tag{7.1}$$

where f_{CCD} =12.5Hz for the PCO camera that we used here.

The complex distribution of the field is then obtained from the recorded sequence of CCD holograms using the M-phases demodulation method, described in Chapter 4.
The object field E_{CCD} on the CCD plane ($z = z_{CCD} = 0$) is thus given by:

$$E_{CCD}(x, y, z = 0) = \sum_{j=1}^{M} i^n \, H_{CCDj} \tag{7.2}$$

where $i^2 = -1$ is the imagery unit, and M is an integer defining the number of frames used for the reconstruction. In Equation 7.2, the coordinates x, y (with $0 < x, y < 511$ for the utilized PCO camera) are integers, that represent the pixel's location within the CCD array. The pixel size is then the physical CCD pixel size, i.e., 6.45 μm.

Reconstruction Procedure

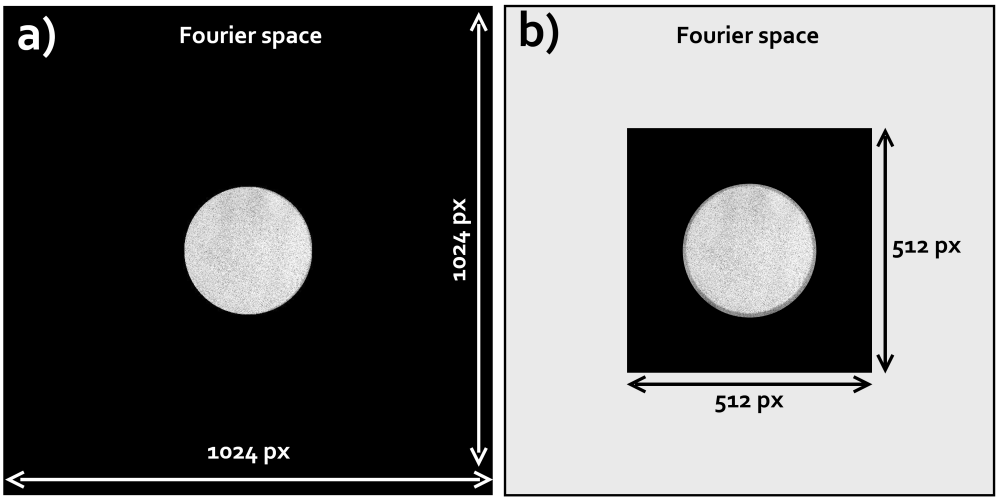

Figure 7.10: Truncation of the calculation matrix from a 1024×1024 pixels' matrix to a 512×512 pixel's matrix

We performed here the same two-steps reconstruction procedure used in the previous chapter (Chapter 6) and described in Chapter 5 . However, since the

CCD chip that we used here is composed of 1280×1024 pixels, the recorded 1280×1024 matrix is truncated to a 1024×1024 matrix in order to facilitate the computations. Furthermore, after the reconstruction of the MO exit pupil's image from the 1024×1024 data matrix, and after the translation for the tilt correction process, the matrix is truncated once again to a 512×512 matrix centered on the translated MO exit pupil image, as illustrated on Figure 7.10, in order to reduce the calculation time during the second step of the reconstruction process which is the free space propagation.

Before propagating the angular spectrum, the magnification factor G was measured by imaging, on the same setup, a USAF target. The obtained pixel size in the conjugate image plane is $d'_{px} = \Delta\xi' = \Delta\eta' = 126$ nm.

Since the physical pixel' size, the pixel' size in the conjugate image and the focal length of the MO (see Table 7.1) are identified quantities ($d_{px} = 6.45\mu m$, $d'_{px} = 126nm$ and $f_l = 4mm$), d, which is the CCD to the MO output aperture distance can be deduced according to Equation 6.3 :

$$d = \frac{d_{px} \cdot f_l}{d'_{px}} = 20.4\, cm \tag{7.3}$$

The obtained d distance, calculated from Equation 7.3 , is consistent with the experimentally measured distance : $d_{exp} \simeq 21\, cm$.

In order to reconstruct the entire volume object, the angular spectrum propagation was done for 512 different z_{S_n}-planes of the specimen. Accordingly, the reconstruction is done for 512 different reconstruction distances d'_n :

$$d'_n = (n - 256)\delta z \tag{7.4}$$

3D volume images, composed of $512 \times 512 \times 512$ voxels, are thus obtained.

7.2.1.2 Experimental Results

In this section, we have investigated specimens of 3T3 fibroblasts labeled with 80 nm fibronectin-coated AuNps, specimens that consists of unmarked 3T3 fibroblasts and specimens of free 80 nm gold particles.

We will first start by presenting experiments of free 80 nm gold particles , then we will expose results obtained on unmarked cells. In the last part of this section, we will describe experiments performed on 3T3 cells labeled with 80 nm gold particles.

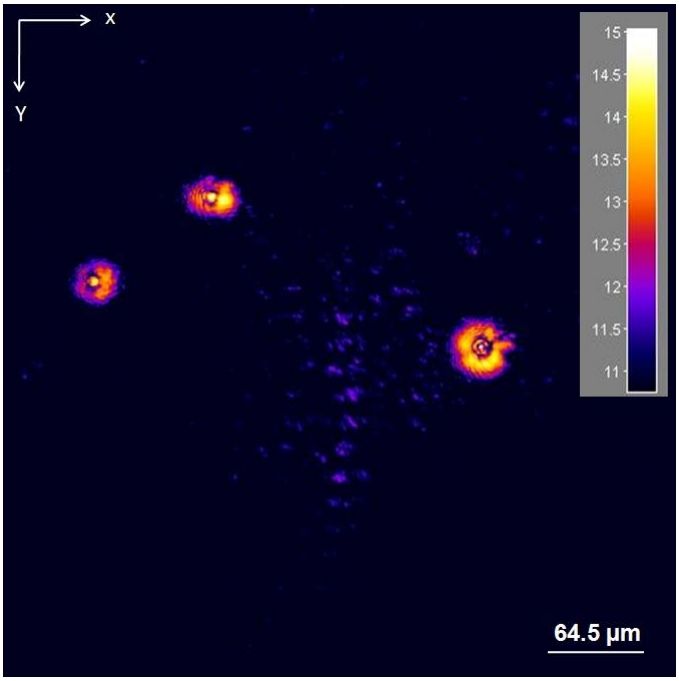

Figure 7.11: Reconstructed holographic intensity image of free 80 nm gold nanoparticles using a dark-field slant illumination geometry displayed in a colored logarithmic scale

All the reconstructed images presented in this chapter consists of 512 pixels per side. Since we obtained that the pixel in the conjugate image equals 126 nm, reconstructed images are thus 64.5 μm wide.

Free 80 nm Gold Nanoparticles

The investigated specimen consists of free 80 nm gold particles (uncoupled to cells) in Brownian motion in a water and agarose suspension. Here, we used agarose to slow down the motion of the particles enough to make the displacement of the particles negligible during the time of acquisition of the sequence of M_{acq} frames.

The free gold nanoparticles specimen is observed in a glass-bottom petri dish similar to the dishes used for manipulating the biological specimens.

Figure 7.11 shows the reconstructed holographic intensity image of the sample in a colored logarithmic scale. The reconstruction is done using 32 CCD frames ($M = 32$) with an exposure time of 80 ms per frame. The displayed reconstructed image is the plane where the brightest point is detected and is obtained for $n = 240$. We can see three bright spots corresponding to particles that are located within the reconstruction plane.

We display on Figure 7.12 the reconstructed image of the MO exit pupil plane of the free 80 nm gold nanoparticles specimen. We can see that this image corresponds to a bright disk with an homogeneous distribution of the signal since the scattering of gold nanoparticles is isotropic ($g_{Au} \simeq 0$) as described in Chapter 2 and as observed on the experimental results of Chapter 6. When illuminated, gold nanoparticles do not keep memory of the illumination direction but scatter light in all directions as illustrated on Figure 7.12b .

Unlabeled 3T3 Fibroblasts

In order to compare the scattering behavior of AuNps with the scattering behavior of cells, we have investigated a specimen that consists of 3T3 cells unlabeled with gold nanoparticles and observed in the glass-bottom petri dish. The direct white light image of the considered unlabeled cells is shown on Figure 7.13a. A direct image obtained when the laser illuminates the cells is displayed on Figure 7.13b. Figure 7.13c is a direct image under white light and laser illumination and Figure 7.13d is a direct image of the investigated cells' hologram.

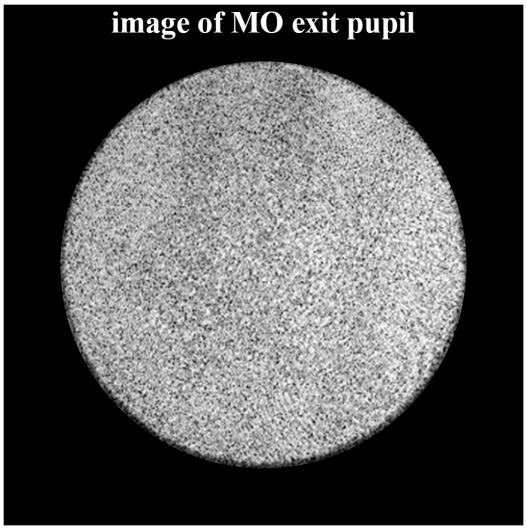

(a) Image of the MO exit pupil plane of the free 80 nm AuNps specimen

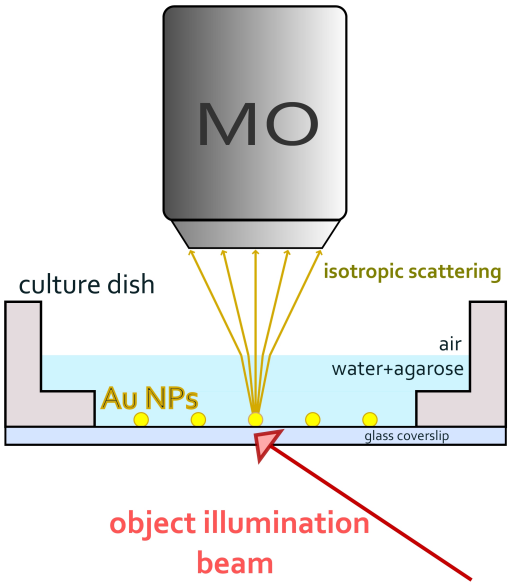

(b) Forward Scattering Regime of free Gold Nanoparticles

Figure 7.12: Scattering of free 80 nm gold nanoparticles

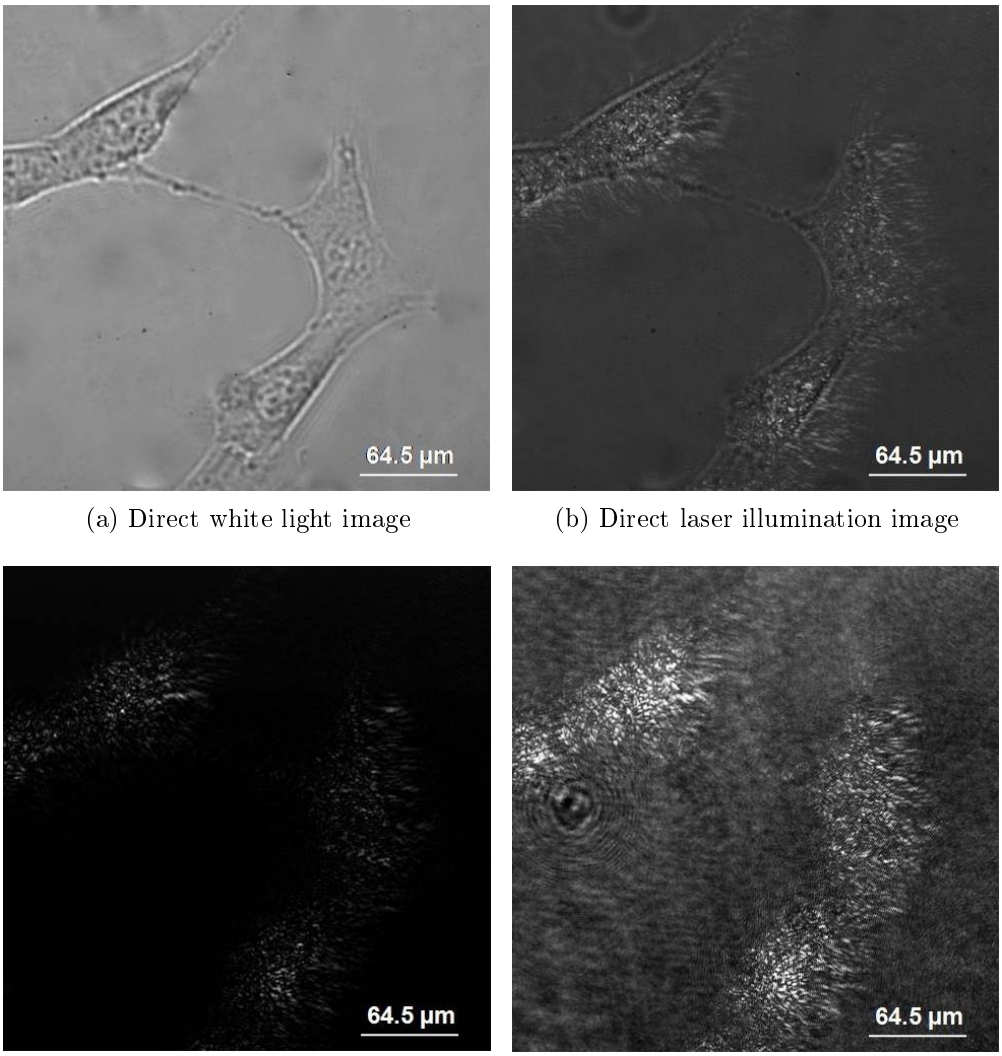

(a) Direct white light image

(b) Direct laser illumination image

(c) Direct white light and laser illumination image

(d) Hologram

Figure 7.13: Direct images of unlabeled 3T3 fibroblasts

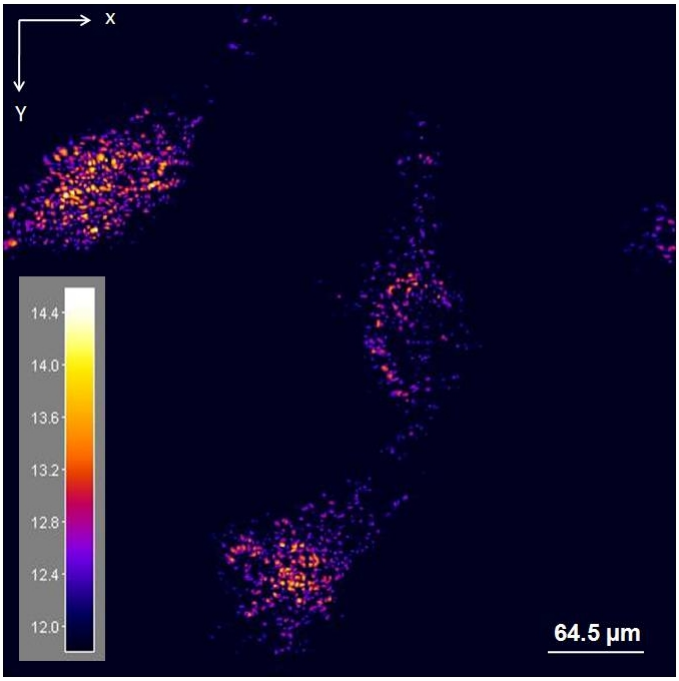

Figure 7.14: Reconstructed holographic intensity image of unlabeled 3T3 fibroblasts using a dark-field slant illumination geometry displayed in a colored logarithmic scale

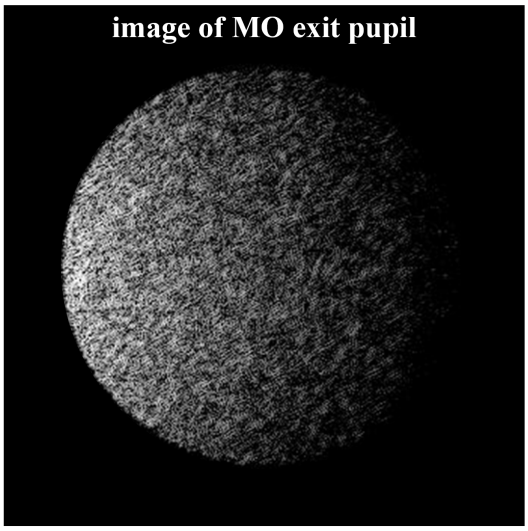

(a) Image of the MO exit pupil plane of the free 80 nm AuNps specimen

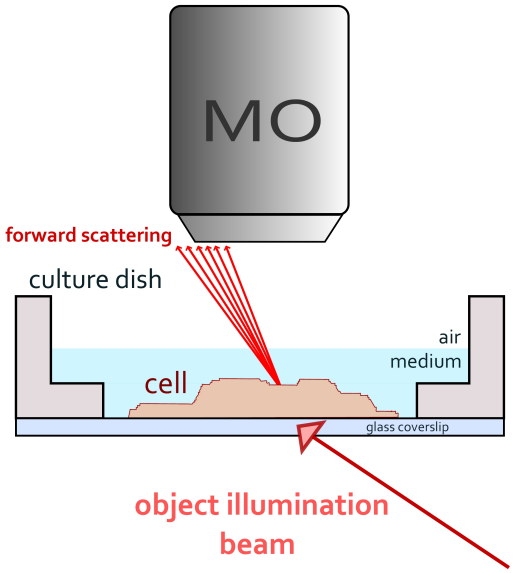

(b) Forward Scattering Regime of free Gold Nanoparticles

Figure 7.15: Scattering of unlabeled cells

Figure 7.14 shows the reconstructed holographic intensity image of the unlabeled cells displayed in a colored logarithmic scale. The reconstruction is done using 32 CCD frames ($M = 32$) with an exposure time of 80 ms per frame. The displayed reconstructed image is the plane where the brightest points are detected. This reconstruction plane is obtained for $n = 370$. We can see that the background parasitic signal that corresponds to signal scattered by the cellular features is high and no relevant signal can be discriminated since cells are not labeled here.

We show on Figure 7.15a the reconstructed image of the MO exit pupil plane of the unlabeled cells specimen. We can see here that the disk, corresponding to the MO exit aperture's image, does not present an homogeneously illuminated structure. In fact, we can see that the left side of the disk is brighter than the right side since biological cells follow the forward scattering regime ($g_{bio} \simeq 1$) as described in Chapter 2 and as observed on the experimental results of Chapter 6. When illuminated, biological cells keep memory of the illumination direction and consequently their scattering is peaked in the forward direction as illustrated on Figure 7.15b .

3T3 Fibroblasts Labeled with 80 nm Gold Conjugates

In this section, the investigated specimen consists of 3T3 cells labeled with fibronectin-coated 80 nm gold nanoparticles and observed in the glass-bottom petri dish. The direct white light image of the considered labeled cells is shown on Figure 7.19a. A direct image obtained when the laser illuminates the cells is displayed on Figure 7.19b. Figure 7.16c is a direct image under white light and laser illumination and Figure 7.16d is a direct image of the investigated cells' hologram.

Figure 7.17 shows the reconstructed holographic intensity image of the labeled cells displayed in a colored logarithmic scale. The reconstruction is done using 32 CCD frames ($M = 32$) with an exposure time of 80 ms per frame. The displayed reconstructed image is the plane where the brightest points are detected. This reconstruction plane is obtained here for $n = 255$. We can see that the background parasitic signal, that corresponds to the signal scattered by the cellular features, is still high. However, we can discriminate some bright spots that corresponds to gold nanoparticles.

We show on Figure 7.15a the reconstructed image of the MO exit pupil plane of the labeled cells specimen. We can see, here that the disk, corresponding to the MO rear aperture's image, presents a quasi homogeneously illuminated

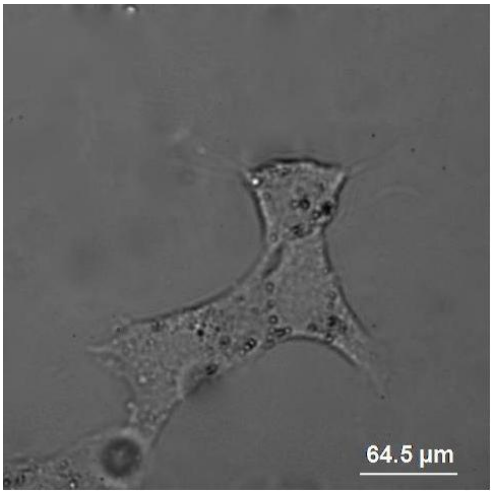

(a) Direct white light image

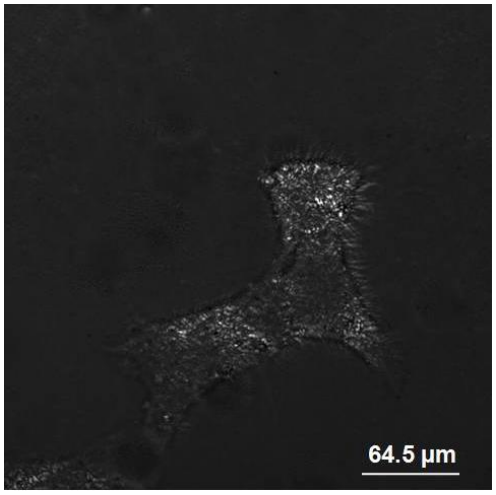

(b) Direct laser illumination image

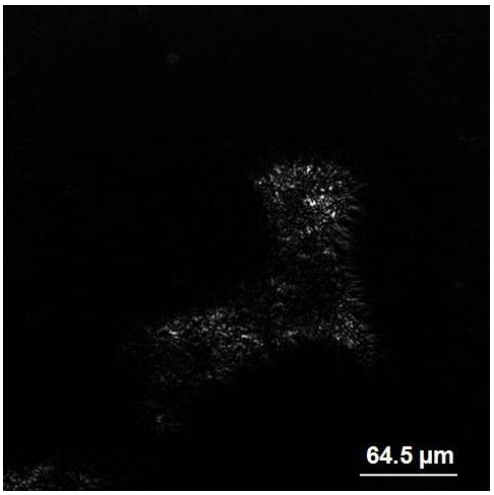

(c) Direct white light and laser illumination image

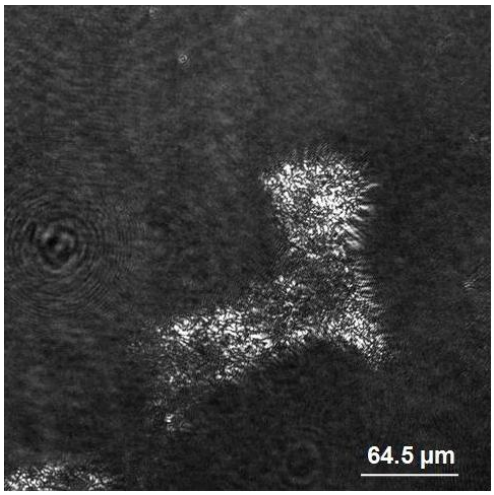

(d) Hologram

Figure 7.16: Direct images of 3T3 fibroblasts labeled with several 80 nm AuNps

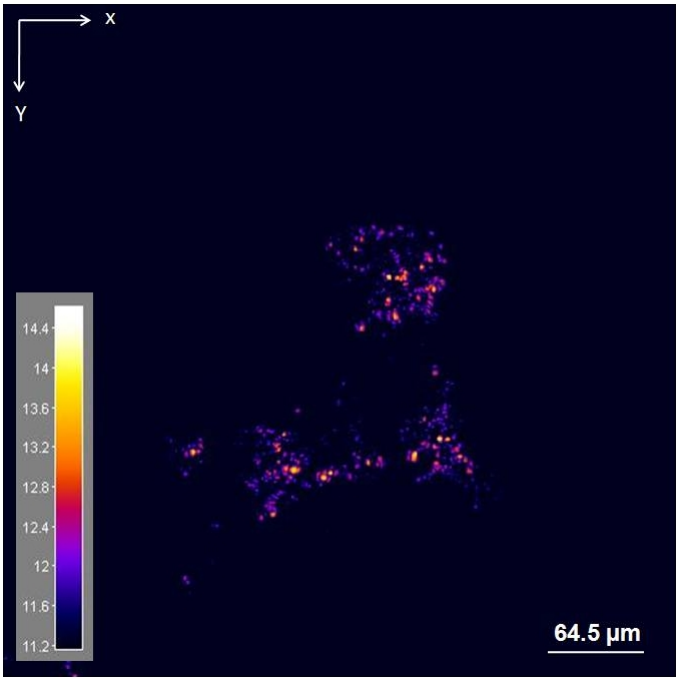

Figure 7.17: Reconstructed holographic intensity image of 3T3 fibroblasts labeled with 80 nm AuNps using a dark-field slant illumination geometry displayed in a colored logarithmic scale

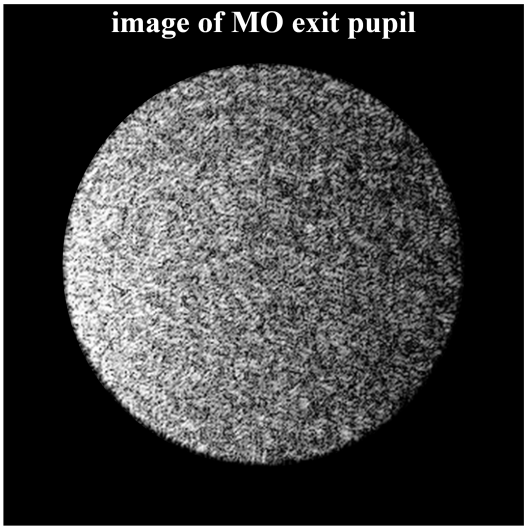

(a) Image of the MO exit pupil plane of the free 80 nm AuNps specimen

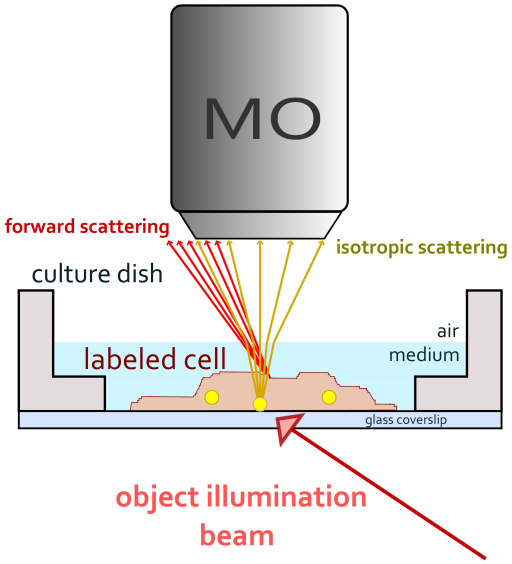

(b) Forward Scattering Regime of free Gold Nanoparticles

Figure 7.18: Scattering of cells labeled with 80 nm AuNps

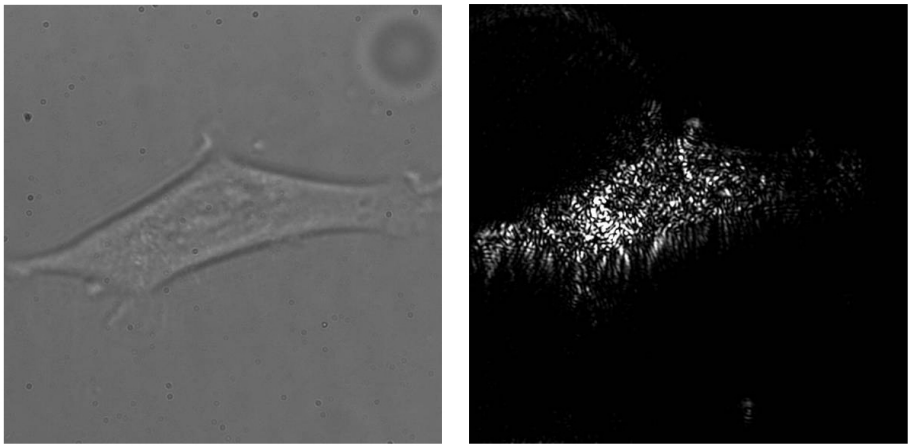

(a) Direct white light image

(b) Reconstructed holographic intensity image using a dark-field slant illumination geometry

Figure 7.19: Images of a 3T3 fibroblast showing the blurry effect of the slant illumination geometry

structure. In fact, even though biological cells follow the forward scattering regime, the total scattered signal is dominated by the isotropic scattering regime of the gold nanoparticles that are conjugated to the cells as illustrated on Figure 7.18b. The total scattered signal is thus isotropic.

Although, from these experimental results of the three different kinds of specimens, the slant illumination geometry allowed us to image biological cells and to detect gold nanoparticles coupled to their surface, the presented results were not easily obtained. In fact, we have tried to image lot of specimens in order to get proper reconstructed images : since the object wave is diagonally tilted, the reconstruction process is arduous. Not only specimens of cells labeled with 80 nm AuNps were investigated using the slant illumination geometry, we have also imaged other specimens where 60 and 80 nm AuNps are conjugated to cells. The quality of the reconstructed images obtained using these specimens was also poor. A parasitic reflection effect at the edges of the illuminated specimens is observed in most of the experiments performed using the slant illumination geometry as it can be depicted on Figure 7.19b.

Subsequently, we have deduced that, for the considered application, the slant illumination geometry is not advantageous and the TIR illumination configuration is better. Accordingly, we have adopted, again, the TIR

illumination geometry for the next presented experiments.

It should be noted that, although in the experiments presented in this section, specimens were illuminated diagonally from the bottom (see Figure 7.9) , one can intuitively thinks that if specimens were illuminated diagonally from the top, as illustrated on Figure 7.20 , the MO will collect less parasitic signal because cells scatter light in the forward direction of the incident beam ($g_{bio} \simeq 0.9$) and consequently, in the supposed slant illumination geometry, the parasitic signal scattered by the cellular structures is far from the entrance aperture of the MO. By a proper adjustment of our optical apparatus that allowed us to switch very easily from a bottom illumination to a top illumination slant geometry, we have performed the two type of experiments on the same specimens. The obtained reconstructed images were, however, much better for the bottom illumination experiments and that's why we decided to display only these experiments in this manuscript. We don't have, so far, an accurate explication for this discrepancy.

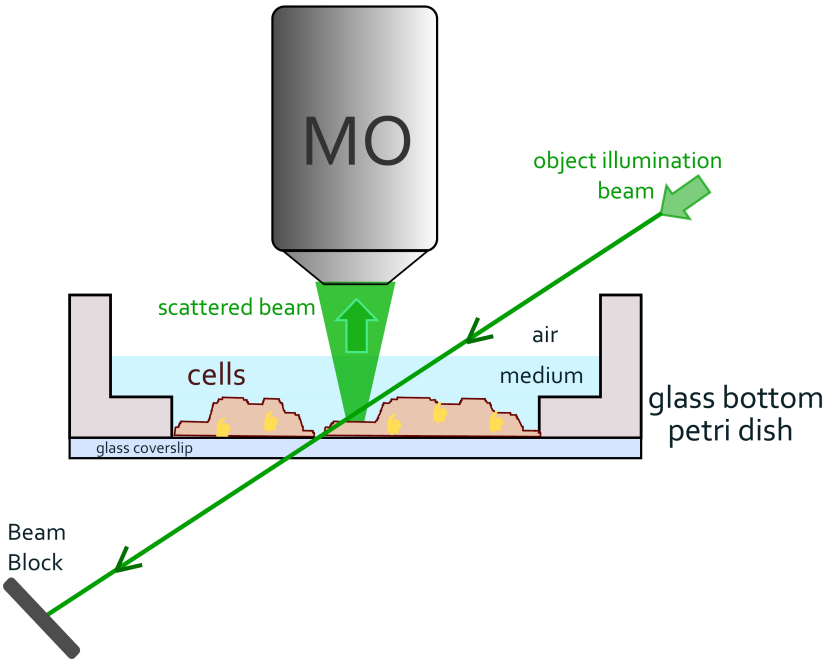

Figure 7.20: Slant illumination geometry. The specimen is illuminated from the top

7.2.2 TIR Illumination Geometry

In this section, we present experimental results obtained on 3T3 fibroblasts labeled with 80 nm fibronectin-coated gold conjugates, with 60 nm fibronectin-coated gold conjugates and with 40 nm gold conjugates using the same experimental setup described in the previous section of this chapter (Section 7.2.1.1), but here the slant illumination configuration is replaced by the TIR illumination geometry, similarly to the geometry described in the previous chapter (Chapter 6). This new optical setup is illustrated on Figure 7.21.

A sequence of M_{acq} CCD holograms is acquired exactly as described in Section 7.2.1.1 and the reconstruction process is also the same.

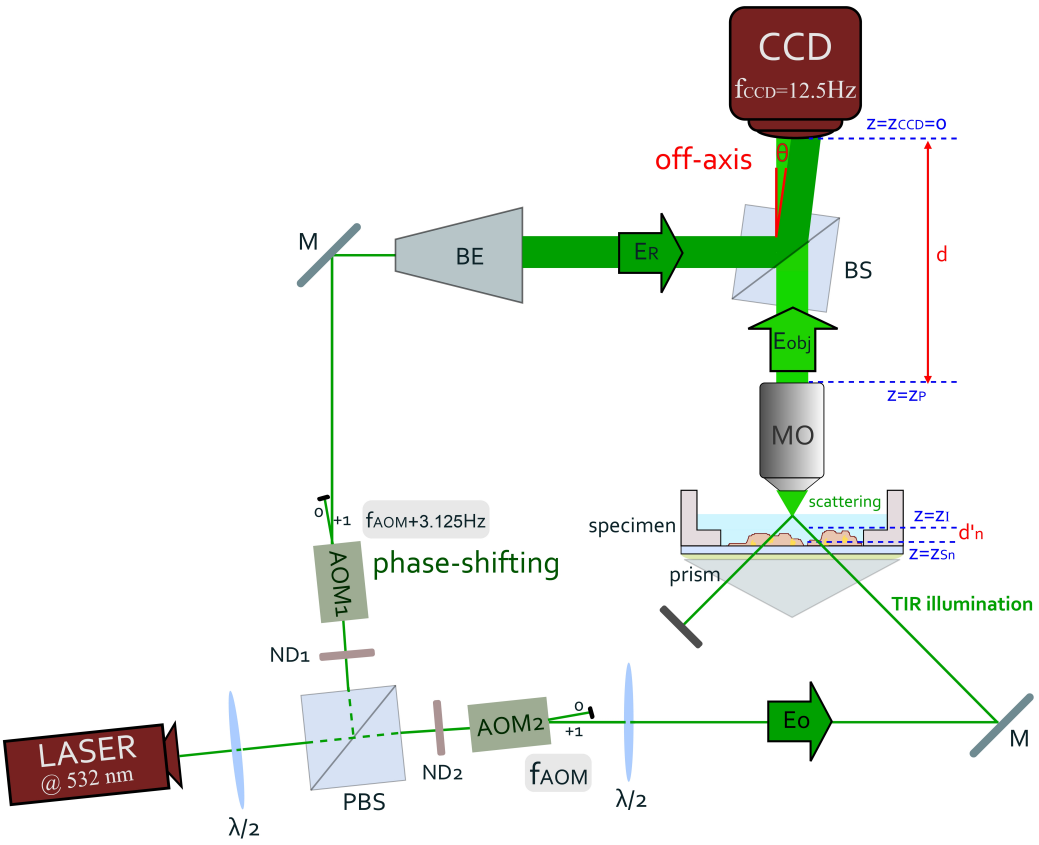

Figure 7.21: Optical apparatus for DHM in total internal reflection

7.2.2.1 3T3 Cells conjugated to 80 nm AuNps

The investigated specimen consists of 3T3 cells labeled with fibronectin-coated 80 nm gold nanoparticles and observed in the glass-bottom petri dish while maintained in the observation medium.

The direct white light image of the considered labeled cells is displayed on Figure 7.22.

Figure 7.23 shows the reconstructed holographic intensity image of the labeled cells displayed in a colored logarithmic scale. The reconstruction is done using 32 CCD frames ($M = 32$) with an exposure time of 80 ms per frame. The displayed reconstructed image is the plane where the brightest points are detected and is obtained for $n = 245$. The background parasitic signal that corresponds to the signal scattered by the cellular features is visible on the reconstructed image and is relatively high. We can, however, discriminate some bright spots that corresponds to gold nanoparticles.

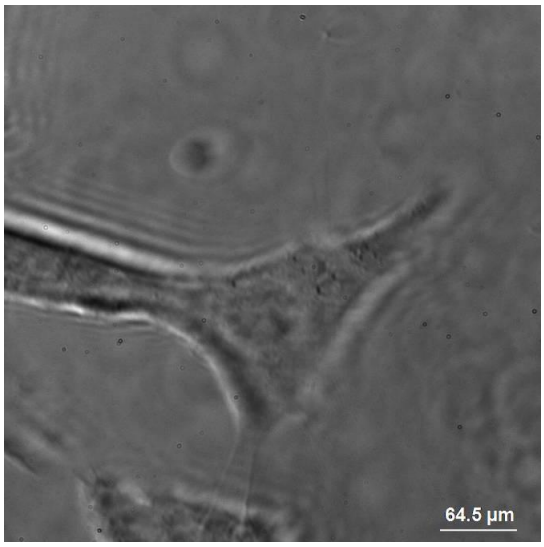

Figure 7.22: Direct white light image of 3T3 fibroblasts conjugated to 80 nm gold nanoparticles

7.2.2.2 3T3 Cells conjugated to 60 nm AuNps

The investigated specimen consists of 3T3 cells labeled with fibronectin-coated 60 nm gold nanoparticles and observed in the glass-bottom petri dish

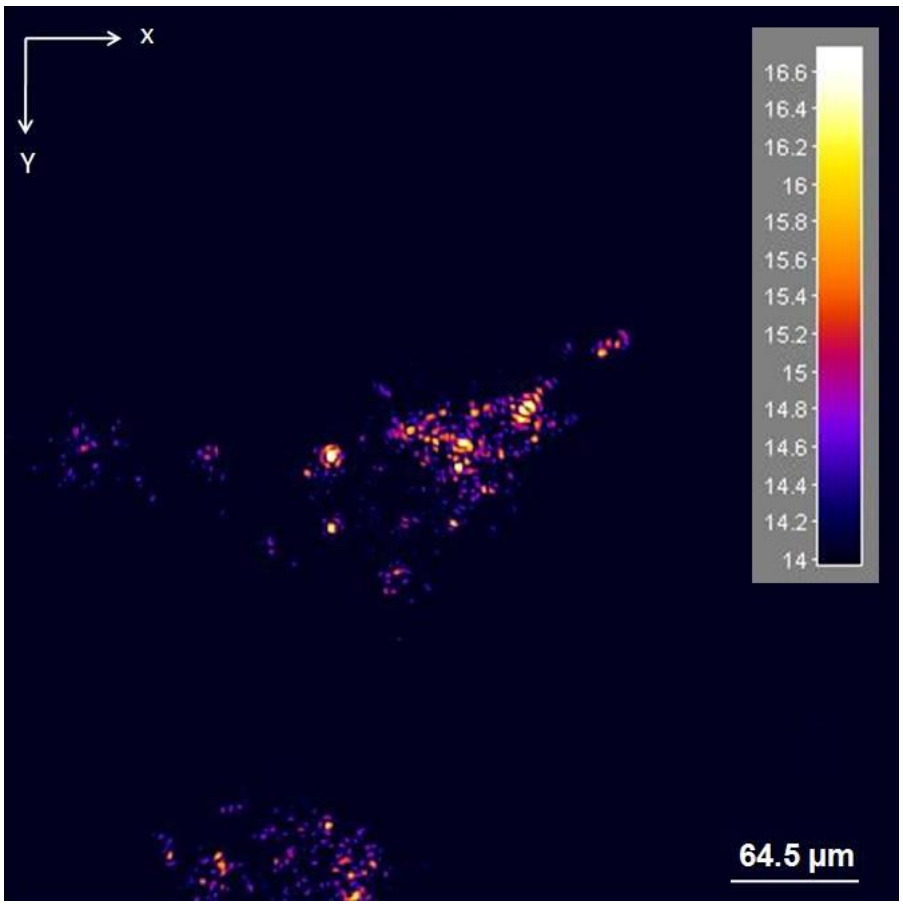

Figure 7.23: Reconstructed holographic intensity image using a TIR illumination geometry in a colored logarithmic scale of 3T3 fibroblasts conjugated to 80 nm gold nanoparticles

while maintained in the observation medium.

The direct white light image of the considered labeled cells is displayed on Figure 7.24.

Figure 7.25 shows the reconstructed holographic intensity image of the labeled cells displayed in a colored logarithmic scale. The reconstruction is done using 32 CCD frames ($M = 32$) with an exposure time of 80 ms per frame. The displayed reconstructed image is the plane where the brightest points are detected and is obtained for $n = 245$. The background parasitic signal that corresponds to the signal scattered by the cellular features is visible on the reconstructed image and is relatively high. We can, however, discriminate some bright spots that corresponds to gold nanoparticles. Here, the intensity of the bright spots that corresponds to the 60 nm gold nanoparticles is lower than the intensity of the bright spots observed in Figure 7.23 , where 80 nm gold nanoparticles are considered. This result is expected since the scattering cross sections of gold nanoparticles varies as a^6, where a is the radius of the particles. Thus, when a decreases, the scattering efficiency decreases as well.

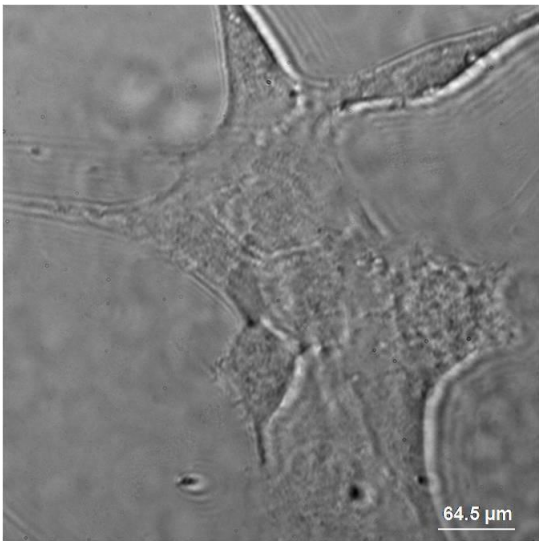

Figure 7.24: Direct white light image of 3T3 fibroblasts conjugated to 60 nm gold nanoparticles

7.2.2.3 3T3 Cells conjugated to 40 nm AuNps

In this section, we have investigated a specimen that consists of 3T3 cells labeled with fibronectin-coated 40 nm gold nanoparticles observed in the

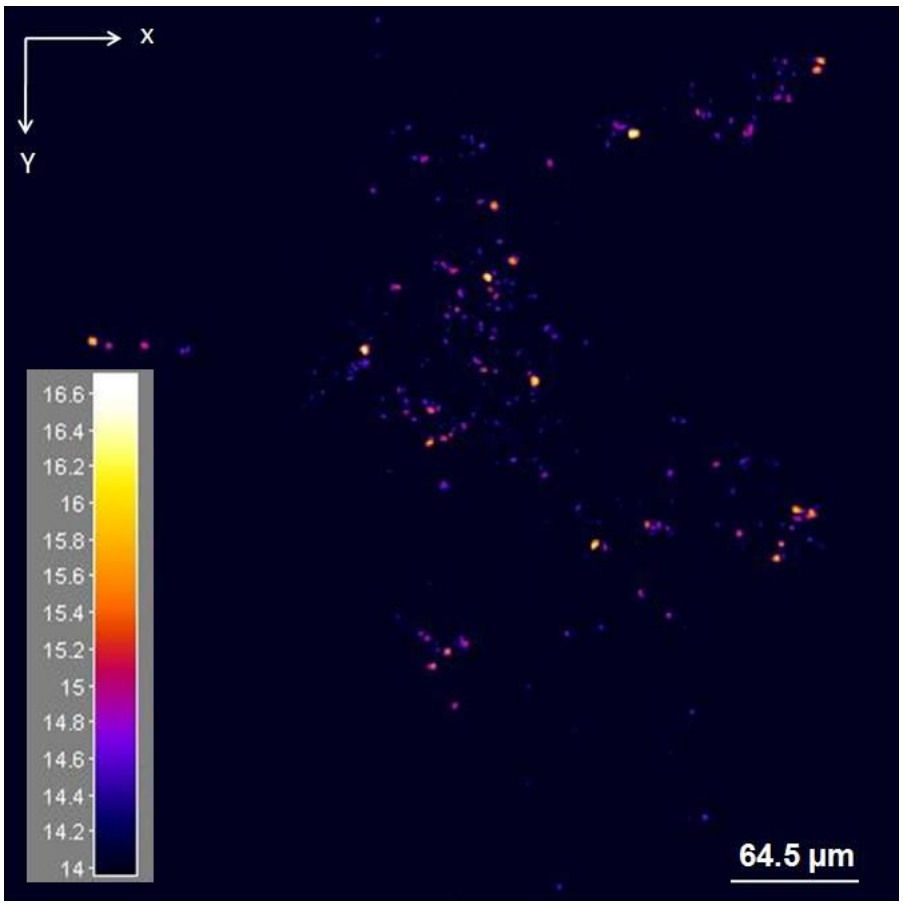

Figure 7.25: Reconstructed holographic intensity image using a TIR illumination geometry in a colored logarithmic scale of 3T3 fibroblasts conjugated to 60 nm gold nanoparticles

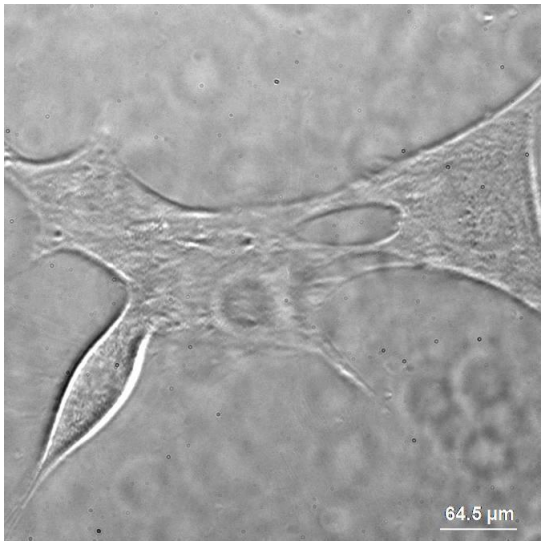

Figure 7.26: Direct white light image of 3T3 fibroblasts conjugated to 40 nm gold nanoparticles

glass-bottom petri dish while maintained in the observation medium.

The direct white light image of the considered labeled cells is displayed on Figure 7.26.

Figure 7.27 shows the reconstructed holographic intensity image of the labeled cells displayed in a colored logarithmic scale. The reconstruction is done using 32 CCD frames ($M = 32$) with an exposure time of 80 ms per frame. The displayed reconstructed image is the plane where the brightest points are detected and is obtained for $n = 221$. The background parasitic signal that corresponds to the signal scattered by the cellular features is visible on the reconstructed image and is relatively high. We can, however, discriminate lot of spherical bright spots that correspond to gold nanoparticles. The quality of this reconstructed image is fascinating. It shows an important improvement over the images presented in the previous chapter. This improvement can be attributed to the following accounts :

- The wavelength of the laser is resonant with the surface plasmons of gold particles
- Specimens are washed with HBSS prior to the observation : an important amount of free gold conjugates are thus eliminated
- Optimized fibronectin-coated gold conjugates are used

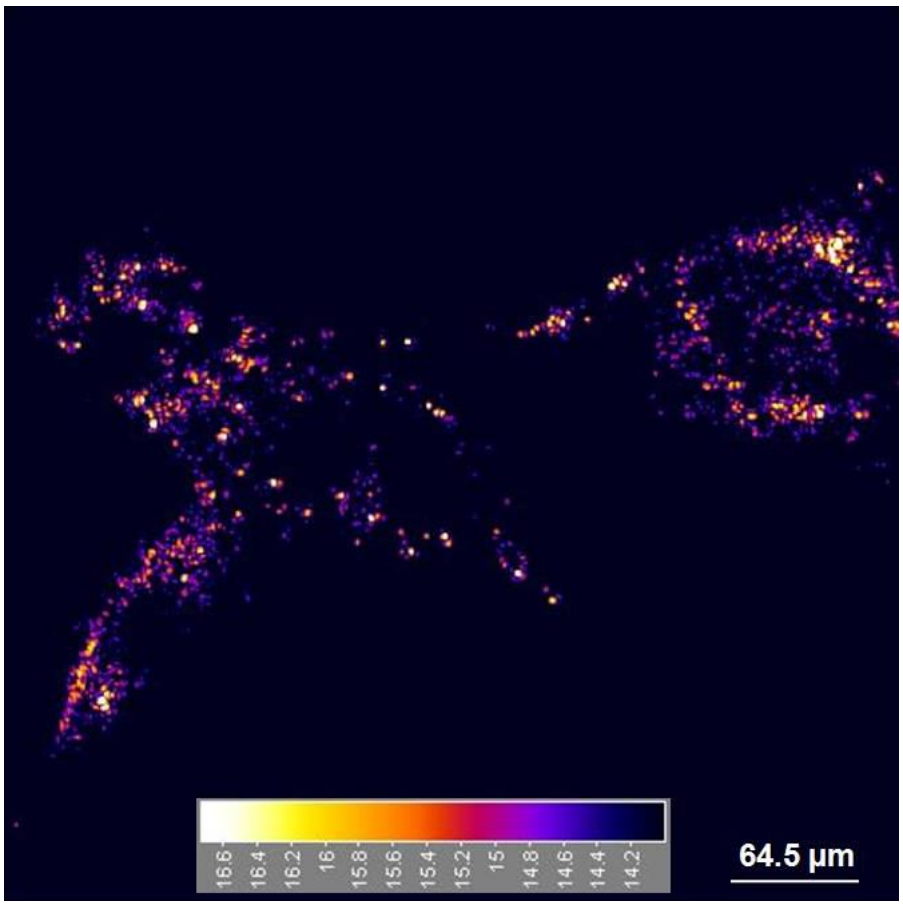

Figure 7.27: Reconstructed holographic intensity image using a TIR illumination geometry in a colored logarithmic scale of 3T3 fibroblasts conjugated to 40 nm gold nanoparticles

Even though the experiments performed using the 80 and 60 nm gold conjugates in TIR geometry (Section 7.2.2.1 and Section 7.2.2.2) were carried out in the same experimental conditions as the experiments performed using the 40 nm gold conjugates, we can clearly see that, by comparing Figure 7.27 to Figure 7.23 and Figure 7.25 , the quality of the reconstructed image obtained by conjugating the 40 nm AuNps to cells is much better than the reconstructed images obtained when 80 and 60 nm AuNps are used. This result leads to the following assumption : The interaction of cells with 40 nm gold conjugates seems to be much efficient than their interaction with 80 and 60 nm gold conjugates. In other words, the interaction probability between a fibronectin-coated gold particle and an integrin receptor increases when the size of the gold conjugates decreases. This effect has been experimentally observed. In fact, when we add 80 or 60 nm AuNps to the cell culture dish, the number of cells that interact with the Au markers is low. However, when 40 nm AuNps are used, lot of cells on the culture slide create links with these markers.

It should be noted here that we have obtained other images of cells labeled with 40 nm AuNps (that are not displayed in this manuscript) with a quality as good as Figure 7.27. This proves the accuracy of the results and the reproducibility ability of our holographic imagery method.

7.3 Experiments using a Short Coherence Length Laser

We have seen, from the experimental results presented in this chapter and in the previous chapter (Chapter 6), that the high parasitic background signal that corresponds to the signal scattered by the cellular features is superimposed to the signal scattered by the gold nanomarkers. In fact, as described in Chapter 2 of this manuscript, biological cells are very heterogeneous : they consists of complex structures composed of different components (cell membranes, nucleus, cellular organelles etc...). Due to mismatches in the refractive index of these different cellular components, optical scattering occurs also at the cellular level. Consequently, the light scattered from the cell is superimposed with the light scattered by the gold nanomarkers reducing by this means the SNR and the localization precision estimation. This is thus a main limitation for the detection and localization of gold nanoparticles in biological environments.

In an attempt to improve our experimental results, by removing the

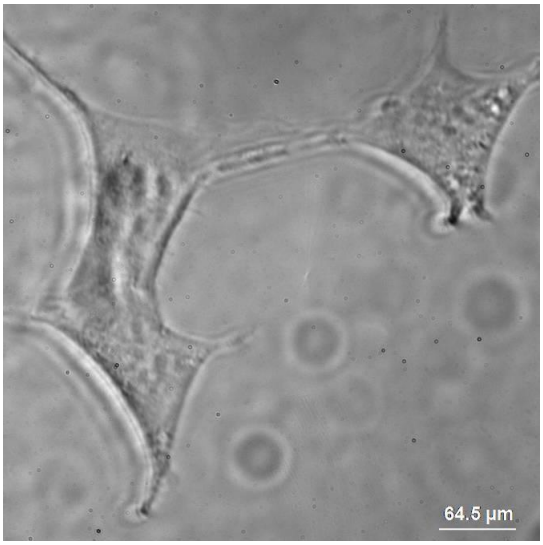

Figure 7.28: Direct white light image of 3T3 fibroblasts

parasitic signal scattered by the cellular features, we have used a short coherence length laser source (Red CrystaLaser, 50 mW) emitting at $\lambda = 660$ nm. The coherence length of this laser source is $\ell_c \simeq 500\mu m$. Using this laser, we expected to eliminate all the parasitic scattered signal that originates from the cellular structures that are larger than the coherence length of this laser.

For this purpose, we imaged a specimen of 3T3 fibroblasts observed in a glass-bottom petri dish using, first, the short coherence length red laser and then using the initial green laser in order to compare the results.

A direct bright field white light image of the investigated fibroblasts is displayed on Figure 7.28 .

Holographic experiments are performed using the same experimental apparatus described in Section 7.2.2 . The acquisition of holograms and the reconstruction procedures are exactly the same as in the previous sections of this chapter.

Figure 7.29a is the reconstructed holographic intensity image of the considered 3T3 fibroblasts illuminated using the short coherence length red laser source while Figure 7.29b is the reconstructed holographic intensity image of the same cells but illuminated using the initial green laser source. Both figures are displayed in a colored logarithmic scale.

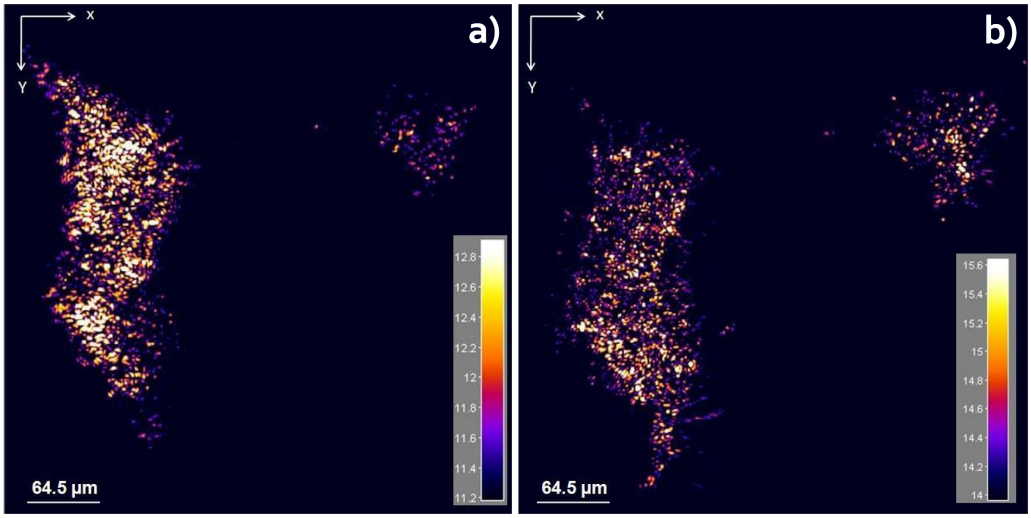

Figure 7.29: Reconstructed holographic intensity image using a TIR illumination geometry in a colored logarithmic scale of 3T3 fibroblasts illuminated by (a) a short coherence length red laser and (b) a green laser

From Figure 7.29a we can clearly see that even when a short coherence length laser is used, the cellular structures still exhibit an important scattering signal. By comparing Figure 7.29a and Figure 7.29b, we can see that the parasitic signal scattered by the cellular structures is not drastically decreased when a short coherence length source is used. This means that the dimensions of the cellular structures are smaller than the coherence length of the red laser and probably on the order of its wavelength. Thus these cellular structures exhibit a coherent scattered signal that cannot be easily eliminated. It should be noted that the scale bars in Figure 7.29a and Figure 7.29b are not the same since, as we have mentioned in Chapter 2 of this manuscript, the scattering efficiency of biological cells depends on the illumination wavelength. In fact, scattering processes in biological tissues are more significant at short wavelengths and their efficiencies decreases when the wavelength of the illumination light increases.

7.4 Overview

In this chapter, we have presented some technical and experimental developments in order to overcome the limitations confronted in the experiments presented in the previous chapter.

First we have reported the developments achieved for the biological preparation procedure of the specimens.

Second, we have tried to image the specimens using an alternative dark-field configuration which is the slant illumination geometry. Nevertheless, images obtained using this illumination configuration were not satisfying and the total internal reflection illumination gives much better results. Accordingly, we have presented experimental results, obtained using the TIR geometry, for 3T3 fibroblasts labeled with 80, 60 and 40 nm AuNps. Gold nanoparticles were detected for theses three cases. However, images of the cells labeled with 40 nm conjugates are much better. In fact, the interaction of cells with 40 nm gold conjugates seems to be much efficient than their interaction with 80 and 60 nm gold conjugates.

Finally, we have tried to use a short coherence length laser source in an attempt to eliminate the inherent parasitic noise induced by the heterogeneous structure of biological cells. However, experimental results show that this parasitic noise has not drastically decreased when this laser is used since the dimensions of the cellular structures are smaller than the coherence length of this laser. They exhibit thus a coherent scattered signal that cannot be easily eliminated.

Chapter 8

Conclusion and Perspectives

In this thesis, we have reported the detection and localization, in three dimensions, of nanometric-sized colloidal gold particles used as biological markers in live cells environments for the first time in the context of digital holographic microscopy.

We have developed a novel heterodyne holographic microscope that combines the off-axis geometry and phase-shifting interferometry. Aliasing-free holograms are thus obtained by applying the phase-shifting technique that is performed using two accurately synchronized Acousto-Optic modulators, and since a heterodyne detection is performed, holograms are only shot-noise limited.

We have also elaborated an ingenious numerical reconstruction method that offers striking advantages. Investigated specimens are reconstructed using the established reconstruction method which is, mainly, a two-steps procedure :

- First, the conjugate image of the specimen is reconstructed, from the recorded hologram, using the Fresnel transformation method that involves a single Fourier transformation
- The specimen is then reconstructed by free-space propagation of the reconstructed conjugate image's angular spectrum. The Angular spectrum method involves two Fourier transformation

The reconstruction of the conjugate image is not straightforward. In fact, the microscope objective, that is employed to image the specimen, induces phase distortions and a magnification effect. Furthermore, the off-axis configuration gives rise to a tilt effect. These three parameters should be determined and compensated in order to achieve a proper reconstruction. Classically, the lens, magnification and tilt parameters are calculated using a plane wave calibration of the optical setup. However, in our established reconstruction approach, these parameters can be automatically obtained, without an additional experimental calibration, by a pioneer reconstruction of the

microscope objective exit aperture's image. Furthermore, by reconstructing the MO exit aperture's image, spatial filtering can be performed very easily.

We have investigated live biological specimens that consist mainly of functionalized gold nanoparticles conjugated to the integrin surface receptors of live NIH 3T3 mouse fibroblasts. A scattering-based detection method is used. Since the intensity of the light scattered by nanometric-sized spherical particles varies as the sixth power of the particle' size, the detected light is relatively weak. Hence a TIR dark-field illumination configuration was adopted in order to detect this weak scattered signal using the full dynamic range of the detector. Furthermore, biological cells are not completely transparent. Their constituents are of the order of the wavelength and are optically very heterogenous with different refractive indexes. They exhibit thus coherent scattered signal that is superimposed to the AuNps signal. Consequently, the detection of gold nanomarkers in biological environments is quite challenging.

Using our developed holographic microscope and our elaborated numerical reconstruction procedure, we have been able to image and localize, gold nanoparticles, down to 40 nm diameter, attached to the integrin surface receptors of live 3T3 fibroblasts with a localization precision of 5 nm laterally and 100 nm in depth, when 32 images averaging is performed. Additionally, by stacking several 2D-reconstructions of selected depths, 3D mapping of the entire scattered field was achieved. The 3D exploration was performed within a relatively big volume $\sim 90\mu m^3$.

We have also characterized the scattering regimes of the gold markers and cellular structures by analyzing the 3D shape of the corresponding scattering patterns that are easily accessible by digital holography :

- For cells, the anisotropy factor g_{bio} is close to one yielding to a scattering that is peaked in the forward direction of the incident light. Consequently the 3D scattering patterns are angularly tilted. Furthermore, the disk that corresponds to the MO exit pupil's image does not present an homogeneously illuminated structure : one of its sides is brighter than the other

- For AuNps, the anisotropy factor g_{Au} is almost null yielding to a relatively isotropic scattering. Consequently the 3D scattering patterns are not angularly tilted. Furthermore, the signal is homogeneously distributed in the disk that corresponds to the MO exit pupil's image

This dissimilarity in the scattering patterns, explained by the inconsistency of the refractive indexes and anisotropy parameters, is easily accessed in holography. Accordingly, the shape of the scattered wavefield can thus be used as a signature that helps to unambiguously discriminate gold nanoparticles from cellular features.

Although good results have been obtained in the TIR illumination geometry using a 90° prism, this configuration presents limitations : the prism should be cleaned before and after each experiment. Furthermore, a problem of standing waves may be encountered especially if long time-tracking experiments are carried out. In the view of overcoming these limitations, we have used an alternative dark field illumination configuration, which is the slant illumination geometry. Nevertheless, images obtained using this illumination configuration were not satisfying and the TIR illumination gave much better results. Using the TIR geometry again, we have imaged 3T3 fibroblasts labeled with 80, 60 and 40 nm AuNps and we have compared the results. For these three cases, we were able to detect the gold nanoparticles. However, images of the cells labeled with 40 nm conjugates are much better. In fact, the interaction of cells with 40 nm gold conjugates seems to be much efficient than their interaction with bigger size gold conjugates. We have been also able to improve our experimental results, obtained on cells labeled with 40 nm AuNps, by washing the cells with Hank's Balanced Salt Solution that has the virtue of removing the free gold conjugates that had not interacted with the cells. Fascinating images of 3T3 fibroblasts labeled with 40 nm gold conjugates were thus obtained.

Finally, we have tried to use a short coherence length laser source in an attempt to eliminate the inherent parasitic noise induced by the heterogeneous structure of biological cells. However, experimental results show that this parasitic noise has not drastically decreased when a short coherence length laser is used since the dimensions of the cellular structures are smaller than the coherence length of this laser. They exhibit thus a coherent scattered signal that cannot be easily eliminated.

During this thesis work, we have tried to monitor the dynamics of the integrin receptors. We were able to track the gold nanoparticles conjugated to these receptors for only short observation times since we don't have a micro-incubator and a heating microscopy stage that are needed to keep the investigated cells alive in proper physiological conditions. The preliminary tracking results that we obtained, for short observation times, show that the nanomarkers are immobile whereas the signal that corresponds to the cells

varies in time.

Now that we have an efficient appropriate microscopy tool with a well defined methodology for the preparation of the biological specimens labeled with 40 nm AuNps, a direct possible future application is long time-tracking experiments in order to characterize the dynamics of the integrin receptors. A characterization of the 3D shape of the cells can also be achieved.

Furthermore, for future developments, it will be interesting to try another illumination geometry that consists of illuminating the specimens in transmission and using a dark-field reflecting objective to collect the scattered light. It will be also interesting to perform holographic microscopy with a partial spatial coherent source [Dubois *et al.* 1999], in order to eliminate, possibly, some of the limiting parasitic signals. After all, it may be advantageous to use different cell lines, neurons for example [Marquet *et al.* 2005] considering that their light scattering efficiency is lower. Subsequently, gold nanoparticles smaller than 40 nm can be expected to be visualized.

Appendix A

Biochemical Protocols

A.1 Biotinylation Protocol

INSTRUCTIONS

PIERCE
3747 N. Meridian Road
P.O. Box 117
Rockford, IL 61105

EZ-Link® Sulfo-NHS-LC-Biotinylation Kit

21435

1776.2

Number	Description
21435	**EZ-Link® Sulfo-NHS-LC-Biotinylation Kit,** sufficient biotin and other reagents for approximately 10 labeling reactions each containing 1-10 mg of antibody or other protein

Kit Contents:

EZ-Link® Sulfo-NHS-LC-Biotin, 25 mg

Molecular Weight: 556.59

Spacer Arm: 22.4 Å

BupH™ Phosphate Buffered Saline Pack, 1 pack, 0.1 M sodium phosphate, 0.15 M sodium chloride; pH 7.2 when reconstituted in 500 ml of ultrapure water

Zeba™ Desalt Spin Columns, 5 ml, 10 columns, for 500-2,000 µl samples, 7,000 MWCO

HABA, 1 ml, 10 mM in 0.01 N NaOH

Affinity Purified Avidin, 10 mg

Storage: Upon receipt store vials of biotin reagent and avidin at -20°C. Store remaining kit components kit at 4°C. Kit is shipped at ambient temperature.

Table of Contents

Introduction 2
Important Product Information 2
Procedure for Biotinylating Proteins 3
A. Calculations 3
B. Biotin Labeling Reaction 3
C. Buffer Exchange and Remove Excess Biotin Reagent Using a Desalting Column 4
HABA Assay for Measuring the Level of Biotin Incorporation 4
A. Reagent Preparation 4
B. Procedure for Estimating Biotin Incorporation 4
C. Calculations for Moles of Biotin Per Mole of Protein 5
Troubleshooting the HABA Assay 6
Website Resources 6
Related Pierce Products 6
Product References 6

Introduction

The EZ-Link® Sulfo-NHS-LC-Biotinylation Kit provides the reagents required for labeling antibodies, proteins and other macromolecules containing primary amino groups with biotin. Besides the biotin reagent and reaction buffer, the kit includes desalting columns for purifying the labeled molecule and HABA and avidin for measuring biotin incorporation. The kit is structured for labeling 1-10 mg of protein in a 1 ml reaction volume but is easily adapted to smaller or larger scales.

Biotin is a small naturally occurring vitamin that binds with high affinity to avidin and streptavidin proteins. Because of its size (244 Da), biotin can be conjugated to many proteins without altering their biological activities. The labeled molecule then can be detected in ELISA, dot blot or Western blot methods using streptavidin or avidin probes.

N-Hydroxysuccinimide (NHS) ester-activated biotins are the most popular type of biotinylation reagent. NHS esters react efficiently with primary amino groups (-NH_2) in pH 7-9 buffers to form stable amide bonds (Figure 1). Because antibodies and other proteins generally contain multiple lysine (K) residues in addition to the N-terminus of each polypeptide, they have multiple primary amines available as targets for labeling with NHS-activated reagents. EZ-Link® Sulfo-NHS-LC-Biotin is water soluble, enabling reactions to be performed in the absence of organic solvents such as DMSO or DMF.

The EZ-Link® Sulfo-NHS-LC-Biotinylation Kit combines the basic reagents, tools and easy-to-follow instructions for biotin-labeling amine-containing macromolecules. With this kit, even researchers who have never before labeled antibodies or other proteins can expect to obtain results comparable to those obtained in commercial laboratories.

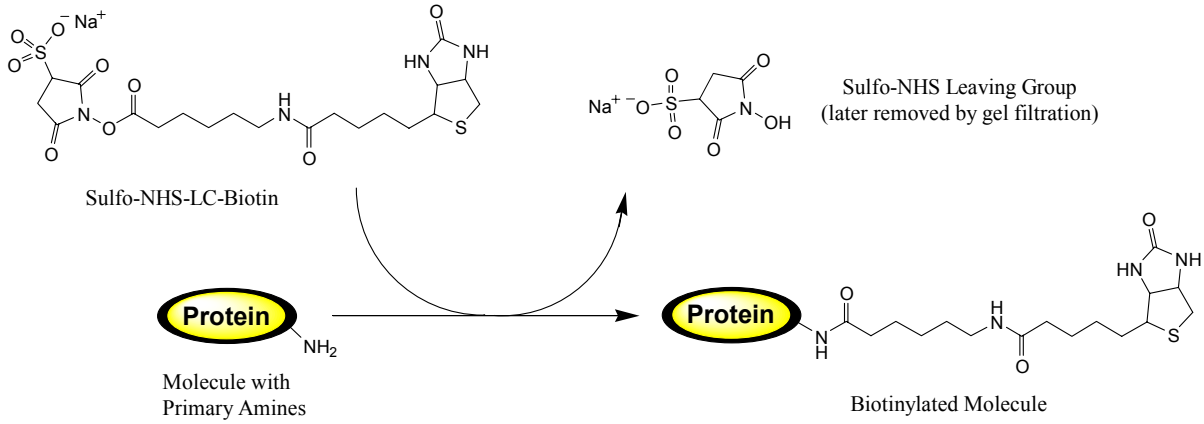

Figure 1. Reaction of Sulfo-NHS-LC-Biotin with primary amine. If drawn to scale, the oval representing the protein would be many times larger than the structures and would likely contain several amino groups. Note that NHS is a leaving group (byproduct) in the reaction. The leaving group and any non-reacted biotin reagent are removed during the desalting step.

Important Product Information

- Sulfo-NHS-LC-Biotin is moisture-sensitive. Store the vial of biotin reagent at -20°C with desiccant. To avoid moisture condensation onto the product, equilibrate vial to room temperature before opening.
- As directed in the procedure, dissolve the biotin reagent immediately before use. The NHS-ester moiety readily hydrolyzes and becomes non-reactive; therefore, weigh and dissolve only a small amount of the reagent at a time, and do not prepare stock solutions for storage. Discard any unused reconstituted reagent.
- Avoid buffers containing primary amines (e.g., Tris or glycine) as these will compete with the reaction (see Figure 1). If necessary, dialyze or otherwise desalt to exchange the protein sample into an amine-free buffer such as phosphate-buffered saline (one packet is included in this kit).
- The desalting columns provided in this kit are best suited for processing biotinylation reactions involving 1-10 mg of protein in approximately 0.5-2 ml. For smaller amounts of protein and/or smaller reaction volumes, perform both the biotinylation reaction and buffer exchanges in a single Slide-A-Lyzer® MINI Dialysis Unit. For reaction volumes that are larger than can be processed with a desalting column, split the sample between two columns or use an appropriate Slide-A-Lyzer® Dialysis Cassette for buffer exchanges. For processing small volumes (i.e. 10-150 µl) of peptides and other low molecular weight molecules, the PepClean™ C-18 Spin Columns (Product No. 89870 or 89873) may be used.

Procedure for Biotinylating Proteins

A. Calculations

The extent of biotin labeling depends on the size and distribution of amino groups on the protein and the amount of reagent used per protein concentration. Compared to reactions involving concentrated protein solutions, labeling reactions with dilute protein solutions require a greater fold molar excess of biotin reagent to achieve the same incorporation level. Experiments performed at Pierce that used a 20-fold molar excess of biotin reagent to label 1-10 mg/ml antibody (IgG) resulted in 4-6 biotin groups per antibody molecule. Adjust the molar ratio of Sulfo-NHS-LC-Biotin to protein to obtain the level of incorporation desired. Instructions for using Sulfo-NHS-LC-Biotin (Product No. 21335) for labeling cells is available for download from the Pierce web site.

1. Calculate millimoles of Sulfo-NHS-LC-Biotin to add to the reaction for a 20-fold molar excess:

$$\text{ml protein} \times \frac{\text{mg protein}}{\text{ml protein}} \times \frac{\text{mmol protein}}{\text{mg protein}} \times \frac{\text{20 mmol Biotin}}{\text{mmol protein}} = \text{mmol Biotin}$$

   - 20 = Recommended molar fold excess of biotin per 1-10 mg/ml protein sample

2. Calculate microliters of 10 mM Sulfo-NHS-LC-Biotin (prepared in Step B.3) to add to the reaction:

$$\text{mmol Biotin} \times \frac{\text{557 mg}}{\text{mmol Biotin}} \times \frac{\text{400 µl}}{\text{2.2 mg}} = \text{µl Biotin Solution}$$

   - 557 = Molecular weight of Sulfo-NHS-LC-Biotin
   - 400 = Microliters of water in which 2.2 mg of Sulfo-NHS-LC-Biotin is dissolved to make a 10 mM solution

Example: For 1 ml of a 2 mg/ml IgG (150,000 MW) solution, ~27 µl of 10 mM Sulfo-NHS-LC-Biotin will be added.

$$\text{1 ml IgG} \times \frac{\text{2 mg IgG}}{\text{1 ml IgG}} \times \frac{\text{1 mmol IgG}}{\text{150,000 mg IgG}} \times \frac{\text{20 mmol Biotin}}{\text{1 mmol IgG}} = 0.000266 \text{ mmol Biotin}$$

$$0.000266 \text{ mmol Biotin} \times \frac{\text{557 mg}}{\text{mmol Biotin}} \times \frac{\text{400 µl}}{\text{2.2 mg}} = 26.9 \text{ µl Biotin Solution}$$

B. Biotin Labeling Reaction

1. Remove the vial of Sulfo-NHS-LC-Biotin from freezer and equilibrate it to room temperature before opening in step 3.
2. Dissolve 1-10 mg protein in 0.5-2 ml of phosphate-buffered saline (PBS) according to the calculation made in section A. Prepare the BupH™ PBS as directed on the package label.

   Note: Protein already dissolved in amine-free buffer at pH 7.2-8.0 may be used without buffer exchange. Proteins in Tris or other amine-containing buffers must be exchanged into PBS. Perform buffer exchange of 0.5-2.0 ml samples by dialysis or using one of the desalting columns included in this kit, as described in Section C. Be aware that this kit contains only 10 single-use desalting columns, sufficient for 10 biotinylation procedures when used only for Section C.
3. Immediately before use, prepare 10 mM Sulfo-NHS-LC-Biotin by dissolving 2.2 mg in 400 µl ultrapure water.
4. Add the appropriate volume of Sulfo-NHS-LC-Biotin solution (see calculations in Section A) to the protein solution.
5. Incubate reaction on ice for two hours or at room temperature for 30-60 minutes.

   Note: There is no harm in reacting longer than the specified time other than the possibility of ordinary protein degradation or microbial growth.

   Note: Although excess non-reacted and hydrolyzed biotin reagent remains in the solution, it is often possible to perform preliminary tests of the labeled protein by ELISA or Western blot. Once function has been confirmed, buffer exchange the labeled protein for optimal performance and stability using the procedure in Section C: Buffer Exchange using a Deslating Column. If the HABA Assay will be performed to determine biotin incorporation, the protein must be purified by buffer exchange first.

C. Buffer Exchange and Remove Excess Biotin Reagent Using a Desalting Column

1. Prepare a Zeba™ Desalt Spin Column by breaking off the bottom plug and placing the column into a 15 ml collection tube. Centrifuge the column at 1,000 × *g* for 2 minutes, discard the storage buffer and return column to the same collection tube.
2. Equilibrate the column by adding 2.5 ml of PBS to the top of the resin bed and centrifuging at 1,000 × *g* for 2 minutes. Discard the flow-through and repeat this step a total of 2-3 times.
3. Place column into a new 15 ml collection tube and apply the protein sample directly onto the center of the resin bed. Allow sample to absorb into the resin.

   Note: For samples < 1,000 µl, add 100 µl ultrapure water on top of the absorbed sample to increase protein recovery.
4. Centrifuge the column at 1,000 × *g* for 2 minutes. The collected flow-through solution is the purified protein sample. Store the protein solution in appropriate conditions.

HABA Assay for Measuring the Level of Biotin Incorporation

To estimate biotin incorporation, a solution containing the biotinylated protein is added to a mixture of HABA and avidin. Because of its higher affinity for avidin, biotin displaces the HABA from its interaction with avidin and the absorbance at 500 nm decreases proportionately. An unknown amount of biotin present in a solution is estimated in a single cuvette by measuring the absorbance of the HABA-avidin solution before and after addition of the biotin-containing sample. The change in absorbance relates to the amount of biotin in the sample.

Note: The biotin-labeled protein sample must be desalted or dialyzed to remove all traces of non-reacted and hydrolyzed biotinylation reagent before the HABA assay is performed.

A. Reagent Preparation

Phosphate-buffered Saline (PBS)	100 mM sodium phosphate, 150 mM sodium chloride; pH 7.2; Product No. 28372
HABA/Avidin Solution	Add 10 mg of avidin and 600 µl of 10 mM HABA to 19.4 ml of PBS. If prepared correctly, the A_{500} of this solution will be 0.9-1.3 in a 1 cm cuvette. The solution is stable for two weeks at 4°C. If a precipitate forms in the HABA solution, it can be filtered and then used.

B. Procedure for Estimating Biotin Incorporation

- **Procedure Option 1 – Cuvette Format**

1. Pipette 900 µl of HABA/Avidin Solution into a 1 ml cuvette.
2. Measure the absorbance of the solution in the cuvette at 500 nm and record the value as A_{500} HABA/Avidin.
3. Add 100 µl of biotinylated protein sample to the cuvette containing HABA/Avidin and mix well.
4. Measure the absorbance of the solution in the cuvette at 500 nm. Once the value remains fairly constant for at least 15 seconds, record the value as A_{500} HABA/Avidin/Biotin Sample. If the A_{500} HABA/Avidin/Biotin is < 0.3, dilute the biotinylated protein sample and repeat the assay, but remember to account for the dilution in during calculations.
5. Proceed to Section C: Calculation of Moles of Biotin Per Mole of Protein.

- **Procedure Option 2 – Microplate Format**

1. Pipette 180 µl of HABA/Avidin Solution into a microplate well.
2. Measure the absorbance at 500 nm of the solution in the well and record the value as A_{500} HABA/Avidin.
3. Add 20 µl of biotinylated sample to the well containing the HABA/Avidin Solution. Mix the plate using an orbital shaker or plate mixer.
4. Measure the absorbance at 500 nm of the solution in the well. Once the value remains fairly constant for at least 15 seconds, record the value as A_{500} HABA/Avidin/Biotin Sample.
5. Proceed to Section C: Calculation of Moles of Biotin Per Mole of Protein.

C. Calculations for Moles of Biotin Per Mole of Protein

Note: An automatic HABA Calculator is available at the Pierce website for performing these calculations.

These calculations are based on the Beer Lambert Law (Beer's Law): $\mathbf{A_\lambda = \varepsilon_\lambda bC}$

Where:

A is the absorbance of the sample at a particular wavelength (**λ**). The wavelength for the HABA assay is 500 nm. There are no units for absorbance.

ε is the absorptivity or extinction coefficient at the wavelength (**λ**). For HABA/avidin samples at 500 nm, pH 7.0 extinction coefficient is equal to 34,000 $M^{-1}cm^{-1}$.

b is the cell path length expressed in centimeters (cm). A 10 mm square cuvette has a path length of 1.0 cm. Using the recommended microplate format volumes, the path length is typically 0.5 cm.

C is the concentration of the sample expressed in molarity (= mol/L = mmol/ml).

The values needed for calculating the number of moles of biotin per mole of protein or sample are as follows:

- Concentration of the protein or sample used, expressed as mg/ml
- Molecular weight (MW) of the protein, expressed as grams per mole (e.g., HRP = 40,000; IgG =150,000)
- Absorbance at 500 nm for HABA/Avidin Solution (**A_{500} H\A**)
- Absorbance at 500 nm for HABA/Avidin/Biotin reaction mixture (**A_{500} H\A\B**)
- Dilution factor, if the sample is diluted before adding it to the HABA/Avidin Solution

1. Calculation #1 is for the concentration of biotinylated protein in mmol/ml (before any dilution for the assay procedure):

$$\text{mmol protein per ml} = \frac{\text{protein concentration (mg/ml)}}{\text{MW of protein (mg/mmol)}} = Calc\#1$$

2. Calculation #2 is for the change in absorbance at 500 nm:

- Cuvette:

$$\Delta A_{500} = (0.9 \times A_{500}\ \text{H\A}) - (A_{500}\ \text{H\A\B}) = Calc\#2$$

- Microplate:

$$\Delta A_{500} = (A_{500}\ \text{H\A}) - (A_{500}\ \text{H\A\B}) = Calc\#2$$

Note: The cuvette format requires the 0.9 correction factor to adjust for dilution of the H\A Solution by the biotinylated protein sample. The microplate format does not require this correction factor because the dilution effect is exactly offset by the increased height and light path length of solution in the well.

3. Calculation #3 is for the concentration of biotin in mmol per ml of reaction mixture:

$$\frac{\text{mmol biotin}}{\text{ml reaction mixture}} = \frac{\Delta A_{500}}{(34{,}000 \times b)} = \frac{Calc\#2}{(34{,}000 \times b)} = Calc\#3$$

Note: ***b*** is the light path length (cm) of the sample. Use ***b*** = 1 with the cuvette format. Use ***b*** = 0.5 with the microplate format when using a standard 96-well plate and the volumes specified in the procedure. The exact path length is the height of the solution through which the plate reader measures the absorbance.

4. Calculation #4 is for the mmol of biotin per mmol of protein:

$$= \frac{\text{mmol biotin in original sample}}{\text{mmol protein in original sample}}$$

$$= \frac{(\text{mmol per ml biotin in reaction mixture})(10)(\text{dilution factor})}{\text{mmol per ml protein in original sample}}$$

$$= \frac{(Calc\#3) \times 10 \times \text{dilution factor}}{Calc\#1}$$

Note: The original biotinylated protein sample was diluted 10-fold in the reaction mixture. Therefore, a multiplier of 10 is used in this step to convert the biotin concentration in the reaction mixture to the biotin concentration in the original sample. If the original sample was diluted before performing the assay, then the dilution factor must be used as well. Calculation #4 yields the biotin:protein molar ratio (average # of biotin molecules per protein molecule).

Example HABA Assay calculation: In this example, the labeled protein is IgG (MW 150,000) at 0.69 mg/ml. The absorbance measurements were A_{500} H\A = 0.904 and A_{500} H\A\B =0.771.

1. $$\text{mmol biotinylated protein per ml} = \frac{0.69\ \text{mg/ml}}{150{,}000\ \text{mg/mmol}} = 4.6\times10^{-6}$$

2. $$\Delta A_{500} = (0.9\times0.904) - 0.771 = 0.0426$$

3. $$\frac{\text{mmol biotin}}{\text{ml reaction mixture}} = \frac{0.0426}{34{,}000} = 1.25\times10^{-6}$$

4. $$\frac{\text{mmol biotin}}{\text{mmol protein}} = \frac{(1.25\times10^{-6})\times10}{4.6\times10^{-6}} = \frac{12.5\times10^{-6}}{4.6\times10^{-6}} = 2.72\ \text{biotin molecules per IgG molecule}$$

Troubleshooting the HABA Assay

Problem	Cause	Solution
ΔA_{500} in HABA assay is ≤ 0	The protein sample has no or a low level of biotinylation because of limited accessible functional groups on the protein	Repeat biotinylation with alternative chemistry (e.g., sulfhydryl-reactive) or use a higher molar ratio of biotinylation reagent
	Incomplete mixing of reagent	Completely solubilize and mix HABA/Avidin before diluting
	Particles in sample contribute to absorbance	Filter protein sample to remove particles
High levels of biotinylation	Nonreacted biotin was not removed	Dialyze or desalt sample before performing the assay

Website Resources

- HABA Calculator for computing the results associated with the HABA Assay measurements
- Tech Tip #14: Perform labeling and other reactions in Slide-A-Lyzer® Dialysis Cassettes

Related Pierce Products

21335 **EZ-Link® Sulfo-NHS-LC-Biotin,** 100 mg, biotin reagent used in this kit

69576 **Slide-A-Lyzer® MINI Dialysis Unit Kit,** for 10-100 µl sample volumes, 10 units plus float

66382 **Slide-A-Lyzer® Dialysis Cassette Kit,** for 0.5-3 ml sample volumes, 10 cassettes, floats and syringes

20347 **ImmunoPure® Immobilized Streptavidin Gel,** 2 ml

21126 **ImmunoPure® Streptavidin, Horseradish Peroxidase Conjugated,** 1 mg

89870 **PepClean™ C-18 Spin Columns**

Product References

Coffman, K.T. *et al.* (2003). Differential EphA2 epitope display on normal versus malignant cells. *Cancer Res.* **63**:7907-12.

Liu, H-B., *et al.* (2003). Estrogen receptor α mediates estrogen's immune protection in autoimmune disease. *J. Immunol.* **171**:6936-40.

Longhurst, C.M., *et al.* (1999). A CD9, $\alpha_{IIb}\beta3$, integrin-associated protein, and GPIb/V/IX complex on the surface of human platelets is influenced by $\alpha_{IIb}\beta3$ conformational states. *Eur. J. Biochem.* **263**:104-11.

Wu, P.C., *et al.* (1999). *In vivo* sensitivity of human melanoma to tumor necrosis factor (TNF)-α is determined by tumor production of the novel cytokine enothelial-monocyte activating polypeptide II (EMAPII). *Cancer Res.* **59**:205-12.

Zhang, L., *et al.* (1999). Calpain inhibitor I increases β-amyloid peptide production by inhibiting the degradation of the substrate γ-secretase. *J. Biol. Chem.* **274(13)**:8966-72.

Zuk, P.A. and Elferink, L.A. (2000). Rab15 differentially regulates early endocytic trafficking. *J. Biol. Chem.* **275(35)**:26754-64.

A.2 Gold Nanoparticles Coating Protocol

"Gold in a Box™" Kit for Preparing highly reactive Antibody and Purified Soluble Protein Gold Conjugates (Cat. #NGIB01-B018)

Introduction:

Lateral flow chromatographic and flow-through tests offer fast detection of critical components for use in point-of-care testing. The key to these tests is the ability to covalently attach antibodies to intensely colored, nanometer particles. Gold sols that bind ligands through a sulfur bond have proved highly successful for this application. For optimal binding of the antibody or protein while retaining a high degree of specific activity, the pH of the gold sol must be adjusted to slightly above the iso-electric point of the coating antibody or protein. This is done through a series of pH titrations with the provided buffers. Varying amounts of buffers A and B, and varying amounts of buffers C and D are added to the gold to create a pH 5-11 range. Next, antibody or protein is added and after 30 minutes the reaction is stopped. This convenient **"Gold in a Box"** kit allows you to quickly (in less than 50 minutes) determine the pI, and optimal coating range for your antibody or soluble protein.

Kit Components:

1. Naked Gold® Sol - 40 nm – 15 OD (1 x 9 ml)
2. Naked Gold® Sol – 20 nm – 15 OD (1 x 9 ml)
3. Buffer Solution A - 1.0 ml (cap with black dot)
4. Buffer Solution B - 1.0 ml (cap with green dot)
5. Buffer Solution C - 1.0 ml (cap with blue dot)
6. Buffer Solution D - 1.0 ml (cap with red dot)
7. BSA Blocking Stabilizer Solution - 2.0 ml (clear cap)
8. Gold Drying Buffer – 2.0 ml (cap with purple dot)

Materials required but not provided:

1. Clean glass or polystyrene test tubes (12 x 75 mm)
2. Pipettes and tips

Sample Preparation:

The antibodies or proteins used with this kit must be at a concentration of 1 mg/ml or greater and should be in a 0.5 X PBS buffer solution. If they are not in a 0.5 X PBS buffer solution, then dialyze the antibody or protein against 0.5 X PBS. Proteins at a concentration of 2 mg/ml or greater should be in 1 X PBS.

Generic Procedure:

Note: Use aseptic technique when handling the gold sol.

1. Shake or swirl gold to resuspend any settled gold. Place 0.5 ml Naked Gold sol into ten (10) clean individual test tubes.
2. Label each tube with the pH value (or, 1 through 10) from the provided pH charts.
3. Use the pH charts to add varying amounts of buffer in microliters to each test tube. Shake to mix.
4. Place each tube on a low speed vortexer and add antibody solution (See Sample Preparation Section) - mix thoroughly (about 2 to 3 seconds)

Ideally, for the 40 nm gold, 7 µl of a 2 mg /ml solution of antibody or protein is optimal. . For the 20 nm gold, ideally, 14 µl of a 2 mg/ml solution of antibody or protein is optimal.

Note: The saturation point for 40 nm gold is typically near 30 mcg of antibody per ml of gold. The saturation point for 20 nm gold is about 60 to 70 mcg of antibody per ml of gold.

5. A deepening purple color and/or black precipitate on some tubes indicates that the antibody or protein is below its iso-electric point, leading to cross-linking of individual gold sols. Cross-linked sols cannot be used in immunological assays and should be discarded. Deep purple sols are usually mostly inactive as well. Only tubes with a slight purple color or no change in color are useful for immunological assays.
6. Allow the reaction to continue for a total of 30 minutes.

Note: See section below on "Stability of Gold Conjugates".

7. Stop the reaction by the addition of 50 µl of Blocking Stabilizer Solution.

Note: In some conjugates that result in non-specific reactivity, it is often best to allow the blocker to react for an additional 16 hours at room temperature.

Stability of Gold Conjugates:

Gold particles completely coated with protein take on the properties of the coating proteins and become very stable in solutions of high ionic strength. An excellent way to test the effectiveness of the conjugation reaction is to combine 10 µl of coated gold sol (prior to the addition of the BSA blocking solution) with 10 µl of 1 M NaCl. Sols with incomplete coating will fall out of solution (turn black), while completely coated sols will remain stable (red).

Testing of BSA Blocked Gold Conjugate:

Conjugate is now ready for use in a rapid assay at nominal usage of 5-15 µl per assay. Tubes that have a slight color change and ones with no color change should be assayed for optimal activity. Tubes with the best activity are usually a good indicator of the approximate iso-electric point of the coated antibody or protein.

BioAssay Works, LLC · 10075 Tyler Place #18 Ijamsville, MD 21754 · (301) 874-8888 · Fax: (301) 874-8889

In order to effectively dry down the gold, add 0.1 ml of Gold Drying Buffer for every 1.0 ml of conjugate. Mix thoroughly. Apply gradually and evenly to either glass fiber or polyester ribbon

Place **polyester ribbon** in a vented 37° C oven or incubator for four (4) hours to dry thoroughly. **Glass fiber** ribbon should be left in the incubator overnight.

The following alternative drying procedure is for polyester ribbon only.
If a vented incubator is not available, use a hairdryer set to deliver 30°C - 37°C heat at a ten (10) inch distance from the ribbon surface. Usually, three (3) or four (4) minutes in a wave-motion will suffice to thoroughly dry the ribbon.

Store all dried ribbons in a glass tightly sealable container containing ample desiccants (granular or pouch-form).

NOTE: This generic procedure may be modified or scaled as needed. When developing a new assay, it is important to determine the optimal amount of ligand to add to the gold particles. Once the tubes have been assayed, it is useful to further optimize binding by both
decreasing or increasing the amount of antibody added to each tube. Often, a 20% increase or decrease in antibody or protein added is sufficient to yield an optimal coating procedure. A few cases require a 40% or more increase or decrease in coating antibody or protein.

Discussion:

A sensitive lateral flow assay requires that all of the antibody or protein that is added to the gold sol be irreversibly bound to the beads. Any free antibody or protein serves to short-circuit the assay. This behavior ultimately sets the sensitivity limits of an assay.

Nano-gold particles remain in solution because they repel each other due to a significant negative charge. This means that proteins bind to gold particles through both ion-exchange attraction and covalent bonding of protein thiols (-SH) with surface gold. The challenge for preparing stable gold conjugates in this “Gold in a Box” format depends upon one's ability to manage the binding of antibody or proteins at or near their iso-electric point. In a few cases, the titration of the pH may need to be fine tuned.

The antibodies or proteins in the sample must display a suitable number of surface thiols (-SH). Proteins with no surface thiol groups bind exchangeably with gold particles through ion-exchange interactions. Such proteins do not form stable gold sols that are suitable for flowing chromatographic assays. Equally problematic are protein preparations where surface thiols have been capped or protected by reaction with N-ethyl maleimide or iodoacetic acid.

Application of Gold conjugates:

Stabilized gold conjugates made from concentrated sols are ready for use in lateral flow and flow-through assays without additional optimizations. Typically, 5-15 µl gold conjugate per test will give optimally sensitive assays.

The gold conjugate is excellent for use in a variety of gold amplified assay procedures. This includes BioAssay Works' patent pending, ultra-sensitive C-FLAT technology. Researchers interested in evaluating this technology may contact BioAssay Works for a research use license with no fee.

pH Charts for Optimal coating at a pH of 5-11 (per 0.5 ml of gold)

Tube Number	pH	Buffer A	Buffer B
1	5.4	9µl	1 µl
2	6.6	8 µl	2 µl
3	7.3	6µl	4 µl
4	7.8	4 µl	6 µl
5	8.2	2 µl	8 µl

Tube Number	pH	Buffer C	Buffer D
6	8.4	10 µl	0 µl
7	8.8	8 µl	2 µl
8	9.2	6 µl	4 µl
9	9.6	4 µl	6 µl
10	10.1	2 µl	8 µl

Please Note:

All buffers and the BSA stabilizer contain less than 0.1 % of sodium azide

Sodium azide is very toxic if ingested or inhaled. Avoid contact with skin, eyes, or clothing. Wear eye or face protection when handling. If skin or eye contact occurs, wash with copious amounts of water. If ingested or inhaled, contact a physician immediately. Sodium azide yields toxic hydrazoic acid under acidic conditions. Dilute azide-containing compounds in running water before discarding to avoid accumulation of potential explosive deposits in lead or copper plumbing.

Appendix B

Published Papers

B.1 3D exploration of light scattering from live cells in the presence of gold nanomarkers using holographic microscopy

Fadwa Joud, Nilanthi Warnasooriya, Philippe Bun, Frédéric Verpillat, Sara Y. Suck, Gilles Tessier, Maïté Coppey-Moisan, Pierre Desbiolles, Michael Atlan, Marie Abboud and Michel Gross, 3D Research, Springer [Joud *et al.* 2011]

Topical Editor: Dr. Tristan Colomb, 3D Res. **02**, 01002 (2011)
10.1007/3DRes.01(2011)2

3DR EXPRESS

3D exploration of light scattering from live cells in the presence of gold nanomarkers using holographic microscopy

Fadwa Joud • Nilanthi Warnasooriya • Philippe Bun • Frédéric Verpillat • Sarah Y. Suck • Gilles Tessier • Michael Atlan • Pierre Desbiolles • Maïté Coppey-Moisan • Marie Abboud • Michel Gross

Received: 16September 2010 / Revised: 05 October 2010 / Accepted: 09 November 2010

Abstract In this paper, we explore the 3D structure of light scattering from dark-field illuminated live 3T3 cells in the presence of 40 nm gold nanomarkers. For this purpose, we use a high resolution holographic microscope combining the off-axis heterodyne geometry and the phase-shifting acquisition of the digital holograms. A comparative study of the 3D reconstructions of the scattered fields allows us to locate the gold markers which yield, contrarily to the cell structures, well defined bright scattering patterns that are not angularly titled and clearly located along the optical axis (z). This characterization is an unambiguous signature of the presence of gold biological nanomarkers, and validates the capability of digital holographic microscopy to discriminate them from background signals in live cells.

Keywords: Digital Holography, Three-dimensional Microscopy, Gold Nanoparticles, and Biological Markers.

Fadwa Joud[1](✉) • Nilanthi Warnasooriya[2] • Philippe Bun[3] • Frédéric Verpillat[4] • Sarah Y. Suck[5] • Gilles Tessier[6] • Michael Atlan[6] • Pierre Desbiolles[4] • Maïté Coppey-Moisan[3] • Marie Abboud[7] • Michel Gross[4]
[1]F. Joud : Laboratoire Kastler Brossel, École Normale Supérieure, 24 Rue Lhomond, 75005 Paris, France
[2]N. Warnasooriya: Institut Langevin, ESPCI, 10 Rue Vauquelin, 75005 Paris, France. Present address: Dept. of Biomedical Engineering, Texas A&M University, College Station, TX 77843, U.S.A.
[3]P. Bun : Institut Jacques Monod, Université Paris-Diderot, 15 Rue Hélène Brion, 75205 Paris, France
[4]F. Verpillat: Laboratoire Kastler Brossel, École Normale Supérieure, 24 Rue Lhomond, 75005 Paris, France
[5]S. Y. Suck : Institut Langevin, ESPCI, 10 Rue Vauquelin, 75005 Paris, France and Fondation Pierre-Gilles de Gennes pour la recherche, 29 Rue d'Ulm, 75005 Paris, France
[6]G. Tessier : Institut Langevin, ESPCI, 10 Rue Vauquelin, 75005 Paris, France
[7]M. Abboud : Département de Physique, Faculté des Sciences, Université Saint-Joseph, Beirut, Lebanon
Tel.: +33-1-44-32-35-12; Fax: +33-1-44-32-34-34
e-mail: fadwa.joud@lkb.ens.fr

1. Introduction

Gold nanoparticles attract great scientific and technological interest because of their physical and chemical characteristics. In particular, the optical tracking of gold nanoparticles in biology has gained popularity for several reasons. Gold nanoparticles provide high scattering efficiencies[1] and they can be detected directly using dark field or total internal reflection (TIR) illumination down to particle diameters of 40 nm as shown by Sönnichsen et al[2]. Unlike fluorescent markers, they are immune to photo bleaching, and they are potentially non-cytotoxic[3]. The shape of gold particles can be engineered to exploit plasmonic resonances and enhance scattering efficiencies, adjust the resonance wavelength, or even to act as local sensors (Murray and Barnes[4], West et al[3]). Because of these properties, the use of simple or specifically designed gold nanoparticles as biomarkers for live cell imaging using photothermal tracking[5], (Boyer et al[6] and Lasne et al[7]) has a high potential. In the present paper, we address the holographic detection of simple, relatively spherical, particles which are easier to fabricate.

As shown by Atlan et al[8], or Cheong et al[9], holography has shown its ability to image and localize nanoparticles in 3D, either for fixed particles spin coated on a glass substrate or in free motion within a water suspension. More recently, Absil et al[10] have shown that heterodyne holography also allows the photothermal detection of 10 nm gold particles, and Warnasooriya et al[11] have imaged 40 nm gold particles in a cellular environment. In that last experiment the particle holographic signal is superimposed with the light scattered by the cell refractive index fluctuations, which yield a speckle field. For particles imaging, this induced speckle is a parasitic signal, but in many other situations, like in Dark Field microscopy, or in Differential Interference Contrast (DIC) microscopy[12] this speckle is the main source of contrast that is used to image the cell itself. It is thus important to discriminate the particle signal from

the cell parasitic speckle.

In this paper, we have imaged biological samples (3T3 cells) labeled with 40 nm gold particles using the digital holographic setup described in Warnasooriya et al[11]. We have performed the 3D holographic reconstruction of the wave-field scattered by the samples, which are illuminated at 45º in a total internal reflection configuration, and we have shown that these wave-fields are noticeably different for the particle, and the speckle signal. We showed here that important information can be derived not only from the intensity of the bright spots caused by the gold particles, but also from the 3D shape of the light scattering pattern, which is easily accessed using holography. We showed, in particular, that the speckle signal keeps memory of the illumination direction, while the particle signal does not. This result has been confirmed by imaging samples of cells that have not been labelled with gold particles, and samples of free gold particles. The shape of the wave-field scattered by the sample can thus be used as a signature that helps to discriminate the particle signal from the speckle.

2. Materials and Methods

The preparation of the biological samples and the holographic setup is the same as in Warnasooriya et al[11]. Nevertheless, in order to help the readers, we have described here the materials and the methods we have used in more details.

2.1 Biological specimen preparation

The biological specimens that we imaged are monolayers of live NIH 3T3 mouse fibroblasts labelled with 40 nm gold particles via their integrin cellular surface receptors. Streptavidin-coated gold nanoparticles were attached to the surface cellular integrin receptors via biotin and fibronectin proteins: see Fig. 1. Streptavidin and biotin are very well known for their strong affinity towards each other, and fibronectin, an extracellular matrix protein, has the property of interacting specifically with cellular surface receptors of integrin family.

Fibronectin proteins (fibronectin from bovine plasma, Sigma, St Louis, MO) were biotinylated using EZ-Link®Sulfo-NHS-LC-Biotin according to the provider protocol (Pierce, Rockford, IL).

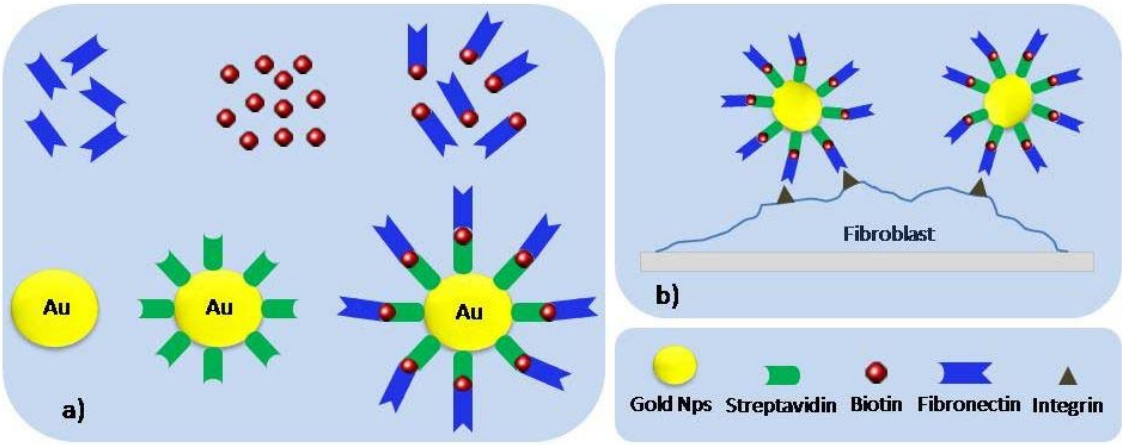

Fig. 1 Gold bioconjugates and fibroblasts preparation procedures: (a) Gold bioconjugates functionalisation. (b) Fibroblasts-gold nanoparticles coupling.

The final concentration of biotinylated-fibronectin solution was 0.447 mg/mL. The streptavidin-coated gold conjugates of 40 nm average diameter (BioAssay, Gentaur, France) were rinsed twice with 1X PBS (Phosphate Buffered Saline) (pH = 7.25). We then diluted 10 µL of the gold solution in 990 µL of the same PBS buffer solution. Then the dilute gold solution was incubated with 50 µL of the biotinylated-fibronectin solution for four hours at room temperature to allow the specific streptavidin-biotin bonding. The final functionalized gold particles solution was kept at 4ºC and used within 24 hours after its preparation in order to ensure maximum functionality. Before every use, the functionalized gold particles solution was sonicated.

48 hours before the observation, monolayers of 3T3 cells were cultured in Duelbecco's modified Eagle's medium (DMEM Gibco, Invitrogen, Carlsbad, CA) supplemented with 10% fetal calf serum (PAA Laboratories GmbH) on 32 mm diameter fibronectin-coated glass cover slips (fibronectin from bovine plasma, Sigma, St Louis, MO) at 37ºC in a 5% CO2 atmosphere. After 24 hours of incubation, we added to each coverslip a solution composed of DMEM (2 mL) plus 500 µL of the functionalized gold particles solution. The binding of integrin and fibronectin occurs at this level allowing the cells to attach, on their surface, the functionalised gold nanoparticles.

The coverslip containing adherent 3T3 cells tagged with 40 nm gold nanoparticles was mounted on a specific observation chamber. In order to maintain the physiological pH condition during the experiments, cells were kept in DMEM-F12 medium (DMEM-F12 without Phenol red, B12 vitamin, Riboflavin, 0.5 % fetal calf serum and supplemented with 20 mM of HEPES [(4-(2-hydroxyethyl)-1-piperazineethanesulfonicacid)] and L-Glutamine from PAA Laboratories). We measured the level of biotin incorporation on an HABA [2-(4' -Hydroxyazobenzene) Benzoic Acid)] quantitation assay to verify the efficiency of the biotinylation protocol. Average number of biotin molecules obtained per fibronectin is 2.5.

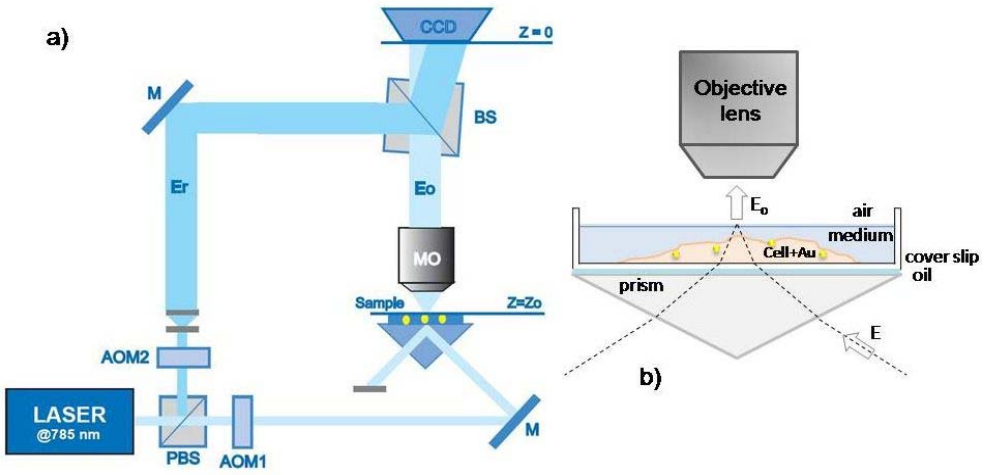

Fig. 2 (a) Experimental setup: AOM1, AOM2: acousto-optic modulators; M: mirror; MO: microscope objective (NA = 0.5); BS: beam splitter; PBS: polarizing beam splitter; CCD: CCD camera; E_r: reference field; E_o: scattered field; z = 0: CCD plane; z = z_0: CCD conjugate plane with respect to MO. (b) Details of the total internal reflection optical arrangement that is used for dark-field illumination of the biological sample

2.2 Holographic Microscope Experimental Setup

Fig. 2 illustrates the optical setup. The illumination source is a single-mode near infrared laser diode emitting at λ = 785nm (DL7140-201S 80 mW Laser Diode @ 90 mA current). A polarizing beam splitter cube (PBS) is used to split the original illumination laser light into two beams, a reference beam (complex field E_R, frequency f_R) and an object illumination beam (complex field E_0, frequency f_0) forming the two arms of a Mach-Zehnder interferometer. A combination of a half wave plate and two neutral density filters is used to prevent the saturation of the detector by controlling the optical power travelling in each arm. Two acousto-optic modulators (AOM1, AOM2) driven around 80 MHz and using the first order of diffraction, shift both frequencies at respectively f_{AOM1} and f_{AOM2}.

The object beam illuminates the sample, prepared as described in Section 2.1, by provoking total internal reflection (TIR) at the medium-air interface in order to prevent direct illumination light from entering the system. A total laser power of 70 mW illuminates a region which is approximately 200 micrometers in diameter, with an optical power density of 56 W.cm^{-2}. This is 5 orders of magnitude lower than the power densities of several MW.cm^{-2} used on living cells in earlier works[5], and can therefore be assumed to be well below their damage threshold. The illumination wave is scattered by the beads and by the local change of refractive index within the cells yielding a propagating scattered wave (complex field E), which is collected by a microscope objective (MO, 50× magnification, NA=0.5, air, focal length f = 3.6 mm). A beam splitter is then used to combine the scattered object wave and the reference wave which is slightly angularly tilted (~ 1°) with respect to the propagation axis of the object wave in an off-axis configuration. A half wave plate on the object illumination arm aligns the polarization of the corresponding beam ensuring its optimal interference with the reference beam. A CCD camera (Roper Cascade 512F, 512×512 square pixels of size d_{pixel} = 16 µm, exposure time 100 ms, frame rate f_{CCD} = 8Hz) detects the interference pattern (hologram) and sends it to a computer. The hologram is then numerically treated and the complex field $E(x,y,z)$ is reconstructed numerically.

2.3 Holographic acquisition

In order to filter out unwanted parasitic signals, we use a heterodyne modulation. A four-phase demodulation method is used to record holograms. This method consists in acquiring a sequence of images with a relative phase shift Δφ = π/2 between two consecutive frames. The reference wave is frequency shifted by tuning the two acousto-optic modulators AOM1 and AOM2 as done by LeClerc et al[13], and we get, as shown by Atlan et al[14], an accurate phase shift Δφ that simplify the phase shifting digital holography demodulation. The heterodyne beat frequency is thus:

$$\Delta f = f_{AOM1} - f_{AOM2} = \frac{f_{CCD}}{4} \quad (1)$$

where f_{CCD} = 8Hz is the frame rate frequency of the CCD camera. The camera records a sequence of 32 frames $I_0,...,I_{31}$, and the object field E on the CCD plane (z = 0) is given by:

$$E(x,y,x=0) = \sum_{n=1}^{M} j^n I_n \quad (2)$$

where j^2 = -1, and M = 32 is the number of frames used for the reconstruction. In Eq.2, the coordinates x,y (with 0 < x,y < 511) are integers, which represent the pixel location within the CCD plane . The pixel size is then the physical CCD pixel size, i.e. 16 µm.

2.4 Holographic reconstruction

The problem of the reconstruction in the context of holographic microscopy has been discussed in details by Colomb et al[15] and Colomb et al[16]. Nevertheless, the Colomb et al. method refers implicitly to the phase-contrast imaging of Marquet et al[17], and is not well suited to the reconstruction of the 3D image of a wave-field as done by Grilli et al[18]. Here, to get a 3D image of the wave-field scattered by the gold particle, we have used a slightly different reconstruction method, which is inspired from the reconstruction method used by Mann et al[19].

First, we considered that the measured hologram represents the field E(x, y, z_0) within the CCD conjugate plane z = z_0 with respect to the Microscope Objective (MO), i.e., the plane, whose image is on focus on the CCD detector.

Since we image the sample through a microscope objective MO, we must compensate the phase curvature, the phase tilt and the enlargement factor that are related to the presence of MO as discussed by Colomb et al[16]. We have thus:

$$E(x,y,z=z_o)=e^{j(k_x x+k_y y)}e^{jA(x^2+y^2)}\sum_{n=0}^{M} j^n I_n \qquad (3)$$

where (K_x, K_y) and A are the tilt and lens parameters respectively that must be determined.

We measured these parameters (or compensated their effect) by an original method that consists in reconstructing the image of the microscope objective output pupil by the one Fourier transform reconstruction method of Schnars and Jüptner[20]. The lens parameter A is then close to the lens parameter that is used in the pupil reconstruction by the Schnars and Jüptner[20] method. On the other hand the tilt parameters (K_x, K_y) are compensated by translating the pupil Schnars and Jüptner[20] image in the center of the calculation grid.

The properly compensated measured hologram represents then the field $E(x, y, z = z_0)$ in the conjugate plane z_0. Then, as done by Mann et al[19] in holographic microscopy, the field $E(x, y, z)$ in the vicinity of the conjugate plane (i.e. $z \approx z_0$) is calculated by the angular spectrum method, which involves two Fourier transforms (see for example [13,21] or [22]). This method is chosen here since it keeps the pixel size δx and δy constant whatever the reconstruction distance z is.

The pixel size $\delta x = \delta y$ which must be calibrated to make a quantitative analysis of the holographic data, is measured by imaging with the same setup geometry a calibrated USAF target located in the CCD conjugate plane. We get $\delta x = \delta y = 177$ nm. The reconstruction is then done for 512 different reconstruction distances

$$z = z_0 + (m_z - 256)\delta z \qquad (4)$$

where $\delta z = 177$ nm and $m_z = 0...511$, and where z_0 is the z coordinate of the CCD conjugate plane (i.e. the plane that is imaged without holographic reconstruction). By this way, we get 3D volume images with 512×512×512 voxels, with the same pixel size $\delta x = \delta y = \delta z = 177$ nm) in the 3 directions x, y and z.

The Schnars and Jüptner[20] reconstruction distance D that makes the MO pupil on focus, and that corresponds to the lens correction factor A, is here $D = 90.0$ cm. Because of the curvature of the reference wavefront, which is not properly calibrated, D is larger than the CCD to pupil physical distance D', which can be deduced from the magnification factor $G = d_{pixel} / d_x \approx D' / f$ yielding $D' \approx 32.5$ cm.

3 Results and Discussion

We have studied different samples of gold marked cell, unmarked cells and of free 40 nm gold particles.

3.1 Samples of marked cells

Fig. 3 show the images of a first sample, with two cells and several particles. Since the holographic setup is adapted on a standard microscope, standard brightfield illumination images are readily obtained. Fig. 3(a) shows a brightfield image obtained, in the same conditions as the holographic images with the laser off and the tungsten lamp on.

The two cells can be seen, but the contrast is low. Fig. 3(b) shows the intensity holographic image of the same region of the sample reconstructed in the $z = z_0$ or $z = 256$ conjugate plane (here and in the following we will express the x, y and z coordinates by the corresponding pixel index m_x, m_y and m_z). The display is made in logarithmic color scale.

Because of the variation of the refractive index within the cells, the illumination light is diffracted yielding a speckle pattern that is superimposed with the particle signal. This speckle is visible on Fig. 3(b), and, from the envelope of the speckled zone, one can guess the shape of the cells. We interpret the brightest points 1, 2 and 3 of Fig. 3(b), which correspond to maximum intensities $I = 11.5\times10^6$, 4.6×10^6, and 8.4×10^6 and Digital Count (DC) respectively, as being particles signal. Many other bright points are also visible, but it is not simple to determine, which points are particles, and which are speckle hot spots. This is especially true within circle 4, where many bright points, close together, are visible.

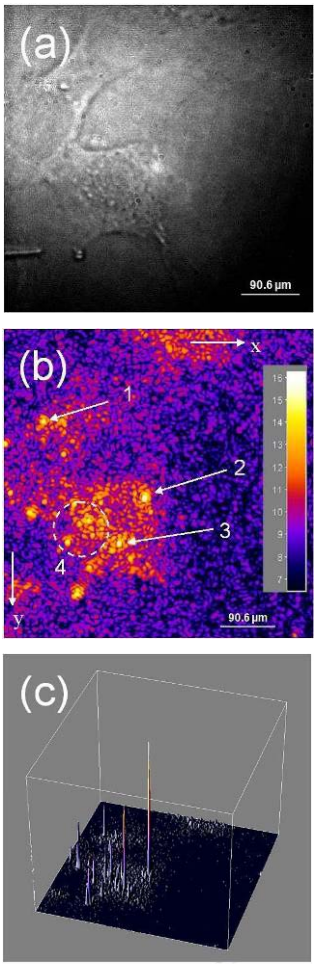

Fig. 3 Images of the first sample with two fibroblast cells marked with 40 nm gold particles. (a) Direct white light illumination image. (b) Holographic intensity reconstructed image near the $z = z_0$ conjugate plane ($z = 255$). The display is made in linear grey scale for the intensity $I = |E|^2$. Black correspond to $\ln I = 5.9$, white to $\ln I = 16.3$ Digital Counts (DC). (c) 3D linear surface plot of the same data

To better visualize the 40 nm gold particles, we have displayed, on Fig. 3(c), by using the Interactive 3D Surface Plot plug-in of Image J[23], a 3D linear surface plot of the region of the sample that is displayed on Fig. 3(b). As seen,

the particles that correspond to sharp peaks can be easily visualized, but some ambiguity remains around the meaning of the lower peaks, which could be attributed either to particles, noises, or scattering by biological features of the cell.

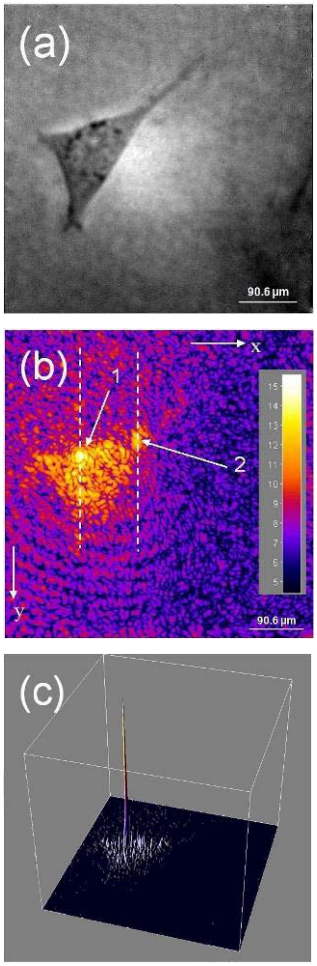

Fig. 4 Images of the second sample with one fibroblast cells marked with one 40 nm gold particle. (a) Direct white light illumination image. (b) Holographic intensity reconstructed image for the z = 325. The display is made in logarithmic color scale for the intensity $I = |E|^2$. Black correspond to ln I = 4.48, white to ln I = 15.56 Digital Counts (DC). (c) 3D linear surface plot. Images are taken from Warnasooriya et al (2010)

The images of Fig. 4 are obtained for a second sample with a single cell, and, as we will see, a single gold particle. Fig. 4(a) shows a white light image of the sample. One can see the cell, whose shape is triangular. Fig. 4(b) shows the intensity holographic image reconstructed for z = 325 (i.e. 6.93 µm above the $z = z_0$ conjugate plane), with logarithmic color scale display. Here again, the speckle related to the light diffracted by the cell is visible on Fig. 4(b), and one can guess the triangular shape of the cell. The brightest point (arrow 1 on Fig. 4(b)) is interpreted as a particle. Since the illumination intensity and focusing area is not well controlled, the particle maximum intensity $I = 2.9\times10^6$ DC obtained here is noticeably lower than for the first sample. Nevertheless, the signal obtained for the bright point marked by arrow 2 is more than 10 times lower (i.e. $I = 1.9\times10^5$), so we can interpret it as a speckle hot spot. This result is confirmed by Fig. 4(c) that shows a 3D linear surface plot of the sample.

The images of Fig. 4 are obtained for a second sample with a single cell, and, as we will see, a single gold particle. Fig. 4(a) shows a white light image of the sample. One can see the cell, whose shape is triangular. Fig. 4(b) shows the intensity holographic image reconstructed for z = 325 (i.e. 6.93 µm above the $z = z_0$ conjugate plane), with logarithmic color scale display. Here again, the speckle related to the light diffracted by the cell is visible on Fig. 4(b), and one can guess the triangular shape of the cell. The brightest point (arrow 1 on Fig. 4(b)) is interpreted as a particle. Since the illumination intensity and focusing area is not well controlled, the particle maximum intensity $I = 2.9\times10^6$ DC obtained here is noticeably lower than for the first sample. Nevertheless, the signal obtained for the bright point marked by arrow 2 is more than 10 times lower (i.e. $I = 1.9\times10^5$), so we can interpret it as a speckle hot spot. This result is confirmed by Fig. 4(c) that shows a 3D linear surface plot of the sample.

To go further, and to better characterize the particle's signal with respect to hot spots, we have analyzed the 3D images of the wave-field obtained by performing the holographic reconstruction for the 512 different reconstruction distances of Eq.4. The 3D data were displayed using the Volume Viewer plug-in of Image J, which is able to display cuts of 3D data in arbitrary planes. By using this plug-in, we have performed cuts parallel to the yz plane of incidence of the sample illumination beam (see Fig. 2(b)).

Fig. 5(a) shows the image of a cut made in the plane x = 128, which intersects the particle signal 1 of Fig. 4(b). The particle is seen as a bright spot on the yz cut image. We can notice here that the particle signal is located at z~325 coordinate, which corresponds to the reconstruction plane of Fig. 4(b). This is expected, since we have chosen to display on Fig. 4(b) the plane where the maximum intensity is reached in 3D, and since this maximum corresponds to the particle we consider here.

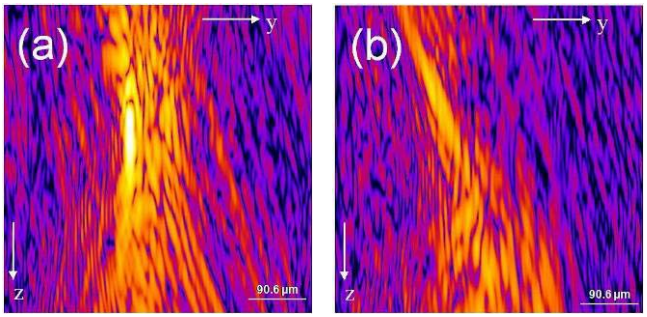

Fig. 5 Images of the second sample obtained by performing cuts of the 3D data parallel to the y and z axis. Cuts are made in planes x = 128 (a) and x = 221 (2), which corresponds to the white dashed lines 1 and 2 of Fig.4 (b) respectively. The display is made in the same logarithmic color scale than Fig.4 (b) by Volume Viewer.

The image of Fig.5(b) corresponds to x = 221 i.e. to a cut that intersect the bright spot 2 of Fig. 4(b) that we interpret as a speckle hot spot. Contrarily to the particle, the hot spot signal extension along the x axis (vertical axis on the Fig. 5 images) is quite large. Moreover, the hot spot image is angularly tilted in the yz plane.

This angular tilt can be simply interpreted by describing how the light propagation is governed in the biological cells. This propagation is dependent on the phase function inside the illuminated cell. Because biological tissues are inhomogeneous, the form of their phase function is not well defined and is thus characterized by the anisotropy

coefficient g, which is the average cosine of the phase function. This parameter g describe the asymmetry of the single scattering pattern ; it is thus null when the scattering is isotropic, equals 1 for forward scattering and equals -1 in the case of backward scattering. In our experiments, the illuminated cells are maintained in DMEM medium that consists mainly of water. Since the refractive index of cells is close to that of water, the cell anisotropy factor g is close to one (g~0.9 in biological tissues as mentioned by Cheong et al[24]). As a consequence, the light scattered by the cells mainly follows the forward scattering regime and the observed light scattering pattern appears to be tilted by approximately 45° since the incident illumination laser beam is initially tilted by 45° in conformity with the TIR illumination geometry (see Fig. 2(b)).

The exact shape of the hot spot's wave-field can be calculated, but it is quite complicated. It involves the calculation of the angular distribution of the scattered light, which depends on the cell anisotropy factor g. One must then calculates the refraction of the scattered light on the medium-air interface, and takes into consideration the collection of light by the microscope objective. The quantitative analysis of the wave-field's shape, which yields the angular tilt, is thus out of the scope in the present paper, and one can simply say that the hot spot signal keeps some memory of the illumination direction, and is thus angularly tilted in the yz plane.

If one considers a gold particle, the average cosine of the scattering phase function g in water can be determined by Mie calculation from the wavelength (λ = 532 nm), the particle diameter (40 nm), and the refractive indexes of gold (n_{au} = 0.46- *j*2.41 at 532 nm) and water (n_w = 1.33). One gets $g < 10^{-3}$ (see: http://omlc.ogi.edu/calc/mie_calc.html). This means that the gold particle scatters light in all directions without memory of the illumination direction.

One can notice that a similar angular tilt effect has been observed recently on the photothermal signal of 50 nm and 10 nm gold particles by Absil et al[10].

3.2 Control experiments performed on free particles or on unmarked-cells

In order to confirm our interpretation of the angular tilt seen on Fig. 5(b), we have performed some control experiments by imaging an unmarked cell sample and another sample of free gold particles.

3.2.1 Unmarked cell sample

Fig. 6 shows the results obtained with a cell sample without particle. The direct white light image is shown in Fig. 6(a). Fig. 6(b) shows the holographic intensity reconstructed image that shows the light scattered by the cell refractive index inhomogeneities. This scattered light, which has a speckle structure, exhibits several hot spots that correspond to bright points on Fig. 6(b), and we have chosen to image on Fig. 6(b) the reconstruction plane z = 252 that corresponds to the maximum hot spot intensity (5.85×10^5 DC).

The image we get here without particle is visually quite similar to Fig. 3(b) which is obtained with several particles. The 3D linear surface plot shown in Fig. 3(c) does not help since it is visually similar to Fig. 3(c). Nevertheless, the maximum of the bead signal (11.6×10^6 DC) in Fig. 3(b) and (c) is much higher than the maximum of the hot spot signal (5.85×10^5 DC) in Fig. 6(b) and (c). This makes the background noise visually higher in Fig. 6(c).

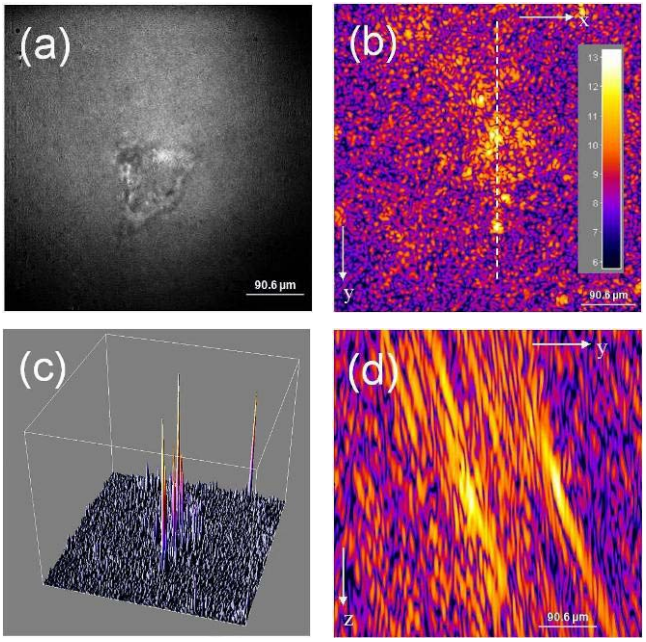

Fig. 6 Images of an unmarked cell sample. (a) Direct white light illumination image. (b) Holographic intensity reconstructed image for the z = 252. The display is made in logarithmic color scale for the intensity $I = |E|^2$. Black correspond to ln I = 5.80, white to ln I = 13.28 Digital Counts (DC). (c) 3D linear surface plot. (d) Image obtained par performing cut of the 3D data in the plane x = 271 that corresponds to the white dashed line seen in (b). The display is made by Volume Viewer with the same logarithmic color scale as in (b)

Fig. 6(d) shows the yz image obtained by performing a cut in the plane x = 271 that intersects the two brightest speckle hot spots of the sample. Now the yz image obtained in Fig. 6(d) without particle is qualitatively different than with a particle in Fig. 5(a). The signal is angularly tilted like in Fig. 5(b), and its extension in the z direction (vertical axis) is larger.

3.2.2 Free particles sample

The images of Fig. 7 are obtained for free particles (uncoupled to cells) in Brownian motion in a water and agarose suspension. Here, we used agarose to slow down the motion of the particles enough to make the displacement of the particles negligible during the time of acquisition of the sequence of M = 32 frames.

Fig. 6(a) is the holographic intensity reconstructed image. The brightest points correspond to particles that are located within the reconstruction plane, while the less bright points are interpreted as out of focus particles. Reconstruction is made here in the plane z = 251 which corresponds to the maximum intensity (4.4×10^7 DC) for the brightest spot (marked by a white arrow on Fig. 6(a)). Many particles can be seen on Fig. 6(a) and on Fig. 6(b) that displays the holographic data with 3D linear surface plot.

Fig. 6(c) shows the yz image in the plane x = 258 that intersects the brightest particle and corresponds to the white dashed line on Fig. 6(a). As expected, the image of the particle (white arrow) has a smaller extension along the z direction (vertical direction) and do not exhibit the angular tilt we get with speckle hot spot in Fig. 5(b) and Fig. 6(d). This result confirms our interpretation of the angular tilt observed with the speckle hot spots.

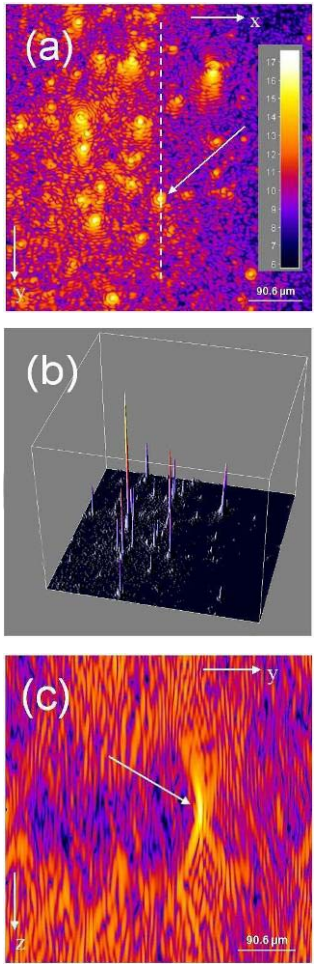

Fig. 7 Images of free gold particles in a water and agarose suspension. (a) Holographic intensity reconstructed image for the z = 251. The display is made in logarithmic color scale for the intensity $I = |E|^2$. Black correspond to ln I = 5.85, white to ln I = 17.61 Digital Counts (DC). (b) 3D linear surface plot. (c) Image obtained par performing cut of the 3D data in the plane x = 258 that corresponds to the white dashed line seen in (a). The display is made by Volume Viewer with the same logarithmic color scale than for (a)

4. Conclusion

To summarize, we have shown that heterodyne holographic microscopy, in the off-axis geometry, is well adapted to the detection of weakly scattering objects. The sensitivity, signal to noise ratio and selectivity of the technique allow the localization of light-scattering gold nanoparticles of a few tens of nanometers, which are good candidates of non-toxic and perennial markers. Biological environments, however, are difficult to address since cell features generate strong parasitic speckle. Here, we have reported the detection of 40 nm particles attached to the surface of live 3T3 mouse fibroblasts. A comparison of these signals with either non-labelled cells or simple gold particles in solution allowed us to unambiguously discriminate particles. We show that, in addition to a stronger scattering signal, gold particles induce a relatively isotropic scattering, whereas biological features are characterized by mostly forward scattering. This dissimilarity in the scattering patterns, explained by the inconsistency of the refractive indexes and anisotropy parameters g, is easily characterized by digital holography, making it an excellent tool for the 3D detection of gold labels in biological environments.

Acknowledgements

Authors wish to acknowledge the French Agence Naionale de la Recherche (ANR) and the “Centre de Compétence NanoSciences Ile de France” (C'nano IdF) for their financial support.

References

1. P. Jain, K. Lee, I. El-Sayed, M. El-Sayed (2006) Calculated absorption and scattering properties of gold nanoparticles of different size, shape, and composition: applications in biological imaging andbiomedicine. *J Phys Chem B*. **110**:7238-7248
2. C. Sönnichsen, S. Geier, N. Hecker, G. Von Plessen, J. Feldmann J, Ditlbacher H, Lamprecht B, Krenn J, Aussenegg, V. Chan, et al (2000) Spectroscopy of single metallic nanoparticles using total internal reection microscopy. *Appl Phys Lett.* **77**:2949
3. JL. West, RA. Drezek, NJ. Halas (2006) Nanotechnology provides new tools for biomedical optics. In: Bronzino JD (ed) Tissue Engineering and Artificial Organs, 3rd Edition, *CRC Press*, pp 25-1-25-9
4. W. Murray, WL Barnes (2007) Plasmonic materials. *Adv Mater*. **19**:3771-3782
5. L. Cognet, C. C Tardin, D. Boyer, D. Choquet, P. Tamarat, B. Lounis (2002) Single metallic nanoparticles imaging for protein detection in cells. *Proc Natl Acad Sci.* **100**:11,350-11,355
6. D. Boyer, P. Tamarat, A. Maali, B. Lounis, M. Orrit (2003) Photothermal imaging of nanometer-sized metal particles among scatterers. *Science.* **297**:1160-1163
7. D. Lasne, GA. Blab, S. Berciaud, M. Heine, L. Groc, D. Choquet, L. Cognet, B. Lounis (2006) Single nanoparticle photothermal tracking (SNaPT) of 5-nm gold beads in live cells. *Biophys J*. **91**:4598-4604
8. M. Atlan, M. Gross, P. Desbiolle, E. Absil, G. Tessier, M. Coppey-Moisan (2008) Heterodyne holographic microscopy of gold particles. *Opt Lett.* **33**:500-502
9. FC. Cheong, BJ. Krishnatreya, DG. Grier (2010) Strategies for three-dimensional particle tracking with holographic video microscopy. *Opt Express*. **18**:13,563-13,573
10. E. Absil, G. Tessier, M. Gross, M. Atlan, N. Warnasooriya, S. Suck, M. Coppey-Moisan, D. Fournier (2010) Photothermal heterodyne holography of gold nanoparticles. *Opt Express.* **18**:780-786
11. N. Warnasooriya, F. Joud, P. Bun, G. Tessier, M. Coppey-Moisan, P. Desbiolles, M. Atlan, M. Abboud,

M. Gross (2010) Imaging gold nanoparticles in living cell environments using heterodyne digital holographic microscopy. *Opt Express.* **18**:3264-3273
12. D. Goldberg, D. Burmeister (1986) Stages in axon formation: observations of growth of Aplysia axons in culture using video-enhanced contrast-differential interference contrast microscopy. *J Cell Biol*. **103**:1921
13. F. LeClerc, L. Collot, M. Gross (2000) Numerical heterodyne holography with two-dimensional photodetector arrays. *Opt Lett.* **25**:716-718
14. M. Atlan, M. Gross, E. Absil (2007) Accurate phase-shifting digital interferometry. *Opt Lett.* **32**:1456-1458
15. T. Colomb, E. Cuche, F. Charrière, J. Kühn, N. Aspert, F. Montfort, P. Marquet, C. Depeursinge (2006a) Automatic procedure for aberration compensation in digital holographic microscopy and applications to specimen shape compensation. *Appl Opt*. **45**:851-863
16. T. Colomb, F. Montfort, J. Kuehn, N. Aspert, E. Cuche, A. Marian, F. Charrière, S. Bourquin, P. Marquet, C. Depeursinge (2006b) Numerical parametric lens for shifting, magnification, and complete aberration compensation in digital holographic microscopy. *J Opt Soc Am A*. **23**:3177-3190
17. P. Marquet, B. Rappaz, P. Magistretti, E. Cuche, Y. Emery, T. Colomb, C. Depeursinge (2005) Digital Holographic microscopy: a noninvasive contrast imaging technique allowing quantitative visualization of living cells with subwavelength axial accuracy. *Opt Lett.* **30**:468-470
18. S. Grilli, P. Ferraro, S. De Nicola, A. Finizio, G. Pierattini, R. Meucci (2001) Whole optical wave_elds reconstruction by digital holography. *Opt Express.* **9**:294-302
19. CJ. Mann, L. Yu, CM. Lo, MK. Kim (2005) High resolution quantitative phase-contrast microscopy by digital holography. *Opt Express.* **13**:8693-8698
20. U. Schnars, W. Jüptner (1994) Direct recording of holograms by a CCD target and numerical reconstruction. *Appl Opt*. 33(2):179-181
21. F. LeClerc, M. Gross, L. Collot (2001) Synthetic-aperture experiment in the visible with on-axis digital heterodyne holography. *Opt Lett.* **26**:1550-1552
22. L. Yu, M. Kim (2005) Wavelength-scanning digital interference holography for tomographic threedimensional imaging by use of the angular spectrum method. *Opt Lett.* **30**:2092-2094
23. M. Abramoff, P. Magalhaes, S. Ram (2004) Image processing with ImageJ. *Biophotonics International*. **11**(7):36-43
24. W. Cheong, S. Prahl, A. Welch (1990) A review of the optical properties of biological tissues. *IEEE journal of quantum electronics.* **26**:2166-2185

B.2 Imaging gold nanoparticles in living cell environments using heterodyne digital holographic microscopy

Fadwa Joud, Nilanthi Warnasooriya, Philippe Bun, Gilles Tessier, Maïté Coppey-Moisan, Pierre Desbiolles, Michael Atlan, Marie Abboud and Michel Gross, Imaging gold nanoparticles in living cell environments using heterodyne digital holographic microscopy, Opt. Express **18**, 3264-3273 (2010) [Joud *et al.* 2010b]

Imaging gold nanoparticles in living cell environments using heterodyne digital holographic microscopy

N. Warnasooriya[1,5], F. Joud[2,4,5]*, P. Bun[3], G. Tessier[1], M. Coppey-Moisan[3], P. Desbiolles[2], M. Atlan[1], M. Abboud[4], and M. Gross[2]

[1] *École Supérieure de Physique et de Chimie Industrielles de la Ville de Paris, Institut Langevin, UMR 7587 CNRS, 10 rue Vauquelin, 75231 Paris Cedex 05; France*
[2] *Laboratoire Kastler Brossel - École Normale Supérieure , UMR 8552 , UPMC, CNRS 24 rue Lhomond , 75231 Paris Cedex 05; France*
[3] *Programme Biologie Cellulaire - Institut Jacques Monod, UMR 7592, CNRS, Université Paris-Diderot, 15 Rue Hélène Brion, 75205 Paris Cedex 13; France*
[4] *Faculté des Sciences - Université Saint Joseph , B.P :11-514 Riad El Solh, Beirut 1107 2050; Lebanon*
[5] *These authors have equally contributed in this paper.*
**fadwa.joud@lkb.ens.fr*

Abstract: This paper describes an imaging microscopic technique based on heterodyne digital holography where subwavelength-sized gold colloids can be imaged in cell environments. Surface cellular receptors of 3T3 mouse fibroblasts are labeled with 40 nm gold nanoparticles, and the biological specimen is imaged in a total internal reflection configuration with holographic microscopy. Due to a higher scattering efficiency of the gold nanoparticles versus that of cellular structures, accurate localization of a gold marker is obtained within a 3D mapping of the entire sample's scattered field, with a lateral precision of 5 nm and 100 nm in the x,y and in the z directions respectively, demonstrating the ability of holographic microscopy to locate nanoparticles in living cell environments.

OCIS codes: (090.1995) Digital holography; (170.0180) Microscopy; (170.1530) Cell analysis; (260.6970) Total internal reflection.

References and links

1. P. K. Jain, K. S. Lee, I. H. El-Sayed, and M. A. El-Sayed, "Calculated absorption and scattering properties of gold nanoparticles of different size, shape, and composition: Applications in biological imaging and biomedicine," J. Phys. Chem. B **110**, 7238–7248 (2006).
2. J. L. West, R. A. Drezek, and H. N. J., "Nanotechnology provides new tools for biomedical optics," in *Tissue Engineering and Artifical Organs, 3rd Edition*, J. D. Bronzino, ed., pp. 25–1–25–9 (CRC Press, 2006).
3. D. Lasne, G. A. Blab, S. Berciaud, M. Heine, L. Groc, D. Choquet, L. Cognet, and B. Lounis, "Single nanoparticle photothermal tracking (SNaPT) of 5-nm gold beads in live cells," Biophys. J. **91**, 4598–4604 (2006).
4. L. Cognet, C. Tardin, D. Boyer, D. Choquet, P. Tamarat, and B. Lounis, "Single metallic nanoparticles imaging for protein detection in cells," Proc. Natl. Acad. Sci. USA **100**, 11350–11355 (2003).
5. D. Boyer, P. Tamarat, A. Maali, B. Lounis, and M. Orrit, "Photothermal imaging of nanometer-sized metal particles among scatterers," Science **297**, 1160–1163 (2003).
6. G. Raschke, S. Kowarik, T. Franzel, C. Sonnichsen, T. A. Klar, and J. Feldmann, "Biomolecular recognition based on single gold nanoparticles light scattering," Nano Lett. **3**, 935–938 (2003).
7. I. H. El-Sayed, X. Huang, and M. A. El-Sayed, "Surface plasmon resonance scattering and absorption of anti-EGFR antibody conjugated gold nanoparticles in cancer diagnostics: Applications in oral cancer," Nano Lett. **5**, 829–834 (2005).

#120483 - $15.00 USD Received 25 Nov 2009; revised 19 Jan 2010; accepted 21 Jan 2010; published 1 Feb 2010

8. U. Schnars and W. P. O. Jüptner, "Digital recording and numerical reconstruction of holograms," Meas. Sci. Technol. **13**, R85–R101 (2002).
9. M. Atlan, M. Gross, and E. Absil, "Accurate phase-shifting digital interferometry," Opt. Lett. **32**, 1456–1458 (2007).
10. F. LeClerc, M. Gross, and L. Collot, "Synthetic-aperture experiment in the visible with on-axis digital heterodyne holography," Opt. Lett. **26**, 1550–1552 (2001).
11. J. Di, J. Zhao, H. Jiang, P. Zhang, Q. Fan, and W. Sun, "High resolution digital holographic microscopy with a wide field of view based on a synthetic aperture technique and use of linear CCD scanning," Opt. Lett. **47**, 5654–5659 (2008).
12. D. Carl, B. Kemper, G. Wernicke, and G. von Bally, "Parameter-Optimized Digital Holographic Microscope for High-Resolution Living-Cell Analysis," Appl. Opt. **43**, 6536–6544 (2004).
13. M. Atlan, M. Gross, and E. Absil, "Digital holography with ultimate sensitivity," Opt. Lett. **32**, 909–911 (2007).
14. F. LeClerc, L. Collot, and M. Gross, "Numerical heterodyne holography with two-dimensional photo-detector arrays," Opt. Lett. **25**, 716–718 (2000).
15. E. Cuche, P. Marquet, and C. Depeursinge, "Spatial filtering for zero-order and twin-image elimination in digital off-axis holography," Appl. Opt. **39**, 4070–4075 (2000).
16. E. Leith and J. Upatnieks, "Microscopy by wave front reconstruction," J. Opt. Soc. Am. **55**, 981–986 (1965).
17. I. Yamaguchi and T. Zhang, "Phase-shifting digital holography," Opt. Lett. **22**, 1268–1270 (1997).
18. M. Gross, M. Atlan, and E. Absil, "Noise and aliases in off-axis and phase-shifting holography," Appl. Opt. **47**, 1757–1766 (2008).
19. W. Xu, M. H. Jericho, I. A. Melnertzhagen, and H. J. Kreuzer, "Digital in-line holography for biological applications," Proc. Natl. Acad. Sci. USA.
20. C. J. Mann, L. Yu, C. M. Lo, and M. K. Kim, "High resolution quantitative phase-contrast microscopy by digital holography," Opt. Express **13**, 8693–8698 (2005).
21. C. J. Mann, L. Yu, and M. K. Kim, "Movies of cellular and sub-cellular motion by digital holographic microscopy," Biomed. Eng. Online **5**, 21 (2006).
22. F. Charriére, A. Marian, F. Montfort, J. Kuehn, and T. Colomb, "Cell refractive index tomography by digital holographic microscopy," Opt. Lett. **31**, 178–180 (2006).
23. M. Atlan, M. Gross, P. Desbiolles, E. Absil, G. Tessier, and M. Coppey-Moisan, "Heterodyne holographic microscopy of gold particles," Opt. Lett **35**, 500–502 (2008).
24. E. Absil, G. Tessier, M. Gross, M. Atlan, N. Warnasooriya, S. Suck, M. Coppey-Moisan, and D. Fournier, "Photothermal heterodyne holography of gold nanoparticles," Opt. Express **18**, 780–786 (2010).
25. D. Goldberg and D. Burmeister, "Stages in axon formation: observations of growth of Aplysia axons in culture using video-enhanced contrast-differential interference contrast microscopy," J. Cell Biol. **103**, 1921–1931 (1986).
26. T. Colomb, F. Montfort, J. Kühn, N. Aspert, E. Cuche, A. Marian, F. Charriére, S. Bourquin, P. Marquet, and C. Depeursinge, "Numerical parametric lens for shifting, magnification, and complete aberration compensation in digital holographic microscopy," J. Opt. Soc. Am. A **23**, 3177–3190 (2006).
27. U. Schnars and W. Jüptner, "Direct recording of holograms by a CCD target and numerical reconstruction," Appl. Opt. **33**, 179–181 (1994).
28. L. Yu and M. Kim, "Wavelength-scanning digital interference holography for tomographic three-dimensional imaging by use of the angular spectrum method," Opt. Lett. **30**, 2092–2094 (2005).

1. Introduction

With recent developments in the fields of nanotechnology and modern optical microscopy, the use of nanometric particles as biomarkers in biological specimens has been rapidly increased. Colloidal gold nanoparticles have gained popularity over other biomarkers for several reasons. First, gold nanoparticles provide high scattering efficiencies [1]. Second, unlike fluorescent markers, they are immune to photo bleaching, and they are potentially non-cytotoxic, which provides a great advantage over semiconductor nanoparticles [2]. Because of these properties, the potential for the use of gold nanoparticles as biomarkers for live cell imaging using photothermal tracking [3–5] and light scattering spectroscopy [6] has been demonstrated. The detection of live oral cancer cells using gold nanoparticles has also been obtained [7]. In this paper, we show the potential of using Digital Holographic Microscopy (DHM) as a powerful tool to detect and localize, in three dimensions, gold nanoparticles attached to living cells.

In digital holography a Charged Coupled Device detector (CCD) records the interference diagram, called hologram, of two waves: the reference wave and the object wave [8]. The

#120483 - $15.00 USD Received 25 Nov 2009; revised 19 Jan 2010; accepted 21 Jan 2010; published 1 Feb 2010

interference pattern is then numerically reconstructed to obtain information about the object wave field. A single hologram can be used to reconstruct the wave field at virtually any plane, thus allowing one to obtain both amplitude and phase information of the whole object. Over the past few decades, different configurations and techniques have been introduced in digital holography, resulting in precise phase shift [9], high resolution [10–12], and high sensitivity measurements [13]. Some of these techniques involve improvement of the experimental setup [14] and data acquisition methods, while others involve additional numerical treatments of the acquired holograms and modification of the numerical reconstruction procedure [15]. In this vision, Leith and Upatnieks [16] suggested an off-axis configuration holography, in which the combination of the two beams is done after angularly tilting the propagation direction of one of the beams with respect to the other. Phase-shifting interferometry adapted to digital holography [17] has been widely used, and our group has proven the potential efficiency of combining off-axis and phase shifting with a spatial filtering technique for reducing noise [13], and eliminating images aliases and overlapping [18]. The progress in various digital holographic techniques has dramatically increased its applications to a large variety of fields, and especially in the fields of cell biology and biomedical microscopy [19–22].

Holography has now proved its ability to localize scattering nanoparticles in 3D, as shown by Atlan et al. in a recent paper [23], either for fixed particles spin coated on a glass substrate or in free motion within a water suspension. More recently, Absil et al. [24] have shown that heterodyne holography also allows the photothermal detection of small nanoparticles.

However, in order to apply these techniques to biological specimens, important issues must be considered. In biological samples, the particle holographic signal is superimposed with the light scattered by cell refractive index fluctuations, which yield a speckle field. While in our case this speckle is a parasitic signal, in many other situations, like in Dark Field microscopy, or in Differential Interference Contrast (DIC) microscopy [25], this speckle is the main source of contrast used to image the cell. In this paper, we study the possibility of 3D holographic imaging in a biological context and we image for the first time 40 nm gold nanoparticles attached to living cells using DHM. Since the cell-scattered speckle field cannot be avoided, it is important for future cell labeling applications, to scale the particle signal with respect to the scattered speckle. We show here that the amplitude of the 40 nm gold particle signal we get is much larger than the cell-scattered field.

2. Sample preparation

We use NIH 3T3 mouse fibroblasts (quoted as 3T3 cells in this paper) with integrin surface receptors labeled with 40 nm gold particles. Streptavidin-coated gold nanoparticles were attached to the cell surface integrin receptors via biotin and fibronectin proteins: see Fig. 1. Streptavidin and biotin are very well known for their strong mutual affinity, and fibronectin, an extracellular matrix protein, has the property of interacting specifically with cell surface receptors of the integrin family.

Fibronectin proteins (fibronectin from bovine plasma, Sigma, St Louis, MO) were labeled with biotin by using EZ-Link®Sulfo-NHS-LC-Biotin according to the provider protocol (Pierce, Rockford, IL). The final concentration of biotinylated-fibronectin solution was 0.447 mg/mL. We used a solution of gold nanoparticles of 40 nm average diameter pre-coated with streptavidin. The streptavidin/gold conjugates (BioAssay, Gentaur, France) were rinsed twice with 1X PBS (Phosphate Buffered Saline) (pH = 7.25). A 1 mL dilute streptavidin-coated gold solution was prepared by diluting 10 μL of the gold solution in 990 μL of PBS buffer. Then the dilute solution was incubated with 50 μL biotinylated-fibronectin solution for four hours at room temperature to allow streptavidin-biotin bonding. The functionalized beads solution was stored at 4°C and used within 24 hours after preparation in order to ensure maximum function-

#120483 - $15.00 USD Received 25 Nov 2009; revised 19 Jan 2010; accepted 21 Jan 2010; published 1 Feb 2010

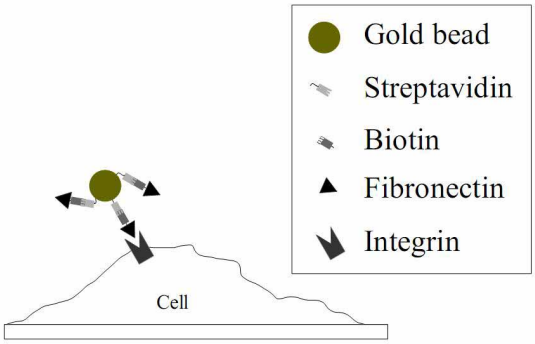

Fig. 1. Schematic representation of the coupling between 3T3 cells and gold beads

ality. Before every use, the functionalized beads solution was sonicated.

3T3 cells were cultured in Duelbecco's modified Eagle's medium (DMEM Gibco, Invitrogen, Carlsbad, CA) supplemented with 10% fetal calf serum (PAA Laboratories GmbH) on 32 mm diameter glass cover slips at 37°C in a 5% CO2 atmosphere, 48 hours before the observation. The cover slips were coated with fibronectin (fibronectin from bovine plasma, Sigma, St Louis, MO) in advance for optimum cell growth. After being incubated for 24 hours, a monolayer of 3T3 fibroblasts was immersed into a solution composed of DMEM (2 mL) plus 500 μL of the functionalized beads solution. The integrin-fibronectin link is created at this level allowing the cells to attach, on their surface, the functionalised gold nanoparticles.

The coverslip containing adherent 3T3 cells tagged with 40 nm gold nanoparticles was mounted on a specific observation chamber. To ensure optimum cell survival conditions during the observation, coverslips were kept in a special DMEM-F12 to maintain the physiologic pH conditions (DMEM-F12 without Phenol red, B12 vitamin, Riboflavin, 0.5% fetal calf serum and supplemented with 20 mM of HEPES [(4-(2-hydroxyethyl)-1-piperazineethanesulfonic acid)] and L-Glutamine from PAA Laboratories). The efficiency of the biotinylation protocol is verified by measuring the level of biotin incorporation on an HABA [2-(4' - Hydroxyazobenzene) Benzoic Acid)] quantitation assay according to the provider's protocol (Pierce, Rockford, IL). Average number of biotin molecules obtained per fibronectin is 2.5.

3. Experimental setup

A schematic representation of the experimental setup is shown in Fig. 2. The illumination source is a single-mode near infrared laser diode emitting at λ=785nm (DL7140-201S 80 mW Laser Diode, 90 mA current). A polarizing beam splitter cube (PBS) is used to split the original illumination laser light into two beams, a reference beam (complex field E_R, frequency f_R) and an object illumination beam (complex field E_O, frequency f_O) forming the two arms of a Mach-Zehnder interferometer. A combination of a half wave plate ($\lambda/2$) and two neutral density filters (ND_1, ND_2) is used to prevent the saturation of the detector by controlling the optical power traveling in each arm. Two acousto-optic modulators (AOM1, AOM2) driven around 80 MHz with a selection of the first order of diffraction, shift both frequencies at respectively f_{AOM1} and f_{AOM2} .

The object beam illuminates the sample, prepared as described in Section 2, by provoking total internal reflection (TIR) at the cell/bead-air interface. The evanescent wave locally frustrated by the beads and cells gives off a propagating scattered wave (complex field E), which

#120483 - $15.00 USD Received 25 Nov 2009; revised 19 Jan 2010; accepted 21 Jan 2010; published 1 Feb 2010

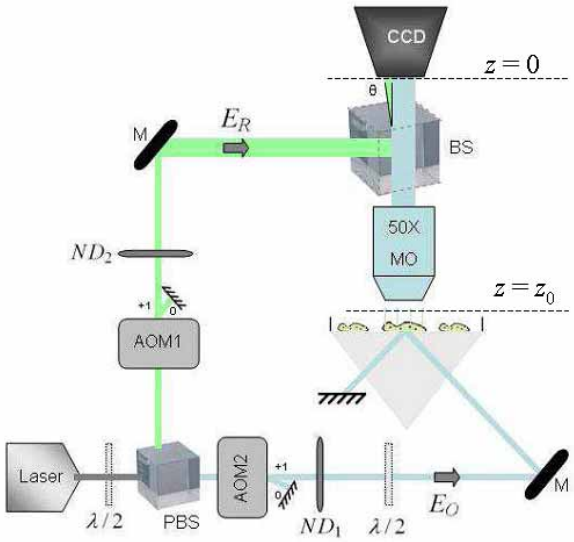

Fig. 2. Experimental setup. AOM1, AOM2: acousto-optic modulators; M: mirror; MO: microscope objective NA = 0.5; $\lambda/2$: half wave plate; BS: beam splitter; PBS: polarizing beam splitter; CCD: CCD camera; E_R: reference wave; E_O: object illumination wave; E: scattered wave; θ: angular tilt; ND_1, ND_2: neutral density filters; $z=0$: CCD plane; $z=z_0$: CCD conjugate plane with respect to MO.

is collected by a microscopic objective (MO, 50× magnification, NA=0.5, air). A beam splitter is then used to combine the scattered object wave and the reference wave which is slightly angularly tilted ($\theta \sim 1°$) with respect to the propagation axis of the object wave in an off-axis configuration. The half wave plate ($\lambda/2$) on the object illumination arm aligns the polarization of the corresponding beam allowing an optimal interference of the beams. A CCD camera (Roper Cascade 512F, 512×512 square pixels of 16μm size, exposure time 100 ms, frame rate $f_{CCD} = 8$ Hz) detects the interference pattern (hologram) and sends it to a computer. The hologram is then numerically treated and the complex field *E(x,y,z)* is reconstructed numerically.

4. Holographic acquisition and reconstruction

A four-phase demodulation method is used to record holograms. This method consists in acquiring a sequence of images with a relative phase shift $\Delta\varphi = \pi/2$ between two consecutive frames. To get an accurate phase shift [9], the reference wave is frequency-shifted by tuning the two acousto-optic modulators AOM1 and AOM2 [14], so that the heterodyne beating frequency is:

$$\Delta f = f_{AOM1} - f_{AOM2} = \frac{f_{CCD}}{4} \tag{1}$$

where f_{CCD} =8Hz is the frame rate frequency of the CCD camera. The camera records a sequence of 32 frames I_0,...,I_{31}, and the object field E on the CCD plane ($z=0$) is given by:

$$E(x,y,z=0) = \sum_{n=1}^{M} j^n I_n \tag{2}$$

where $j^2 = -1$, and M is the number of frames used for the reconstruction, which is equal either to 1 or to 32 in the experiments we present here. In Eq. (2), the coordinates x,y (with

#120483 - $15.00 USD Received 25 Nov 2009; revised 19 Jan 2010; accepted 21 Jan 2010; published 1 Feb 2010

$0 < x,y < 511$) are integers, which represent the pixel location within the CCD plane. The pixel size is then the physical CCD pixel size, i.e., 16 μm.

Since we image the sample through a microscope objective (MO), the measured hologram represents the field $E(x,y,z=z_0)$ within the CCD conjugate plane $z=z_0$ with respect to the MO, i.e., the plane, whose image is on focus on the CCD detector. In that case, one must compensate the phase curvature, the phase tilt and the enlargement factor that are related to the presence of MO [26]. We have thus:

$$E(x,y,z=z_0) \;=\; e^{j(K_x x+K_y y)}\, e^{jA(x^2+y^2)} \sum_{n=0}^{M} j^{\,n} I_n \tag{3}$$

where (K_x,K_y) and A are the tilt and lens parameters respectively. These parameters are determined by reconstructing the image of the microscope objective output pupil using the one-Fourier-transform method [27]. The lens parameter is close to the lens parameter that is used in the pupil reconstruction, and the tilt parameter to the translation that pushes the pupil in the centre of the reconstructed image. The magnification factor of the conjugate plane is measured by imaging a USAF target. We get, in the conjugate plane, pixel sizes of $\delta x, \delta y = 177$ nm.

The object field $E(x,y,z)$ is calculated in the vicinity of conjugate plane (i.e. for $z \simeq z_0$) by the angular spectrum method, which requires two Fourier transforms [10, 14, 28]. This method is chosen in order to keep the pixel size constant in the reconstruction. The reconstruction is done for 512 different reconstruction distances $z = z_0 + m\delta z$ where $\delta z = 177$ nm and $m = -256... + 255$. Using this method, we get 3D volume images with $512 \times 512 \times 512$ voxels, with the same pixel size (177 nm) in the 3 directions x,y and z.

5. Experimental results

We have considered a 3T3 cell with integrin cellular surface receptors tagged with a single 40 nm gold particle. Since we are interested in tracking the particle, the camera exposure time is an important issue, and we will first reconstruct the 3D image of the sample using one CCD frame. Then, to improve the Signal to Noise Ratio and to confirm our results, we will reconstruct the 3D image of the sample from the whole sequence of 32 frames. Figure 3(a) shows a direct image of the sample under white light illumination. While the cell is well defined on the left hand side of the image, the attached gold particle cannot be seen.

Figure 3(b) shows the reconstructed intensity image of the sample in a colored logarithmic scale. The reconstruction is done using 1 CCD frame ($M = 1$) with an exposure time of 100 ms. The reconstruction plane is $z = z_0 + 12.2$ μm i.e. $n_z = 325$ where n_z is the z index on the 3D matrix, which is the plane where the brightest point is detected. It also corresponds to the cell plane. The red and blue triangular structure with a few speckle yellow high spots, which correspond to the cell location on Fig. 3(a), is the holographic signal generated by the cell refractive index inhomogeneities, which scatter light. The gold particle corresponds to the brightest spot in Fig. 3(b). It is located on the left bottom of the cell, and marked with a white arrow.

To illustrate the ability of our technique to localize the gold particle in 3D, we have displayed in Fig. 3(c) a volume view of the $512 \times 512 \times 512$ reconstructed intensity image 3D data, i.e., we have plotted $I(x,y,z) = |E(x,y,z)|^2$ for different reconstruction z distances. The bright light bluish zone on the 3D image corresponds to the 40 nm gold particle signal. This wavefield has the shape of a cigar roughly oriented along the microscope objective axis (z axis).

To better visualize the 40 nm gold particle, we have displayed, on Fig. 4(a), a 3D linear surface plot of the corresponding logarithmic scale colored image of Fig. 3(b). As can be seen, the gold particle signal is much higher than the signal generated by the cell refractive index inhomogeneities. The particle can thus be easily located.

#120483 - $15.00 USD Received 25 Nov 2009; revised 19 Jan 2010; accepted 21 Jan 2010; published 1 Feb 2010

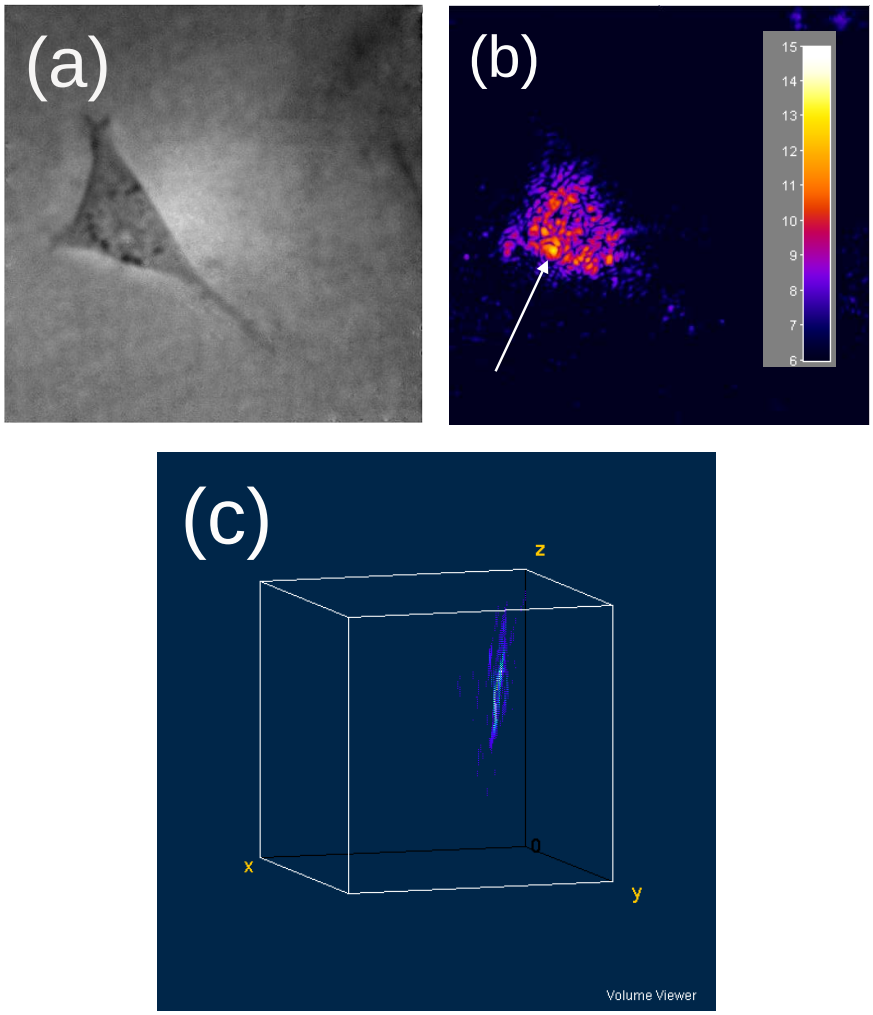

Fig. 3. Fibroblast cell tagged with a 40 nm gold particle. (a) Direct image under white light illumination. (b) Reconstructed Holographic intensity I image. The 40 nm gold particle is marked with a white arrow. The color scale corresponds to $6 < \ln(I) < 15$). (c) Volume view of the 3D reconstructed data ($512 \times 512 \times 512$ voxels; voxel size 177 nm in all directions). The holographic reconstruction is made in (b) and (c) from 1 CCD frame with an exposure time of 100 ms.

#120483 - $15.00 USD Received 25 Nov 2009; revised 19 Jan 2010; accepted 21 Jan 2010; published 1 Feb 2010

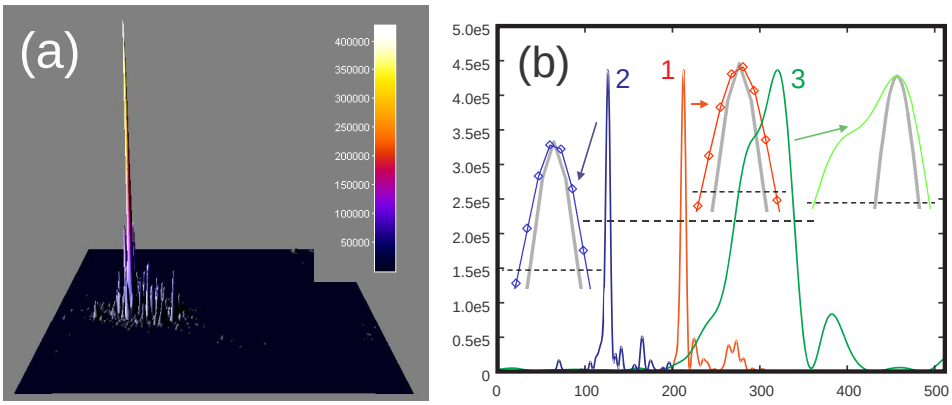

Fig. 4. A fibroblast cell tagged with a 40 nm gold particle using 1 frame acquisition. (a) 3D linear-scale surface plot of the intensity image reconstructed from a single frame. (b) Experimental linear-scale plot of cuts made within the intensity signal I along the three axis x, y and z at the brightest voxel of Fig. 3(b) corresponding to the gold nanoparticle location. Curves 1, 2 and 3 correspond to the x, y and z axis respectively. The horizontal dashed line represents the half maximum of the curves. Curves marked with arrows are zooms of the corresponding curves from maximum to half maximum. Light grey curves correspond to the different ideal theoretical curves.

To perform a quantitative analysis of the precision we expect in the 3D localization of the gold particle, we have considered the 3D volume intensity image of Fig. 3(c), and we have made cuts along the 3 axes (x, y and z) at the gold particle crossing point (i.e. where the three axis cross the highest intensity voxel of the 3D image). The intensity signals I along the 3 axes are plotted on Fig. 4(b). Curves 1 (red), 2 (blue) and 3 (green) correspond to x, y and z axis respectively. The horizontal dashed line indicates the half maximum of the curves. In order to measure the curves widths, we have displayed zooms of the curves from maximum to half maximum. The individual pixels are visible on curves 1 and 2 zooms (x and y axis). The Full Width at Half Maximum (FWHM) is about 6 pixels in the x and y directions ($6 \times 177 = 1060$ nm), and about 60 pixels in the z direction (10.6 μm).

To compare the resolution obtained here with that expected from the NA of the microscope objective, we have computed the wavefield $E_I(x,y,z)$ that is expected in the ideal case for a NA=0.5 objective, and we have made cuts along x, y and z directions of the $512 \times 512 \times 512$ ideal cube of data for $|E_I(x,y,z)|^2$. The corresponding theoretical cuts are plotted with the zooms in heavy grey line. Like for the experimental cuts, the horizontal axis is in pixels. In the x and y directions, the obtained FWHM is close to the expected one. Yet in the z direction the shape of the curve is not symmetric, and the measured FWHM is about 3 times larger than the expected FWHM in the ideal case. As illustrated below, this is due to the holographic signal generated by the light scattered by the cell, which adds to the bead signal.

Using a parabolic approximation for the local field, the location of the gold particle can be calculated by fitting the data points that are above half maximum. The accuracy of the measurement made by this method is ± 5 nm in the x and y directions (uncertainty given by the fit software Gnuplot). It corresponds also to the variation of the particle when the number of data points used for the fit is increased from 8 to 7. In the z direction, the measured curve is not perfectly symmetric, so the fit technique is not very accurate because the result of the fit strongly depends on the data points that are used in the calculation.

In order to visualize the gold particle with a better Signal to Noise Ratio (SNR), we have also

#120483 - $15.00 USD Received 25 Nov 2009; revised 19 Jan 2010; accepted 21 Jan 2010; published 1 Feb 2010

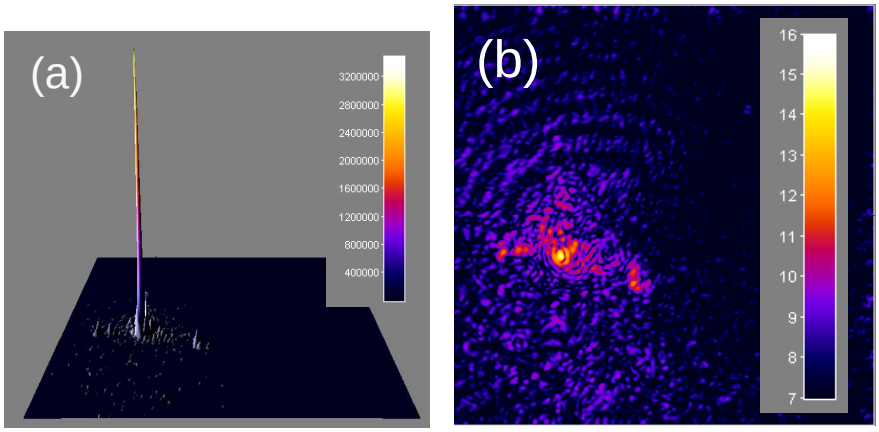

Fig. 5. A fibroblast cell tagged with a 40 nm gold particle using 32 frames acquisition. (a) 3D linear-scale surface plot of the 32 frames reconstructed holographic intensity image. (b) Reconstructed Holographic intensity I image. The color scale corresponds to $6 < \ln(I) < 15$).

reconstructed the holographic images using a sequence of $M = 32$ acquired CCD frames. In this case, the total exposure time is 32×100 ms=3.2 s, while the measurement time is $32/f_{CCD}$ = 4 s. Figure 5(a) shows the 3D linear surface plot of the reconstructed intensity image in the $z = z_0 + 6.1\mu$m plane. Figure 5(a) is similar to Fig. 4(a) but obtained with 32 frames, instead of 1 frame. Here again, not only the gold particle signal is much higher than the light scattered by the cell, but the ratio of the particle signal versus the light scattered by the cell is increased with respect to the ratio obtained for Fig. 4(a), and the visibility of the gold particle is improved. This visibility improvement is confirmed by Fig. 5(b), which shows the reconstructed intensity image of the sample in a colored logarithmic scale. The cell signal, corresponding to the triangular bluish and reddish structure, is still visible. The particle signal in yellow is visible too, but with a much better contrast than in Fig. 3(b).

Figure 6(a) shows the cuts made along the 3 axes (x, y and z) obtained for the 32 frames data. Here again, we have displayed zooms of the three cross sections from maxima to half maxima as well as zooms of the theoretical curves. These cross sections are similar to the cross sections obtained in the case of 1 frame acquisition, but in this case (32 frames) the heavy grey lines corresponding to the theoretical zoomed curves are closer to the experimental curves. In particular, in the z direction, the experimental curve is now in agreement with the theoretical one, because the relative weight of the cell- scattered signal is now lower, as seen by comparing Fig. 5(a) with Fig. 4(a). Here again, the location of the particle can be calculated by fitting the measured data point with a parabola. The accuracy is still ± 5 nm in the x and y directions, but since the curve 3 is now roughly symmetric, the fit can also be performed in the z direction, and the particle can be located with an accuracy estimated to ± 100 nm in the z direction.

To better compare the particle signal with respect to the light scattered by the cell, we plotted the intensity signal along x [which corresponds to curve 1 of Fig. 6(a)] in logarithmic scale on Fig. 6(b). As seen, the particle signal is 2 to 3 orders of magnitude larger than the cell scattered signal. It has the same order of magnitude as the signal obtained in a control experiment of 40 nm gold particles within a water and agarose suspension. We plotted also (black curve 4) the background signal obtained without illuminating the sample. This background corresponds to the ultimate sensitivity limit of the holographic detection [13], i.e. to the shot noise on the

#120483 - $15.00 USD Received 25 Nov 2009; revised 19 Jan 2010; accepted 21 Jan 2010; published 1 Feb 2010

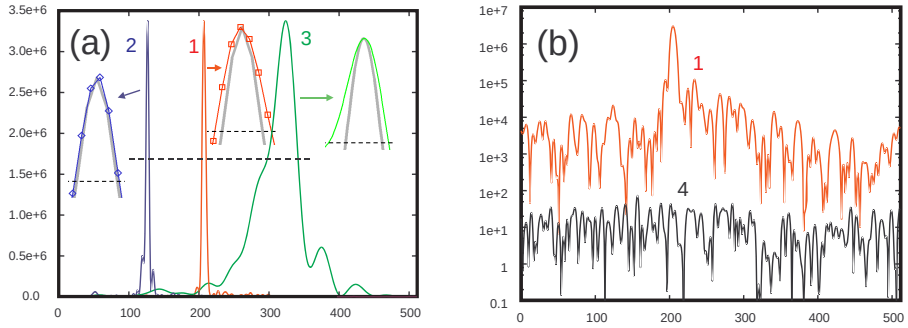

Fig. 6. (a) Experimental linear plot of cuts made within the intensity signal I along the three axis x, y and z at the brightest voxel of Fig. 5(b) corresponding to the gold nanoparticle location. Curves 1, 2 and 3 corresponds to the x, y and z axis respectively. The horizontal dashed line represents the half maximum of the curves. Curves marked with arrows are zooms of the corresponding curves from maximum to half maximum. Light grey curves correspond to the different ideal theoretical curves. (b) Intensity plot of the cut along the x axis in logarithmic scale 1 at the nanoparticle location and 4 without illuminating the sample

local oscillator beam. As seen, the shot noise background is about 100 times lower than the cell-scattered signal. This means that if the exposure time is reduced by the same factor (from 3.2 s down to 32 ms), one expects to get roughly the same Signal to Noise Ratio (SNR$\simeq$ 100) on the particle signal. Since the illumination area (about 1 mm^2) is much larger than the imaged region, it is possible, by focusing the illumination, to reduce further the exposure time without significally decreasing the SNR.

6. Conclusion

In conclusion, we have reported in this article a digital holographic microscopy technique capable of imaging 40 nm gold nanoparticles attached to the surface receptors of living cells. Since the intensity of the nanoparticle scattered signal is much larger than the field scattered by the cell structures, we show that the acquisition of a single image is sufficient to localize in 3D the nanoparticle within a 90 micrometer thick sample, with localization accuracy similar to that obtained in conventional light microscopy. This method provides significant progress towards the development of 3D microscopy in living cell environments, since the 3D reconstruction of such a thick sample by conventional light microscopy would require the acquisition of a stack of hundreds of slices. With an exposure time of 100 ms for each slice, the total acquisition time for the stack would be of the order of one minute. Even if our method requires the acquisition of a sequence of several consecutive images to obtain a better signal-to-noise ratio and, subsequently, a better z-position estimation, the acquisition time needed for the localization of the nanoparticle using holographic microscopy is still one order of magnitude smaller than that needed using conventional 3D-reconstruction microscopy. Overall, we showed that we can use our technique for the complete 3D mapping of a thick sample scattered field using a single hologram and without any mechanical scanning.

Acknowledgements

The authors wish to acknowledge the French National Research Agency (ANR) and the “Centre de Compétence NanoSciences Île de France”(C’nano IdF) for their support.

#120483 - $15.00 USD Received 25 Nov 2009; revised 19 Jan 2010; accepted 21 Jan 2010; published 1 Feb 2010

B.3 Shot Noise in Digital Holography

Fadwa Joud, Frédéric Verpillat, Michael Atlan, Pierre André Taillard and M. Gross, *in Information Optics & Photonics: Algorithms, Systems & Applications*, 163 (Springer,2010) [Joud *et al.* 2010a]

Chapter 13
Shot Noise in Digital Holography

Fadwa Joud, Frédéric Verpillat, Michael Atlan, Pierre-André Taillard, and Michel Gross

Abstract We discuss on noise in heterodyne holography in an off-axis configuration. We show that, for a weak signal, the noise is dominated by the shot noise on the reference beam. This noise corresponds to an equivalent noise on the signal beam of one photoelectron per pixel, for the whole sequence of images used to build the digital hologram.

13.1 Introduction

Demonstrated by Gabor [1] in the early 1950s, the purpose of holography is to record, on a 2D detector, the phase and the amplitude of the radiation field scattered by an object under coherent illumination. The photographic film used in conventional holography is replaced by a 2D electronic detection in digital holography [2] enabling quantitative numerical analysis. Digital holography has been waiting for the recent development of computer and video technology to be experimentally demonstrated [3]. The main advantage of digital holography is that, contrary to holography with photographic plates [1], the holograms are recorded by a CCD, and the image is digitally reconstructed by a computer, avoiding photographic processing [4].

Off-axis holography [5] is the oldest configuration adapted to digital holography [3, 6, 7]. In off-axis digital holography, as well as in photographic plate holography, the reference or local oscillator (LO) beam is angularly tilted with respect to the object's observation axis. It is then possible to record, with a single hologram, the two quadratures of the object's complex field. However, the object's field of view is reduced, since one must avoid the overlapping of the image with the conjugate image alias [8]. In Phase shifting digital holography, which has been introduced later

F. Joud (✉)
Laboratoire Kastler Brossel École Normale Supérieure, UMR 8552, UPMC, CNRS,
24 rue Lhomond, 75231 Paris Cedex 05, France
e-mail: joud@lkb.ens.fr

T. Fournel and B. Javidi (eds.), *Information Optics and Photonics: Algorithms, Systems, and Applications*, DOI 10.1007/978-1-4419-7380-1_13,

[9], several images are recorded with different LO beam phases. It is then possible to obtain the two quadratures of the object's field in an in-line configuration even though the conjugate image alias and the true image overlap, because aliases can be removed by taking image differences.

We have developed an alternative phase shifting digital holography technique, called heterodyne holography, that uses a frequency shift of the reference beam to continuously shift the phase of the recorded interference pattern [10]. One of the advantages of this technique is its ability to provide accurate phase shifts that allow to suppress twin images aliases [11]. This greatly simplifies holographic data handling, and improves sensitivity. Moreover, it is possible to perform holographic detection at a frequency different from illumination. One can, for example, detect "tagged photons" [12, 13] in ultrasound-modulated optical imaging [14]. One can also image vibrating objects at the frequencies corresponding to vibration sidebands [15, 16]. To the end, it is possible to perform Laser Doppler imaging [17] within microvessels [18–20].

More generally, our setup can be viewed as a multipixel heterodyne detector that is capable of recording the complex amplitude of the signal electromagnetic field $\mathscr{E}$ onto all pixels of the CCD camera in parallel. We get the map of the field over the array detector (i.e., $\mathscr{E}(x, y)$ where x and y are the pixels coordinates). Since the field is measured on all pixels at the same time, the relative phase that is measured for different locations (x, y) is meaningful. This means that the field map $\mathscr{E}(x, y)$ is an hologram that can be used to reconstruct the field $\mathscr{E}$ in any location, in particular in the object's plane.

In this chapter, we will discuss on noise in digital holography, and we will try to determine what is the ultimate noise limit both theoretically, and in real time holographic experiments. We will see that, in the theoretical ideal case, the limiting noise is the Shot Noise on the holographic reference beam. In reference to heterodyne detection, the reference beam is also called LO. We will see that the ultimate theoretical limiting noise can be reached in real life holographic experiment, by using heterodyne holography [10] in off-axis configuration. This combination makes possible to fully filter off the technical noise, whose main origin is the LO beam technical noise, opening the way to holography with ultimate sensitivity [21, 22].

13.2 Theoretical Noise

To discuss on noise in digital holography, we will consider both the case of off-axis holography, where the hologram is obtained from one frame of the CCD camera, and the case of phase shifting holography, where the holographic information is extracted from a sequence of M frames.

We will thus consider a sequence of M frames: I_0 to I_{M-1} (where $M = 1$ in the one shot, off-axis case). For each frame I_k, let us note $I_{k,p,q}$ the CCD camera signal on each pixel, where k is the frame index, and p, q the pixel indexes along the x

and y directions. The CCD signal $I_{k,p,q}$ is measured in Digital Counts (DC) units. In the typical case of the 12 bit digital camera used in experiments below, we have $0 \leq I_{k,p,q} < 4{,}096$. For each frame k, the optical signal is integrated over the acquisition time $T = 1/f_{\text{ccd}}$ of the CCD camera. The pixel signal $I_{k,p,q}$ is thus defined by

$$I_{k,p,q} = \int_{t_k - T/2}^{t_k + T/2} \mathrm{d}t \iint_{(p,q)} \mathrm{d}x\mathrm{d}y \;\; |E(x,y,t) + E_{\text{LO}}(x,y,t)|^2, \tag{13.1}$$

where $\int\int_{(p,q)} \mathrm{d}x\mathrm{d}y$ represents the integral over the pixel (p,q) area, and t_k is the recording moment of frame k. Introducing the complex representations $\mathscr{E}$ and $\mathscr{E}_{\text{LO}}$ of the fields E and E_{LO}, we get

$$E(x,y,t) = \mathscr{E}(x,y)\mathrm{e}^{j\omega_I t} + \text{c.c.} \tag{13.2}$$

$$E_{\text{LO}}(x,y,t) = \mathscr{E}_{\text{LO}}(x,y)\mathrm{e}^{j\omega_{\text{LO}} t} + \text{c.c.} \tag{13.3}$$

$$I_{k,p,q} = a^2 T \left(|\mathscr{E}_{p,q}|^2 + |\mathscr{E}_{\text{LO}}|^2 + \mathscr{E}_{p,q}\mathscr{E}_{\text{LO}}^* \cdot \mathrm{e}^{(j(\omega_I - \omega_{\text{LO}})t_k)} + \text{c.c.} \right), \tag{13.4}$$

where a is the pixel size. To simplify the notations in (13.4), we have considered that the LO field $\mathscr{E}_{\text{LO}}$ is the same in all locations (x,y), and that signal field $\mathscr{E}_{p,q}$ does not vary within the pixel (p,q). If $\mathscr{E}_{\text{LO}}$ varies with location, one has to replace $\mathscr{E}_{\text{LO}}$ by $\mathscr{E}_{\text{LO},p,q}$ in (13.4).

In the single-shot, off-axis holography case, the hologram H is simply $H \equiv I_k$. To simplify the discussion in the phase shifting digital holography case [9], we will consider four phases holographic detection ($M = 4n$). In that case, the phase shift of the LO beam is equal to $\pi/2$ from one recorded frame to the next. Because of this shift, the complex hologram H is obtained by summing the sequence of M frames I_1 to I_M with the appropriate phase coefficient:

$$H \equiv \sum_{k=1}^{M} (j)^{k-1} I_k, \tag{13.5}$$

where H is a matrix of pixel $H_{p,q}$, $M = 4n$ in the four-phases phase shifting case, and $M = 1$ in the single-shot, off-axis case. We get from (13.4):

$$H_{p,q} = \sum_{k=1}^{M} (j)^k I_{k,p,q} = 4na^2 T \mathscr{E}_{p,q}\mathscr{E}_{\text{LO}}^*. \tag{13.6}$$

The complex hologram $H_{p,q}$ is thus proportional to the object's field $\mathscr{E}_{p,q}$ with a proportionality factor that involves $\mathscr{E}_{\text{LO}}^*$.

13.2.1 The Shot Noise on the CCD Pixel Signal

Because of spontaneous emission, laser emission and photodetection are random processes, the signal that is obtained on a CCD pixel exhibits a Poisson noise called "shot noise". The effect of this Poisson noise on the signal, and on the holographic images, is the Ultimate Theoretical Limiting noise, which we will study here.

We can split the signal $I_{k,p,q}$ we get for frame k and pixel (p, q) in : a noiseless average component $\langle I_{k,p,q}\rangle$ (here $\langle\ \rangle$ is the statistical average operator) and a noise component $i_{k,p,q}$:

$$I_{k,p,q} \equiv \langle I_{k,p,q}\rangle + i_{k,p,q}. \tag{13.7}$$

To go further in the discussion, we will use photoelectrons (e) Units to measure the signal $I_{k,p,q}$.

We must notice that the LO signal $\mathscr{E}_{\mathrm{LO}}$ is large, and corresponds to a large number of photoelectrons. In real life, this assumption is true. For example, if we adjust the power of the LO beam to be at the half maximum for the camera signal in DC unit (2,048 DC for a 12 bits camera), the pixel signal will be about 10^4 e for the camera used below in experiments, since the "Camera Gain" is 4.8 e per DC. This yields two consequences, which simplify the analysis. First, the signal $I_{k,p,q}$ exhibits a gaussian distribution around its statistical average. Second, both the quantization noise of the photoelectron signal ($I_{k,p,q}$ is an integer in photoelectron units), and the quantization noise of the Digital Count signal ($I_{k,p,q}$ is an integer in DC units) can be neglected. These approximations are valid, since the width of the $I_{k,p,q}$ gaussian distribution is much larger than one in both photoelectron and DC units. In the example given above, $\langle I_{k,p,q}\rangle \simeq 10^4$, and this width is $\simeq 10^2$ in photoelectron units, and $\simeq$20 in DC units. One can thus consider that $I_{k,p,q}$, $\langle I_{k,p,q}\rangle$ and $i_{k,p,q}$ are floating numbers (and not integers). Moreover, $i_{k,p,q}$ is a random Gaussian distribution, with

$$\langle i_{k,p,q}\rangle = 0, \tag{13.8}$$

$$\langle i^2_{k,p,q}\rangle = \langle I_{k,p,q}\rangle. \tag{13.9}$$

To analyse the shot noise's contribution to the holographic signal $H_{p,q}$, one of the most simple methods is to perform Monte Carlo simulation from (13.7), (13.8), and (13.9). Since $I_{k,p,q}$ is ever large in real life (about 10^4 in our experiment), $\langle I_{k,p,q}\rangle$ can be replaced by $I_{k,p,q}$ (which is measured in experiment) in the right member of (13.9). One has thus:

$$\langle i^2_{k,p,q}\rangle = \langle I_{k,p,q}\rangle \simeq I_{k,p,q}. \tag{13.10}$$

Monte Carlo simulation of the noise can be done from (13.7), (13.8), and (13.10).

13.2.2 The Object Field Equivalent Noise for One Frame

To discuss the effect of the shot noise on the heterodyne signal $\mathscr{E}_{p,q}\mathscr{E}^*_{\mathrm{LO}}$ of (13.4), let us consider the simple situation sketched on Fig. 13.1. A weak object field E, with

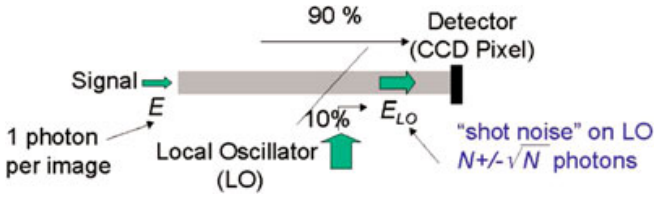

Fig. 13.1 One-photon equivalent signal (accounting Heterodyne gain) and shot noise on the holographic local oscillator beam

one photon or one photoelectron per pixel and per frame, interferes with a LO field E_{LO} with N photons, where N is large ($N = 10^4$, in the case of our experiment). Since the LO beam signal $a^2T|\mathscr{E}_{\mathrm{LO}}|^2$ is equal to N photons, and the object field signal $a^2T|\mathscr{E}_{p,q}|^2$ is one photon, we have

$$I_{k,p,q} = N + 1 + i_{k,p,q} + a^2T\mathscr{E}_{p,q}\mathscr{E}^*_{\mathrm{LO}}\mathrm{e}^{\cdots} + \mathrm{c.c.} \tag{13.11}$$

The heterodyne signal $\mathscr{E}_{p,q}\mathscr{E}^*_{\mathrm{LO}}$ is much larger than $|\mathscr{E}_{p,q}|^2$. This is the gain effect, associated to the coherent detection of the field $\mathscr{E}_{p,q}$. This gain is commonly called "heterodyne gain", and is proportional to the amplitude of the LO field $\mathscr{E}^*_{\mathrm{LO}}$.

The purpose of the present discussion is to determine the effect of the noise term $i_{k,p,q}$ in (13.11) on the holographic signal $H_{p,q}$. Since $H_{p,q}$ involves only the heterodyne term $\mathscr{E}_{p,q}\mathscr{E}^*_{\mathrm{LO}}$ [see (13.6)], we have to compare, in (13.11), the shot noise term $i_{k,p,q}$, and the heterodyne term $\mathscr{E}_{p,q}\mathscr{E}^*_{\mathrm{LO}}$.

Consider first the shot noise term. We have

$$\langle i^2_{k,p,q}\rangle = \langle I_{k,p,q}\rangle = N + 1 \simeq N. \tag{13.12}$$

The variance of the shot noise term is thus $N^{1/2}$. Since this noise is mainly related to the shot noise on the LO (since $N \gg 1$), one can group together, in (13.11), the LO beam term (i.e., N) with the noise term $i_{k,p,q}$, and consider that the LO beam signal fluctuates, the number of LO beam photons being thus "$N \pm N^{1/2}$", as mentioned on Fig. 13.1.

Consider now the heterodyne beat signal. Since we have N photons on the LO beam, and one photon on the object beam, we get

$$a^2T|\mathscr{E}_{p,q}\mathscr{E}^*_{\mathrm{LO}}| \equiv \left[\left(a^2T|\mathscr{E}_{p,q}|^2\right)\left(a^2T|\mathscr{E}_{\mathrm{LO}}|^2\right)\right]^{1/2} = N^{1/2}. \tag{13.13}$$

The heterodyne beat signal $\mathscr{E}_{p,q}\mathscr{E}^*_{\mathrm{LO}}$ is thus $N^{1/2} = 100$.

The shot noise term $i_{k,p,q}$ is thus equal to the heterodyne signal $\mathscr{E}_{p,q}\mathscr{E}^*_{\mathrm{LO}}$ corresponding to one photon on the object field. This means that shot noise $i_{k,p,q}$ yields an equivalent noise of one photon per pixel, on the object beam. This result is obtained here for one frame. We will show that it remains true for a sequence of M frames, whatever $M = 4n$ is.

13.2.3 The Object Field Equivalent Noise for $M = 4n$ Frames

Let us introduce the DC component signal D, which is similar to the heterodyne signal H given by (13.5), but without phase factors:

$$D \equiv \sum_{k=1}^{M} I_k. \tag{13.14}$$

The component D can be defined for each pixel (p, q) by

$$D_{p,q} \equiv \sum_{k=1}^{M} I_{k,p,q}. \tag{13.15}$$

Since $I_{k,p,q}$ is always large in real life (about 10^4 in our experiment), the shot noise term can be neglected in the calculation of $D_{p,q}$ by (13.15). We have thus:

$$D_{p,q} \equiv \sum_{k=1}^{M} I_{k,p,q} = Ma^2T\left(|\mathscr{E}_{p,q}|^2 + |\mathscr{E}_{\mathrm{LO}}|^2\right). \tag{13.16}$$

We are implicitly interested by the low signal situation (i.e., $\mathscr{E}_{p,q} \ll \mathscr{E}_{\mathrm{LO}}$) because we focus on noise analysis. In that case, the $|\mathscr{E}_{p,q}|^2$ term can be neglected in (13.16). This means that $D_{p,q}$ gives a good approximation for the LO signal.

$$D_{p,q} \equiv \sum_{k=1}^{M} I_{k,p,q} \simeq Ma^2T|\mathscr{E}_{\mathrm{LO}}|^2. \tag{13.17}$$

We can get then the signal field $|\mathscr{E}_{p,q}|^2$ from (13.6) and (13.17):

$$\frac{|H_{p,q}|^2}{D_{p,q}} \simeq Ma^2T|\mathscr{E}_{p,q}|^2. \tag{13.18}$$

In this equation, the ratio $|H_{p,q}|^2/D_{p,q}$ is proportional to the number of frames of the sequence ($M = 4n$), This means that $|H_{p,q}|^2/D_{p,q}$ represents the signal field $|\mathscr{E}_{p,q}|^2$ summed over the all frames.

Let us calculate the effect of the shot noise on $|H_{p,q}|^2/D_{p,q}$. To calculate this effect, one can make a Monte Carlo simulation as mentioned above, but a simpler calculation can be done here. Let us develop $|H_{p,q}|$ in statistical average and noise components [as done for $I_{k,p,q}$ in (13.7)]:

$$H_{p,q} = \langle H_{p,q}\rangle + h_{p,q} \tag{13.19}$$

with

$$h_{p,q} = \sum_{k=1}^{4n} j^{\,k} i_{k,p,q}. \tag{13.20}$$

Let us calculate $\langle |H_{p,q}|^2 / D_{p,q} \rangle$ from (13.18). Since $D_{p,q} \simeq \langle D_{p,q} \rangle$, we get

$$\left\langle \frac{|H_{p,q}|^2}{D_{p,q}} \right\rangle \simeq \frac{|\langle H_{p,q} \rangle|^2 + \langle |h_{p,q}|^2 \rangle + \langle \langle H_{p,q} \rangle h^*_{p,q} \rangle + \langle \langle H^*_{p,q} \rangle h_{p,q} \rangle}{\langle D_{p,q} \rangle}. \tag{13.21}$$

In (13.21), the $\langle \langle H_{p,q} \rangle h^*_{p,q} \rangle$ term is zero since $h^*_{p,q}$ is random while $\langle H_{p,q} \rangle$ is not. The two terms $\langle \langle H_{p,q} \rangle h^*_{p,q} \rangle$ and $\langle \langle H^*_{p,q} \rangle h_{p,q} \rangle$ can be thus removed. On the other hand, we get for $|h_{p,q}|^2$

$$|h_{p,q}|^2 = \sum_{k=1}^{4n} |i_{k,p,q}|^2 + \sum_{k=1}^{4n} \sum_{k'=1, k' \neq k}^{4n} j^{\,k-k'} i_{k,p,q} i_{k',p,q}. \tag{13.22}$$

Since $i_{k,p,q}$ and $i_{k',p,q}$ are uncorrelated, the $i_{k,p,q} i_{k',p,q}$ terms cancel in the calculation of the statistical average of $|h_{p,q}|^2$. We get then from (13.9)

$$\langle |h_{p,q}|^2 \rangle = \sum_{k=1}^{4n} \langle |i_{k,p,q}|^2 \rangle = \sum_{k=1}^{4n} \langle I_{k,p,q} \rangle = \langle D_{p,q} \rangle. \tag{13.23}$$

Equation 13.21 becomes thus:

$$\left\langle \frac{|H_{p,q}|^2}{D_{p,q}} \right\rangle = \frac{|\langle H_{p,q} \rangle|^2}{\langle D_{p,q} \rangle} + 1. \tag{13.24}$$

Equation 13.24 means that the average detected intensity signal $\langle |H_{p,q}|^2 / D_{p,q} \rangle$ is the sum of the square of the average object field $\langle |H_{p,q}| \rangle / (\langle D_{p,q} \rangle^{1/2})$ plus one photoelectron. Without illumination of the object, the average object field is zero, and the detected signal is one photoelectron. The equation establishes thus that the LO shot noise yields a signal intensity corresponding exactly to one photoelectron per pixel.

The 1 e noise floor, we get here, can be also interpreted as resulting from the heterodyne detection of the vacuum field fluctuations [23].

13.3 Reaching the Shot Noise in Real Life Holographic Experiment

In Sect. 13.2, we have shown that the theoretical noise on the holographic reconstructed intensity images is one photoelectron per pixel whatever the number of recorded frames is. We will now discuss the ability to reach this limit in real

life holographic experiment. Since we consider implicitly a very weak object beam signal ($\mathscr{E} \ll \mathscr{E}_{\mathrm{LO}}$), the noises that must be considered are the readout noise of the CCD camera, the technical noise from laser amplitude fluctuations on the LO beam, and the LO beam shot noise, which yields the theoretical noise limit.

Consider a typical holographic experiment made with a PCO Pixelfly 12 bit digital camera. The LO beam power is adjusted in order to be at half saturation of the digital camera output. Since the camera is 12 bits, and since the camera "gain" is 4.8 e per DC, half saturation corresponds to 2,000 DC on the A/D Converter, that is, about 10^4 e on the each CCD pixel. The LO shot noise, which is about 100 e, is thus much larger than the Pixelfly Read Noise (20 e), Dark Noise (3 e/s) and A/D quantization noise (4.8 e, since 1 DC corresponds to 4.8 e). The noise of the camera can be neglected, and is not a limiting factor for reaching the noise theoretical limit.

The LO beam that reaches the camera is essentially flat field (i.e., the field intensity $|\mathscr{E}_{\mathrm{LO}}|^2$ is roughly the same for all the pixels). The LO beam technical noise is thus highly correlated in all pixels. This is in particular the case for the noise induced by the fluctuations of the main laser intensity, or by the vibrations of the mirrors within the LO beam arm. To illustrate this point, we have recorded a sequence of $M = 4n = 4$ frames I_k (with $k = 0 \ldots 3$) with a LO beam, but without signal from the object (i.e., without illumination of the object). We have thus recorded the hologram of the "vacuum field". We have calculated then the complex hologram $H(x, y)$ by (13.5), and the reciprocal space hologram $\tilde{H}(k_x, k_y)$ by Fourier transform:

$$\tilde{H}(k_x, k_y) = \mathrm{FFT}\ \ H(x, y) \tag{13.25}$$

The reciprocal space holographic intensity $|\tilde{H}|^2$ is displayed on Fig. 13.2 in arbitrary logarithm grey scale. On most of the reciprocal space (within for example circle 1), $|\tilde{H}|^2$ corresponds to a random speckle whose average intensity

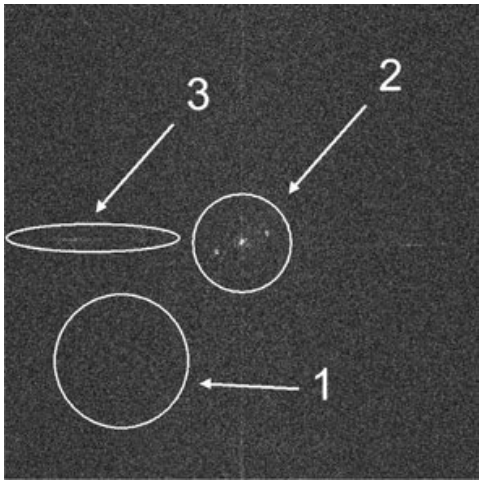

Fig. 13.2 Intensity image of $\tilde{H}(k_x, k_y, 0)$ for $M = 4n = 4$ frames without illumination of the object (no signal field $\mathscr{E}$). Three kind of noises can be identified. *Down left* (1): shot noise; *center* (2): technical noise of the CCD; *left* (3): FFT aliasing. By truncating the image and keeping only the *left down part*, the shot noise limit is reached. The image is displayed in arbitrary logarithm grey scale

is uniformly distributed along k_x and k_y. One observes nevertheless bright points within circle 2, which corresponds to $(k_x, k_y) \simeq (0, 0)$. These points correspond to the technical noise, which is a flat field within the CCD plane (x, y), and which corresponds thus to low spatial frequency components gathered around the center of the (k_x, k_y) reciprocal space. One see also, on the Fig. 13.2 image, an horizontal and a vertical bright line, which corresponds to $k_y \simeq 0$ and $k_x \simeq 0$ (zone 3 on Fig. 13.2). These parasitic bright lines are related to Fast Fourier Transform aliases, that are related to the discontinuity of the signal I_k and H at edge of the calculation grid, in the (x, y) space.

We have measured $\langle|\tilde{H}|^2\rangle$ by replacing the statistical average $\langle\ \rangle$ by a spatial average over a region of the conjugate space without technical noise (i.e., over region 1). This gives a measurement of $\langle|\tilde{H}|^2\rangle$, that is, a measurement of $\langle|H|^2\rangle$, since the space average of $|\tilde{H}|^2$ and $|H|^2$ are equal, because of the FFT Parceval theorem. We have also measured D from the sequence of frames I_k with $k = 0 \ldots 3$ [see (13.14)]. Knowing the camera Analog Digital (A/D) conversion factor (4.8 e per DC), we have calculated the noise intensity $\langle|\tilde{H}|^2\rangle/\langle D\rangle$ in photoelectron units, and we get, within 10%, one photoelectron per pixel for the average noise within region 2, as expected theoretically for the shot noise [see (13.21)].

To verify that we have truly reached the shot noise limit, we have performed a control experiment with a camera illuminated by a tungsten lamp powered by a battery. The lamp provides here a clean white light source. The lamp voltage is adjusted to get half saturation of the camera (about 2,000 DC). Similarly to the laser experiment described above, we have recorded a sequence of $M = 4n = 4$ frames I_k with $k = 0 \ldots 3$, and we have calculated $H(x, y)$, and $\tilde{H}(k_x, k_y)$. The image of $|\tilde{H}(k_x, k_y)|^2$ we get is very similar to Fig. 13.2. Moreover, the average noise intensity in region 2 is exactly the same as with a laser (one photoelectron per pixel). One has thus:

$$\langle|\tilde{H}|^2\rangle/\langle D\rangle = 1. \tag{13.26}$$

This result is expected since the camera "gain" is measured by assuming that the noise obtained in clean lamp control experiment is shot noise limited [24]. Since $\langle|\tilde{H}|^2\rangle/\langle D\rangle$ is dependent of the camera "gain" (13.26) indirectly allows the determination of the "gain" in e per DC units. The control experiment made here, redoes the "gain" calibration made by the camera manufacturer (i.e., PCO). We simply get here, within 10%, the same camera gain (4.8 e per DC).

13.3.1 Experimental Validation with an USAF Target

We have verified that it is possible to perform shot noise limited holography in real life, by recording the hologram of an USAF target in transmission. The holographic setup is sketched on Fig. 13.3. We have recorded sequences of $M = 4n = 12$ frames, and we have reconstructed the image of the USAF target.

Figure 13.4 shows the holographic reconstructed images of the USAF target. The intensity of the signal illumination is adjusted with neutral density filters.

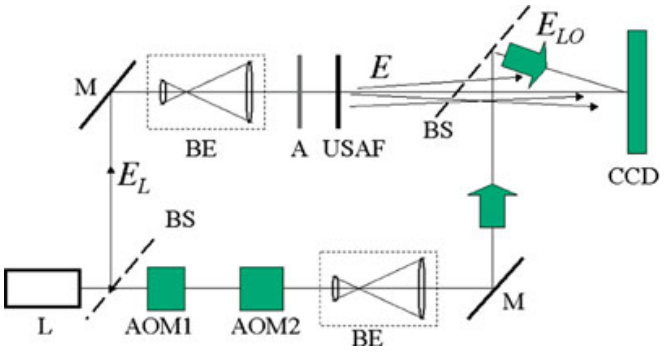

Fig. 13.3 Setup of the test experiment with USAF target. *L* main laser, *BS* beam splitter, *AOM1* and *AOM2* acousto-optic modulators, *BE* beam expander, *M* mirror, *A1 and A2* light attenuators, *USAF* transmission USAF target that is imaged, *CCD* CCD camera

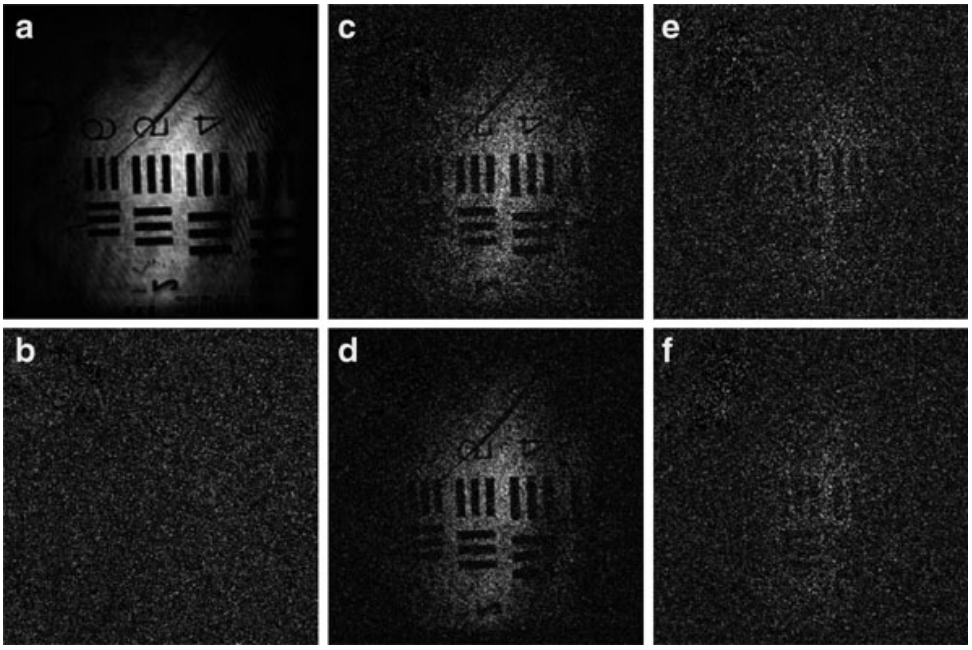

Fig. 13.4 (**a**, **c**, **d**): Reconstructions of an USAF target with different level of illumination 700 (**a**), 1 (**c**), and 0.15 e per pixel (**d**). (**b**) Simulated Shot Noise noise image. (**e**, **f**): Simulated reconstructed image obtained by mixing image (**a**) with weight X, and image (**b**) with weight $1-X$. The weight X is 1/700 (**e**), and 0.15/700 (**f**). Images are displayed in arbitrary logarithmic grey scale

To filter-off the technical noise, the reconstruction is done by selecting the order 1 image of the object, within the reciprocal space [8]. Since the 400×400 pixels region that is selected is off-axis, the low spatial frequency noisy region, which correspond to the zero order contributions (region 1 on Fig. 13.2), is filtered-off.

Figure 13.4a,c,d shows the reconstructed images obtained for different illumination levels of the USAF target. For each image, we have measured the average number of photoelectrons per pixel corresponding to the object beam, within the reciprocal space region that has been selected for the reconstruction (i.e., 400×400 pixels). The images of Fig. 13.4 correspond to 700 (a), 1 (c), and 0.15 (d) electron per pixel for the sequence of $M = 4n = 12$ frames respectively (i.e., $700/12$, $1/12$, and $0.15/12$ e per pixel and per frame).

Here, the object beam intensity hhas been measured as follows: we have first calibrated the response of our camera with an attenuated laser whose power is known. We have then measured with the camera, at high level of signal, the intensity of the signal beam alone (without LO beam). We have decreased, to the end, the signal beam intensity by using calibrated attenuators in order to reach the low signal level of the images of Fig. 13.2a,c,d. In the case of image (a) with 700 e per pixel, we also have measured the averaged signal intensity from the data themselves by calculating $|H|^2/D$ [see (13.18)]. The two measurements gave the same result: 700 e per pixel.

On Fig. 13.4a, with 700 e per pixel, the USAF signal is much larger than the shot noise, and the Sinal to Noise Ratio (SNR) is large. On Fig. 13.4c, with 1 e per pixel, the USAF signal is roughly equal to the shot noise, and the SNR is about 1. With 0.15 e per pixel, the SNR is low on Fig. 13.4d (about 0.15), and the USAF is hardly seen.

It is nevertheless quite difficult to evaluate the SNR of an image. To perform a more quantitative analysis of the noise within the images, we have synthesized the noisy images of Fig. 13.4e,f by adding noise to the Fig. 13.4a noiseless image. We have first synthesized a pure Noise image, which is displayed on Fig. 13.4b. The Noise image, which corresponds to the image that is expected without signal, is obtained by the following way. From one of the measured frames (e.g., I_0), we have calculated the noise components $i_{k,p,q}$ by Monte Carlo drawing with the condition:

$$\langle i_{k,p,q}^2 \rangle = I_{0,p,q}. \tag{13.27}$$

This condition corresponds to (13.9) since $\langle I_{k,p,q} \rangle \simeq I_{0,p,q}$. We have synthesized the image sequence I_k in the following manner:

$$I_{k,p,q} = I_{0,p,q} + i_{k,p,q}. \tag{13.28}$$

The Shot Noise image of Fig. 13.4b is reconstructed then from the $I_{k,p,q}$ sequence with $k = 0 \ldots 12$ since $M = 4n = 12$.

We have synthesized noisy images by summing the noiseless image of Fig. 13.4a with weight X, with the Noise image of Fig. 13.4b with weight $(1-X)$. The image of Fig. 13.4e is obtained with $X = 1/700$. Figure 13.4e corresponds thus to the same signal, and the same noise than Fig. 13.4c (i.e., 1 e of signal, and 1 e of noise respectively). As expected, Figs. 13.4c,e are visually very similar. The image of Fig. 13.4 is similarly obtained with $X = 0.15/700$. It corresponds to the same Signal and Noise than Fig. 13.4d (i.e., 0.15 e of signal, and 1 e of noise). As expected, Figs. 13.4d,f are visually very similar too.

Here we demonstrated our ability to synthesize a noisy image with a noise that is calculated by Monte Carlo from (13.27) and (13.28). Moreover, we have verified that the noisy image is visually equivalent to the image we have obtained in experiments. These results prove that we are able to assess quantitatively the noise, and that the noise that is obtained in experiments reaches the theoretical limit of 1 e of noise per pixel for the whole sequence of $M = 4n = 12$ frames.

13.4 Conclusion

In this chapter, we have studied the noise limits in off-axis, heterodyne digital holography. We have shown that because of the heterodyne gain of the holographic detection, the noise of the CCD camera can be neglected. Moreover, by a proper arrangement of the holographic setup, that combines off-axis geometry with phase shifting acquisition of holograms by heterodyne holography, it is possible to reach the theoretical shot noise limit. We have studied theoretically this limit, and we have shown that it corresponds to one photoelectron per pixel for the whole sequence of frame that is used to reconstruct the holographic image. This paradoxical result is related to the heterodyne detection, where the detection bandwidth is inversely proportional to the measurement time. We have verified all our results experimentally, and we have shown that is possible to image objects at very low signal levels. We have also shown that is possible to mimic the very weak illumination levels holograms obtained in experiments by Monte Carlo noise modeling.

References

1. D. Gabor. Microscopy by reconstructed wavefronts. *Proc. R. Soc. A*, 197:454, 1949.
2. A. Macovsky. Consideration of television holography. *Opt. Acta*, 22(16):1268, August 1971.
3. U. Schnars. Direct phase determination in hologram interferometry with use of digitally recorded holograms. *JOSA A.*, 11:977, July 1994.
4. J. W. Goodmann and R. W. Lawrence. Digital image formation from electronically detected holograms. *Appl. Phys. Lett.*, 11:77, 1967.
5. E. N. Leith, J. Upatnieks, and K. A. Haines. Microscopy by wavefront reconstruction. *J. Opt. Soc. Am.*, 55(8):981–986, 1965.
6. U. Schnars and W. Jüptner. Direct recording of holograms by a CCD target and numerical reconstruction. *Appl. Opt.*, 33(2):179–181, 1994.
7. T. M. Kreis, W. P. O. Juptner, and J. Geldmacher. Principles of digital holographic interferometry. *SPIE*, 3478:45, July 1988.
8. E. Cuche, P. Marquet, and C. Depeursinge. Spatial filtering for zero-order and twin-image elimination in digital off-axis holography. *Appl. Opt.*, 39(23):4070–4075, 2000.
9. I. Yamaguchi and T. Zhang. Phase-shifting digital holography. *Opt. Lett.*, 18(1):31, 1997.
10. F. LeClerc, L. Collot, and M. Gross. Numerical heterodyne holography using 2D photodetector arrays. *Opt. Lett.*, 25:716, 2000.
11. M. Atlan, M. Gross, and E. Absil. Accurate phase-shifting digital interferometry. *Opt. Lett.*, 32(11):1456–1458, 2007.
12. M. Gross, P. Goy, and M. Al-Koussa. Shot-noise detection of ultrasound-tagged photons in ultrasound-modulated optical imaging. *Opt. Lett.*, 28(24):2482–2484, 2003.
13. M. Atlan, B. C. Forget, F. Ramaz, A. C. Boccara, and M. Gross. Pulsed acousto-optic imaging in dynamic scattering media with heterodyne parallel speckle detection. *Opt. Lett.*, 30(11):1360–1362, 2005.
14. L. Wang and X. Zhao. Ultrasound-modulated optical tomography of absorbing objects buried in dense tissue-simulating turbid media. *Appl. Opt.*, 36(28):7277–7282, 1997.
15. F. Joud, F. Laloe, M. Atlan, J. Hare, and M. Gross. Imaging a vibrating object by sideband digital holography. *Opt. Exp.*, 17:2774, 2009.
16. F. Joud, F. Verpillat, F. Laloë, M. Atlan, J. Hare, and M. Gross. Fringe-free holographic measurements of large-amplitude vibrations. *Opt. Lett.*, 34(23):3698–3700, 2009.

17. M. Atlan, M. Gross, and J. Leng. Laser Doppler imaging of microflow. *J. Eur. Opt. Soc.*, 1:06025-1, 2006.
18. M. Atlan, M. Gross, B. C. Forget, T. Vitalis, A. Rancillac, and A. K. Dunn. Frequency-domain wide-field laser Doppler in vivo imaging. *Opt. Lett.*, 31(18):2762–2764, 2006.
19. M. Atlan, B. C. Forget, A. C. Boccara, T. Vitalis, A. Rancillac, A. K. Dunn, and M. Gross. Cortical blood flow assessment with frequency-domain laser Doppler microscopy. *J. Biomed. Opt.*, 12:024019, 2007.
20. M. Atlan, M. Gross, T. Vitalis, A. Rancillac, J. Rossier, and A. C. Boccara. High-speed wave-mixing laser Doppler imaging in vivo. *Opt. Lett.*, 33(8):842–844, 2008.
21. M. Gross and M. Atlan. Digital holography with ultimate sensitivity. *Opt. Lett.*, 32(8):909–911, 2007.
22. M. Gross, M. Atlan, and E. Absil. Noise and aliases in off-axis and phase-shifting holography. *Appl. Opt.*, 47(11):1757–1766, 2008.
23. H. A. Bachor, T. C. Ralph, S. Lucia, and T. C. Ralph. *A guide to experiments in quantum optics*. Wiley-VCH, New York, 1998.
24. M. Newberry. Measuring the gain of a CCD camera. *Axiom Technical Note: 1*, 1:1–9, 1998–2000.

B.4 Fringe-free holographic measurements of large-amplitude vibrations

F. Joud, F. Verpillat, F. Laloë, M. Atlan, J. Hare and M. Gross, Opt. Lett. **34**, 3698-3700 (2009) [Joud *et al.* 2009b]

Fringe-free holographic measurements of large-amplitude vibrations

F. Joud,[1] F. Verpillat,[1] F. Laloë,[1] M. Atlan,[2] J. Hare,[1] and M. Gross[1,*]

[1]*Laboratoire Kastler-Brossel, UMR 8552 CNRS, École Normale Supérieure, Université Paris 6, 24 rue Lhomond 75231 Paris Cedex 05 France*

[2]*Institut Langevin, UMR 7587 CNRS INSERM, ESPCI ParisTech, Université Paris 6, Université Paris 7, 10 rue Vauquelin, 75 231 Paris Cedex 05, France*

**Corresponding author: gross@lkb.ens.fr*

Received August 19, 2009; accepted September 25, 2009;
posted October 21, 2009 (Doc. ID 115962); published November 24, 2009

In the measurement of the amplitude of vibration of objects, holographic imaging techniques usually involve fringe counting; because of the limited resolution of the images, measurements of large amplitudes are not accessible. We demonstrate a technique that suppresses the necessity of fringe counting—frequency sideband imaging—where the order of the sideband is considered a marker of the amplitude. The measurement is completely local: no comparison with another reference point on the object is necessary. It involves a sharp variation of a signal, which makes it robust against perturbations. The method is demonstrated in an experiment made with a vibrating clarinet reed; phase modulations as large as 1000 rad have been measured.

OCIS codes: 090.1760, 200.4880, 040.2840, 100.2000.

The observation of interference fringes in holographic methods provides accurate measurements of the amplitude of vibration of objects. Powell and Stetson [1] have shown that the fringes on the holographic reconstruction of a vibrating object correspond, after time averaging, to zeros of the Bessel function $J_0(\Phi)$, where $\Phi(x,y)$ is the amplitude of phase modulation of the optical field emitted by the object at point x,y. Digital holography was introduced in 1994 by Schnars and Jüptner [2]. In 2003 Picard *et al.* [3] transposed the time averaging method to digital holography.

In a previous Letter [4], we described sideband digital holography, based on the detection of the light backscattered by a vibrating object at different sideband frequencies; the fringes for sideband n then correspond to the zeros of the nth-order Bessel function $J_n(\Phi)$. As in the work by Aleksoff [5] in 1971, the reference beam was frequency shifted to select one sideband n, but the use of acousto-optic modulators and numerical techniques provided much more flexibility. In [4], we showed how the comparison of dark fringes for different sideband leads to a determination of the vibration amplitude $\Phi(x,y)$ at each point of the object. This determination is nonlocal, since it involves counting fringes from one reference point of the image to the point of interest, so that large amplitudes are not accessible.

In this Letter, we demonstrate another approach that completely eliminates the necessity of counting fringes; it gives a local measurement of the amplitude of vibration, even for large values. For any pixel of coordinate x,y, we consider the sideband order n a variable and we plot the intensity I as a function of n. One can then easily determine Φ, since $I(n)$ exhibits a sharp variation from maximum to zero near $n \simeq \Phi$. The method is robust and can easily be used even when the fringes become so narrow that they cannot be resolved, which gives immediate access to large amplitudes of vibration.

Consider a point of the object vibrating at frequency ν_A and amplitude $z_{\max}$; its displacement $z(t)$ is

$$z(t) = z_{\max} \sin(2\pi\nu_A t). \tag{1}$$

In backscattering geometry, this corresponds to a phase modulation:

$$\varphi(t) = 4\pi z(t)/\lambda = \Phi \sin(2\pi\nu_A t), \tag{2}$$

where λ is the optical wavelength and $\Phi = 4\pi z_{\max}/\lambda$. The scattered field is then

$$E(t) = \mathcal{E} e^{j(\nu_0 t + \varphi(t))} = \mathcal{E} \sum_n J_n(\Phi) e^{j(\nu_0 + n\nu_A)t}, \tag{3}$$

where $\mathcal{E}$ is the complex amplitude of the field, ν_0 is the frequency of the illumination optical field, and J_n is the nth-order Bessel function of the first kind; $J_{-n}(z) = (-1)^n J_n(z)$ for integer n and real z. The scattered field is then the sum of sidebands with frequencies $\nu_0 + n\nu_A$ and intensities I_n, given by

$$I_n(\Phi) = |\mathcal{E} J_n(\Phi)|^2. \tag{4}$$

Figure 1(a) shows the intensity of the sidebands as a function of n, assuming $\Phi = 30.3$ rad. When n is considered a continuous variable $n = (\nu - \nu_0)/\nu_A$ giving the Doppler frequency shift in units of ν_A, one obtains the light gray shade corresponding to the Doppler spectrum deduced from the vibration velocity distribution. This continuous spectrum is proportional to $[1 - (n/\Phi)^2]^{-1/2}$, where n is confined between the values $\pm\Phi$ that correspond to the maximum Doppler shift. The discrete spectrum has a similar behavior, remaining mostly confined between the same n values and dropping abruptly from a maximum reached close to $n = \pm\Phi$ to almost zero. This is the key idea of our method: we measure the frequency position of this sharp variation and deduce from it the value of the vibration amplitude. This method can be seen as a discrete spectrum version of laser Doppler imaging of nonperiodic motions reported in [6,7].

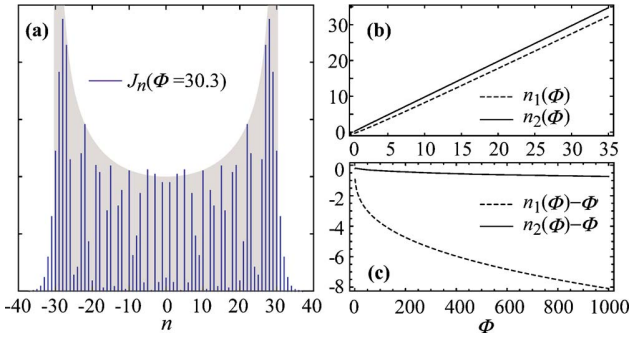

Fig. 1. (Color online) (a) Relative intensities of the sidebands as a function of n for fixed $\Phi=30.3$ rad. The vertical lines show the intensities of the discrete n components of the real spectrum. The light gray shade shows the Doppler spectrum obtained from the vibration velocity distribution, with a continuous variable on the horizontal axis $n=(\nu-\nu_0)/\nu_A$. Both spectra fall abruptly beyond $n=\pm 30.3$, which corresponds to the Doppler shift associated with the maximum velocity. (b) The dashed line shows the values n_1 as a function of Φ, where n_1 is the value of n giving the maximum intensity in the discrete spectrum; the solid line shows n_2, where n_2 is the value of n for which the intensity is half the maximum, which gives a very good approximation of Φ. (c) The dashed and solid curves, respectively, show $n_1-\Phi$ and $n_2-\Phi$ as a function of Φ.

Figures 1(b) and 1(c) give more detail on this sharp variation. For each value of Φ we calculate the value $n_1(\Phi)$ of n that, in Eq. (4), gives the maximum intensity. To avoid the quantization noise induced by discrete variables, the calculation is made with Bessel functions of fractional order, but of course only integer values of n are relevant to the experiment. It is known [8] that $n_1(\Phi)\simeq\Phi$, within a correction of order $\Phi^{1/3}$; the dashed curves show $n_1(\Phi)$ [Fig. 1(b)] and the difference $n_1(\Phi)-\Phi$ [Fig. 1(c)]. To determine more precisely the location of the abrupt drop from maximum to zero, we calculate the n value $n_2(\Phi)$ for which the intensity is half the maximum. The $n_2(\Phi)$ and the difference $n_2(\Phi)-\Phi$ are shown by the solid curves in Figs. 1(b) and 1(c), respectively. Clearly, n_2 gives an accurate evaluation of Φ.

The experimental setup is the same as described in [4]. As in [4], we have chosen a clarinet reed as the vibrating object to experimentally demonstrate the method. The reed, vibrating on its first flexural resonance mode at frequency $\nu_A\sim 2100$ Hz, is illuminated at $\lambda=650$ nm by a laser field E_I at frequency ν_0. The CCD camera (frame frequency $\nu_{\mathrm{CCD}}=10$ Hz) records the interference pattern (the hologram) between the scattered light and the local oscillator beam (field E_{LO}, frequency ν_{LO}). Two acousto-optic modulators (Bragg cells) with frequencies ν_{AOM1} and ν_{AOM2} are used to adjust the frequencies $\nu_0=\nu_L+\nu_{\mathrm{AOM2}}$ and $\nu_{\mathrm{LO}}=\nu_L+\nu_{\mathrm{AOM1}}$; an arbitrary sideband n can then be selected by adjusting these frequencies. A four-phase detection of sideband n is obtained by adjusting them to fulfill the relation

$$\nu_0+n\nu_A-\nu_{\mathrm{LO}}(n)=\nu_{\mathrm{CCD}}/4. \tag{5}$$

We record a sequence of consecutive CCD images $I_0,I_1,\ldots I_{M-1}$, where M is a multiple of 4. The complex hologram H in the plane of the CCD is then

$$H=\sum_{m=0}^{M-1} j^m I_m. \tag{6}$$

From H, the images are reconstructed as in [4] by the standard convolution method [2], which provides the map of the complex field $E(x,y,n)$ in the plane of the object. By successively adjusting the frequency $\nu_{\mathrm{LO}}(n)$ of the local oscillator to appropriate values, we then record the intensity images $|E(x,y,n)|^2$ of the sidebands as a function of x and y and n. We then obtain a cube of data with three axes x, y, and n, where x and y are expressed in units of pixels of the reconstructed image of the reed. Figure 2 shows the images obtained for for $n=0,20,\ldots 120$ that correspond to cuts of the cube along the x,y planes. The right part of the reed ($x>800$) is clamped on the mouthpiece. The images illustrate how, when n increases, the fringes move toward regions with larger amplitudes of vibrations: no signal is obtained in regions where $\Phi=4\pi z_{\max}/\lambda\leqslant n$. This well-known property of Bessel functions allows one to get a marker on the object, signaling regions where the amplitude corresponds to $\Phi\simeq 120$ rad. Figure 3(a) displays a cut of the cube of data along the x,n horizontal plane $y=750$ (horizontal white dashed line in Fig. 2). The envelope of the nonzero (nonblack) part of the image provides a measurement of the amplitude of vibration in units of $\lambda/4\pi$. We actually obtain a direct visualization of the shape of the reed at maximal elongation, from the right part clamped on the mouthpiece to the tip on the left. The maximum amplitude correspond to $\Phi\simeq 20, 40, 60,\ldots 120$ rad. Figure 3(b) displays a transverse cut along the y,n vertical $x=249$ plane (vertical white dashed line in Fig.

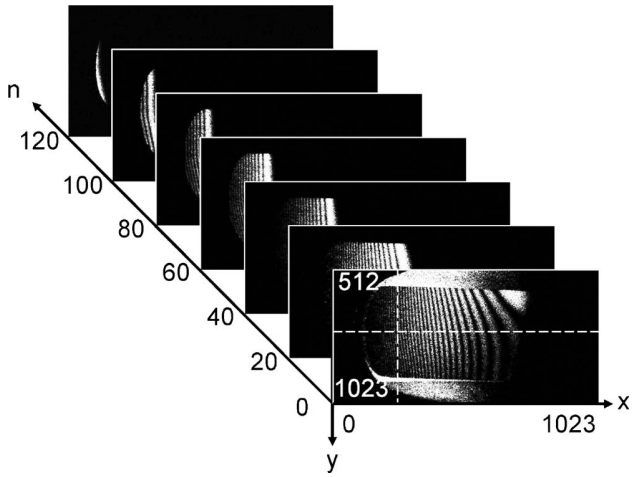

Fig. 2. Cube of data obtained from the reconstructed holographic images of a vibrating clarinet reed; sideband images with $n=0,20,40\ldots 120$ are shown in arbitrary linear scale. By choosing n, one moves the border of the illuminated region on the object, obtaining a local marker of the amplitude of vibration. The white dashed lines correspond to $x=249$ and $y=750$, i.e., to the point chosen for Fig. 3.

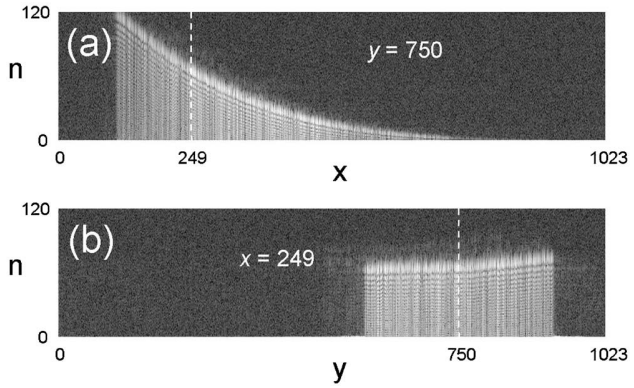

Fig. 3. Images corresponding to cuts of 3D data of the reconstructed images along the planes $y=750$ (a) and $x=249$ (b). (a) Deformation of the object along its axis. (b) Transverse cut with a slight vibration asymmetry. A logarithmic intensity scale is used.

2); a slight asymmetry of the reed vibration is clearly visible.

Figures 2 and 3 have been obtained by exciting the reed at the resonance frequency $\nu_A=2123$ Hz and at moderate excitation level. The consistency of amplitude measurements obtained in this way with those obtained by fringe counting is illustrated in Fig. 3 of [4]. We have also used higher excitation amplitudes, about 10 times larger (the frequency of reed resonance is then shifted to $\nu_A=2020$ Hz). Figure 4(a) shows the images obtained for $n=330$: the fringes are now completely unresolved, but the transition from zero to nonzero intensity remains very clear. With a single hologram, and without fringe counting, one obtains a clear marker of the line where $\Phi(x,y)=330$ rad.

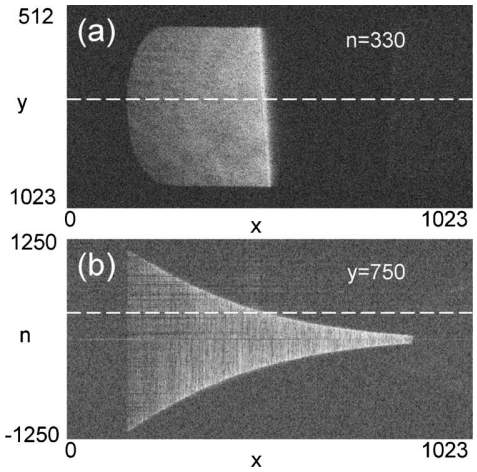

Fig. 4. (a) Image reconstructed with sideband $n=330$, with a large amplitude of vibration. (b) Equivalent of Fig. 3(a), but with positive and negative n values quantized by steps $\Delta n=10$; one measures a maximum vibration amplitude of $z_{\max}\simeq 60$ μm. An enlarged view of the $n\geqslant 0$ part of the image is provided in supplementary material (Media 1). A logarithmic intensity scale is used.

Figure 4(b) shows the equivalent of Fig. 3(a) but with a higher excitation level, and this time for positive and negative values of n; data range up to about $|n|\simeq 1140$, corresponding to $z_{\max}\simeq 58.4$ μm. Since the vibration amplitude is much larger than λ, the continuous approximation for n is valid, and the images of Fig. 3 can be reinterpreted in terms of the classical Doppler effect: if the signal intensity $I_n(x,y)$ at frequency $\nu_0+n\nu_A$ is nonzero, at some time t of the periodic motion the Doppler shift $\nu_0+2v(x,y,t)/c$ is equal to $n\nu_A$ (v and c are the reed and light velocities). The accuracy of the measurement of the amplitude corresponds to about one step: $\Delta n=10$, i.e., to 0.5 μm [see Fig. 4 (Media 1)]. A fine analysis of the 3D data shows a slight asymmetry between the positive and the negative n values. In Fig. 4(b), for example, the maximum value for $|n|$ is about 1160 for $n>0$ and 1120 for $n<0$. This means that the motion of the reed is not perfectly sinusoidal and that maximum velocities (i.e., maximum Doppler shifts) are slightly different for the up and down motion of the reed. A more detailed study of the modification of the spectrum due to the superposition of several harmonic motions can be done but falls beyond the scope of this Letter.

In conclusion, taking advantage of the frequency (or the sideband order n) of the light scattered by a vibrating object adds a new dimension to digital holography. Each pixel of the image then provides information that is completely independent of the others, which results in redundancy and robustness of the measurements. Looking at the edges of the spectrum provides an accurate determination of the vibration amplitude and avoids a cumbersome analysis of the entire data cube, giving easy access to measurements of large amplitudes of oscillation. Our method could be combined with other techniques, such as phase modulation of the reference beam [9,10], to yield information on the phase of the mechanical vibration without losing the robustness of the measurement.

References

1. R. Powell and K. Stetson, J. Opt. Soc. Am. **55**, 1593 (1965).
2. U. Schnars and W. Jüptner, Appl. Opt. **33**, 179 (1994).
3. P. Picart, J. Leval, D. Mounier, and S. Gougeon, Opt. Lett. **28**, 1900 (2003).
4. F. Joud, F. Laloë, M. Atlan, J. Hare, and M. Gross, Opt. Express **17**, 2774 (2009).
5. C. Aleksoff, Appl. Opt. **10**, 1329 (1971).
6. M. Atlan and M. Gross, Rev. Sci. Instrum. **77**, 116103 (2006).
7. M. Atlan, M. Gross, B. Forget, T. Vitalis, A. Rancillac, and A. Dunn, Opt. Lett. **31**, 2762 (2006).
8. M. Abramowitz and I. Stegun, *Handbook of Mathematical Functions with Formulas, Graphs, and Mathematical Table* (Courier Dover, 1965).
9. O. Lokberg, J. Acoust. Soc. Am. **96**, 2244 (1994).
10. F. Zhang, J. Valera, I. Yamaguchi, M. Yokota, and G. Mills, Opt. Rev. **11**, 297 (2004).

List of Figures

2.1 Scattering of a light wave by a localized scatterer 11
2.2 Real part of the refractive index of gold in function of the wavelength 17
2.3 Imaginary part of the refractive index of gold in function of the wavelength 18

3.1 Dennis Gabor 24
3.2 Dennis Gabor initial experimental holographic setup 25
3.3 Michelson's interferometer 32
3.4 Young's double slit interferometer 33
3.5 Huygens' principle 35
3.6 Schematic drawing of the hologram recording procedure in classic holography 38
3.7 Optical reconstruction in classical holography 40
3.8 Schematic drawing of the hologram recording procedure in off-axis classic holography 42
3.9 Schematic drawing of the hologram recording procedure in in-line digital holography 45
3.10 Holograms Off-axis recording in digital holography 46
3.11 Off-axis holographic signal recording by a CCD device 47
3.12 CCD array architecture 48
3.13 Interfringe distance 50
3.14 Coordinate system for digital holography 52
3.15 Coordinate system of the angular spectrum propagation 60
3.16 Numerical reconstruction by the angular spectrum method . . 63

4.1 Phase-Shifting of the reference wave using a mirror mounted on a Piezoelectric Transducer 67
4.2 Acousto-Optic Modulator or Bragg Cell 68
4.3 Arrangement for holographic heterodyne detection using two Acousto-Optic Modulators 70

5.1 General Experimental setup for Heterodyne Digital Holographic Microscopy 82
5.2 Optical arrangement for reconstruction in Digital Holographic Microscopy 84

5.3 Holograms of a flat phase object in the CCD image conjugate plane ($z = z_I$), in the rear focal plane $z \simeq z_p$ and in CCD plane $z = z_{CCD}$. 88
5.4 Reconstructed image of the MO rear focal plane with plane wave illumination and without sample 89
5.5 Example of an off-axis reconstructed holographic image: image from [Schnars & Jüptner 2002] (a) and zoom from [Schnars & Jüptner 1994] (b) 91
5.6 Standard USAF resolution target 92
5.7 Reconstructed intensity image of a microscope objective exit pupil in a gray logarithmic scale 95
5.8 Numerical spatial filtering and off-axis tilt correction 96
5.9 Size of the pixels in the MO pupil plane 98
5.10 Etendue for the holographic signal collection 100
5.11 Second step of the reconstruction by free space propagation of the Angular Spectrum 104
5.12 Gold nano particles on cell membranes in Petri dish imaged with Total Internal Reflexion (TIR) illumination. 107
5.13 Zoom of the TIR setup without (a) and with (b) culture medium and gold particles 108
5.14 Reconstructed images of 200 nm gold particles from the holographic data of [Atlan *et al.* 2008] 109
5.15 Zoom of gold nanoparticles imaging setup with an improper cover glass thickness compensation 110
5.16 Plot of the intensity $I_{max}(n)$ of the brightest point M_{max} of the intensity image $I(x, y) = |E(x, y, z = d'_n)|^2$ of the 200 nm gold particles 112
5.17 Reconstructed images of 200 nm gold particles from the holographic data of [Atlan *et al.* 2008]. Reconstruction is performed without (a,b) and with (c,d) glass coverslip thickness correction 113
5.18 Overview of the reconstruction procedure in holographic microscopy 114

6.1 NIH 3T3 fibroblasts under bright-field microscopy (10X) . . . 119
6.2 Biotinylation 122
6.3 Streptavidin-coated Gold Nanoparticles solution from BioAssay Works 123
6.4 Fibronectin-functionalized gold nanoparticles 124
6.5 Labeled Cell 124
6.6 Observation chamber for live biological specimens 126

6.7 Optical apparatus for DHM in total internal reflection 127
6.8 Roper cascade 512F CCD camera 128
6.9 Specimen microscopy stage 129
6.10 Dark field illumination of the specimen in Total Internal Reflection 130
6.11 White light direct image of a USAF chart for calibrating the MO 132
6.12 Direct images of 3T3 fibroblasts labeled with several 40 nm Au Nps 135
6.13 Reconstructed holographic intensity image of 3T3 cells labeled with several Au Nps 136
6.14 3D visualizations of cells marked with several 40 nm Au Nps . 137
6.15 Intensity cuts along x axis at positions of spots 1, 2 and 3 of the cells specimen marked with several Au Nps 138
6.16 Intensity cuts along y axis at positions of spots 1, 2 and 3 of the cells specimen marked with several Au Nps 141
6.17 Cross sections reconstruction planes of Au labeled cells 142
6.18 Reconstructed images in the (y,z) plane obtained by performing a cut along x axis at the positions of the selected spots for the multi Au Nps marked 3T3 cell sample 142
6.19 Fibroblast cell tagged with a single 40 nm gold particle 144
6.20 A fibroblast cell tagged with a 40 nm gold particle using 1 frame acquisition 145
6.21 Experimental linear-scale plot of cuts made within the intensity signal I along the three axis x, y and z at the brightest voxel of Figure 6.20b corresponding to the gold nanoparticle location. 146
6.22 A fibroblast cell tagged with a 40 nm gold particle using 32 frames acquisition 148
6.23 32 frames reconstructed holographic intensity image of a 3T3 cell labeled with a single Au Np 149
6.24 Experimental linear plot of cuts made within the intensity signal I along the three axis x, y and z at the brightest voxel of Figure 6.22a corresponding to the gold nanoparticle location . 150
6.25 Intensity plot of the cut along the x axis in logarithmic scale : (1) at the nanoparticle location and (4) without illuminating the sample 151
6.26 Reconstructed images in the (y,z) plane obtained by performing a cut along x axis at the positions of the selected spots for the single Au Np marked 3T3 cell sample 153
6.27 Direct images of an unmarked 3T3 fibroblast 154
6.28 Reconstructed holographic intensity image of an unmarked 3T3 cell 155

6.29 3D visualizations of an unlabeled fibroblast cell 155
6.30 Cross sections reconstruction planes of an unmarked 3T3 cell . 156
6.31 Reconstructed images in the (y,z) plane obtained by performing a cut along x axis at the positions of the selected spots for the unmarked 3T3 cell sample 157
6.32 Images of free 40 nm gold nanoparticles 157
6.33 Reconstructed holographic intensity image of free 40 nm gold nanoparticles 159
6.34 3D linear-scale surface plot of the reconstructed holographic intensity image of free 40 nm gold nanoparticles 160
6.35 Intensity cuts along x axis at positions of nanoparticles 1, 2 and 3 of the free 40 nm Au Nps 161
6.36 Intensity cuts along y axis at positions of nanoparticles 1, 2 and 3 of the free 40 nm Au Nps 162
6.37 Cross sections reconstruction planes of free gold nanoparticles 163
6.38 Reconstructed images in the (y,z) plane obtained by performing a cut along x axis at the positions of the selected spots of the free Au Nps sample 163
6.39 Reconstructed images in the (x,z) plane obtained by performing a cut along x axis at the positions of the selected spots of the free Au Nps sample 164

7.1 Glass bottom cell culture dish from World Precision Instruments 168
7.2 Fibronectin-functionalized gold nanoparticles 169
7.3 Glass bottom cell culture dish from World Precision Instruments 170
7.4 Glass bottom cell culture dish from World Precision Instruments 171
7.5 Labeled Cell 172
7.6 Specimen microscopy stage 173
7.7 Optical apparatus for DHM in slant illumination geometry . . 174
7.8 PCO Pixelfly QE CCD camera 176
7.9 Slant illumination of the specimen for dark field microscopy . 177
7.10 Truncation of the calculation matrix from a 1024×1024 pixels' matrix to a 512×512 pixel's matrix 178
7.11 Reconstructed holographic intensity image of free 80 nm gold nanoparticles using a dark-field slant illumination geometry displayed in a colored logarithmic scale 180
7.12 Scattering of free 80 nm gold nanoparticles 182
7.13 Direct images of unlabeled 3T3 fibroblasts 183
7.14 Reconstructed holographic intensity image of unlabeled 3T3 fibroblasts using a dark-field slant illumination geometry displayed in a colored logarithmic scale 184

7.15 Scattering of unlabeled cells 185
7.16 Direct images of 3T3 fibroblasts labeled with several 80 nm AuNps 187
7.17 Reconstructed holographic intensity image of 3T3 fibroblasts labeled with 80 nm AuNps using a dark-field slant illumination geometry displayed in a colored logarithmic scale 188
7.18 Scattering of cells labeled with 80 nm AuNps 189
7.19 Images of a 3T3 fibroblast showing the blurry effect of the slant illumination geometry 190
7.20 Slant illumination geometry. The specimen is illuminated from the top 191
7.21 Optical apparatus for DHM in total internal reflection 192
7.22 Direct white light image of 3T3 fibroblasts conjugated to 80 nm gold nanoparticles 193
7.23 Reconstructed holographic intensity image using a TIR illumination geometry in a colored logarithmic scale of 3T3 fibroblasts conjugated to 80 nm gold nanoparticles 194
7.24 Direct white light image of 3T3 fibroblasts conjugated to 60 nm gold nanoparticles 195
7.25 Reconstructed holographic intensity image using a TIR illumination geometry in a colored logarithmic scale of 3T3 fibroblasts conjugated to 60 nm gold nanoparticles 196
7.26 Direct white light image of 3T3 fibroblasts conjugated to 40 nm gold nanoparticles 197
7.27 Reconstructed holographic intensity image using a TIR illumination geometry in a colored logarithmic scale of 3T3 fibroblasts conjugated to 40 nm gold nanoparticles 198
7.28 Direct white light image of 3T3 fibroblasts 200
7.29 Reconstructed holographic intensity image using a TIR illumination geometry in a colored logarithmic scale of 3T3 fibroblasts illuminated by (a) a short coherence length red laser and (b) a green laser 201

List of Tables

5.1 Specifications of the Olympus UPLFLN 60X MO 110

6.1 Specifications of the Olympus LMPLFLN 50X MO 128

7.1 Specifications of the Mitutoyo 50X MO 176

Bibliography

[Abramoff *et al.* 2004] MD Abramoff, PJ Magalhaes and SJ Ram. *Image processing with ImageJ.* Biophotonics International, vol. 11, no. 7, pages 36–43, 2004. (Cited on page 137.)

[Absil *et al.* 2010] E. Absil, G. Tessier, M. Gross, M. Atlan, N. Warnasooriya, S. Suck, M. Coppey-Moisan and D. Fournier. *Photothermal heterodyne holography of gold nanoparticles.* Opt. Express, vol. 18, pages 780–786, 2010. (Cited on page 153.)

[Alvarez *et al.* 1997] M.M. Alvarez, J.T. Khoury, T.G. Schaaff, M.N. Shafigullin, I. Vezmar and R.L. Whetten. *Optical absorption spectra of nanocrystal gold molecules.* The Journal of Physical Chemistry B, vol. 101, no. 19, pages 3706–3712, 1997. (Cited on page 17.)

[Atlan & Gross 2007] M. Atlan and M. Gross. *Digital holography with ultimate sensitivity.* Opt. Lett., vol. 32, pages 909–911, 2007. (Cited on page 150.)

[Atlan *et al.* 2007] M. Atlan, M. Gross and E. Absil. *Accurate phase-shifting digital interferometry.* Opt. Lett., vol. 32, pages 1456–1458, 2007. (Cited on page 131.)

[Atlan *et al.* 2008] M. Atlan, M. Gross, P. Desbiolles, E. Absil, G. Tessier and M. Coppey-Moisan. *Heterodyne holographic microscopy of gold particles.* Opt. Lett, vol. 35, pages 500–502, 2008. (Cited on pages 3, 109, 111, 112, 113 and 256.)

[Bohren & Huffman 1983] C.F. Bohren and D.R. Huffman. *Absorption and scattering of light by small particles.* Research supported by the University of Arizona and Institute of Occupational and Environmental Health. New York, Wiley-Interscience, 1983, 541 p., vol. 1, 1983. (Cited on pages 10, 17, 18, 19 and 20.)

[Born *et al.* 1999] M. Born, E. Wolf and A.B. Bhatia. Principles of optics: electromagnetic theory of propagation, interference and diffraction of light. Cambridge Univ Pr, 1999. (Cited on pages 35 and 36.)

[Boyer *et al.* 2003] D. Boyer, P. Tamarat, A. Maali, B. Lounis and M. Orrit. *Photothermal imaging of nanometer-sized metal particles among scatterers.* Science, vol. 297, pages 1160–1163, 2003. (Cited on page 3.)

[Brevier] Julien Brevier. *Symétrie brisée et renforcement de contacts cellulaires*. PhD thesis. (Cited on page 118.)

[Cheong *et al.* 1990] W.F. Cheong, S.A. Prahl and A.J. Welch. *A review of the optical properties of biological tissues*. IEEE journal of quantum electronics, vol. 26, no. 12, pages 2166–2185, 1990. (Cited on pages 10, 15 and 152.)

[Cognet *et al.* 2002] L. Cognet, C. C. Tardin, D. Boyer, D. Choquet, P. Tamarat and B. Lounis. *Single metallic nanoparticles imaging for protein detection in cells*. Proc. Natl. Acad. Sci., vol. 100, pages 11350–11355, 2002. (Cited on page 129.)

[Cognet *et al.* 2003] L. Cognet, C. C. Tardin, D. Boyer, D. Choquet, P. Tamarat and B. Lounis. *Single metallic nanoparticles imaging for protein detection in cells*. In Proc. Natl. Acad. Sci., volume 100, pages 11350–11355, USA, 2003. (Cited on pages 3 and 17.)

[Colomb *et al.* 2006a] T. Colomb, E. Cuche, F. Charrière, J. Kühn, N. Aspert, F. Montfort, P. Marquet and C. Depeursinge. *Automatic procedure for aberration compensation in digital holographic microscopy and applications to specimen shape compensation*. Applied optics, vol. 45, no. 5, pages 851–863, 2006. (Cited on page 87.)

[Colomb *et al.* 2006b] T. Colomb, J. Kühn, F. Charrière, C. Depeursinge, P. Marquet and N. Aspert. *Total aberrations compensation in digital holographic microscopy with a reference conjugated hologram*. Optics Express, vol. 14, no. 10, pages 4300–4306, 2006. (Cited on pages 2 and 87.)

[Colomb *et al.* 2006c] T. Colomb, F. Montfort, J. Kuehn, N. Aspert, E. Cuche, A. Marian, F. Charriére, S. Bourquin, P. Marquet and C. Depeursinge. *Numerical parametric lens for shifting, magnification, and complete aberration compensation in digital holographic microscopy*. J. Opt. Soc. Am. A, vol. 23, pages 3177–3190, 2006. (Cited on pages 87 and 131.)

[Cuche *et al.* 1999] E. Cuche, F. Bevilacqua and C. Depeursinge. *Digital holography for quantitative phase-contrast imaging*. Optics Letters, vol. 24, no. 5, pages 291–293, 1999. (Cited on pages 91 and 93.)

[Daniel & Astruc 2004] M.C. Daniel and D. Astruc. *Gold nanoparticles: assembly, supramolecular chemistry, quantum-size-related properties,*

and applications toward biology, catalysis, and nanotechnology. Chemical Reviews, vol. 104, no. 1, pages 293–346, 2004. (Cited on page 16.)

[Debailleul *et al.* 2008] M. Debailleul, B. Simon, V. Georges, O. Haeberlé and V. Lauer. *Holographic microscopy and diffractive microtomography of transparent samples.* Measurement Science and Technology, vol. 19, page 074009, 2008. (Cited on page 2.)

[Demetrakopoulos & Mittra 1974] TH Demetrakopoulos and R. Mittra. *Digital and optical reconstruction of images from suboptical diffraction patterns.* Applied Optics, vol. 13, no. 3, pages 665–670, 1974. (Cited on page 51.)

[Doremus 1964] R.H. Doremus. *Optical properties of small gold particles.* The Journal of Chemical Physics, vol. 40, page 2389, 1964. (Cited on page 17.)

[Dubois *et al.* 1999] F. Dubois, L. Joannes and J.C. Legros. *Improved three-dimensional imaging with a digital holography microscope with a source of partial spatial coherence.* Applied optics, vol. 38, no. 34, pages 7085–7094, 1999. (Cited on page 206.)

[Dubois *et al.* 2008] F. Dubois, C. Yourassowsky, N. Callens, C. Minetti and P. Queeckers. *Applications of digital holographic microscopes with partially spatial coherence sources.* In Journal of Physics: Conference Series, volume 139, page 012027. IOP Publishing, 2008. (Cited on page 2.)

[Duck 1990] F.A. Duck. Physical properties of tissue: a comprehensive reference book. Academic Pr, 1990. (Cited on page 15.)

[El-Sayed *et al.* 2005] I. H. El-Sayed, X. Huang and M. A. El-Sayed. *Surface plasmon resonance scattering and absorption of anti-EGFR antibody conjugated gold nanoparticles in cancer diagnostics: Applications in oral cancer.* Nano Lett., vol. 5, pages 829–834, 2005. (Cited on page 3.)

[Faraday 1857] M. Faraday. *The Bakerian lecture: experimental relations of gold (and other metals) to light.* Philosophical Transactions of the Royal Society of London, vol. 147, pages 145–181, 1857. (Cited on page 16.)

[Feng & Lee 1991] S. Feng and P.A. Lee. *Mesoscopic conductors and correlations in laser speckle patterns.* Science, vol. 251, no. 4994, page 633, 1991. (Cited on page 101.)

[Ferraro *et al.* 2003] P. Ferraro, S. De Nicola, A. Finizio, G. Coppola, S. Grilli, C. Magro and G. Pierattini. *Compensation of the inherent wave front curvature in digital holographic coherent microscopy for quantitative phase-contrast imaging.* Applied optics, vol. 42, no. 11, pages 1938–1946, 2003. (Cited on page 86.)

[Frens 1973] G. Frens. *Controlled nucleation for the regulation of the particle size in monodisperse gold suspensions.* Nature, vol. 241, no. 105, pages 20–22, 1973. (Cited on page 16.)

[Gabor 1948] D Gabor. *A new microscopic principle.* Nature, vol. 161, pages 777–778, 1948. (Cited on page 23.)

[Gabor 1949] D Gabor. *Microscopy by reconstructed wave-fronts.* Proc. Roy. Soc. A, vol. 197, pages 454–487, 1949. (Cited on page 24.)

[Goodman & R.W. 1967] J. W. Goodman and Lawrence R.W. *"Digital image formation from electronically detected holograms.* Appl. Phys. Lett., vol. 11, pages 77–79, 1967. (Cited on page 44.)

[Goodman 1968] J. W. Goodman. Introduction to fourier optics. McGraw-Hill, San Francisco, CA, second édition, 1968. (Cited on pages 36, 43 and 58.)

[Green 1975] N.M. Green. *Avidin.* Advances in protein chemistry, vol. 29, pages 85–133, 1975. (Cited on page 118.)

[Hecht 2001] E. Hecht. *Optics 4th edition.* Optics 4th edition, vol. 1, 2001. (Cited on pages 35 and 36.)

[Hulst 1981] H.C. Hulst. Light scattering by small particles. Dover Pubns, 1981. (Cited on pages 10, 18, 19 and 20.)

[Imry 1986] Y. Imry. *Active transmission channels and universal conductance fluctuations.* EPL (Europhysics Letters), vol. 1, page 249, 1986. (Cited on page 101.)

[Ishimaru 1978] A. Ishimaru. Wave propagation and scattering in random media, volume 1. Academic Press, New York, 1978. (Cited on page 10.)

[Jacques *et al.* 1987] SL Jacques, CA Alter and SA Prahl. *Angular dependence of HeNe laser light scattering by human dermis.* Lasers Life Sci, vol. 1, no. 4, pages 309–333, 1987. (Cited on page 15.)

[Jain *et al.* 2006] P. K. Jain, K. S. Lee, I. H. El-Sayed and M. A. El-Sayed. *Calculated absorption and scattering properties of gold nanoparticles of different size, shape, and composition: Applications in biological imaging and biomedicine.* J. Phys. Chem. B, vol. 110, pages 7238–7248, 2006. (Cited on page 16.)

[Jeong *et al.* 2007] K. Jeong, J.J. Turek and D.D. Nolte. *Volumetric motility-contrast imaging of tissue response to cytoskeletal anti-cancer drugs.* Opt. Express, vol. 15, no. 21, pages 14057–14064, 2007. (Cited on page 2.)

[Johansson *et al.* 1997] S. Johansson, G. Svineng, K. Wennerberg, A. Armulik and L. Lohikangas. *Fibronectin-integrin interactions.* Front Biosci, vol. 2, pages d126–d146, 1997. (Cited on page 118.)

[Johnson & Christy 1972] P.B. Johnson and RW Christy. *Optical constants of the noble metals.* Physical Review B, vol. 6, no. 12, page 4370, 1972. (Cited on page 17.)

[Joud *et al.* 2009a] F. Joud, F. Laloë, M. Atlan, J. Hare and M. Gross. *Imaging a vibrating object by Sideband Digital Holography.* Opt. Express, vol. 17, pages 2774–2779, 2009. (Cited on page 74.)

[Joud *et al.* 2009b] F. Joud, F. Verpillat, F. Laloë, M. Atlan, J. Hare and M. Gross. *Fringe-free holographic measurements of large-amplitude vibrations.* Opt. Letters, vol. 34, pages 3698–3700, 2009. (Cited on pages 74 and 251.)

[Joud *et al.* 2010a] F. Joud, F. Verpillat, M. Atlan, P.A. Taillard and M. Gross. *Shot Noise in Digital Holography.* Information Optics and Photonics: Algorithms, Systems, and Applications, page 163, 2010. (Cited on pages 73, 131 and 237.)

[Joud *et al.* 2010b] F. Joud, N. Warnasooriya, P. Bun, G. Tessier, M. Coppey-Moisan, P. Desbiolles, M. Atlan, M. Abboud and M. Gross. *Imaging gold nanoparticles in living cell environments using heterodyne digital holographic microscopy.* Opt. Express, vol. 18, pages 3264–3273, 2010. (Cited on page 226.)

[Joud *et al.* 2011] F. Joud, N. Warnasooriya, P. Bun, F. Verpillat, S.Y. Suck, G. Tessier, M. Atlan, P. Desbiolles, M. Coppey-Moisan, M. Abboud*et al.* *3D exploration of light scattering from live cells in the presence of gold nanomarkers using holographic microscopy.* 3D Research, vol. 2, no. 1, pages 1–8, 2011. (Cited on page 217.)

[Kemper & von Bally 2008] B. Kemper and G. von Bally. *Digital holographic microscopy for live cell applications and technical inspection.* Applied optics, vol. 47, no. 4, pages A52–A61, 2008. (Cited on page 2.)

[Kemper *et al.* 2006] B. Kemper, D. Carl, J. Schnekenburger, I. Bredebusch, M. Sch
"afer, W. Domschke and G. von Bally. *Investigation of living pancreas tumor cells by digital holographic microscopy.* Journal of biomedical optics, vol. 11, page 034005, 2006. (Cited on page 2.)

[Kreibig & Vollmer 1995] U. Kreibig and M. Vollmer. *Optical properties of metal clusters.* Vold. 25 of Springer Series in Materials Science, 1995. (Cited on pages 3, 16 and 17.)

[Kreis *et al.* 1997] T.M. Kreis, M. Adams and W.P.O. Jueptner. *Methods of digital holography: a comparison.* In Proceedings of SPIE, volume 3098, page 224, 1997. (Cited on page 51.)

[Kreis 2002] T.M. Kreis. *Frequency analysis of digital holography.* Optical Engineering, vol. 41, page 771, 2002. (Cited on page 51.)

[Kreis 2005] Thomas Kreis. Handbook of holographic interferometry, optical and digital methods. Wiley-VCH, 2005. (Cited on pages 26, 31 and 66.)

[Lasne *et al.* 2006] D. Lasne, G. A. Blab, S. Berciaud, M. Heine, L. Groc, D. Choquet, L. Cognet and B. Lounis. *Single nanoparticle photothermal tracking (SNaPT) of 5-nm gold beads in live cells.* Biophys. J., vol. 91, pages 4598–4604, 2006. (Cited on page 3.)

[LeClerc *et al.* 2000] F. LeClerc, L. Collot and M. Gross. *Numerical heterodyne holography with two-dimensional photo-detector arrays.* Opt. Lett., vol. 25, pages 716–718, Mai 2000. (Cited on pages 66, 131 and 132.)

[LeClerc *et al.* 2001] F. LeClerc, M. Gross and L. Collot. *Synthetic-aperture experiment in the visible with on-axis digital heterodyne holography.* Opt. Lett., vol. 26, pages 1550–1552, 2001. (Cited on page 132.)

[Lee *et al.* 2009] C.W. Lee, E.H. Lin, J.Y. Cheng and P.K. Wei. *Study of gold nanoparticles and live cells interactions by using planar evanescent wave excitation.* Journal of Biomedical Optics, vol. 14, page 021005, 2009. (Cited on page 3.)

[Leith & Upatnieks 1962] E.N. Leith and J. Upatnieks. *Reconstructed wavefronts and communication theory.* J. Opt. Soc. Am., vol. 52, pages 1123–1130, 1962. (Cited on pages 25, 41 and 65.)

[Leith & Upatnieks 1963] E.N. Leith and J. Upatnieks. *Wavefront reconstruction with continuous-tone objects.* Journal of the Optical Society of America, vol. 53, no. 12, pages 1377–1381, 1963. (Cited on page 25.)

[Leith & Upatnieks 1964] E.N. Leith and J. Upatnieks. *Wavefront reconstruction with diffused illumination and three-dimensional objects.* Journal of the Optical Society of America, vol. 54, no. 11, pages 1295–1301, 1964. (Cited on page 41.)

[Lewinski *et al.* 2008] N. Lewinski, V. Colvin and R. Drezek. *Cytotoxicity of nanoparticles.* Small, vol. 4, no. 1, pages 26–49, 2008. (Cited on page 20.)

[Li *et al.* 2010] J. Li, Z. Peng, P. Tankam and P. Picart. *Design of the spatial filter window for digital holographic convolution reconstruction of object beam field.* Optics Communications, 2010. (Cited on page 93.)

[Liddington & Ginsberg 2002] RC Liddington and MH Ginsberg. *Integrin activation takes shape.* The Journal of cell biology, vol. 158, no. 5, page 833, 2002. (Cited on page 118.)

[Link & El-Sayed 1999] S. Link and M.A. El-Sayed. *Size and temperature dependence of the plasmon absorption of colloidal gold nanoparticles.* The Journal of Physical Chemistry B, vol. 103, no. 21, pages 4212–4217, 1999. (Cited on page 17.)

[Maiman 1960] T.H. Maiman. *Stimulated optical radiation in ruby.* 1960. (Cited on page 25.)

[Mann *et al.* 2005] C. J. Mann, L. Yu, C. M. Lo and M. K. Kim. *High resolution quantitative phase-contrast microscopy by digital holography.* Opt. Express, vol. 13, pages 8693–8698, 2005. (Cited on page 132.)

[Mann *et al.* 2006] C. J. Mann, L. Yu and M. K. Kim. *Movies of cellular and sub-cellular motion by digital holographic microscopy.* Biomed. Eng. Online, vol. 5, page 21, 2006. (Cited on page 2.)

[Marquet *et al.* 2005] P. Marquet, B. Rappaz, P.J. Magistretti, E. Cuche, Y. Emery, T. Colomb and C. Depeursinge. *Digital holographic microscopy: a noninvasive contrast imaging technique allowing quantitative visualization of living cells with subwavelength axial accuracy.*

Optics letters, vol. 30, no. 5, pages 468–470, 2005. (Cited on pages 87 and 206.)

[Mertz 2010] Jerome Mertz. Introduction to optical microscopy. Roberts and company, 2010. (Cited on page 66.)

[Mie 1908] G. Mie. *Beiträge zur Optik trüber Medien, speziell kolloidaler Metallösungen.* Annalen der Physik, vol. 330, no. 3, pages 377–445, 1908. (Cited on pages 10 and 18.)

[Mölder *et al.* 2008] A. Mölder, M. Sebesta, M. Gustafsson, L. Gisselson, A.G. WINGREN and K. Alm. *Non-invasive, label-free cell counting and quantitative analysis of adherent cells using digital holography.* Journal of Microscopy, vol. 232, no. 2, pages 240–247, 2008. (Cited on page 2.)

[Montfort *et al.* 2006] F. Montfort, F. Charrière, T. Colomb, E. Cuche, P. Marquet and C. Depeursinge. *Purely numerical compensation for microscope objective phase curvature in digital holographic microscopy: influence of digital phase mask position.* JOSA A, vol. 23, no. 11, pages 2944–2953, 2006. (Cited on page 87.)

[Nicola *et al.* 2002] S.D. Nicola, P. Ferraro, A. Finizio and G. Pierattini. *Wave front reconstruction of Fresnel off-axis holograms with compensation of aberrations by means of phase-shifting digital holography.* Optics and lasers in engineering, vol. 37, no. 4, pages 331–340, 2002. (Cited on page 87.)

[Paciotti *et al.* 2004] G.F. Paciotti, L. Myer, D. Weinreich, D. Goia, N. Pavel, R.E. McLaughlin and L. Tamarkin. *Colloidal gold: a novel nanoparticle vector for tumor directed drug delivery.* Drug delivery, vol. 11, no. 3, pages 169–183, 2004. (Cited on page 3.)

[Palik 1991] E.D. Palik. Handbook of optical constants of solids ii, volume 2. Academic press, 1991. (Cited on pages 17 and 18.)

[Pasquato *et al.* 2004] L. Pasquato, P. Pengo and P Scrimin. Biological and biomimetic applications of nanoparticles, pages 251–282. Springer Us, 2004. (Cited on page 21.)

[Prahl 1988] S. A. Prahl. *Light Transport in Tissue.* PhD thesis, University of Texas at Austin, 1988. (Cited on page 15.)

[Raschke *et al.* 2003] G. Raschke, S. Kowarik, T. Franzel, C. Sonnichsen, T. A. Klar and J. Feldmann. *Biomolecular recognition based on single*

gold nanoparticles light scattering. Nano Lett., vol. 3, pages 935–938, 2003. (Cited on page 3.)

[Richards-Kortum & Sevick-Muraca 1996] R. Richards-Kortum and E. Sevick-Muraca. *Quantitative optical spectroscopy for tissue diagnosis.* Annual review of physical chemistry, vol. 47, no. 1, pages 555–606, 1996. (Cited on pages 13 and 14.)

[Saleh *et al.* 1991] B.E.A. Saleh, M.C. Teich and B.E. Saleh. *Fundamentals of photonics.* 1991. (Cited on pages 41 and 43.)

[Scheffold & Maret 1998] F. Scheffold and G. Maret. *Universal conductance fluctuations of light.* Physical review letters, vol. 81, no. 26, pages 5800–5803, 1998. (Cited on page 101.)

[Scheffold & Maret 2001] Frank Scheffold and Georg Maret. Dynamic speckle correlation in waves and imaging through complex media p. sebbah ed. Kluwer Academic, 2001. (Cited on page 101.)

[Schnars & Jueptner 2005] U. Schnars and W. Jueptner. Digital holography: digital hologram recording, numerical reconstruction, and related techniques. Springer Verlag, 2005. (Cited on pages 29, 35, 55 and 56.)

[Schnars & Jüptner 1994] U. Schnars and W. Jüptner. *Direct recording of holograms by a CCD target and numerical reconstruction.* Applied Optics, vol. 33, no. 2, pages 179–181, 1994. (Cited on pages 44, 90, 91, 98, 102, 131 and 256.)

[Schnars & Jüptner 2002] U Schnars and W. P. O. Jüptner. *Digital recording and numerical reconstruction of holograms.* Meas. Sci. Technol., vol. 13, pages R85–R101, 2002. (Cited on pages 91 and 256.)

[Sperling *et al.* 2008] R.A. Sperling, P.R. Gil, F. Zhang, M. Zanella and W.J. Parak. *Biological applications of gold nanoparticles.* Chem. Soc. Rev., vol. 37, no. 9, pages 1896–1908, 2008. (Cited on pages 3, 20 and 21.)

[Storhoff *et al.* 2004] J.J. Storhoff, A.D. Lucas, V. Garimella, Y.P. Bao and U.R. Müller. *Homogeneous detection of unamplified genomic DNA sequences based on colorimetric scatter of gold nanoparticle probes.* Nature biotechnology, vol. 22, no. 7, page 883, 2004. (Cited on page 3.)

[Todaro & Green 1963] G.J. Todaro and H. Green. *Quantitative studies of the growth of mouse embryo cells in culture and their development into established lines.* The Journal of cell biology, vol. 17, no. 2, page 299, 1963. (Cited on page 119.)

[Tuchin 2002] V.V. Tuchin. Handbook of optical biomedical diagnostics, volume 107. Society of Photo Optical, 2002. (Cited on page 15.)

[Tuchin 2007] V.V. Tuchin. *Tissue optics: light scattering methods and instruments for medical diagnosis*. SPIE-International Society for Optical Engineering, 2007. (Cited on page 15.)

[Turkevich *et al.* 1951] J. Turkevich, P.C. Stevenson and J. Hillier. *A study of the nucleation and growth processes in the synthesis of colloidal gold*. Discuss. Faraday Soc., vol. 11, pages 55–75, 1951. (Cited on page 16.)

[Van Dijk *et al.* 2006] MA Van Dijk, AL Tchebotareva, M. Orrit, M. Lippitz, S. Berciaud, D. Lasne, L. Cognet and B. Lounis. *Absorption and scattering microscopy of single metal nanoparticles*. Phys. Chem. Chem. Phys., vol. 8, no. 30, pages 3486–3495, 2006. (Cited on pages 16, 19 and 20.)

[Verpillat *et al.* 2010] F. Verpillat, F. Joud, M. Atlan and M. Gross. *Digital holography at shot noise level*. Display Technology, Journal of, vol. 6, no. 10, pages 455–464, 2010. (Cited on page 131.)

[Vo-Dinh 2003] Tuan Vo-Dinh. *Biomedical Photonics Handbook*. vol. 1, 2003. (Cited on page 15.)

[West *et al.* 2006] J. L. West, R. A. Drezek and N. J. Halas. *Nanotechnology provides new tools for biomedical optics*. In J. D. Bronzino, editeur, Tissue Engineering and Artifical Organs, 3rd Edition, pages 25–1–25–9. CRC Press, 2006. (Cited on page 20.)

[Yamaguchi & Zhang 1997] I. Yamaguchi and T. Zhang. *Phase-shifting digital holography*. Opt. Lett., vol. 22, pages 1268–1270, 1997. (Cited on pages 48 and 66.)

[Yamaguchi *et al.* 2001] I. Yamaguchi, J. Kato, S. Ohta and J. Mizuno. *Image formation in phase-shifting digital holography and applications to microscopy*. Applied Optics, vol. 40, no. 34, pages 6177–6186, 2001. (Cited on page 66.)

[Yamagushi 2006] I. Yamagushi. Phase-shifting digital holography, principles and applications, pages 145–171. Springer, 2006. (Cited on page 66.)

[Yoon 1988] G. Yoon. *Absorption and Scattering of Laser Light in Biological Media – Mathematical Modeling and Methods for Determining Optical Properties*. PhD thesis, University of Texas at Austin, 1988. (Cited on page 15.)

[Yu & Kim 2005] L. Yu and M. Kim. *Wavelength-scanning digital interference holography for tomographic three-dimensional imaging by use of the angular spectrum method.* Opt. Lett., vol. 30, pages 2092–2094, 2005. (Cited on pages 51 and 132.)

[Yu *et al.* 2009] L. Yu, S. Mohanty, J. Zhang, S. Genc, M.K. Kim, M.W. Berns and Z. Chen. *Digital holographic microscopy for quantitative cell dynamic evaluation during laser microsurgery.* Optics express, vol. 17, no. 14, pages 12031–12038, 2009. (Cited on page 2.)

[Zhang & Yamaguchi 1998] T. Zhang and I. Yamaguchi. *Three-dimensional microscopy with phase-shifting digital holography.* Optics letters, vol. 23, no. 15, pages 1221–1223, 1998. (Cited on page 66.)

About The Author

Fadwa Joud El Merabi was born and grew up in Tripoli - Lebanon, a coastal city in the north of the country located on the east of the Mediterranean sea, in the Middle East area. She is originally from Akkar region in North Lebanon. She received her Bachelor of Science degree in 2006 and a Masters degree in Fundamental Physics in 2007 from Université Saint-Joseph, Beirut - Lebanon.

In fall 2007, she traveled to France and received, in summer 2008, her Masters of Science degree in Condensed Matter and Radiation Physics from Université Joseph Fourier Grenoble 1 - France. In fall 2008, she joined the team Optics of Nano-Objects at the Laboratoire Kastler Brossel, École Normale Supérieure, Paris - France, working toward the PhD degree in Nanophotonics. She worked also on a joint program with the Department of Physics, Faculty of Sciences at Université Saint-Joseph, Beirut.

She has two journal papers in "Optics Express", a paper in "Optics Letters", a paper in "3D Research Journal", a paper in "IEEE Journal of Display Technology" and a paper in "Ultramicroscopy Journal". Additionally, she has a book chapter in "Information Optics & Photonics : Algorithms, Systems & Applications" and several conference proceedings.

She participated to numerous International and European technical conferences and gave talks at the SPIE Photonics West (San Francisco, USA), European Conference in Biomedical Optics (Munich, Germany), European Optical Society Annual Meeting (Paris, France) and International Symposium on Modern Optics & its Applications (Bandung, Indonesia).